A Thesis Submitted for the Degree of PhD at the University of Warwick

http://go.warwick.ac.uk/wrap/59439

THE UNIVERSITY OF
WARWICK

Library Declaration and Deposit Agreement

1. STUDENT DETAILS

Please complete the following:

Full name: MOHD HASHIMI ROSLI

University ID number: 0502249

2. THESIS DEPOSIT

2.1 I understand that under my registration at the University, I am required to deposit my thesis with the University in BOTH hard copy and in digital format. The digital version should normally be saved as a single pdf file.

2.2 The hard copy will be housed in the University Library. The digital version will be deposited in the University's Institutional Repository (WRAP). Unless otherwise indicated (see 2.3 below) this will be made openly accessible on the Internet and will be supplied to the British Library to be made available online via its Electronic Theses Online Service (EThOS) service.
[At present, theses submitted for a Master's degree by Research (MA, MSc, LLM, MS or MMedSci) are not being deposited in WRAP and not being made available via EthOS. This may change in future.]

2.3 In exceptional circumstances, the Chair of the Board of Graduate Studies may grant permission for an embargo to be placed on public access to the hard copy thesis for a limited period. It is also possible to apply separately for an embargo on the digital version. (Further information is available in the *Guide to Examinations for Higher Degrees by Research.*)

2.4 *If you are depositing a thesis for a Master's degree by Research, please complete section (a) below. For all other research degrees, please complete both sections (a) and (b) below:*

(a) Hard Copy

I hereby deposit a hard copy of my thesis in the University Library to be made publicly available to readers (please delete as appropriate) ~~EITHER~~ immediately ~~OR after an embargo period of~~ ………………………. ~~months/years~~ as agreed by the Chair of the Board of Graduate Studies.

I agree that my thesis may be photocopied. YES / ~~NO~~ (*Please delete as appropriate*)

(b) Digital Copy

I hereby deposit a digital copy of my thesis to be held in WRAP and made available via EThOS.

Please choose one of the following options:

EITHER My thesis can be made publicly available online. ~~YES~~ / NO (*Please delete as appropriate*)

OR My thesis can be made publicly available only after…..[date] (Please give date)
~~YES~~ / NO (*Please delete as appropriate*)

OR My full thesis cannot be made publicly available online but I am submitting a separately identified additional, abridged version that can be made available online.
YES / ~~NO~~ (*Please delete as appropriate*)

OR My thesis cannot be made publicly available online. ~~YES~~ / NO (*Please delete as appropriate*)

3. GRANTING OF NON-EXCLUSIVE RIGHTS

Whether I deposit my Work personally or through an assistant or other agent, I agree to the following:

Rights granted to the University of Warwick and the British Library and the user of the thesis through this agreement are non-exclusive. I retain all rights in the thesis in its present version or future versions. I agree that the institutional repository administrators and the British Library or their agents may, without changing content, digitise and migrate the thesis to any medium or format for the purpose of future preservation and accessibility.

4. DECLARATIONS

(a) I DECLARE THAT:

- I am the author and owner of the copyright in the thesis and/or I have the authority of the authors and owners of the copyright in the thesis to make this agreement. Reproduction of any part of this thesis for teaching or in academic or other forms of publication is subject to the normal limitations on the use of copyrighted materials and to the proper and full acknowledgement of its source.
- The digital version of the thesis I am supplying is the same version as the final, hard-bound copy submitted in completion of my degree, once any minor corrections have been completed.
- I have exercised reasonable care to ensure that the thesis is original, and does not to the best of my knowledge break any UK law or other Intellectual Property Right, or contain any confidential material.
- I understand that, through the medium of the Internet, files will be available to automated agents, and may be searched and copied by, for example, text mining and plagiarism detection software.

(b) IF I HAVE AGREED (in Section 2 above) TO MAKE MY THESIS PUBLICLY AVAILABLE DIGITALLY, I ALSO DECLARE THAT:

- I grant the University of Warwick and the British Library a licence to make available on the Internet the thesis in digitised format through the Institutional Repository and through the British Library via the EThOS service.
- If my thesis does include any substantial subsidiary material owned by third-party copyright holders, I have sought and obtained permission to include it in any version of my thesis available in digital format and that this permission encompasses the rights that I have granted to the University of Warwick and to the British Library.

5. LEGAL INFRINGEMENTS

I understand that neither the University of Warwick nor the British Library have any obligation to take legal action on behalf of myself, or other rights holders, in the event of infringement of intellectual property rights, breach of contract or of any other right, in the thesis.

Please sign this agreement and return it to the Graduate School Office when you submit your thesis.

Student's signature: [redacted] Date: 4/12/2013

Surface defect characterisation using non-contact ultrasound

Mohd Hashimi Rosli

THE UNIVERSITY OF
WARWICK

A thesis submitted for the degree of

Doctor of Philosophy in Physics

Department of Physics, University of Warwick

December 2013

Contents

List of figures **v**

List of tables **xii**

Acknowledgements **xiv**

Declaration **xv**

Abstract **xvii**

Abbreviations **xviii**

1 Introduction **1**

1.1 Non-destructive evaluation (NDE) 1

1.2 Requirements for NDE 3

1.3 Review of conventional NDE techniques 3

1.3.1 Visual inspection 3

1.3.2 Dye penetrant inspection 4

1.3.3 Magnetic methods 5

1.3.4 Alternating current potential drop 7

1.3.5 Eddy current testing 8

1.4 Review of ultrasonic testing techniques 10

1.4.1 Conventional UT 11

1.4.2 Time-of- flight diffraction 12

1.4.3 Piezoelectric transducer 13

1.4.4 Non-contact ultrasonic generations and detections 15

1.5 Surface defects in metals 18

1.5.1 Rail defects 19

1.5.2 Stress corrosion cracking 21
1.6 The interaction of ultrasonic waves with surface features 22
1.6.1 Reflection and transmission of Rayleigh wave at a notch 23
1.6.2 Interaction of Rayleigh waves with different surface features . . 25
1.6.3 Enhancement of Rayleigh wave close to a crack 26
1.7 Machine learning methods in NDE 27
1.8 Outline of following chapters 29

2 Background theory and review 31

2.1 Ultrasonic wave theory 31
2.1.1 Stress, strain and the Christoffel equation 32
2.1.2 Phase velocity, group velocity and dispersion. 35
2.1.3 Surface acoustic waves 36
2.1.3.1 Rayleigh waves 37
2.1.3.2 Lamb waves 40
2.2 Electromagnetic Acoustic Transducers (EMATs) 43
2.2.1 EMAT transduction mechanism 44
2.2.1.1 Eddy currents and skin effect 45
2.2.1.2 Lorentz mechanism 47
2.2.1.3 Magnetisation force mechanism 49
2.2.1.4 Magnetostriction force mechanism 49
2.2.2 EMAT detection mechanism 51
2.3 Laser ultrasonic receiver 52
2.4 Machine learning 53
2.4.1 Decision tree learning 53
2.4.2 Artificial neural network 55
2.4.3 Genetic algorithm and genetic programming 57

3 Experimental details and finite element analysis 60

3.1 EMAT designs 60
3.2 Surface crack samples 63
3.3 Pitch-catch EMAT system 66
3.4 EMAT generation and laser detection 71
3.5 EMAT lift-off effects 73
3.6 Finite element analysis model 77

4 In-plane and out-of-plane EMAT measurements of Rayleigh wave interactions with full-width surface cracks 81
4.1 Wave modes identification 82
4.2 Angle dependence of transmission measurements in the far-field 87
4.3 Crack characterisation using B-scan images 92
4.4 Mode conversion and signal enhancements 97
4.5 Signal enhancement measurements in the near-field 105
4.6 In-plane and out-of-plane dominance and sensitivity to EMAT measurements 111
4.7 Summary 113

5 Classification and characterisation of full-width surface cracks using EMAT measurements 115
5.1 Automated B-scan image classification using machine learning 116
  5.1.1 Feature extraction using Genetic Programming 117
  5.1.2 Fitness functions 119
  5.1.3 Classification using Weka 121
  5.1.4 Results 121
  5.1.5 Discussion of automated B-scan image classification using machine learning. 122
5.2 Crack characterisation procedure 123
  5.2.1 Validation on two unknown machined slots 125
  5.2.2 Discussion on the validation of the procedure 128
  5.2.3 Test of procedure on rough cracks on the surface of an aluminium billet 130
  5.2.4 Discussion on the test of procedure on the rough cracks 134

6 Effects of crack width on Rayleigh wave transmission 135
6.1 Rayleigh wave diffraction around narrow-width cracks 136
  6.1.1 Diffraction around 90° cracks 137
  6.1.2 Diffraction around 25° cracks 139
6.2 Signal enhancement in the near-field of the crack 140
6.3 Spatial averaging effect 148
6.4 Comparison of EMAT measurements on cracks with different widths . . 150
6.5 Conclusions 154

7 Rayleigh wave interaction with branched surface cracks: an FEA model approach 156

7.1 Consideration of the geometry of branched crack 157

7.2 FEA model results 158

7.3 Analysis of Rayleigh wave reflections and mode-conversions 164

7.4 Effects of the branch length on Rayleigh wave transmission 169

7.5 Characterisation of branched cracks 172

7.6 Conclusions 174

8 Conclusions 175

8.1 Main findings 175

8.2 Development for future work 177

References 179

List of Figures

1.1 Alternating current potential drop (ACPD) method for measuring crack depth. Reproduced from [12]. 8

1.2 Set up for time-of-flight diffraction measurements. The figure is reproduced from [21]. 13

1.3 Surface defects in in continous casting of steel.Reproduced from [6]. . . 18

1.4 A section of rail containing a type of rolling contact fatigue crack, known as head checks (after Railtrack PLC [3]).) 19

1.5 Traditional ultrasonic inspection of rolling contact fatigue cracks. The narrow crack on the left-hand side shields the ultrasonic beam from reaching the deeper crack on the right-hand side. 21

1.6 Stress corrosion cracking, reproduced from [49]. 22

1.7 Reflection k_{re} and transmission k_{tr} coefficents plotted as a function of normalised depth h/λ. The sum of the squared coefficients $k_{re}^2 + k_{tr}^2$ represent the total energy reflected and transmitted. Reproduced from Viktotov [53].. 24

2.1 Rayleigh wave velocity behaviour with normalised depth, d/λ. d is equivalent to z in the equations used in the text. Theoretical calculation and finite element analysis (FEA) model results of in-plane and out-of-plane Rayleigh wave velocity components (a), and the ratio of the in-plane to the out-of-plane component in (b). 39

2.2 Dispersion curves for aluminium showing the phase velocity c_p (a) and group velocity c_g (b) of Lamb wave modes for the given range of frequency-thickness fh. S indicates the symmetric mode and A indicates the antisymmetric mode. The subscripts indicate the order of the modes. 41

2.3 Lorentz force generation mechanisms showing the static field contribution, $\mathbf{F}_s$ (left) and the dynamic field contribution, $\mathbf{F}_d$ (right). 48

2.4 Magnetic domains orientation in magnetostrictive materials when there is no external magnetic field ($\mathbf{H} = 0$) and when the field is present ($\mathbf{H} > 0$). 50
2.5 Magnetostriction response in polycrystalline materials. (a) Magnetisations of magnetic domains are at random orientations in the absence of the external magnetic field, **H**. (b) A domain that has magnetisation near to the field direction expands its volume at the expense of other domains. (c) Once the rearrangement is done, the magnetisation rotates to align with the external field. 50
2.6 Schematic diagram of a laser ultrasonic receiver based on two-wave mixing taken from reference [107].. 53
2.7 A typical structurure of decision tree learning. 55
2.8 A structure of artificial neural network. 56
2.9 Crossover of two parent strings using the crossover mask producing two new offsprings. The underlined bit in the parent strings indicates the bit used to form the offspring on the top right. 58
2.10 Tree representation of $\tan(x)+\sqrt{x^2+e^y}$ typically used in Genetic Programming. 58
2.11 Cross over operation between two nodes (shown in bold) producing two new offspring. 59

3.1 An EMAT made from a copper wire coil, wound around a cylindrical permanent magnet, is placed in a brass holder for protection from physical damage. 61
3.2 Magnetic fields and coil arrangement for transmitter and receiver EMATs. (a) The static, B_s and dynamic, B_d fields produce Lorentz forces F_s and F_d respectively. The predominantly in-plane (b) and out-of-plane (c) sensitivity of the receivers are shown by the open arrows. 62
3.3 (a) Experimental set up to measure the directionality of the transmitter EMAT on a square aluminium sample. The transmitter (T) is fixed approximately at the centre of the sample, and the receiver (R) detects the signal at different angles θ at a fixed distance away. The result is plotted in (b). The angle axes represents θ and the radius is the amplitude of the signal (arbitrary units). 63

3.4 Full-width crack on the surface on an aluminium bar. The inset shows the geometry of the crack, where θ is the inclination angle from surface, and d is the vertical depth. The list of all cracks with different θ and d values are given in Table 3.1(a). 65
3.5 Narrow crack geometry 66
3.6 A photo of a machined surface of an aluminium billet containing two rough cracks. The inset shows a close up view of Crack 1. 68
3.7 Schematic diagram of the experimental set up 69
3.8 Pulsed current sent to the transmitter EMAT. 69
3.9 Methods of scanning EMATs on aluminium bar sample. (a) Scan receiver only, while keeping transmitter at a fixed position, (b) Both EMATs are scanned together with fixed separation. 70
3.10 The transmitter and receiver EMATs used in pitch-catch mode with fixed separation, for scanning as illustrated in Figure 3.9(b). 71
3.11 Schematic diagram of the set up for EMAT-IOS experiment 72
3.12 Method for scanning the laser receiver on the surface of an aluminium sample containing a narrow crack. 74
3.13 Experimental set up to study the effects of lift-off. To increase the lift-off, layers of 100 μm thick plastic sheet are stacked beneath the transmitter and receiver, held in fixed separation. The spacing between the plastic layers is exaggerated in the figure. 75
3.14 Rayleigh wave peak-peak amplitude for increasing lift-off from sample surface (a). Comparison measurements are shown for a section with no slot (open circles) and for a section containing a 90° 3 mm deep slot (closed points). The error in calculating the transmission coefficient of Rayleigh passing underneath the slot increases with the lift-off (b). . . 76
3.15 Normalised fast Fourier transform of a Rayleigh wave for various lift-offs from the sample surface,for a a section that contains no slot (a) and in a section that contains a 90° 3 mm deep slot (b). 77
3.16 Plot of centre frequency of FFT as a function of lift-off. 78
3.17 Fast Fourier transform of Rayleigh waves, showing the in-plane (IP) and out-of-plane (OP) components for the experiment and model. 79

3.18 The full-width cracks are modelled as a two-dimensional finite element analysis model using PZFlex. Ultrasound generation is set at 200 mm from the crack. Wave velocity is recorded at at each element within 50 mm of the crack as indicated by the black arrows. The top surface boundary is set as free and the other boundaries are set as absorbing. . 80

4.1 (a) In-plane B-scan of a normal (90^o) crack, depth = 5 mm from experiment and (b) 2D FEM model . The main wave modes are the incident Rayleigh (R), reflected Rayleigh (R-R), and mode-converted surface skimming longitudinal wave (R-L). 84

4.2 (a) Geometry of a normal (90°) crack with generation (Gen.) and detection points (Det.1 and Det. 2). (b)-(e) Travel paths of waves reflected, transmitted and mode converted at the crack. R denotes Rayleigh wave, L denotes longitudinal wave, and S denotes shear wave. L/S indicates that the mode can either be L or S. 85

4.3 Experimental B-scans of an inclined crack, 22.5°, depth=5 mm, from two directions. (a) The acute angle, 22.5° and (b) The obtuse angle, 157.5° relative to the incident wave direction. 86

4.4 Model B-scans from 2D models of an inclined crack, of angle 22.5° and vertical depth=5 mm, scanned from two directions; (a) the acute angle, (22.5°) and (b) the obtuse angle, (157.5°). 88

4.5 A-scans of the out-of-plane measurements of a sample with a 5 mm deep 90° slot, and over a section with no slot. The dotted box indicates the Rayleigh wave. 89

4.6 Experimental transmission calibration curve. In-plane(a) and out-of-plane(b) components. 90

4.7 2D FEA model transmission calibration curve. In-plane (a) and out-of-plane (b) components. 90

4.8 Variation of transmission coefficient, C_t with slot inclination, θ for 3 mm deep slots. 91

4.9 Experimental B-scans of the data from out-of-plane measurements showing the enhancement pattern from 3 mm cracks of different inclinations, θ; (a) 90^o, (b) 22.5^o , and (c) 157.5^o, and expected arrival times for selected mode. 93

4.10 Experimental B-scans of the data from in-plane measurements showing the enhancement pattern from 3 mm cracks of different inclinations, θ; (a) 90°, (b) 22.5° , and (c) 157.5°, and expected arrival times for selected mode. 94

4.11 Bulk-wave reflection on the underside on aluminium sample. (a) No mode conversion. (b) Mode conversion. 96

4.12 B-scan of out-of-plane measurement of a 22.5°, 5 mm (vertical depth) crack. 97

4.13 Snapshots of 2D FEA model showing the interaction of in-plane Rayleigh wave velocity component with a 22.5°, 5 mm deep crack. (a) Incoming wave approaching the crack, (b) interaction caused mode conversion to Lamb-like wave, and (c) aftermath of the interaction. 98

4.14 Snapshots of 2D FEA model showing the interaction of out-of-plane Rayleigh wave velocity component with a 22.5°, 5 mm deep crack. (a) Incoming wave approaching the crack, (b) interaction caused mode conversion to Lamb-like wave, and (c) aftermath of the interaction. 99

4.15 The tapered section formed by the crack can be viewed as a wedge. It is divided into N elements of constant width, $\triangle x$ and local thickness, d_i. l is the horizontal projection of the crack length on the surface. T and R show the position of the EMAT transmitter and receiver. 101

4.16 Arrival time of A0 Lamb wave mode appended on the experimental out-of-plane B-scan of 22.5^o, 5 mm deep crack. The lines show the arrival time calculated for different frequencies. 103

4.17 A-scans from out-of-plane measurements of 22.5, 5 mm deep crack recorded in the far-field (a) and at the crack's wedge tip (b). 104

4.18 Spectrogram of the out-of-plane signal recorded experimentally at the wedge tip of 22.5, 5 mm deep crack (Figure 4.17 (b)). The solid lines show the calculated arrival times of the $S0$ and $A0$ modes for the different frequencies present in the ultrasound pulse. 106

4.19 Variation of the Rayleigh wave amplitude with the scan distance for samples containing 3 mm vertical depth slots of different inclinations. (a) In-plane, and (b) out-of-plane. 107

4.20 Enhancement factor F_E as a function of depth for 90° and 45° cracks, for (a) in-plane and (b) out-of-plane experimental measurements. The lines are a guide to the eye to show the trend of the data. 108

4.21 Variation of enhancement factor, F_E with crack inclination, θ. 109
4.22 Variation of enhancement factor ratio, F_{ER} with crack inclination, θ. . . 110
4.23 Depth profile of in-plane (solid line) and out-of-plane (dotted line) displacement of Lamb wave A0 mode on an aluminium plate with various frequency-thickness, fd 112

5.1 The "station" shows an example of how the Genetic Programming program performs image and mathematical functions to an input B-scan image. 118
5.2 Procedure for characterising surface crack 124
5.3 Experimental set up for validating the procedure shown in Figure 5.2. The details are explained in the text. 126
5.4 B-scans using the out-of-plane receiver in the direction shown by the solid arrow in Figure 5.3. The dotted lines indicate the position of the first crack edge encountered in the scan. 127
5.5 B-scan of Crack 2 for a scan in the direction shown by the open arrow in Figure 5.3, made using the out-of-plane receiver. 128
5.6 Normalised Rayleigh wave peak-to-peak amplitude in the in-plane and out-of-plane components as a function of scan distance for Crack 1(a) and Crack 2 (b). 129
5.7 A photograph of the rough cracks with the blue arrow showing the direction of scan. The red square indicates the area covered by the EMAT coil when scanning over the cracks on the aluminium billet. 131
5.8 Out-of-plane (a) and in-plane (b) B-scans of the rough cracks. Two sets of enhancement and reflections are observed in the B-scans, with the in-plane B-scan showing clearer features. 132
5.9 Rayleigh wave peak-to-peak amplitude plotted as a function of the scan distance. (a) shows the out-of-plane component and (b) shows the in-plane component. The dotted lines indicate the reference line for the peak on the right that correspond to Crack 1. 133
5.10 The depths of Crack and Crack 1 from APCD measurements in reference [13] is compared with the estimated depths using in-plane and out-of-plane EMAT measurements following procedure in Figure 5.2. . 134

6.1 Diffraction on 5 mm deep, 90° cracks of 10 mm width (left) and 20 mm width (right). 138
6.2 Diffraction on 5 mm deep, 25° cracks of 10 mm width (left) and 20 mm width (right) 141
6.3 Enhancement observed from IOS measurement made across the centre of 5 mm deep, 20 mm wide cracks; (a) 90° and (a) 25°. 143
6.4 Rayleigh wave peak-peak amplitude as a function of scan distance at various position relative to the centre of the aluminium bar containing a 5 mm deep, 20 mm wide, 25° crack. 145
6.5 Rayleigh wave peak-peak amplitudes are plotted in colour scale to show the enhancement effects around a 5 mm deep, 20 mm wide 25° crack. The crack position is at scan distance=130 mm. 146
6.6 Enhancement factor across the 90° (a) and 25° (b) cracks with different widths. 146
6.7 Enhancement factor for 90° and 25° cracks with crack width of (a)10 mm and (b) 20 mm. The x-axes show the offset from the centre of the aluminium bar. 146
6.8 First (a) and second (b) steps of spatial averaging analysis on 5 mm deep, 20 mm wide cracks of two inclinations to the surface: 90° and 25°. . . . 148
6.10 Enhancement factors F_E calculated for 90° and 25° cracks with 10 mm and 20 mm crack widths after second step of spatial averaging analysis. 149
6.9 First (a) and second (b) steps of spatial averaging analysis on 5 mm deep, 10 mm wide cracks of two inclinations to the surface: 90° and 25°. . . . 149
6.11 Enhancement observed from outof-plane EMATs measurement made across the 5 mm deep, 10 mm wide cracks; (a) 90° and (a) 25°. 151
6.12 Enhancement observed from outof-plane EMATs measurement made across the 5 mm deep, 20 mm wide cracks; (a) 90° and (a) 25° 152
6.13 Plot of normalised Rayleigh wave peak-peak amplitude as a function of scan distance using out-of-plane EMAT measurements on 5 mm deep 90° cracks of different widths; 10 mm, 20 mm and full-width. The origin indicates the position of the cracks. 153
6.14 Plot of normalised Rayleigh wave peak-peak amplitude as a function of scan distance using out-of-plane EMAT measurements on 5 mm deep 25° cracks of 10 mm and 20 mm widths, and on a 5 mm deep 22.5° crack with full-width. The origin indicates the position of the cracks. 154

7.1 Simplified geometry of surface breaking cracks. (a) Rolling contact fatigue and (b) Stress corrosion cracking. 157
7.2 FEA showing the interaction of out-of-plane Rayleigh wave velocity with 5 mm deep 22.5° crack with a branch of 5 mm in length. 159
7.3 FEA showing the interaction of in-plane Rayleigh wave velocity with 5 mm deep 22.5° crack with a branch of 5 mm in length 160
7.4 B-scan of a modelled branched crack with θ= 22.5°, d_1= 5 mm, and d_2= 5 mm. The greyscale shows the magnitude of the out-of-plane velocity component. R denotes the Rayleigh wave. 161
7.5 Spectrogram (top) of the out-of-plane velocity signal (bottom) at -50 mm from a 5 mm deep 22.5° crack with 5 mm branch. 163
7.6 Difference between the Rayleigh wave reflected from (a) two closely spaced cracks with different depth, and from (b) a branched crack. The red arrow labelled with H represents the high frequency component and the green arrow labelled with L represents the low frequency components. . 164
7.7 (a) Geometry of the modelled branched crack with generation (Gen.) and detection points (Det.1 and Det. 2). (b)-(g) Travel paths of waves reflected, transmitted and mode converted at the crack. R denotes Rayleigh wave, C denotes longitudinal wave, and S denotes shear wave. 166
7.8 In-plane (a) and out-of-plane (b) velocity B-scans for Rayleigh interaction with 5 mm deep 22.5° crack with 5 mm branch. 168
7.9 A-scans of 5 mm deep 22.5° crack for different branch length at -40 mm distance to slot. In-plane (a) and out-of-plane (b) data. 170
7.10 Reflection coefficient as a function of branch length for 22.5° 5 mm deep crack. 171
7.11 Calculated transmission coefficient of branch cracks with θ=22.5°, d_1 =5 mm appended on the experimental in-plane depth calibration curve for 90° and 45° cracks. The lengths of the branch d_2 are 1 mm, 3 mm, 5 mm, 7 mm and 10 mm. 172

List of Tables

3.1 List of full-width cracks and narrow cracks. 67

5.1 Comparison of results of the unknown cracks from the visual measurement and the ultrasound measurement following the procedure in Figure 5.2. 128

6.1 Average enhancement factors F_E calculated over crack width and EMAT coil width for 90° and 25° cracks of 10 mm and 20 mm crack widths. . 147

7.1 List of branched cracks modelled in FEA with geometry specified by θ, d_1, and d_2 (see Figure 7.1). 158

Acknowledgements

This project is fully funded by European Research Council (ERC) and supported by University of Warwick.

I would like to thank my supervisor, Dr. Rachel Edwards who gave me this great oppurtunity to work on this project. It has been an excellent experience for me, particularly in developing my scientific and research skills, and also guiding me in my career development. Thanks also to Prof. Steve Dixon who is my second supervisor.

My father, Rosli Saad and my mother, Rosidah Endut have always encouraged me to work hard, and stay focused on what I am doing. Thanks to both of them. The person I loved most, Ria Lai knows how the pursuit of this PhD has affected our lives, and I cannot thank her enough for being here. Soon, I hope I can spend more time with you and our little Hasif.

There are strong support I received from the ultrasound group, and everyone in the group has been brilliant. Thanks to Charley Fan being the master of EMAT, who has helped me to design and produce mine. I also would like thank him for his expert advice on the modelling side of my project. The next two person I would like to thanks are Ben Dutton and Andy Clough, who helped in me in setting up my experiments in the laser room, and allow me to use their equipments. Thanks also to Phil Petcher, Francisco Hernandez-Valle, and Sam Hill for their kindness and their help when I needed it. Thank you to anybody else I have missed to mention here for providing great support.

Declaration

I declare that the work presented in this thesis is my own except where stated otherwise in the references. The work was carried out at the University of Warwick during the period between September 2008 and April 2013, under the supervision of Dr. Rachel Edwards. The research reported here has not been submitted, either wholly or in part, in this or any other academic institution, for admission to a higher degree. Part of this work, and other work not reported in thesis, have been published as shown in the list below.

Peer reviewed journals:

1. M. H. Rosli, R. S. Edwards, Y. Fan, "In-plane and out-of-plane measurements of Rayleigh waves using EMATs for characterising surface cracks", *NDT & E International*, vol 49, pp. 1-9, 2012.

2. R. S. Edwards, B. Dutton, A. R. Clough, M. H. Rosli, "Enhancement of ultrasonic surface waves at wedge tips and angled defects", *Applied Physics Letters*, vol 99, Issue 24, Dec 2011.

3. B. Dutton, A. R. Clough, M. H. Rosli, R. S. Edwards, "Non-contact ultrasonic detection of angled surface defects", *NDT & E International*, vol 44, Issue 4, July 2011

Conference proceedings (ISI index):

1. F. Hernandez-Valle, R. S. Edwards, A. Clough, M. H. Rosli, B. Dutton, "Laser generation and detection for surface wave interaction with different defect geometries" in *Review of Progress in Quantitative Nondestructive Evaluation*, vol. 32, 2012, pp. 324-329.

2. M. H. Rosli, R. S. Edwards, "Analysis of Rayleigh wave enhancement close to

inclined surface cracks", *Review of Progress in Quantative Non-destructive Evaluations,* vol 31 2012.

3. R. S. Edwards, B. Dutton, M. H. Rosli, "Non-contact ultrasonic characterization of angled surface defects", *Review of Progress in Quantative Non-destructive Evaluations,* vol 30, 2011, pp. 647-654.
4. M. H. Rosli, R. S. Edwards, B. Dutton, C. G. Johnson, P. Cattani, "Identifying surface angled cracks on aluminium bar using EMATs and automated computer system", *Review of Progress in Quantative Non-destructive Evaluations conference*, vol 29
5. B. Dutton, R. S. Edwards, M. H. Rosli, "Defect feature extractions using surface wave interactions and time-frequency behaviour", *Review of Progress in Quantative Non-destructive Evaluations,* vol 29, 2010, pp. 647-654.

In-progress for journal publications:

1. M. H. Rosli, R. S. Edwards, *Effects of crack widths on Rayleigh wave transmission.*
2. M. H. Rosli, R. S. Edwards, *The interaction of Rayleigh wave with branched surface cracks: an FEA approach.*
3. M. H. Rosli, R. S. Edwards, *Rayleigh wave application for characterising surface defects: inclined and branched cracks.*

Abstract

Electromagnetic acoustic transducers (EMATs) have been used as a non-contact ultrasound approach for detecting and characterising surface defects in aluminium bars and billet. The characterisation was made from understanding the interaction of broadband Rayleigh surface waves with surface crack growing normal or inclined to the sample surface, based on rolling contact fatigue (RCF) cracks in rail tracks.

The interaction with normal cracks have been previously reported. For inclined cracks, mode conversion of Rayleigh waves to Lamb-like waves occur in the wedge section formed by the crack, resulting in strong and prominent enhancement in the signal detected. This is confirmed by finite element analysis (FEA) models and Lamb waves arrival times calculation. Signal enhancement from the interaction creates features in B-scan images, and they have been used for initial crack classifications. Then, a number of analyses were performed to estimate the crack inclination, and accurately determine the crack vertical depth. A feature extraction and image classification program based on genetic programming have been developed (through a collaboration work) to perform automated classification on the B-scans. The program produces more than 90% accuracy using the experimental data set.

The viability of EMATs to detect and fully characterise narrow cracks have been investigated through experiments using laser interferometer and comparison with EMATs measurements. The results confirmed that narrow cracks can be detected with EMATs, with initial classification (in B-scans) to normal/inclined. However, the depth sizing may not be accurate, and suggestion for better designs of EMATs have been made. FEA models have been used to study the interaction of the Rayleigh waves with branched cracks. Interesting results are observed in terms of Rayleigh waves reflections, which helps to determine the presence of a branch on RCF-like cracks. A method has been proposed for calculating the length of the branch, following a number of analyses.

Abbreviations

AC	Alternating Current
ACPD	Alternating Current Potential Difference
ADC	Analogue-to-Digital Converter
ANN	Artificial Neural Network
DC	Direct Current
DPI	Dye Penetrant Inspection
EMAT	Electromagnetic Acoustic Transducer
EMF	Electromotive Force
FEA	Finite Element Analysis
FEM	Finite Element Method
FFT	Fast Fourier Transform
GA	Genetic Algorithm
GP	Genetic Programming
MFL	Magnetic Flux Leakage
MPI	Magnetic Particle Imaging
NDE	Non Destructive Evaluation
NDT	Non Destructive Testing
UT	Ultrasonic Testing
RCF	Rolling Contact Fatigue
SAW	Surface Acoustic Wave
SCC	Stress Corrosion Cracking
SH	Shear Horizontal
SNR	Signal-to-Noise Ratio
SV	Shear Vertical
TOFD	Time-of-Flight Diffraction

Chapter 1

Introduction

This chapter describes the definition and the requirement for non-destructive evaluation (NDE). The research reported within this thesis has used an NDE method, in particular non-contact ultrasonics, to detect and characterise surface defects. A number of conventional NDE techniques are reviewed, with more attention given to ultrasonic testing due to the topic of this thesis. Different types of surface defect in metals, and the available NDE methods of detecting and characterising them are reviewed. Ultrasonic techniques offer practicality for accurate measurements, and the capability for fast inspection. To make use of knowledge from previous work on characterisation of surface defects using ultrasonic techniques, a literature review is conducted on the interaction of ultrasonic wave with surface features. Machine learning methods have been used for classification of ultrasound images (B-scans) in this study, and previous work on the use of machine learning in NDE is also reviewed.

1.1 Non-destructive evaluation (NDE)

Metallic components and structures which are highly in use require regular checks to make sure they are in safe condition to operate [1]. Consider a power plant environment for example, where there are large numbers of pipes carrying gas, fuel and water for coolant. Depending on the enviromental exposure of the pipes, they can develop defects such as corrosion and cracking [2]. Such defects, if left undetected, can cause damage to the individual pipes, and potentially can also trigger destruction on a larger scale, if the damage is affecting other pipes or the power plant structure . A second example can be found in the rail environment, where there is a need to check railtracks regularly for defects that can cause train derailments [3, 4]. In addition to the exposure to different weather conditions, the railtracks are also in contact with the train wheels when they are passing, which exert load and friction on the surface and body of the rails.

Regular checks are also required for metal components that are not continually in service [5]. This applies to the manufacturing environment, where the components which could be the final products need to be inspected to ensure they meet the specifications. Steel and aluminium billet production is one example where the component is the final product [6]. However, in some cases, the component is not the final product, but forms part of it, for example, the rotating blades for aircraft engines. Each blade is produced separately, and they would require a thorough check before installed in the main engine. If any of the blades contain defects, or do not meet the specifications standard, the whole engine would be at risk of failure. Ideally, any imperfections on the blades need to be detected immediately after their production, before being passed to the next process.

The examples given above show that regular checks are important for components that are in service and also for components in the manufacturing process. The regular checks typically consist of a test or a series of tests conducted on the components. The test can be destructive, such as removing a small part of the components to be inspected under a microscope or a similar device. An immediate disadvantage of this is that the component is damaged after the test, as it would not be in the same state as it was prior to the test. This is somehow defeating the purpose of the regular checks, as it can cause more damage to the component than any potential defects. In some situations, a sampling method is used, where the test is conducted on one component from say a hundred samples. Although this can reduce the number of components being damaged from the test, it does not rule out the possibility of missing components with defects. Ideally, the same test should be conducted on each sample or component.

A test performed on samples or components without causing damage to them is known as non-destructing evaluation (NDE). With NDE, following the test the sample will be in the same condition as it was prior to the test, and the test should not affect its functionality. NDE is sometimes referred to as non-destructive testing (NDT) and non-destructive inspection (NPI). Throughout this thesis, NDE will be used.

1.2 Requirements for NDE

The need for the test to be done non-destructively can arise in several situations, the most basic of which is when the sample is not tolerable to any damage, or when the sample to be tested is permanently installed as part of a larger structure, and is not viable to remove the sample for a test to be done elsewhere [7]. NDE techniques allow the test to be done on the site. In addition, the environment where the sample is located sometimes restricts the access to the sample, and any test that is going to be performed must be able to work around this restriction [7]. There are also considerations for the time taken to perform the test. If the sample is removed from service and needs to be taken elsewhere, the time of it being out of service can cause a major disruption. For example, consider if a power plant needs to be shut down each time a test is performed, or a train service is cancelled each time a section of rail needs to be tested. Clearly, the test should be done on site with the least amount of time disruptions.

The test for checking reliability or for detecting defects is normally considered as part of the maintenance service, so will be done at a certain frequency [5]. Here, practicality is an attractive point for the test to be done non-destructively. A non-destructive practical approach is preferable compared to laborious non-practical methods. Frequent inspections will increase the probability of detecting defects in the samples. Although NDE normally does not involve inspection at the microscopic level, the accuracy of the chosen measurements performed will be good enough to provide information of any defects presents in the sample. For this reason, NDE serves the purpose of detecting defects in the sample, giving a good indication of the severity of any problems based on the defect size.

1.3 Review of conventional NDE techniques

In this section, a number of conventional NDE techniques are reviewed. The basic principles and uses of these techniques are explained briefly. Ultrasonic NDE technique will be described separately in Section 1.4.

1.3.1 Visual inspection

Visual inspection is the most basic form of NDE. The inspection of test samples is performed using the human eye, with or without visual aids, for example, hand-held lenses. [1, 7]. It is a simple technique, but it is also an important step in NDE, and visual inspection can be performed even when there are more advanced NDE technique available. Surface breaking defects are often visible on the sample surface. A quick inspection of the defect features on the surface can help to decide the appropriate inspection method, and for the case of ultrasonic testing, it can help to decide which area to inspect.

Optical aids, such as hand- held lenses and industrial telescopes (boroscopes and introscopes), are commonly used for magnification. The holographic method has also been used to reconstruct a three-dimensional image of an object superimposed at its original position. In this method, a slight movement or a local deformation on the object, can be detected through the change in the interference fringes produced. A high resolution digital camera can be employed to record the image of the surface condition, and the processing can be made in real-time or at a later time. In order to enhance the visibility of the defect indications, high contrast and coloured liquids or powders can be applied on the sample surface. Examples of this are magnetic particle inspection and penetrant inspection.

1.3.2 Dye penetrant inspection

Dye penetrant inspection (DPI) is another technique for imaging surface defects, with similarities to magnetic particle imaging (MPI) [5]. A contrast agent or penetrant, usually in the form of a liquid, is applied to a defective area of sample. The penetrant will fill up the opening of any defects and follow the shape of the defect on the surface [8]. When the area is viewed under a visible light or an ultraviolet light, the defects will apear in high contrast against the background, creating a suitable condition for capturing a good image. The area is then scanned to look for particular indications of defects. This can be done on the test site using human observation, or the image of the area can be captured using a camera and read into an image analyser for pattern recognition.

In DPI, the defective area of a sample needs to be clean before the penetrant is applied. The presence of dirt, scale or grease will tend to accumulate the penetrant, thus affecting the features on the image produced. This can either mask a real indication of defect, or give a false indication when there is no defect present. When the inspection process can be done in a controlled environment using an automated system [5] , this technique can perform well. However, in the case where the sample requires extensive cleaning or removal of paint or coating, DPI needs to be done manually, which is time consuming. In addition, the application of penetrant on samples means that this technique requires direct access to the sample surface. Therefore, it cannot be used when direct access to the sample is not possible, for example, in a high temperature environment, or when the sample is constantly moving.

Technical details of the application of DPI for surface cracks are covered in great length in [1, 5]. DPI has similarities to MPI in terms of the advantages and drawbacks. These methods are capable of revealing the shape of the defect on the surface, but cannot provide information on the defect depth underneath the surface. DPI has a slight advantage over MPI, that it can can work on a wider range of materials as it does not require the sample to be magnetic. It is also important to mention that the application of dye penetrant on samples can sometimes cause harmful effects, if the penetrant is left on the sample without a proper cleaning after the inspection. The chemical reactions from the penetrant residue could initiate crack growth in the sample.

1.3.3 Magnetic methods

Magnetic methods refer to techniques that work based on the distortion of magnetic fields in ferromagnetic samples. Examples of this method are magnetic flux leakage (MFL) and magnetic particle inspection (MPI), which can be used to detect surface and sub-surface defects [7]. Although, each of these methods has a different origin in NDE, their basic principles are similar. The sample that is going to be tested is initially magnetised, using either a permanent magnet or an electromagnet. A magnetic field will be generated in the inspected area and acting in a specific direction. The magnetic flux density increases with the field strength. When a defect is present within the area, the magnetic field is distorted, and causes a flux leakage above the surface on the sample. Therefore, the presence of the flux leakage indicates the presence of the defect. Once the test is completed, the sample is demagnetised to its initial state.

MFL and MPI are different in the way they detect the flux leakage. In MFL, the flux leakage is detected either using an inductive coil or a Hall effect probe. The inductive coil gives an indication of the flux leakage by producing a voltage known as electromotive force (emf), when the coil is in motion above the flux, or when there is a change in the field if the coil is stationary [9]. This is based on Faraday's law of electromagnetic induction. Meanwhile, the Hall effect probe works based on the effect of the field B acting on the probe element. An element is made from a conductor of area A, and thickness t, and a current I is assumed to flow along one axis. When the element is exposed to the a B acting normal to the plane of the element, a voltage V is induced at right angles to the direction of the current. The voltage V is given by

$$V = \frac{BA}{Rt}, \tag{1.1}$$

where R is the Hall coefficient of the material.Hence, the MFL method gives an indication of the flux leakage as a voltage. The MPI on the other hand, gives the indication visually. This is done by applying ferromagnetic particles in the form of powder, or in a liquid suspension, to the inspected area. The particles will accumulate around the area of the flux leakage at the position of the crack. In addition, the particles' accumulation will follow the shape of the defect; thus, if it is surface breaking, allowing for the defect shape and size to be visible on the sample surface,highlighting one of its advantages. In practical application, the inspected area can be painted with white paint to enhance visibility. Coloured particles are also used to achieve a good contrast of the defect shape with surrounding areas.

When applying magnetic methods to evaluate a sample, there are considerations for the direction of the magnetisation. Ideally, the magnetisation direction must be normal to the main axis of the defect, in order to maximise the distortion of the magnetic field. As the defect becomes more aligned to the magnetisation direction, the magnetic field will be less distorted, and consequently less flux leakage is present above the surface. To overcome the problem of low visibility for MPI or low voltage for MFL, the magnetisation direction can be applied initially in one direction, then gradually turned until a maximum visibility (MPI) or voltage (MFL) is achieved.

These magnetic methods have a number of drawbacks. As the defect identification is done using the flux leakage, there is no clear indication of the defect below the surface. However, an NDE operator can make an educated guess based on the relationship of the defect surface length with the defect depth [3]. Some preparation is needed to conduct this inspection, such as surface cleaning, and applying contrast agent (e.g paint for the case of MPI). This subsequently would also require a cleaning after the test is conducted. Most importantly, in the demagnetisation process, the sample should be brought back to its original magnetic field state. Any magnetic field residue left can cause error in future tests, or cause the sample to behave differently when close to other materials.

1.3.4 Alternating current potential drop

Alternating current potential drop (ACPD) is an electromagnetic technique for used NDE. It is suitable for monitoring crack growth [10], and to estimate the depth of surface breaking cracks [11]. Typically, APCD measurements are performed using a four-point probe, as illustrated in the schematic diagram in Figure 1.1 [12]. The probe is divided into two pairs of electrodes. The first pair inject current to the sample, and the second pair measures the resulting potential difference (voltage) between two points on the surface. Alternating currents (AC) flow between the current electrodes, and within the skin depth of the sample. When a crack is present between the voltage electrodes as shown in the figure, the current is forced to flow around and below the crack, resulting in a longer path being taken. The extra path travelled can be approximated as the distance from the surface to the bottom of the crack and coming back to the surface on the other side of the crack, or simply the depth of the crack h times two.

The constant current technique is the usual method typically applied to ACPD. The distance of the current flow between two electrodes is related to the resistance, and can be used as the measure of the resistance. The current will be constant when the crack is either present or not. If the voltage across the two voltage probes is V_1 when there is no crack present, and V_2 when the crack is present, the relationship between them can be calculated using Ohm's law. The relationship can be simplified to:

$$\frac{V_1}{D} = \frac{V_2}{D + 2h}. \tag{1.2}$$

where D is the distance between the current electrodes [1]. From Equation 1.2, the depth of the crack h can be calculated using the measured value of V_1 and V_2, and known value of D. The equation also implies that there is no prior calibration required to obtain the value of h. This, however, depends strongly on the sample properties. Thus, the relationship given in Equation 1.2 is true for a specific material, and can only be applied to samples of the same material. The quality of the contract between the probe and sample can also have some effect on the ACPD measurements. To overcome this, the electrodes are spring loaded to the sample surface to keep the quality of the contact consistent in all measurements.

The ACPD technique has been used as a comparison to the depth measurement made using another technique [13]. It can also be used as a complimentary method to other imaging technique such as the MPI and the DPI. The imaging techniques reveal the surface characteristic of the crack, such as the surface length, while the ACPD

This figure has been blanked out due the
author has no permission to reproduce.

Figure 1.1: Alternating current potential drop (ACPD) method for measuring crack depth. Reproduced from [12].

estimates the crack depth. It is important to note that the crack depth measured here is the actual length of the crack. For a crack oriented normal to the surface, as shown in Figure 5.10, the actual length equals the crack depth, but if the crack is inclined at an angle to the surface, the length and vertical depth are not the same. For this reason, the ACPD technique cannot accurately determine the actual depth of inclined cracks, nor give an indication of whether the crack is normal or inclined to the surface. Thus, it is not always the best method for fully characterising inclined cracks such as RCF and SCC.

1.3.5 Eddy current testing

The underlying principle of eddy current testing is based on the physics of electromagnetic induction [9]. An oscillating current flowing in a coil generates a changing magnetic field B_p around the coil. When the coil is brought close to a conductive material, the magnetic fields induce a current in the material according to Lenz's law [14]. This current is known as an eddy current, and it flows in the opposite direction to the current in the coil. The depth in which the eddy current is present is known as the skin depth δ , and is given by [5] (Section 2.2.1.1).

$$\delta = (\pi \mu \sigma f)^{-1/2} \tag{1.3}$$

where the test material is described by its permeability μ and conductivity σ, and f is the source current frequency. The eddy current itself generates a changing magnetic field B_s in the sample which opposes B_p, and therefore the resultant field B_t would be the difference between B_p and B_s, i.e

$$B_t = B_p - B_s. \tag{1.4}$$

B_t oscillates at the same frequency as the source current in the coil. As the magnetic field is changing through the coil, according to Faraday's law [9], an electromotive force (emf) will be induced in the coil. A voltmeter can be connected across the coil to measure the voltage, and the coil impedance Z can be calculated using Ohm's law, $Z = V/I$, where I is the oscillating current in the coil. When defects such as surface and sub-surface cracks, or flaws such as material degradation and corrosion are present on the material surface, the induced eddy current is disturbed. This causes a change in the resultant field B_t, and the calculated impedance Z of the coil. The change in B_t can be detected using a Hall-effect sensor [5, 15]. In practice, the change in voltage or impedance are recorded in the time domain. Following this, signal processing analysis can be applied to the recorded signal to reveal any useful features, such as amplitude change or phase change, that can be associated with size and position of defects relative to the surface [16].

The depth of penetration of eddy current testing is typically given by the skin depth δ. As shown in Equation 1.3, δ depends on the frequency of the AC current. Therefore, for a single frequency current, this technique can only probe to a certain depth. This can limit the usability of this technique. To overcome this problem, eddy current testing can be performed using a number of different frequencies to increase the detection range [17], or by sweeping the current with a range of frequencies. A more recent method, known as pulsed eddy current (PEC), has been developed [18]. This method uses a step function voltage to excite the current in the probe, which results in a broadband frequency pulse. With just a single pulse, the probe can measure a range of depths. PEC has been used with other NDE technqiue for better characterisation of defects [19].

The eddy current testing technique in general has an advantage over other conventional NDE techniques described above in the sense that it does not require the probe to be in contact with the sample. An air gap between the probe and the sample surface, which is known as lift-off, is allowed, but it can affect the efficiency of the measurements. Thus, the lift-off is kept to a minimum to get an optimal electromagnetic induction from the coil to the sample. In addition, an eddy current generated in the sample is dependant on the material properties such as the permeability and conductivity, as shown in Equation 1.3. If the flaw which is present is changing any of these properties, it can complicate the interpretation of the measurement results.

1.4 Review of ultrasonic testing techniques

Ultrasonic testing (UT) is one of the most developed branches of NDE techniques. In UT, a vibrational wave which has a frequency typically greater than 20 kHz is set to propagate into a material in order to look for defects, or to gain information about the material properties [20, 21]. In the former, the interaction of the wave with defects, such as reflection, transmission and diffraction of the wave, are utilised for locating and sizing the defect. The latter is used to calculate material properties that are related to the ultrasound propagation in the material, such as the elastic constants, which are related to the wave speed [22]. In this research, the interest is in defect detection. UT is attractive for this task because it allows for fast inspection and accurate measurements of defect location and size. Measurements made using UT for defect detection include the time of flight of the wave, the path length, frequency, phase angle, amplitude, impedance, and angle of deflection [5, 20, 21, 23, 24].

The vibrational waves used in UT include longitudinal waves, shear waves, and surface waves. To some materials, the advantage of the use of ultrasound compared to other NDE techniques is that it can penetrate into the bulk of the sample. For materials that are good at scattering ultrasonic waves like rubber, concrete and certain type of welds, UT is not a good option. UT can be performed either in pulse-echo mode, in pitch-catch mode, or in through-transmission mode. The first two modes are suitable when access is only from one surface. In pulse-echo mode, an ultrasonic transmitter sends waves into a sample and detects the reflections from defects or the backwall. The same transducer is used to transmit the waves and to receive the reflection signals. In pitch-catch mode, the waves sent by the transmitter propagate along a sample, passing a defect, and are detected by a receiver located behind the defect. The through-transmission mode is similar to the pitch-catch mode, except the receiver is located on the opposite surface of the sample. It can be used to detect internal defects, or for thickness measurement. Relatively, the pulse-echo mode is often slower for scanning than the pitch-catch mode, as there is a time delay while the incident wave is reflected back to the transducer.

Significant progress has been made in the development of UT to date, with recent example of progress including time-of-flight diffraction (TOFD) and phased array ultrasonics. The following subsections review these techniques, including the conventional UT methods that have been widely used in industry. A review of the generation and detection methods of ultrasound has also been conducted, and is presented in Section 1.4.3 for commonly used piezoelectric transducers, and in Section 1.4.4 for various non-contact methods.

1.4.1 Conventional UT

Conventional UT generally employs the pulse echo method. The commonly used technique is known as the 6dB drop [20]. It is best used for detecting defects propagating perpendicular to the ultrasound beam, in order to get the maximum reflection. An angle probe can be used to detect a defect at an angle to the perpendicular line. In the 6dB drop technique, a transducer is moved along the suspected area containing a defect until the amplitude of the reflected wave from the crack drops by 6dB. This occurs when the ultrasound beam is over the edge of the defect. To get the lateral size of the defect, the transducer is then moved in the opposite direction to detect the other end of the defect. The distance of the defect from the transducer (usually the "depth") can be calculated from the arrival time of the reflected signal. This technique however is not accurate for detecting defects which have dimensions smaller than the size of the ultrasound beam. For small defects, such as in welds, the 20dB drop method is more suitable [20]. Prior measurements are made on calibration blocks containing holes of different sizes to obtain the ultrasound beam profile. This is then used to determine the position and the depth of defects from surface.

There are also methods available that do not require the movement of the transducer. These methods are known as amplitude methods, such as the distance amplitude correction (DAC) and the distance gain size (DGS) [20]. In the DAC method, the amplitude of the reflection from a defect is compared with a calibration made on known artificial target, such as a flat-bottom hole in a block made of the same material. A correction to the amplitude is made for a defect located at the distance known as the far-field of the ultrasound beam, where the distance varies inversely with the ultrasound wavelength. The use of the calibration block is eliminated in the DGS method, where a calculation of how the amplitude from disc reflectors of different diameter would behave is made and plotted in a graph as a function of distance from the source. This would cover the near-field, and the far-field region of the beam.

The basic UT techniques described here have similar disadvantages. The region immediately behind the target defect, known as the blind zone cannot be probed by the ultrasound beam as it is shadowed by the defect. If another smaller defect is present within this region, it would not be detected. Artificial target defects (flat bottom holes) of different sizes are required to established the correct amplitude to be used as a reference for the comparison. For the DGS method, the calculation made should be initially verified with actual measurements because there can be irregularities in the shape and surface finish of the actual block.

1.4.2 Time-of- flight diffraction

The time-of-flight diffraction (TOFD) technique was invented in the late 1970s, at the National NDT Centre, Harwell by Dr Maurice Silk [21]. Before the invention of TOFD, UT was based on pulse-echo inspection, which relies on the detection of the reflections from defects. In TOFD, the detection is aimed to detect the diffracted waves, and to avoid the specular reflections which may mask them.

A typical set up for TOFD is shown in Figure 1.2, which is reproduced from [21]. In the set up, an ultrasonic transmitter T and receiver R are set in pitch-catch mode, and positioned at 2S distance apart on the surface of the test material. A defect of size a, is located a distance l beneath the surface, in the bulk of the material, and is symetrical between the transmitter and the receiver. Ultrasonic waves are generated by the transmitter and detected by the receiver. The defect detection and sizing in TOFD are based on the arrival times of the diffracted waves from the tips of the defect. In theory, the surface wave is the first one to arrive at R, followed by the diffraction from the upper tip shown by the path $d_1 + d_2$, then from the the lower tip $d_3 + d_4$, and finally the backwall echo. The surface wave and the backwall echo set the time limits on when the diffraction arrival times should take place. The depth of the defect beneath the surface l can be calculated from the arrival times by considering the geometry. Similarly, the size of the defect a can also be calculated from the difference in the arrival times of the diffracted waves from the upper and the lower crack tips. In practice, the transmitter and the receiver are scanned on the material surface while maintaining a fixed separation, in order to achieve the symmetrical configuration as shown in Figure 1.2. This is determined when the delays between the diffracted waves area at minimum .

The time domain signals (A-scans) recorded during the scan are normally presented as B-scans. A-B-scan is formed by stacking a number of A-scans in a matrix, where

This figure has been blanked out due the
author has no permission to reproduce.

Figure 1.2: Set up for time-of-flight diffraction measurements. The figure is reproduced from [21].

each column in the matrix corresponds to an A-scan at a different scan position, and the matrix is plotted as colour plot. The amplitudes of the A-scans are shown by the grayscale in the B-scan, where the amplitudes increase from dark to bright. In B-scans, normally most wavemodes present in the scan can be observed. They can be identified from their arrival times [20], or by specific features. A defect in the test material can be assumed to act as a point scatterer to the incoming wave from the transmitter, thus the defect can be recognised by parabolic features in the B-scan [25]. As the diffractions at the crack tips occur weakly, their amplitude can be much smaller than the direct surface wave, and so the diffractions' parabolic pattern can be obscured by the higher amplitude surface wave in the B-scan. Moreover, the reflection of the surface wave from the edge of the material can also disrupt the signal diffracted by the receiver, adding complexity in interpreting the B-scan. A recent development in signal processing of TOFD measurements has created a method to remove the direct and reflected surface waves, using a modified Hough transform, allowing for easier intepretation of the B-scan [26].

1.4.3 Piezoelectric transducer

Standard ultrasonic transducers work based on the piezoelectric effect [20]. A material which is piezoelecric produces electric charges on the surface when deformed by an external stress σ. When the stress is applied in the opposite direction, the electric charges are reversed in sign. The electric charges produced are proportional to the applied stress σ within the elastic limit, and the relationship is given by

$$P = \sigma d, \tag{1.5}$$

where P is the polarisation (charge per unit area), and d is the piezoelectric strain constant. The piezoelectric effect also works inversely; If two electrodes are now connected to the piezoelectric material, and an electric potential E is applied, the material will change shape. The mechanical strain S produced from this is proportional to the electric potential E, provided that there is no mechanical loading and assuming the elastic limit, and their relationship is given by

$$S = Ed. \tag{1.6}$$

Equation 1.6 indicates that, when the electric potential E is alternating, the material will repeatedly change its shape, creating a mechanical oscillation in the material which can be coupled into a sample to generate ultrasonic waves. Piezoelectic transducers require couplant, such as a liquid or gel, in order to efficiently transfer the vibration into a test sample, due to the acoustic impedance mismatch with air. The choice of the couplant would take account of the acoustic impedance of the piezoelectric transducer, the couplant itself and the test sample. A good acoustic impendance matching would allow maximum transfer of energy from the transducer to the sample. A bad acoustic impedance matching results in more of the wave energy being reflected back into the transducer, thus low energy transfer.

Natural crystals like quartz and lithium sulphate are known to be piezoelectric, and fabricated polycrstalline ceramics such as barium titanate can be polarised to exhibit piezeoelectricity [27]. These materials are used to make piezoelectric transducers.

Piezoelectric transducers have been used extensively in NDE due to their high efficiency, and good signal to noise ratio (SNR) depending on sample. However, in some situations,there are limitations to their use. As an example, in a hostile high temperature environment, the standard piezoelectic materials will change properties as they pass through their low Curie temperature, and therefore are no longer piezoelectrically active [20] . Some ferroelectric/piezoelectric materials, such as bismuth titanate and aluminium nitride, possess high Curie temperatures, and have been developed for high temperature measurements [28]. However, the bismuth titanate transducer described in [27], for example, requires direct contact with the sample, and therefore is more suitable for permanently installed monitoring rather than online inspection.

In addition, the use of piezoelectric transducers sometimes can require the removal of any coating or the paint in order to get access to the test sample. In some cases, this is not possible, or would require extensive surface preparation, and this can increase the inspection cost and time. In these cases, a non-contact method is preferable to keep the sample clean and to run a fast inspection.

1.4.4 Non-contact ultrasonic generations and detections

There are several techniques available for non-contact ulrasonic measurements. The most common are laser generation and detection, air-coupled transducers, and electromagnetic acoustic transucers (EMATs) [29, 30]. Each of these techniques can be used with other techniques as a hybrid system, for example laser generation with EMAT detection [25,31], or a laser generation with air-coupled detection [32] . The techniques are discussed briefly here, with discussion of their advantages and the disadvantages. The basic theory of the laser detection used in the experiments reported in this thesis will be explained in Section 2.3, and the theory of EMAT operation and the full review of previous work on EMATs will be covered in Section 2.2.

A pulsed laser beam can be used to generate ultrasound in materials through thermoelastic or ablative generation [33]. In thermoelastic generation, no damage is caused to the sample surface as the energy density of the laser beam used is low [34]. When the laser beam illuminates a region on the material surface it causes a rapid increase in the temperature and a small thermal expansion. The volume is free to expand in the direction normal to and away from the surface, but it is constrained from expanding in the plane of the surface, due to the colder surrounding material. This expansion causes an elastic strain that creates a compression wave normal to the surface. Due to mode conversion, a shear wave will also be present. In ablative generation, a higher energy density of laser beam is used which will ionise part of the surface, forming a plasma. This creates a force for the generation of waves. This process causes a small amount of damage to the surface which can be observed as a mass ejector crater. Essentially, ablative generation is destructive to the material, however, the damage caused by this method is considerably small to the whole structure of the material. A later development of this type of laser generation focuses the laser beam to create a plasma just above the material surface [29,35]. This way, the high energy density laser beam is not applied directly to the material surface, avoiding damage. The advantage of ablative generation is that it generates large amplitude signals compared to the signals generated by thermoelastic generation.Laser detection of ultrasound can be performed in various ways [33, 36, 37]. To choose the most suitable method, the requirements of the measurements and the capability of each laser detector must be considered. For example, if the measurement is to be performed on rough surfaces, requiring the detector to be scanned along the sample surface, the detector must be able to work without sample polishing, and without realignment after every scan step. In general, laser detection falls into two categories; interferometric technique and amplitude variation technique. The interferometric method makes use of the difference between a reference beam and the reflected beam from the sample surface, to relate to the sample surface displacement as the ultrasound wave propagates. Examples of this method are Michelson and Fabry-Perot interferometers [33]. The amplitude variation methods, such as the knife-edge technique [37], work based on the idea that when ultrasonic waves arrive at a point on the sample surface illuminated by a laser beam, the reflected beam will move, at the same rate at which the ultrasonic wave disturbs the point. The knife-edge technique is easier to align compared to the interformetric detector, but it is less sensitive and relatively lower in cost.

The combination of laser generation and laser detection of ultrasound allows the UT to be performed without having contact with the sample, with the possibility of a large separation or stand-off from the sample (of the order of metres). Thus, it has the advantage that it can be remotely used in a hostile environment, such as a high temperature environment, where piezoelectric transducers may not work. However, the drawbacks are that a laser system is usually significantly more expensive than any other non-contact ultrasonic method, and the use of a laser beam raises health and safety issues.

Air-coupled transducers have been developed as an alternative to standard piezoelectric transducers, for inspecting materials that can be damaged by water (or other couplant), such as paper, foam type materials, electronic circuits, certain types of woods, and advanced material in the aerospace industry [38]. The working principle of air-coupled transducers is similar to that of standard piezoelectric transducers . A piezoelectric material is used to convert electrical potential into mechanical vibrations, and the vibrations are transferred to the test material through the air. The characteristic impedance of air is usually very different to that of the test material, and therefore a matching layer of a quarter-wavelength of the frequency used is introduced. However, the problem with the use of a matching layer is that it limits the overall bandwidth of the transducer.

Air-coupled transducer designs based on capacitance or electrostatic principles have been developed with better bandwidth than standard air-coupled transducers [39]. Capacitive transducers consist of a thin membrane film and a rigid conducting back plate to form a capacitor. When a voltage is applied, the membrane vibrates and generates ultrasound. A change in the charge across the membrane can be used for detection. Typically, the air-coupled transducers are used as transmitter and receiver in the through-transmission set up [40]. Ultrasonic waves transmitted by the air-coupled transducer propagate through the volume of the test material, and any abnormalities in the material can be deduced from the wave detected by the receiver. EMATs or laser generation can also be with used with the air-coupled transducer in this set up, depending on sample properties.

EMATs offer a relatively inexpensive alternative for non-contact UT [29]. EMATs can generate and detect ultrasound only in electrically conducting materials with a lift-off (height from sample surface) up to a few milimetres. Normally, the use of EMATs does not require the sample to be cleaned prior to inspection, except when the presence of scales on the sample surface can affect the properties of the permanent magnet in the EMATs. With EMATs, acoustic energy is coupled directly to the ions in the sample through the electromagnetic wave propagation [41]. The ultrasound generation occurs in the sample skin depth δ, through the Lorentz mechanism in all conducting materials, and with additional magnetostriction and magnetisation mechanisms occuring in magnetic materials [42, 43] (described in detail in Section 2.2.1). EMATs have lower efficiency compared to piezoelectric transducers. Recent developments in EMATs has shown different designs of EMATs that can work in a high temperature environment using active cooling [31], and without active cooling, when using a pulsed electromagnet [44].

Each non-contact UT method has advantages and disadvantages, as explained above. The decision to choose a particular method over others, therefore, requires some justification. In the research presented in this thesis, EMAT generation and detection was chosen as the main system to be developed. This is because it is relatively low cost, reliable for fast inspection, and has the potential to be used in many areas, including rail inspection, metal manufacturing, and pipeline inspections. Laser detection is also used to get a higher spatial resolution of the detected signal for cracks with narrow widths (Chapter 6), and both techniques are described in more detail in Chapter 2.

This figure has been blanked out due the
author has no permission to reproduce.

Figure 1.3: Surface defects in in continous casting of steel.Reproduced from [6].

1.5 Surface defects in metals

Metal structures and components can exhibit surface defects while in service [4] or during manufacturing [6]. The exposure to harsh conditions during service, such as cyclic loading of stress and strain in a corrosive environment can initiate the growth of defects near to the surface. Additional factors, such as corrosive chemicals or even water can contribute to the defect growth into the sample [3]. In manufacturing, surface defects can occur as a result of chemical, processs, and engineering parameters [5]. Figure 1.3 shows examples of surface defects in metal slab and bloom/billet, defined and categorised by the International Iron and Steel Institute (IISI) [6]. Transverse and longitudinal cracks can be present on the top surface and at the corner (marked as 1, 2, 3, and 4). Star cracks, deep oscillation marks, pinholes and macro inclusions can be found on the top surface. The causes of these defects include non-uniform heat transfer due to chemical composition, faults in the mould, uneven cooling, and also the presence of impurities. For some metals that are put under processes such as annealing or cold work, the material properties can change [45]. The metal can become more brittle and easier to break, if a crack is initiated on the surface. A test for this sortof cracking at high temperature can be used to feedback information to the operator to improve the casting process during operation.

Generally, surface defects may not be harmful if they are relatively small in size [3]. However, if left undetected they can continue to grow into the material, which has various consequences; for example bridges can collapse, underground or overground pipelines carrying chemicals or oils can leak, causing damage and pollution to surround-

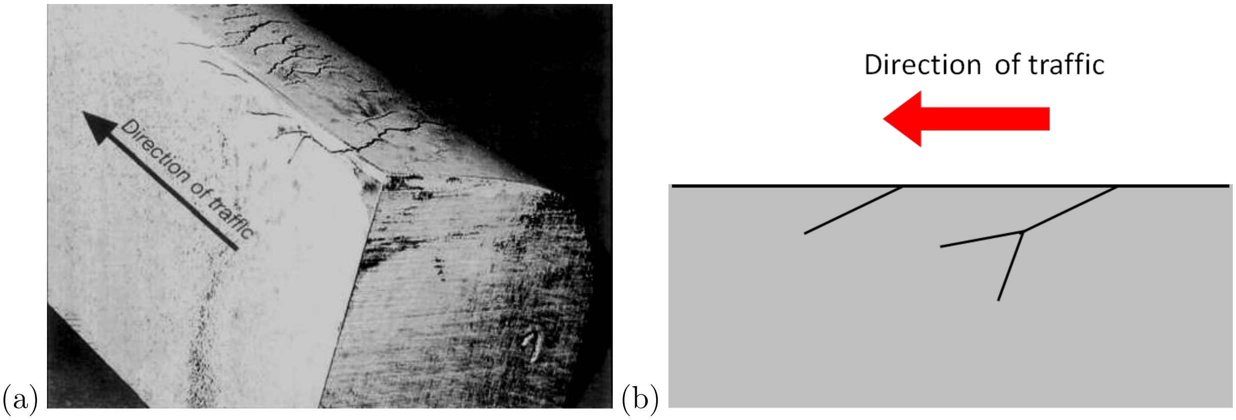

Figure 1.4: A section of rail containing a type of rolling contact fatigue crack, known as head checks (after Railtrack PLC [3]).)

ings, on top of the financial loss which occrus. The final product when manufacturing e.g billets may not meet market specifications and will need to be reprocessed, with additional cost added to the manufacturing process. Two specific types of surface defects, rolling contact ratigue (RCF) on rail tracks and stress corrosion cracking (SCC), which are of most interest for this thesis, are described in Sections 1.5.1 and 1.5.2.

1.5.1 Rail defects

A real life example of the severe impact which can be caused by surface defects in rail is given by the train derailment near Hatfield in the UK, in October 2000, where four people died and over seventy people suffered injuries [46]. The investigation into the incident revealed that the derailment was caused by surface defects in the rails known as rolling contact fatigue (RCF) cracks [3, 4, 46, 47]. An example of this type of crack is shown in the photgraph in Figure 1.4(a) (taken from [3]). The photograph shows a form of RCF crack, known as “head check”, with the section of rail cut to reveal the geometry of head checks below the surface. The cracks initiate on the surface, and continue growing at an angle of about 20° to the surface, in the direction of the train traffic [47]. As the cracks propagate deeper than about 5 mm vertically into the rail, they can grow branches, as depicted in the simplified diagram in Figure 1.4(b). At this point, the branch can either can grow back to the surface, causing a spallation of the surface, or continue growing into the rail, causing a breakage [3].

Traditionally, RCF cracks are characterised through visual and/or ultrasonic inspection [3,47]. The former relates the crack depth to the crack length on the surface based on an establised relationship, while the later utilises reflections of ultrasound waves from the crack. The visual inspection method is considerably slow and time consuming, especially if hundreds of miles of rail need to be inspected. Despite being adapted for standard practice, the accuracy of this method is also questionable as the crack length-depth relationship is not fully understood, as it is based on common observation. It is also not convenient to shut down train services for a long period of time in order to conduct the inspection. The ultrasonic inspection can give a more accurate estimation of the crack depth compared to the visual inspection in a shorter time.

Figure 1.5 illustrates how an ultrasonic probe (contact piezoelectric transducer) is used in pulse-echo mode to detect and characterise RCF cracks. The probe generates a specific mode in a particular incident angle as indicated in the figure, and detects any reflections coming from the cracks. The incident angle is decided based on the knowledge of the expected crack angles, and maximum reflection can be achieved if the ultrasonic beam is perpendicular to the crack [20]. One of the drawbacks of this method is that a deeper crack present behind the crack (shown to Figure 1.5) can be masked. The part of the crack on the right hand side that lies within the shadowed region behind the crack cannot be detected, and this can cause underestimation of the depth of the crack on the right hand side, and missing serious defects.

The remedial action following inspection depends on the estimated crack depth. A remedial grinding is carried out in a region where RCF is expected or known to occur, as a preventive measure [3]. The top layer of the rail containing the crack is ground off, in order to remove the part where the crack initiated. If the crack is measured to be deeper than this, normally the crack is classified as severe and would require the section of rail to be replaced. Each of these actions is associated with a different cost and time required. Rerailing is more expensive and therefore is not cost efficient. The accuracy, consistency and speed of the inspection is very important in making the right decision at the right time. Ideally, an inspection of the rail must be able to identify a defect as an RCF crack from any other type of crack such as weld joint failure. This can be done by determining if the crack is inclined to the surface at certain angle, and finding its orientation, i.e. if it is either following the direction of traffic or not. The remedial action required would be different for non-RCF type cracks. Another important feature for the rail inspection is that it must give an accurate measure of the crack depth. With this, the decision for action to be taken can be made with confidence.

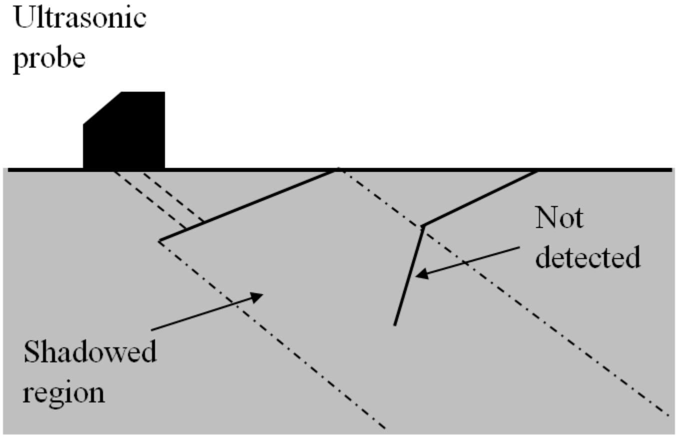

Figure 1.5: Traditional ultrasonic inspection of rolling contact fatigue cracks. The narrow crack on the left-hand side shields the ultrasonic beam from reaching the deeper crack on the right-hand side.

1.5.2 Stress corrosion cracking

Another type of surface crack that is of similar interest to the research reported in this thesis is stress corrosion cracking (SCC) [48, 49]. This is normally found in boilers, pipelines and weld joints, where it is known to cause breakage, putting the intregrity of these structures at risk. SCC is particularly dangerous because fast mechanical fracture can be triggered, which leads to catastrophic failure of the structures. Typically, SCC initiates on the surface before starting to branch into the bulk of the material, as depicted in Figure 1.6. The exact mechanism of SCC is still an active area of research [45, 50], but generally it is known to be due to the combination of stress and corrosive environment. The need to detect and characterise SCC is clear, based on the structural risk it could impose [51]. Therefore, a fast, efficient and reliable technique is required to achieve this.

The two main examples given here, RCF and SCC, are the motivation for this study, in seeking the most suitable method for detecting and characterising surface cracks, compared to the available methods reviewed in Section 1.1. The ultrasonic methods, particularly the non-contact approach have been chosen, mainly due to their high accuracy and potential for fast inspection, in addition to other advantages. This will be discussed further in Section 1.6.

This figure has been blanked out due the
author has no permission to reproduce.

Figure 1.6: Stress corrosion cracking, reproduced from [49].

1.6 The interaction of ultrasonic waves with surface features

Ultrasound has been used previously for characterising surface defects [23, 24, 52–59]. It has the advantages of allowing for fast inspection and potentially giving an accurate measurement of the defect location and size. When ultrasound is generated in a sample, various types of ultrasonic wave can be generated, known as the wavemodes [22]. In general, wavemodes can be described by either longitudinal (compression) or transverse (shear) motion of the particle in the wave, however, there are wavemodes that have a combination of both motions. In order to accurately detect defects in sample, suitable wavemodes must be selected, with the main criteria that they can provide useful information following interaction with the defects. For detecting surface discontinuities, surface waves are the best candidates.

A surface wave known as the Rayleigh wave has been used in this work for detecting surface defects. This has the advantages of being non-dispersive, and with low attenuation, due to the fact that the majority of its energy is confined within a wavelength from the sample surface. The theoretical details of Rayleigh waves will be presented in Section 2.1.3. Rayleigh waves are technically only present in a half-space of a sample, but can be approximated in thick samples where the product of the wave frequency and the sample thickness is large. When the frequency-thickness product is low, a guided wave known as a Lamb wave will be generated, and these will also be discussed in Section 2.1.3.

In this section, previous work on the interaction of Rayleigh wave with various surface features will be reviewed, in the light of characterising surface defects. This section will cover both theoretical and experimental approaches, and has been used as a starting point for developing improved techniques.

1.6.1 Reflection and transmission of Rayleigh wave at a notch

It is common that in the study of the interaction of Rayleigh waves with surface cracks, the cracks are approximated as a notch oriented normal (i.e at an angle of 90°) to the sample surface. Viktorov studied the reflection and the transmission of Rayleigh waves interacting with this type of crack [53]. The notches were cut on dural bars (93.5% aluminium, 4.4% copper, 1.5% magnesium, 0.6% manganese), oriented perpendicular to the Rayleigh wave propagation. Reflection and transmission coefficients were measured for notches with depths in the range of 0.2 to 2.7 of the normalised depth, $^h/_\lambda$, where h is the actual depth and λ is the Rayleigh wave wavelength. When the reflection and transmission coefficients are plotted as a function of the normalised depth, as shown in Figure 1.7, an oscillating pattern is observed for both coefficients as the value of the normalised depth increases. In general, the reflection coefficient shows an underlying increase as the normalised depth increases, while the transmission coefficent shows an overall decreases as the normalised depth increases. The oscillating patterns in k_{re} and k_{tr} are related to the interference of Rayleigh waves reflected or transmitted from the top and the bottom of the slot. The length between the top and the bottom of the slot Δh can be related to the period of the oscillation in Figure 1.7 according to $\Delta h = \lambda$. Another important finding is that the transmission coefficient k_{tr} no longer depends strongly on the depth when the value of the normalised depth is greater than 1.5. This means that Rayleigh wave can pass under a crack of any finite depth.

Vu and Kinra created a method known as the parallel-path method to detect cracks of a similar type [54]. In the parallel path method, two sets of measurements are made on two separate samples simultaneously. One sample contains no defect (used as a reference) and the other one has a defect (test sample). Comparison between the measurements of the reference and the test samples are made in real-time during the experiment. Their results confirmed the earlier findings by Viktorov [53], showing oscillations in the reflection and transmisison coefficients. Other researchers have used the approach of using the arrival time of reflected and transmitted Rayleigh waves to estimate the crack depth [55,60]. For the case of using a reflected Rayleigh wave, Cooper et, al [60] employed a non-contact system consisting of a Q-switched Nd:YAG laser for generation, and either a ball capacitance probe or laser interfometer for detection.

This figure has been blanked out due the
author has no permission to reproduce.

Figure 1.7: Reflection k_{re} and transmission k_{tr} coefficents plotted as a function of normalised depth h/λ. The sum of the squared coefficients $k_{re}^2 + k_{tr}^2$ represent the total energy reflected and transmitted. Reproduced from Viktotov [53]..

The principle of the depth calculation is based on the difference in the arrival time between two reflected Rayleigh waves from the crack. The first one is the direct reflected Rayleigh wave from the top of the crack, while the second one is the Rayleigh wave that propagates down to the crack tip, then mode-converts to a shear bulk wave in the radial direction to reach the material surface. Upon reaching the surface, the shear wave is mode-converted to a Rayleigh wave. The relationship between the difference in the arrival time and the crack depth was shown to valid for cracks with depths in the range of 0.1 mm to 1.0 mm, with a slot width of 0.1 mm or less..

Hirao et, al. studied the scattering of Rayleigh waves by edge cracks (cracks normal, i.e. 90°, to surface) through numerical simulations using the finite-difference method, and experiments conducted on mild-steel test pieces containing machined slots normal to the surface [55]. Two PZT transducers were set in pitch-catch mode, to measure the frequency spectra of Rayleigh wave reflection and transmission coefficients. Crack depths were calculated from the time-of-flight measurements following Rayleigh wave transmission. This method works for deep cracks with $h > \lambda$, where h is the actual crack depth and λ is the Rayleigh wavelength. However, for shallow cracks ($h < \lambda$), the method leads to an underestimation of the crack depth, because the whole crack acts as an obstacle to the propagation of the Rayleigh wave. As a consequence, although the effect of the crack as an obstacle increases with depth, the time-of-flight is hardly affected. On the other hand, for the case of deep cracks ($h > \lambda$), the edges and the crack tip form a set of geometrical discontinuities which the Rayleigh wave must pass around to transmit past the crack. The Rayleigh wave is forced to travel down to the crack tip and up to the trailing edge, thus, the time it takes to transmit is proportional to twice the crack depth, $2h$.

The exact solution for scattering of Rayleigh waves by an edge crack was also obtained by Achenbach, Mendelsohn and their co-workers [56, 61]. Mendelsohn et, al. investigated the scattering of surface waves by a surface-breaking crack in a two dimensional geometry [56]. Their theoretical approach also showed an oscillating pattern in the reflection coefficients similar to [53], both in the in-plane and in the out-of-plane of components. Further work using the ray-theory approach was reported in [61]. These researchers showed that crack depth can be calculated using the relation: $k_R h = \pi$, where k_R is the Rayleigh wavenumber and h is the crack depth. This showed a good agreement with earlier work in [56] for $k_R d > 6$.

1.6.2 Interaction of Rayleigh waves with different surface features

The work on the interaction of Rayleigh wave with surface defects with geometry other than 90° notches or slots has progressed slowly mainly through the use of computer models. A number of authors have approached the problem using either numerical or analytical techniques [59, 62–67]. Bond [62] employed the finite difference formulation to model the interaction of Rayleigh waves with surface discontinuties. The authors discussed various geometries which can be considered as dicontinuities, including up and down steps. A comparison of transmission and reflection coefficients for scattering at a down step were made with other studies, to show the power of this technique to give a detailed understanding of the interaction, and it showed a good agreement with them. Successive works by the author covered the interaction at up-steps and troughs [63], and wedges and down-steps [59].

Earlier work was conducted by Viktorov [53] on dihedral surfaces of different angles. He calculated reflection and transmission coefficients of Rayleigh wave propagating from one surface to the other surfaces. The coefficients showed an oscillating pattern with angle similar to a 90° notch. The sum of the value of the coefficients ($k_{re}^2 + k_t^2$) is always less than one, indicating that there is energy loss due to mode conversion to bulk waves. Rayleigh wave scattering by a wedge was studied by Budaev and Bogy [65–67] using the method of Sommerfield's integral. The reflection and transmission coefficients were obtained as functions of the wedge angle and they show a good agreement with experimental results obtained in [68]. A more recent work reported by Babich et, al. [64] shows progress made using Somerfield-Malyuzhinets-Budaev semi analytical approach, to model the scatter of Rayleigh wave by tiltled surface breaking cracks. The reflection and transmission coefficients calculated based on the model agree well with earlier experimental work reported in [66, 67].

1.6.3 Enhancement of Rayleigh wave close to a crack

When detection of a Rayleigh wave is made close to and in front of a surface crack, the amplitude of the signal detected has been shown to increase significantly compared to the signal detected far from the crack [57, 69]. The increase in the ampitude is known as the Rayleigh wave enhancement, and is primarily due to the incident Rayleigh wave interfering constructively with the reflected wave and various mode converted waves. This behaviour of Rayleigh waves has been reported by many several authors [13, 57, 70–75]. Blackshire and Sathish studied the scattering of Rayleigh waves in the near-field of surface breaking cracks using heterodyne interferometry [57]. Three different types of cracks were investigated; a through-thickness crack and a long surface crack in aluminium, and a fatigue crack in titanium. The laser detector measurement successfully detected the three cracks based on signal enhancement observed close to the crack, i.e within the near-field of the crack. Signal enhancements of up to a factor of twice the incident amplitude were observed for the samples used. The authors explained the source of the enhancement using the wave propagation and free-boundary reflection.

Boonsang and Dewhurst investigated similar behaviour of the Rayleigh wave using laser generated ultrasound and an in-plane (parallel to the sample surface) EMAT detection system [76, 77]. They modeled the enhancement based on the interaction of the wave with a 90° corner. They predicted that the cause of the enhancement was due to physical interaction of the Rayleigh wave with the EMAT at the corner. However, to say that the cause of the enhancement is solely due to the Rayleigh wave interaction with the EMAT is not correct. As reported in [57], the enhancement is also observed for laser interferometer measurements as discussed above. Edwards et, al. explained the enhancement from the wave interference picture [69, 70]. When an incident Rayleigh wave reaches the 90° corner of the crack, a portion of the wave is reflected, while some is mode converted to a surface skimming longitudinal wave, which propagates on the surface in the opposite direction to the incident wave. At a position close to the crack, the incident wave arrives very close to the mode-converted surface skimming longitudinal wave and the reflected Rayleigh wave. These three waves interfere, and when the interference is constructive, the enhancement in the signal amplitude is observed.

Recent research has built on the previous work. Dutton et, al. employed a laser generation and detection system to detect and characterise surface cracks machined on aluminium samples [74, 78]. A significantly strong enhancement of the Rayleigh wave was observed when the detection was made in close proximity to cracks growing at an angle to the sample surface. The authors used enhancement features in the signal and time-frequency analysis (Wigner transform) to characterise surface defects [78]. A comparison between scanning laser source (SLS) and scanning laser detection (SLD) was reported in [74], discussing the advantages and disadvantages of each method in detecting the enhancement. In addition to the mode-converted surface skimming longitudinal wave generated at the opening of the crack as, reported in [70], there are other mode conversions taking place during the Rayleigh wave interaction that contribute to the enhancement. Dutton et. al calculated the arrival time of these mode-converted waves for angled cracks, and the results show a good agreement with the experimental findings [79] . The approach of calculating the arrival time of different wave modes was also reported by Shen for estimating the crack angle to surface [80].

The work reported in this thesis explains the source of the strong prominent enhancement of Rayleigh waves close to angled cracks. A non-contact approach using EMATs in pitch-catch method has been used in the experiment, and the results are validated by a finite element analysis model. Crack characteristics such as depth and angle are determined from the enhancement and the transmission of Rayleigh waves underneath the crack. Full details of this will be explained in Chapter 4.

1.7 Machine learning methods in NDE

One of the main challenges in NDE is dealing with the large amount of data recorded during tests or inspections of materials. The recorded data usually needs to be interpreted quickly by an operator on the test site, to reveal any indication of defects in the material. However, the size of the data set can slow down the processing. In addition, data processing conducted fully by an operator can be prone to human errors [81]. This includes the human reaction time, lack of concentration due to tiredness or distraction, and also different perceptions in interpreting data. Therefore, a computer program that can choose useful information from the test data, and decide whether a section of sample is defective or not, could significantly increase the speed of a given NDE procedure. The useful information is usually termed as ‘features’, and these give the basic paramaters for classification of the section. For a good classification, the features should be similar for all data in one class (e.g defective) and significantly different for data in different class (e.g non defective) [82].

Machine learning methods have previously been used for data classification [83–86]. They can be beneficial and potentially a good substitute in the area where expert knowledge is currently required for a simple yes or no decision. For example, in DPI of surface defects, a trained NDT operator can distinguish the difference between defective and non-defective surfaces through eye observation. If the image generated is captured and fed into a computer, the knowledge of the operator can be used to train a program to recognise specific features in the images, and decide whether to indicate a defect or non-defect.

Among many methods in machine learning, artificial neural networks (ANN) are one of the most commonly used methods. They have been used in a wide range of areas including facial recognition, speech, finance, handwriting [87], medical diagnosis [88], modelling fatigue crack growth [89] and automatic defect classification [85]. ANN is inspired by the observation of biological learning systems, such as the human brain. Such systems are made from interconnected individual units referred to as “neurons”. Each neuron takes a real value input into the system, and produces a single value output. For example, in recognising a person’s face, some features of the face such as the eyebrow, lip, nose, and skin tone can be used as input for an ANN system. In Section 2.4.2, the theory of ANN is described in more detailed.

Another method in machine learning is called genetic algorithms (GA), and its application is known as genetic programming (GP). This method is inspired by biological evolution, where processes such as natural selection, mating, and mutation in evolutionary theory, are adapted in computer programs with the aim of producing better outputs. Worden et, al. used GA as a feature selection algorithm in combination with ANN as a classifier to improve the results for locating damage in aircraft wings [90]. A classifier is an algorithm that uses the selected features and groups them based on their similarities. They have found that GA have improved the results compared to the earlier work using standard multi-layer perceptron (MLP) neural networks [91], and recommend GA to be used in general feature selection problems as it is computationally inexpensive.

The two machine learning methods discussed above offer great potential for use in NDE, and in particular in ultrasonic testing. Scan images are often generated in ultrasound testing, such as B-scans and C-scans. In the presence of defects, the images would show specific features that can be associated with the defects. There are also differences in the features between different type of defects. The machine learning methods described above can learn these features quickly from a set of experimental and/or simulation data, and be used to classify other ultrasonic images of similar type. This can reduce human dependancy for recognising the features during inspection.

Chapter 5 explores the viability of using genetic programming to classify ultrasound B-scan images from EMAT measurements. There are two types of classification considered; firstly, the classification to discrimate between B-scan images that indicate the presence of surface cracking from those showing no cracks. Secondly, the classification for surface cracks that grow normal (90°) to the surface from those that grow at an angle to the surface (inclined).

1.8 Outline of following chapters

Chapter 2 explains the background theory of ultrasonic wave propagation, the theory of EMAT operation and a review of previous work in EMAT development, the theory of the laser ultrasonic receiver, and some basic algorithms used in machine learning.

Chapter 3 explains the experimental details and the finite element analysis (FEA) used for the research presented in this thesis.

Chapter 4 covers the in-plane and out-of-plane EMAT measurements on full-width (same width as the sample width) cracks. The transmission of Rayleigh waves is found to be different for normal and inclined cracks, due to the different Rayleigh wave interactions with the defects. For inclined cracks, the Rayleigh wave is found to be mode converted to a Lamb-like wave in the tapered section formed by the crack.

Chapter 5 explains the genetic progam and the procedure developed to automatically classify B-scan images into defect/no defect and normal crack/inclined crack. This chapter also explains a procedure developed to fully characterise surface cracks, giving the validation of this procedure on two machined cracks, and the procedure is used to detect and characterise rough cracks on an aluminium billet.

Chapter 6 explains the effects of the crack width on EMAT measurements. Experiments were conducted on normal and inclined narrow-width (finite width compared to the sample width) cracks using a laser interferometer detector. For each type of crack, there are two different crack widths. The measurements are compared with EMAT measurements made on the same crack to show the validity of the EMAT measurements and the characterisation procedure for detecting more realistic cracks.

Chapter 7 explains the interaction of Rayleigh waves with cracks with branch features, using based on FEA models. This is a step towards understanding the interaction for more realistic surface cracks, such as RCF cracks in rail.

Chapter 8 concludes the findings of each chapter within the context of the whole thesis. The main findings in this study will be highlighted.

Chapter 2

Background theory and review

This chapter covers the theoretical background for the scientific understanding assumed for this thesis. It is divided into three main themes; 1. ultrasonic wave theory, 2. theory of EMATs and the laser ultrasonic receiver, and 3. theory for machine learning algorithms. The first theme deals with the stress and strain relation for ultrasonic waves and the basic concepts of wave propagation in solid media, with an emphasis on Rayleigh and Lamb waves. The second theme focuses on EMAT transduction and detection mechanisms, plus an explanation of the laser ultrasonic receiver used for some experiments. The final theme gives a tour of the main machine learning algorithms used for classifying the ultrasound B-scan image data in Chapter 5. The machine learning theme is also covered by briefly comparing the various techniques currently used in NDE.

2.1 Ultrasonic wave theory

The term ‘ultrasonics’ covers the study and application of acoustic waves of frequency greater than 20kHz [22]. Ultrasonic waves can propagate in solids, liquids and gaseous media. In solids, a periodic stress applied to a material can cause a time-varying deformation, which creates mechanical vibrations and in turn ultrasonic waves. The applied stresses give rise to periodic strains, through a linear relationship described by Hooke’s law [92].

The propagation of ultrasonic waves in solids is typically described by the wave behaviour. Longitudinal (or compression) waves have disturbances in the same direction as the propagation direction. Transverse (or shear) waves have disturbances in the direction orthogonal to the propagation direction, and the disturbances can be vertically (y-axis) polarised or horizontally (x-axis) polarised. Surface waves propagate on the material surface, and have characteristics of both longitudinal and transverse waves. An example of this is Rayleigh waves. Guided waves (for example Lamb waves) exists through the sample, and also have characteristic of longitudinal and transverse waves.

In this section, the stress-strain relationship (Hooke's law) that describes the propagation of ultrasonic waves is explained. This is followed by discussions on phase and group velocities touching on wave dispersion. Finally, the theoretical description of surface waves are given, with particular attention to Rayleigh and Lamb waves.

2.1.1 Stress, strain and the Christoffel equation

The propagation of ultrasonic waves in solid mediaoccurs as disturbances that cause deformation in the material [92]. Understanding the propagation involves understanding the stress-strain relation in the material and how it is transfered across the material body to produce a transient wave. At the surface free-boundary the stress components drop to zero allowing for the solution of the expression for particle displacement. All the derivation and discussion presented here is intended for explaining the properties in an isotropic material, due to the type of sample used in the study, which is aluminium.

The relationship between stress σ and strain ε is given by Hooke's law in tensor form,

$$\sigma_{ik} = C_{iklm}\varepsilon_{lm} \tag{2.1}$$

where C_{iklm} is a 4th rank tensor called the stiffness tensor or elasticity tensor. The stress σ_{ij} and strain ε_{lm} are 2nd rank tensors and defined as

$$\sigma = \begin{bmatrix} \sigma_{11} & \sigma_{12} & \sigma_{13} \\ \sigma_{21} & \sigma_{22} & \sigma_{23} \\ \sigma_{31} & \sigma_{32} & \sigma_{33} \end{bmatrix}, \quad \varepsilon = \begin{bmatrix} \varepsilon_{11} & \varepsilon_{12} & \varepsilon_{13} \\ \varepsilon_{21} & \varepsilon_{22} & \varepsilon_{23} \\ \varepsilon_{31} & \varepsilon_{32} & \varepsilon_{33} \end{bmatrix}. \tag{2.2}$$

The indices 1, 2, and 3 in Equation 2.2 map to the x, y, and z axes in cartesian coordinates. The tensor can be reduced to a matrix following symmetry arguments described in [93]. Since the tensors are symmetric, each component can then be described by only one subscript rather than two. They can then be written in a six-element column matrix rather than a nine-element matrix, as follows

$$\sigma = \begin{bmatrix} \sigma_1 & \frac{1}{2}\sigma_6 & \frac{1}{2}\sigma_5 \\ \frac{1}{2}\sigma_6 & \sigma_2 & \frac{1}{2}\sigma_4 \\ \frac{1}{2}\sigma_5 & \frac{1}{2}\sigma_4 & \sigma_3 \end{bmatrix} or\, \sigma = \begin{bmatrix} \sigma_1 \\ \sigma_2 \\ \sigma_3 \\ \sigma_4 \\ \sigma_5 \\ \sigma_6 \end{bmatrix}. \tag{2.3}$$

Similar treatment can be applied to the strain tensor, ε_{lm} to give

$$\varepsilon = \begin{bmatrix} \varepsilon_1 & \frac{1}{2}\varepsilon_6 & \frac{1}{2}\varepsilon_5 \\ \frac{1}{2}\varepsilon_6 & \varepsilon_2 & \frac{1}{2}\varepsilon_4 \\ \frac{1}{2}\varepsilon_5 & \frac{1}{2}\varepsilon_4 & \varepsilon_3 \end{bmatrix} or\, \varepsilon = \begin{bmatrix} \varepsilon_1 \\ \varepsilon_2 \\ \varepsilon_3 \\ \varepsilon_4 \\ \varepsilon_5 \\ \varepsilon_6 \end{bmatrix}. \tag{2.4}$$

Now Hooke's law (Equation 2.1) becomes

$$\sigma_i = C_{ik}\varepsilon_k \tag{2.5}$$

The implication of this is that the C_{iklm} tensor is reduced from a 4th rank to a 2nd rank tensor. This greatly reduces the elasticity constant effectively from a 9×9 matrix to a 6×6 matrix. In other words, from 81 elements now we have only 36, following symettry consideration.

$$C = \begin{bmatrix} C_{11} & C_{12} & C_{13} & C_{14} & C_{15} & C_{16} \\ C_{21} & C_{22} & C_{23} & C_{24} & C_{25} & C_{26} \\ C_{31} & C_{32} & C_{33} & C_{34} & C_{35} & C_{36} \\ C_{41} & C_{42} & C_{43} & C_{44} & C_{45} & C_{46} \\ C_{51} & C_{52} & C_{53} & C_{54} & C_{55} & C_{56} \\ C_{61} & C_{62} & C_{63} & C_{64} & C_{65} & C_{66} \end{bmatrix}. \tag{2.6}$$

For an isotropic medium, the equation must meet the isotropy conditition ($C_{12} = C_{11} - 2C_{44)}$ [93]. Thus, Equation 2.6 becomes

$$C = \begin{bmatrix} C_{11} & C_{12} & C_{12} & 0 & 0 & 0 \\ C_{12} & C_{11} & C_{12} & 0 & 0 & 0 \\ C_{12} & C_{12} & C_{11} & 0 & 0 & 0 \\ 0 & 0 & 0 & C_{44} & 0 & 0 \\ 0 & 0 & 0 & 0 & C_{44} & 0 \\ 0 & 0 & 0 & 0 & 0 & C_{44} \end{bmatrix}. \tag{2.7}$$

The elasticity tensor C is useful for finding an expression for an ultrasonic plane wave propagation. The propagation of ultrasonic plane wave in a freely vibrating medium (body field is zero) can be described by the Christoffel equation [93],

$$k^2\Gamma_{ij}v_j = \rho\omega^2 v_i \tag{2.8}$$

where Γ_{ij} is the Christoffel tensor, k is the wave number, v_i and v_j are the phase velocity, ρ is the density, and ω is the angular frequency. Γ_{ij} is given by

$$\Gamma_{ij} = l_{ik}C_{kl}l_{lj}. \tag{2.9}$$

In tensor form, the Christoffel equation is written as

$$k^2 \begin{bmatrix} \Gamma_{11} & \Gamma_{12} & \Gamma_{13} \\ \Gamma_{21} & \Gamma_{22} & \Gamma_{23} \\ \Gamma_{31} & \Gamma_{32} & \Gamma_{33} \end{bmatrix} \begin{bmatrix} v_x \\ v_y \\ v_z \end{bmatrix} = \rho\omega^2 \begin{bmatrix} v_x \\ v_y \\ v_z \end{bmatrix}. \tag{2.10}$$

In an isotropic medium, the stiffness-tensor C_{kl} is given by Equation 2.7, thus the Christoffel equation becomes purely diagonal matrix and reduces to

$$k^2 \begin{bmatrix} C_{44} & 0 & 0 \\ 0 & C_{44} & 0 \\ 0 & 0 & C_{11} \end{bmatrix} \begin{bmatrix} v_x \\ v_y \\ v_z \end{bmatrix} = \rho\omega^2 \begin{bmatrix} v_x \\ v_y \\ v_z \end{bmatrix}. \tag{2.11}$$

This gives three independant equations

$$k^2C_{44}v_x = \rho\omega^2 v_x, \quad k^2C_{44}v_y = \rho\omega^2 v_y, \quad k^2C_{11}v_z = \rho\omega^2 v_z. \tag{2.12}$$

These equations suggest that x-polarised (z-propagating) and y-polarised (z-propagating) transverse waves solutions must satifsy

$$k^2 C_{44} = \rho\omega^2, \tag{2.13}$$

and the longitudinal wave solution must satisfy

$$k^2 C_{11} = \rho\omega^2. \tag{2.14}$$

2.1.2 Phase velocity, group velocity and dispersion.

A wave propagating in a medium may consist of more than one frequency, and each frequency component may travel at a slightly different velocity [22]. Phase velocity c_p is defined as the velocity of a specific frequency component of a wave. It is given by the product of the frequency f and the wavelength λ,

$$c_p = f\lambda. \tag{2.15}$$

It is sometimes convenient to use the angular frequency ω and wavenumber k in describing variables that are related to frequency f and wavelength λ. They are given by

$$\omega = 2\pi f \tag{2.16}$$

and

$$k = \frac{2\pi}{\lambda} \tag{2.17}$$

and hence $c_p = \omega/k$.

A simple plane wave can take the form

$$u = A\cos(kx - \omega t) \tag{2.18}$$

where u is the particle displacement, A is a constant, and x is the position of the wave at time t. For a wave that consists of more than one frequency, the velocity of the wave can be described as a result of the combination of all frequency components. This velocity is called the group velocity c_g. To explain the concept of group velocity mathematically, consider two harmonic waves of equal amplitude with slightly different frequency; the first wave has frequency ω_1 and the second wave has frequency ω_2. The sum of the two waves can be written as

$$u = A\cos(k_1 x - \omega_1 t) + A\cos(k_2 x - \omega_2 t) \tag{2.19}$$

where $k_1 = \omega_1/c_1$ and $k_2 = \omega_2/c_2$. Using the trigonometic identity

$$A(\cos\alpha + \cos B) = 2A\left[\cos(\frac{\alpha - B}{2})\cos\left(\frac{\alpha + B}{2}\right)\right]$$

and using the substitution $\Delta\omega = \omega_2 - \omega_1$ and $\Delta k = k_2 - k_1$, Equation 2.19 can be re-written as

$$u = 2A\cos\left(\frac{1}{2}\Delta kx - \frac{1}{2}\Delta\omega t\right)\cos\left(kx - \omega t\right). \tag{2.20}$$

Based on Equation 2.20, the group velocity is defined as

$$c_g = \frac{\Delta\omega}{\Delta k} \tag{2.21}$$

which in the limit of $\Delta\omega \to 0$, and $\Delta k \to 0$ becomes

$$c_g = \frac{d\omega}{dk}. \tag{2.22}$$

A wave is said to be dispersive when its velocity is dependent on frequency. A simple example of the dispersion phenomena can be observed when a white light enters a dispersive prism, producing a spectrum of colour like a rainbow. Each colour is refracted in the prism according to the wavelength. The dispersion behaviour adds more complexity to understanding the wave propagation and consequently analysing the wave interaction with defects. Therefore, for dispersive waves the relationship between the velocity (phase and group velocity) and the frequency is required to calculate the wave arrival times and the subsequent effects such as mode conversion. Such a relationship can be depicted by a dispersion curve, as shown in Figure 2.2. This is discussed further in the context of Lamb waves in the next section.

2.1.3 Surface acoustic waves

Surface acoustic waves are the waves that propagate on the material surface, with energy concentrated within approximately one wavelength from the surface.

2.1.3.1 Rayleigh waves

Rayleigh waves were first identified by Lord Rayleigh in 1885 [94]. He demonstrated theoretically that waves can propagate over the plane boundary between an elastic half-space and a vacuum or medium like air, in which the amplitude of the waves decays rapidly with distance into the half-space from surface. This wave has been observed to be in the primary waves present in earth tremors. The use of Rayleigh waves has led to many applications in material surface inspection [58]. In particular, they have been used to detect surface and near-surface flaws in metals, glasses, plastics and other materials through the use of ultrasonic detection [62].

Rayleigh waves have characteristics that are attractive for NDT applications. They have low attenuation compared to longitudinal and shear waves, as they spread into the sample in two-dimensions, in contrast to longitudinal and shear waves which spread in three-dimension. The properties of a sample surface layer can have an influence on the Rayleigh wave velocity [95]. The Rayleigh waves have both longitudinal and transverse characteristics, which makes it possible to have motion parallel to the material surface and in the same direction as the propagation.

The expression for the particle displacement due to propagation of a Rayleigh wave can be obtained by solving the stress component at the boundary of the elastic half-space as detailed in [53]. This leads to a characteristic equation to determine the wavenumber k. The equation, also known as Rayleigh equation, has the form

$$\eta^6 - 8\eta^4 + 8(3 - 2\xi^2) - 16(1 - \xi^2) = 0 \tag{2.23}$$

where $\eta = k_t/k = c/c_t$, $\xi = k_l/k_t = c_t/c_l$, and c_l and c_t denote the phase velocites of the longitudinal and shear wave respectively. The solution to Equation 2.23 has six roots that depend only on the Poisson ratio, v for the given elastic medium. The Rayleigh wave corresponds to the root η_R which lies between zero and one. An approximate expression for this root is given by [53]:

$$\eta_R = \frac{0.87 + 1.12v}{1 + v}. \tag{2.24}$$

From Equation 2.24 it can be seen that the Rayleigh wave does not exhibit phase velocity dispersion as the root η_R does not depend on frequency, which is another advantage of using Rayleigh waves. Following solution of the Rayleigh equation (Equation 2.23), the particle displacement due to propagation of the Rayleigh wave can be written as [53]

$$U = Ak_R\left(e^{-qz} - \frac{2qs}{k_R^2+s^2}e^{-sz}\right)\sin(k_R x - \omega t) \tag{2.25}$$

$$W = Aq\left(\frac{2k_R^2}{k_R^2+s^2}e^{-sz} - e^{-qz}\right)\cos(k_R x - \omega t). \tag{2.26}$$

U and W are the in-plane (parallel to the wave propagation) and out-of-plane (normal to the wave propagation) displacement components. k_R, k_l and k_t are the wave numbers of the Rayleigh, longitudinal and shear waves respectively, $q = \sqrt{k_R^2 - k_l^2}$, $s = \sqrt{k_R^2 - k_t^2}$, A is a constant and x and z are the in-plane (x axis) and out-of-plane (z axis) coordinates. It is useful for this work to calculate the particle velocity in addition to the displacement as EMATs are velocity sensors (Section 2.2.2). The particle velocity for the Rayleigh wave is the time differential of the displacements in Equations 2.25 and 2.26, and it is given by

$$\frac{dU}{dt} = -A\omega k_R\left(e^{-qz} - \frac{2qs}{k_R^2+s^2}e^{-sz}\right)cos(k_R x - \omega t) \tag{2.27}$$

$$\frac{dW}{dt} = A\omega q\left(\frac{2k_R^2}{k_R^2+s^2}e^{-sz} - e^{-qz}\right)sin(k_R x - \omega t). \tag{2.28}$$

The velocity of both components normalised to the velocity at the surface, are plotted as a function of normalised depth d/λ in Figure 2.1(a). The results from a computer simulation using finite element analsyis (FEA described in Section 3.6) are also appended to show the agreement with the calculation. The out-of-plane component drops rapidly with depth from the surface. At approximately $d/\lambda = 1$, the velocityreaches close to a constant value but this is higher than the value of the in-plane component. The in-plane component changes phase at approximately a quarter of the wavelength below the surface, and gradually tends to zero, as with the out-of-plane component at higher normalised depth values. In Figure 2.1(b), the ratio of the in-plane to the out-of-plane velocity component is plotted as a function of d/λ. Again, there is a good agreement between the theoretical calculation and the FEA model results. The ratio increases rapidly from -0.6 to an approximate value of 0.2 at $d/\lambda \approx 0.4$. At higher depths, the ratio becomes approximately constant at about 0.3.

The combination of longitudinal and transverse motion of the particle displacement

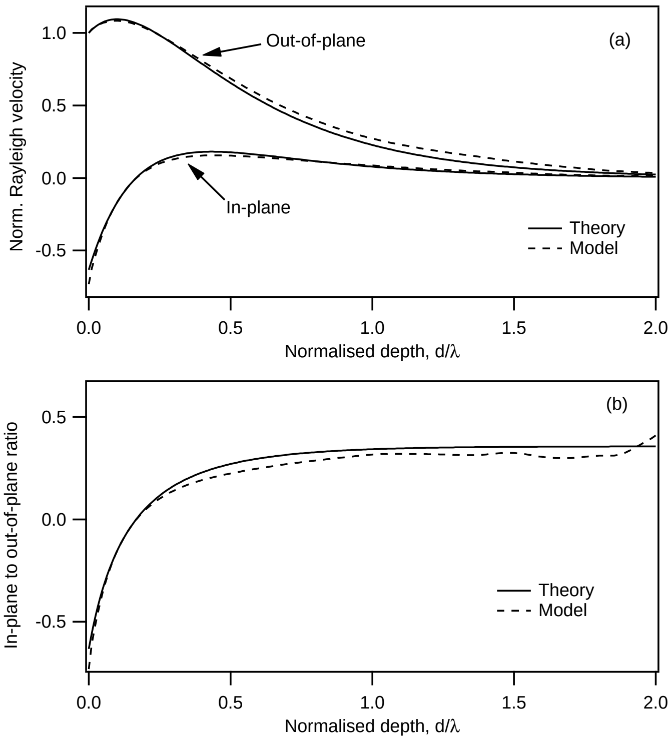

Figure 2.1: Rayleigh wave velocity behaviour with normalised depth, d/λ. d is equivalent to z in the equations used in the text. Theoretical calculation and finite element analysis (FEA) model results of in-plane and out-of-plane Rayleigh wave velocity components (a), and the ratio of the in-plane to the out-of-plane component in (b).

in the Rayleigh wave results in a particle motion that follows the shape of an ellipse. This can be shown by combining Equation 2.25 and Equation 2.26 using the trigonometric identity $\sin^2\theta + \cos^2\theta = 1$, which yields

$$\left[\frac{U}{Ak_R\left(e^{-qz} - \frac{2qs}{k_R^2+s^2}e^{-sz}\right)}\right]^2 + \left[\frac{W}{Aq\left(\frac{2k_R^2}{k_R^2+s^2}e^{-sz} - e^{-qz}\right)}\right]^2 = 1. \tag{2.29}$$

This is the equation of an ellipse. It also indicates that the elliptical shape motion varies with depth from the surface, z. The particle motion remains as an ellipse at all times because the equation does not depend on time. However, going deeper into the bulk of the material, i.e increasing z , will result in a smaller ellipse. The size of the semi-major and semi-minor axes of the ellipse decay with depth in the material, and at a certain depth, the particle motion reverses its rotation direction. This corresponds to the value of depth for which the ratio of in-plane to the out-of-plane velocities crosses zero in Figure 2.1(b), or the depth where the in-plane velocity is zero.

2.1.3.2 Lamb waves

In contrast to the Rayleigh waves which propagate on the plane boundary of elastic half-space and a medium (e.g air), waves that propagate in a solid medium bounded by upper and lower boundaries are known as guided waves [22]. Lamb waves are a type of guided waves which are related to the Rayleigh waves [53]. Lamb waves present in thin samples (e.g plates), where the wavelength is comparable or longer than the sample thickness. When the sample thickness is signifcantly larger than the wavelength, the waves are said to become Rayleigh waves. Lamb waves are dispersive; their speed depends on the frequency and the thickness of the sample [96]. There are more than one wave mode can be generated for a given frequency value, and the wave modes are grouped into symmetric and antisymmetric. Symmetric modes have the particle displacements on the upper and lower boundaries symmetric about the centre of the sample thickness, and antisymmetric modes are the opposite.

The particle displacement for Lamb waves can be obtained by solving the stress components at the elastic boundaries using the method of displacement potential [22]. The solution yields two equations that correspond to two family of modes; symmetric and antisymmetric modes, which refer to the wave symmetry about the plane axis. The equations for each mode are given in Equations 2.30 and 2.31, where $p^2 = (\frac{\omega}{c_L})^2 - k^2$ and $q^2 = (\frac{\omega}{c_T})^2 - k^2$. k is the wavenumber which is equal to ω/c_p, where c_p is the phase velocity of the Lamb wave mode and is related to the wavelength by the relation $c_p = \omega/2\pi\lambda$. h is the thickness of the plate.

For the symmetric mode

$$\frac{\tan(qh)}{\tan(ph)} = -\frac{4k^2pq}{(q^2-k^2)^2} \tag{2.30}$$

For the antisymmetric mode

$$\frac{\tan(qh)}{\tan(ph)} = -\frac{(q^2-k^2)^2}{4k^2pq} \tag{2.31}$$

Equations 2.30 and 2.31 are known as the Rayleigh-Lamb frequency equations, and relate the frequency ω to the wavenumber k of the Lamb wave modes giving the frequency spectrum, or relate the phase velocity c_p to the frequency ω, giving the dispersion curve. For a given frequency, there are a set of wave number that cam satisfy Equa-

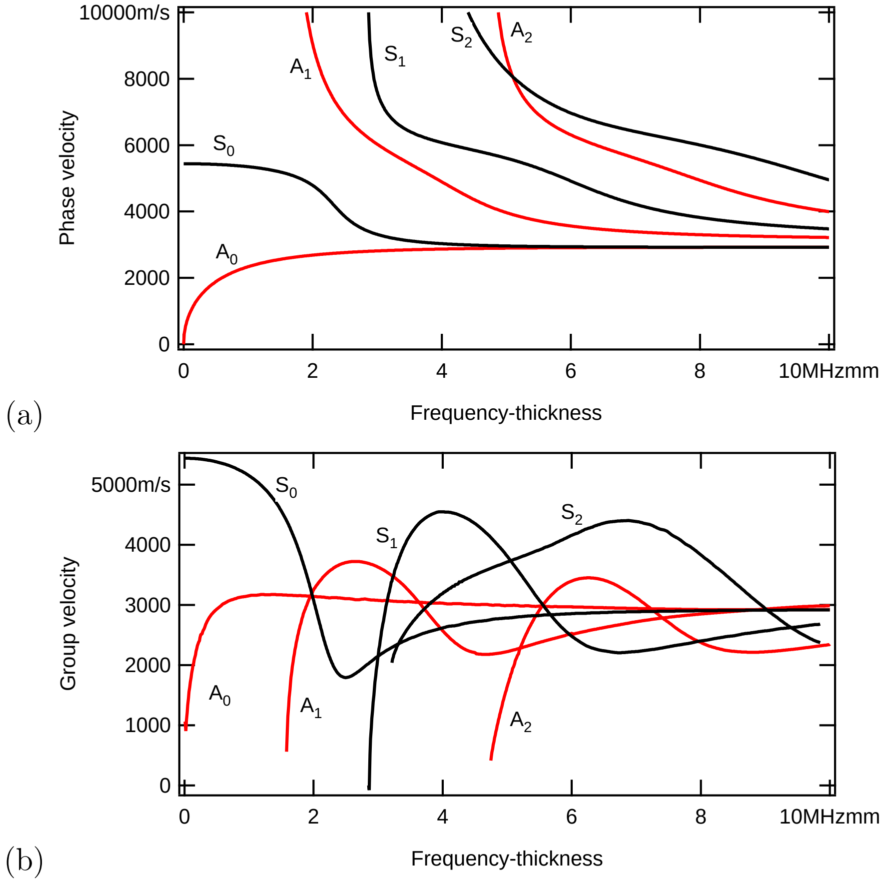

Figure 2.2: Dispersion curves for aluminium showing the phase velocity c_p (a) and group velocity c_g (b) of Lamb wave modes for the given range of frequency-thickness fh. S indicates the symmetric mode and A indicates the antisymmetric mode. The subscripts indicate the order of the modes.

tions 2.30 and 2.31. The method for solving the equations numerically is explained in [22]. A new parameter called the frequency-thickness is defined as the product of the frequency and the thickness of the plate. For a given frequency-thickness, there will be a number of velocity values can be found that correspond to different modes [97]. Generally, each mode have a different phase velocity c_p, but it is also possible to have a crossing value, where two modes can have the same phase velocity. This is illustrated in the dispersion curve of aluminium in Figure 2.2(a), where the phase velocities are plotted as a function of frequency-thickness.

The dispersion curve for alumimium is presented in Figure 2.2, shows the phase velocity for fundamental, first order and second order Lamb wave modes for frequency-thickness from zero to 10 MHz.mm. The symmetric mode is labelled as S and the antisymmetric mode is labelled as A. The subscripts indicate the order, i.e fundamental 0, first order 1, and second order 2. From the solution which give rise to the phase velocity shown in Figure 2.2, the group velocity c_g can be obtained by subsituting $k = \omega / c_p$ into $c_g = \frac{d\omega}{dk}$, thus

$$c_g = c_p^2 \left[c_p - \omega \frac{dc_p}{d\omega} \right]^{-1}, \tag{2.32}$$

or by substituting $\omega = 2\pi f$, the equation can be written as

$$c_g = c_p^2 \left[c_p - (fd) \frac{dc_p}{d(fd)} \right]^{-1}. \tag{2.33}$$

In these equations, the plate thickness is denoted by d instead of h.

The group velocity corresponding to the phase velocity shown in Figure 2.2(a) is shown in Figure 2.2(b). In both figures, it can be seen that, as the frequency-thickness increases the velocities of all modes gradually converge to a common value. It is easier to see this in the phase velocity c_p of the S0 and A0 modes (Figure 2.2(a)). For frequency-thickness greater than 5 MHz.mm, the S0 and the A0 converge to a value of around 3000 m/s. For higher order modes, the phase velocity c_p converge at a higher value of frequency-thickness. The convergence behaviour of the phase velocity c_p of Lamb wave modes shows the relationship between Lamb wave and Rayleigh wave. At low frequency-thickness value Lamb wave is present, and Rayleigh wave is present when the value becomes very high.

The frequency-thickness of interest for the Lamb wave used in the experiments reported in thesis is in the range of 0-2 MHz.mm, which corresponds to the broadband low frequency (50 kHz-500kHz) signal generated by the EMATs on aluminium samples used in th experiments.In this range, the fundamental modes S0 and A0 are the main modes present, and they are easily distinguishable based on their group velocities c_g. The S0 mode travels significantly faster than the A0 at all frequency-thickness value in this range. Furthermore, below 1 MHz.mm, the A0 mode is more dispersive than the S0, thus it will appear broader in the recorded signal (A-scan). To get more accurate determination of the wave modes in the A-scan, a time-frequency representation of the signal, such as a spectrogram can be computed [71]. This shows the frequency components present at each time in the A-scan in the time domain and the presence of a particular wave modes can be determined by calculating their arrival time [96, 97]. This will be discussed in detail in Chapter 4.

2.2 Electromagnetic Acoustic Transducers (EMATs)

An electromagnetic acoustic transducer (EMAT) is a non-contact ultrasonic transducer that can be used on electrically conducting and/or magnetic materials. With EMATs, ultrasonic waves are generated within the material itself through the coupling of the electromagnetic wave to the sample [98]. This method allows the EMATs to have a small stand-off from the sample while generating or detecting ultrasonic waves. One of the main attractions for the use of EMATs in NDE is their contactless nature that allows non-contact inspection to be carried out [19]. The versatility of EMAT design also makes it possible to generate a wide range of different type of waves in the sample [41,42,99]. Nonetheless, the justification for using EMATs must be clear, as EMATs are much less efficicent than standard piezoelectric transucers.

EMATs consist of a coil and a magnet. In a typical configuration, a linear coil is wrapped around a permanet magnet, and placed in an aluminium or brass holder. Figure 3.1 shows an example of this, which is also the EMAT used in the experiment reported in this thesis. For ultrasonic waves generation, current is pulsed to the coil from a pulse generator, and an EMAT is hold close to the sample to be inspected [23]. For ultrasonic waves detection, the pulsed current is not required, and an EMAT is only needed to be hold close to the sample surface [100]. Spiral or meander coils can also be used as with permanent magnets to generate specifc wave modes [29]. In recent year, a new design employing a ferrite black-plate have been reported [101,102]. With this design, EMAT can generate ultrasonic waves without a permanent magnet. A new design using pulsed electromagnet is also reported in [44].

The application of EMATs can be traced back to as early as 1939 when Randall generated longitudinal vibrations in a brass bar using an EMAT to study the contribution of intercrystalline thermal currents to the internal friction of polycrystalline metals [103]. He used a coil encircling one end of the brass bar, to induce Eddy currents around the circumference of the bar, with the coil in magnetic field of a permanent magnet placed beyond the end of the bar. Another coil with similar design was placed at the other end of the bar to pick up the signal. In 1959, D. O. Thompson used a similar coil-magnet arrangement to study the effects of neutron radiation on single crystals of copper [104]. The objective of the study was to determine the effects of radiation damage on the mechanical properties of metals.

Dobbs [105] developed and optimised practical EMAT transducers by showing what parameters were important as well as establishing the performance characteristics that could be achieved. EMATs often seen as less attractive compared to piezoelectric transducers due to a number of reasons. The transfer impedance was in the order of $\mu\Omega$ which is very small compared to piezoelectric transducers. The EMATs lift-off from the sample was only a fraction of a milimetre at 1 MHz frequency. Therefore, it demanded special transmitter circuits, with low-noise pre-amplifiers and magnetic fields approaching 1T. However, when magnetostriction in magnetic materials such as steel was identified as additional form of transduction mechanism and thus increasing the efficiency, it opens to a wide variety of application in NDE.

The first commercial application of EMATs in NDE was the inspection of gas pipeline [99]. For this technique, a self contained probe was driven through the pipeline using the gas pressure, at 15 mph. It employed meander coils driven in a pulse echo mode to transmit and receive guided ultrasonic waves in the circumferential direction in order to detect longitudinal cracks. Another application is in a rolling mill, where EMATs were used to inspect the welding joint between sheet metal [99]. The inspection process must be performed quickly so that sheet metal can be fed to the rolling and stamping process.

The following subsections will describe the theory of the ultrasonic transduction and detection mechanisms of EMATs. For transduction, particular attention is given to the Lorentz force mechanism in electrically conducting materials. The magnetisation force and magnetostriction force mechanisms are covered briefly. The experiments reported in this thesis were conducted on aluminium samples, where the Lorentz force mechanism is important.

2.2.1 EMAT transduction mechanism

The principle of the EMAT generation and detection mechanisms involves an understanding of electromagnetism. It is therefore important to introduce the four Maxwell's equations [9]:

$$\nabla \cdot \vec{D} = \rho, \qquad \nabla \cdot \vec{B} = 0 \tag{2.34}$$

$$\nabla \times \vec{E} = -\frac{\partial \vec{B}}{\partial t} \tag{2.35}$$

$$\nabla \times \vec{H} = \vec{J}_f + \frac{\partial \vec{D}}{\partial t}. \tag{2.36}$$

where $\vec{D}$ is the displacement current, $\vec{B}$ is the magnetic field, $\vec{E}$ is the electric field, $\vec{H}$ is the magnetic field intensity and $\vec{J_f}$ is the current density. Equations 2.35 and 2.36 are also known as Faraday's and Ampere's laws respectively. The relations below follow the Maxwells equations:

$$\vec{D} = \varepsilon_0 \varepsilon_r \quad \vec{B} = \mu_0 \mu_r \vec{H} \tag{2.37}$$

2.2.1.1 Eddy currents and skin effect

When a current is pulsed through a coil which is placed close to an electrical conductor, an image current is induced on the surface on the conductor. The image current is known as an eddy current, and the depth in which it propagates is known as the electromagnetic skin depth [14]. In EMAT generation in electrically conducting samples, eddy currents play a significant role in coupling the current pulse generated by the coil, to the electrons and ions in the sample to create an acoustic vibration. This coupling mechanism is known as the Lorentz force mechanism and it will work for all electrically conducting samples, both non-magnetic and magnetic.

A coil carrying a pulsed current generates a time varying magnetic field when located close to a conductor. An electric field is induced in the conductor following Faraday's law (Equation 2.35). To get the expression for the electromagnetic wave that penetrate through the sample, the following steps can be applied as described in [14].

Applying curl to both sides of Equation 2.35, the Faraday's law becomes

$$\nabla \times (\nabla \times \vec{E}) = -\frac{\partial}{\partial t}(\nabla \times \vec{B}) \tag{2.38}$$

Using a vector identity $\nabla \times (\nabla \times \vec{E}) = -\nabla^2 \vec{E} + \nabla(\nabla \cdot \vec{E})$, and assuming that the net charge density in the sample remains zero ($\nabla \cdot \vec{E} = 0$), Equation 2.38 is reduced to

$$\nabla^2 \vec{E} = \frac{\partial}{\partial t}(\nabla \times \vec{B}). \tag{2.39}$$

The right hand side of Equation 2.39 can be expressed in terms of the electrical field as

$$\nabla^2 \vec{E} = \mu_0 \mu_r \sigma \frac{\partial \vec{E}}{\partial t} + \mu_0 \mu_r \epsilon_0 \epsilon_r \frac{\partial^2 \vec{E}}{\partial t^2}. \tag{2.40}$$

The second term in the right hand side of this equation can be neglected since the sample is conductive and the frequency of EMAT generation is typically below 100 MHz [42]; which implies that $\sigma >> \omega\epsilon_0\epsilon_r$. Thus, Equation 2.40 can be be reduced to

$$\nabla^2\vec{E} = \mu_0\mu_r\sigma\frac{\partial\vec{E}}{\partial t}. \tag{2.41}$$

A solution to this equation that represents an attenuated plane wave moving towards the sample (z-direction), should satisfy

$$\nabla^2\vec{E} = \frac{\partial^2\vec{E}}{\partial z^2}. \tag{2.42}$$

To make Equation 2.41 be in this form, it can be written as

$$\frac{\partial^2\vec{E}}{\partial z^2} = \mu_0\mu_r\sigma\frac{\partial\vec{E}}{\partial t} \tag{2.43}$$

The measure of how rapidly the plane wave is attenuated in the sample is called the skin depth or penetration depth δ and can be derived from Equation 2.43 [9];

$$\delta = \sqrt{\frac{2}{\mu_0\mu_r\sigma\omega}} \tag{2.44}$$

where μ_r denotes the relative magnetic permeability,μ_0 denotes the permeability of free space and σ is the electrical conductivity.

The attenuated plane wave solution of Equation 2.42 in terms of the skin depth δ can be written as

$$\vec{E_z} = \vec{E_{z0}}e^{i(\omega t-\frac{z}{\delta})}e^{-\frac{z}{\delta}} \tag{2.45}$$

where $\vec{E_z}$ is the electric field inside the conductive sample at a depth z below the sample surface, $\vec{E_{z0}}$ is the electric field at the sample surface, t is the time and ω is the angular frequency. The term $e^{-\frac{z}{\delta}}$ is the attenuation of the electric field as it going deeper into the sample, and the term $e^{-i(\frac{z}{\delta})}$ is its phase relationship.

The force on the electrons in the electrical conductor is proportional to the electric field, and the current density is also proportional to the electric field. The current density, J is given by Ohm's law as

$$J = \sigma E. \tag{2.46}$$

The current density J can be expressed in terms of the depth, z into the sample using Equation 2.42 as

$$J = J_0 e^{i(\omega t - \frac{z}{\delta})} e^{-\frac{z}{\delta}}. \tag{2.47}$$

Equation 2.47 shows that the phase changes with the depth into the sample, and the amplitude of the current density decays exponentially with depth.

2.2.1.2 Lorentz mechanism

Figure 2.3 shows a cross section of a linear coil positioned close to the surface of an electrically conducting sample. When a current is pulsed through the coil, an image current (also known as the eddy current) is generated within the skin depth of the sample [9]. The eddy current acts in the opposite direction to the current in the coil. In the presence of a static biasing magnetic field $\mathbf{B}_s$ supplied by a permanent magnet, the Lorentz force acts on the charge carriers in the eddy current according to

$$\mathbf{F} = q(\mathbf{E} + \mathbf{v} \times \mathbf{B_s}), \tag{2.48}$$

where q is the charge of the particle the force is acting upon, $\mathbf{E}$ is the electric field, and $\mathbf{v}$ is the charged particle velocity. In the case of EMAT generation, Equation 2.48 becomes

$$\mathbf{F} = -e(\mathbf{E} + \mathbf{v_e} \times \mathbf{B_s}) \tag{2.49}$$

where e is the electron charge and $\mathbf{v_e}$ is the electron velocity. According to Newton's second law, the total force acting upon the electron of mass m is

$$\mathbf{F} = m\frac{d\mathbf{v_e}}{dt}. \tag{2.50}$$

If τ is the mean time of electron-ion collision, the equation of motion of an electron can then be written as [42]

$$m\frac{d\mathbf{v}_e}{dt} = -e(\mathbf{E} + \mathbf{v}_e \times \mathbf{B}_0) - \frac{m\mathbf{v}_e}{\tau}. \tag{2.51}$$

The electrons are attracted to the oppositely charged ions due to the Coulomb force. For common metals at room temperature, τ is of the order of 10^{-14} s [42]. If the electric field oscillates with angular frequency ω and $\omega\tau << 1$, it implies that the mean electron

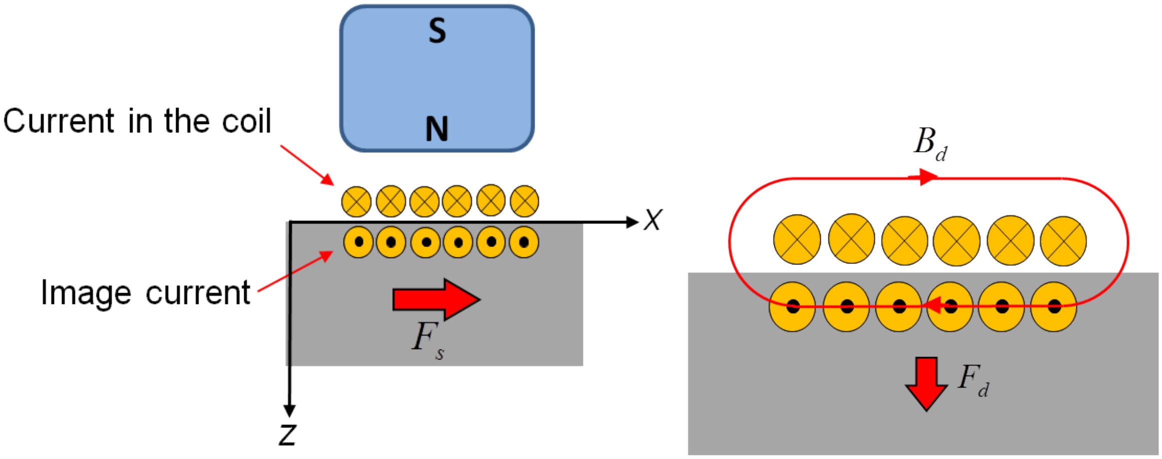

Figure 2.3: Lorentz force generation mechanisms showing the static field contribution, $\mathbf{F}_s$ (left) and the dynamic field contribution, $\mathbf{F}_d$ (right).

velocity, $\mathbf{v}_e$ is not changing with time. Thus, the Equation 2.51 reduces to

$$\frac{m\mathbf{v}_e}{\tau} = -e(\mathbf{E} + \mathbf{v}_e \times \mathbf{B}_s) \tag{2.52}$$

The Lorentz force moves the ions through the attraction of the electrons to the ions. This creates a transient force that generates ultrasound. For a volume of metal with electron density n_e, ion with charge Z_e, density N and mean velocity $\mathbf{v}_{ion}$, the body forces act on the ions by the electrons can be approximated as

$$\mathbf{f} = NZ_e(\mathbf{E} + \mathbf{v}_{ion} \times \mathbf{B}_s) + n_e\frac{m\mathbf{v}_e}{\tau}. \tag{2.53}$$

Given that the sample has neutral charge, $\mid NZ_e = n_e e \mid$, and given that the mean electron velocity is much greater than the mean velocity of the ions, $\mathbf{v}_e >> \mathbf{v}_{ion}$, the force per unit volume on ions reduces to

$$\mathbf{f} = -\, n_e e\mathbf{v}_e \times \mathbf{B}_s = \mathbf{J_e} \times \mathbf{B}_s \tag{2.54}$$

where $\mathbf{J}_e = -n_e e\mathbf{v}_e$, is the electron Eddy current density. The force shown in Equation 2.54 is thefore the resultant Lorentz force that causes an acoustic vibration in the material.

So far, only the contribution from the static field has been considered. The current pulsed through the coil will also generate a dynamic field $\mathbf{B}_d$ surrounding the coil. The resultant field, as illustrated in Figure 2.3, will also contribute to the generation via the

Lorentz force in the sample. In this case the total Lorentz force acting on the electrons generated from the static and dynamic field is

$$\mathbf{F}_{total} = \mathbf{F}_s + \mathbf{F}_d = e\mathbf{v}_e \times (\mathbf{B}_s + \mathbf{B}_d). \tag{2.55}$$

2.2.1.3 Magnetisation force mechanism

Classical electromagnetism defines magnetisation as the vector field that describes the density of permanent or induced magnetic dipole moments in a magnetic material [9]. When a ferromagnetic material is exposed to an external magnetic field $\mathbf{H}$, magnetisation $\mathbf{M}$ arises in the volume and on the surface of the material, with a corresponding force acting on the volume and surface of the material. These forces can be summed as

$$\mathbf{F} = \int_{\mathbf{v}} \nabla^*(\mathbf{M} \cdot \mathbf{H}) dV + \frac{1}{2}\mu_0 \int_S \mathbf{n} M_n^2 dS. \tag{2.56}$$

The operation ∇^* in the first term of the right hand side means that ∇ is only operating on $\mathbf{H}$. $\mathbf{n}$ the is unit vector normal to the material surface and M_n is the normal component of the magnetisation at the surface. The first term corresponds to the force acting on the material volume and is called the magnetisation force. The second term on the right hand side corresponds to the force on the surface of the material. It accounts for the steep change of the electromagnetic fields at the surface and disappears inside the material. EMAT generation of acoustic waves in ferromagnetic materials concerns the first term which is the body force per unit volume.

2.2.1.4 Magnetostriction force mechanism

When a ferromagnetic material is exposed to an external magnetic field, such as during magnetisation, there is a dimensional change in the shape or size of the material, depending on the magnitude and direction of the field [106]. This property of ferromagnetic materials is known as magnetostriction. The cause of magnetostriction can be viewed from the microscopic structure, i.e the electron configuration. For example, in iron, the external magnetic field affects the $3d$ subshell and changes the shape and size of the $3d$-electron orbits to minimise energy in the presence of the field [42]. At the macroscopic level, changes occur in the magnetic domains that cause the dimensional change. In the absence of an external magnetic field, the magnetic domains are randomly oriented. When an external field is applied, the domains rotate to align with

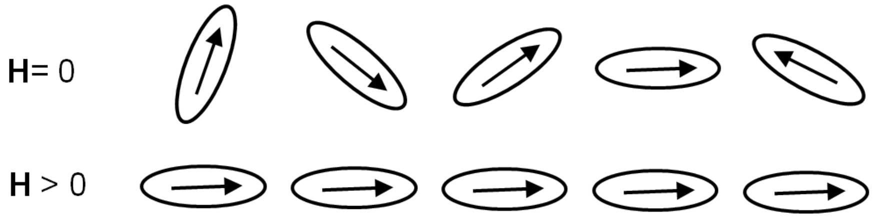

Figure 2.4: Magnetic domains orientation in magnetostrictive materials when there is no external magnetic field ($\mathbf{H} = 0$) and when the field is present ($\mathbf{H} > 0$).

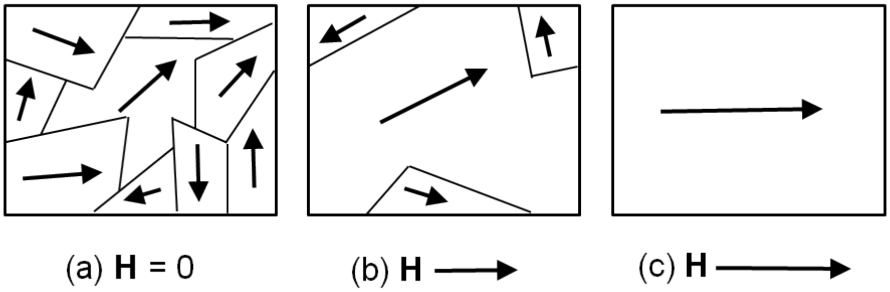

Figure 2.5: Magnetostriction response in polycrystalline materials. (a) Magnetisations of magnetic domains are at random orientations in the absence of the external magnetic field, **H**. (b) A domain that has magnetisation near to the field direction expands its volume at the expense of other domains. (c) Once the rearrangement is done, the magnetisation rotates to align with the external field.

the direction of the field, as illustrated in Figure 2.4.

The response of the magnetostriction in polycrystalline materials is more complex than the mechanism explained above. This is due to the varying size and shape of the magnetic domains in the structure. This process is illustrated in Figure 2.5. Initially in (a), without the external magnetic field, the magnetic domains have random orientations. When an external field **H** is applied in the direction shown in (b), the domain that has magnetisation oriented near to the external magnetic field expands in volume. The expansion is at the expense of other domains and is also causes an elongation in the field direction. Once the domain rearrangement is done, the magnetisation rotates about its easy axis to align with the external field in (c). The magnitude of magnetostriction in the direction of the field now is a function of the field.

2.2.2 EMAT detection mechanism

Propagating ultrasonic waves cause a dynamic deformation in an electrically conducting material. In EMAT detection, vibrating atoms and electrons, which are ‘glued’ together through the Coulomb force, move under the applied static magnetic field which forms part of the EMAT. As both atoms and electrons have a velocity associated with the ultrasonic vibration, and both are charged, they experience the Lorentz force. The atoms are a few orders of magnitude heavier than the electrons and therefore move only a small amount.However, the electrons are a lot lighter and free to move to create a current in the material. Once the current is generated within the skin depth of the material, this creates an electromagnetic wave that generates a time varying magnetic field.An EMAT coil placed above the sample detects the time varying magnetic field, and an electromotive force (emf) is generated, which in turn produces current in the coil.

Essentially, the EMAT detection mechanism involves the consideration of three main factors. Firstly, the current induced by the ultrasonic wave moving under the presence of the static magnetic field. Secondly, the boundary at the material surface, where the generated electromagetic fields propagates into an air gap between the EMAT and the material. Finally, the electromagnetic fields in the air gap , where the EMAT coil is inducing emf. The electromagnetic fields generates an electric field **E** in the coil through Faraday’s law (Equation 2.35), which is proportional to the cross product of the rate of change of displacements **u** of the vibrating electrons that form the eddy current in the material and the static magnetic field, $\mathbf{B_0}$,

$$\mathbf{E} \propto \frac{\partial \mathbf{u}}{\partial t} \times \mathbf{B}_0. \tag{2.57}$$

The right hand side of Equation 2.57 resembles the term $\mathbf{v} \times \mathbf{B}$ in the Lorentz force (Equation 2.48). In a way this is the reversed Lorentz force, but it is only true for electrons with energy above Fermi energy [29]. This means that the current generated in the coil is proportional to the electric field induced by the electrons displacement in the material. Since the electron displacement is governed by the dynamic deformation caused by the elastic wave, the current induced in the coil is proportional to the vibration of the elastic wave. Effectively, this means that the EMAT is a velocity sensor.

2.3 Laser ultrasonic receiver

An EMAT receiver detects ultrasonic waves over the finite area covered by the coil. The area can be considerably wide (approximately 1-1.5 mm), such that any defect smaller than this area cannot be fully resolved by the EMAT receiver. This is because the EMAT effectively averages the signals detected within the area (this is described in Section 6.3). Surface cracks of size comparable to the width of the coil can still be detected by the EMAT. The results however are not fully understood. In order to understand better, the interaction of Rayleigh wave with surface cracks of narrow widths, a laser based ultrasonic receiver is used for detection of ultrasound waves. With the laser detection, a smaller detection area (approximately 200 µm) can provide more information of the interaction. This is rather useful when dealing with cracks of small widths (narrow width), as there are diffractions of ultrasonic waves around the crack edges. The use of laser detection allow for finer detection around the crack edges for better understanding of the wave diffractions.

A laser interferometer is occasionally used as a lab tool to measure the small displacements produced when an ultrasonic wave reaches and distorts an external surface. There are various interferometer designs available depending on the need of detection or work [36]. For this study, a reference-beam interferometer with an adaptive beam combiner that uses two-wave mixing in a photorefractive polymer [107] have been used. The method uses the two-wave mixing to combine a distorted signal beam (reflected beam from the sample surface) with a plane-wave reference beam and match their wavefronts for homodyne detection. Some of the advantages of this type of interometer are that it require no path-length stabilisation, and it can also process speckled beams from rough surfaces.

A schematic diagram of the interferometer used for measuring the out-of-plane displacement ,reproduced from [107] is shown in Figure 2.6. The main principle behind this is the two-wave mixing in the photorefractive material that creates a real-time holograph. A probe laser is used to generate a signal beam, and a reference beam is formed by splitting the probe beam using a half-mirror. The signal beam is directed towards the workpiece, interrogating the surface during ultrasonic vibration and reflecting back to the photorefractive material. The reference beam is reflected by a mirror to create an angle to the signal beam, and also directed towards the photorefractive material to be combined with the signal beam.

The two beams interfere in the photorefractive materialto create a real-time holo-

This figure has been blanked out due the author has no permission to reproduce.

Figure 2.6: Schematic diagram of a laser ultrasonic receiver based on two-wave mixing taken from reference [107]..

gram that records the interference pattern between the signal beam and the reference beam. The created hologram acts to combine the transmitted signal beam with the refracted reference beam, and provide a perfect wavefront overlap for coherent detection. When the surface of the workpiece is displaced as a result of ultrasonic vibration, there is a transient phase change induced onto the beam. The coherent detection process converts this phase change into an amplitude change that is proportional to the phase change.

2.4 Machine learning

In machine learning computer programs are trained to learn a specific task based on a set of training examples. There are various methods available. The commonly used methods; decision tree learning, genetic algorithm and programming, and artificial neural network are described here. These methods are applicable to the program developed to classify ultrasound B-scans images (Section 5.2).

2.4.1 Decision tree learning

Decision tree learning is one of the most popular methods for forming a general classification principle based on a set of training data [82, 108, 109]. It has been successfully applied to a number of applications including fault diagnosis of bearings [110], classification of clinical specimens as diseased/non-diseased from lung cancer patients [111], and sales forecasting [112]. This method approximates discrete-valued target functions, in which the learned function is represented by a decision tree. In some cases, it can also be represented by a set of if-then rules to improve better human readability.

Instances in decision tree are classified by sorting them down the tree from the root to some leaf node, as illustrated in the example in Figure 2.7. Each node in the tree specifies a testof some of the attributes of the instance, and each branch descending from the node corresponds to one of the possible values for this attribute. An instance is classified by starting at the root node of the tree, testing the attribute specified by this node, and moving down the tree branch corresponding to the value of the attribute as in the given example. This process is then repeated for the subtree rooted at the new node, until a decision is reached.

Decision tree algorithms learn various attributes from the available training data set. There are a number of different algorithms available such as ID3 [82] and C4.5 [113]. The later is used in this study through its Java implementation, J48 in the data mining software, Weka [114], which will be explained later in Chapter 5. Generally, most decision tree learning algorithms follow the same core structure. First, in order to a classify a new item, it has to create a decision tree based on the attributes known from the available data. To do this, it identifies the attribute that discriminates the various instances clearly. The attribute feature chosen should tell the most about the data instances such that it has the highest information gain (measure of effectiveness of an attribute in classifying the training data). If there is any value for which there is no ambiguity such that it has the same value for the target sample, then the branch is terminated and the value is assigned to the target value that is going to be obtained.

For other cases where there is no unambigous results, another attribute that has the most information gain is identified following the same manner as the first attribute. The procedure is repeated to search for other attributes until a clear decision of the combination of attributes that gives a particular target value and hence classifies the data, is found. In the case where there is no clear combination of attributes, or the procedure has run out of attributes, a target value is assigned to the branch based on the values of the majority of items the branch holds.

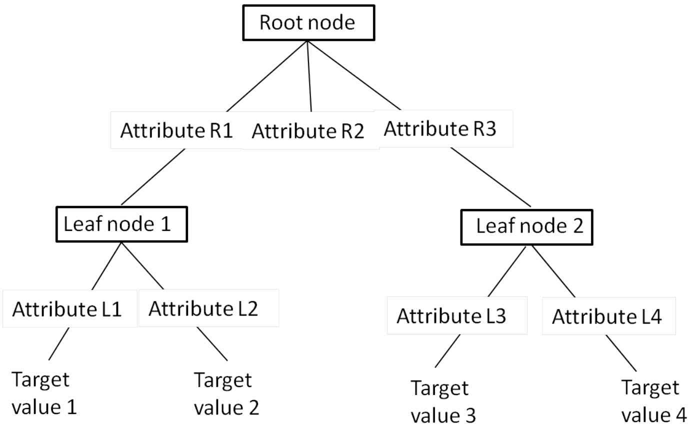

Figure 2.7: A typical structurure of decision tree learning.

2.4.2 Artificial neural network

Artificial neural network (ANN) is a machine learning method inspired by the observation of biological learning systems. Such systems are made from interconnected sets of simple units, which are sometimes referred to as "neurons", "neurodes", and "processing elements". For a given system, each unit takes real value inputs and produces a single value output. The inputs can be the outputs of other units, and similarly, the output of this system can become the input to other units. What makes ANN attractive is its speed in learning and making complex decision. For example, a human brain takes approximately 10^{-1} seconds for a person to visually recognise its mother. This is significantly faster than the time it takes for a computer to complete the calculation. As the human brainlearns at faster rate than expected, many speculated that any biological neural system must have a highly parallel processing abiliy. ANN find applications in many areas including face recognition, speech recognition, autonamous vehicle driving and handwriting character recognition [87]. In NDE applications, ANN has been used in automatic defect classification [85] and modelling fatique crack growth [89]. At the current time the application of ANN is still an active area of research.

An example of the structure of ANN is shown in Figure 2.8. It consists of three layers; input layer, hidden unit layer and output layer. The number of units in each layer can be of any size, and they are not restricted. In the example given, there are five units in the input layer, four units in the hidden layer, and seven units in the output layer. Each unit in the hidden layer takes the values of all input and produce a single value output.To achieve the output in this form, each input is multiplied by a weight,

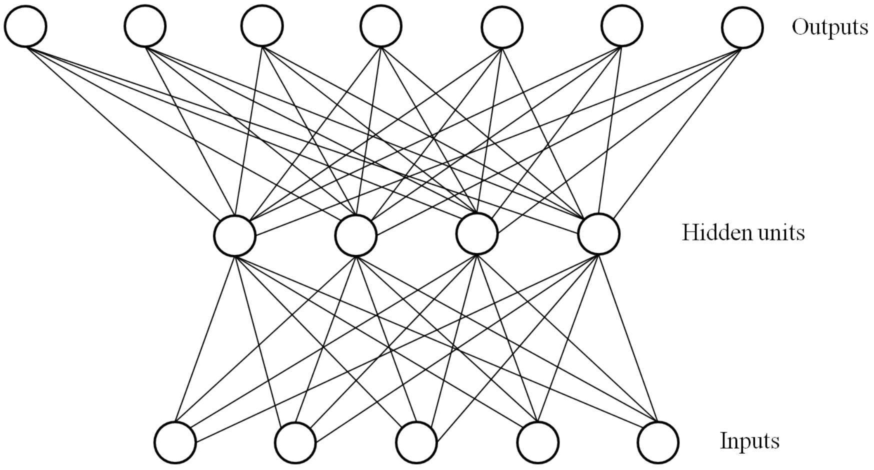

Figure 2.8: A structure of artificial neural network.

w_i, which represents the contribution of input x_i to the output. Thus the output can be written as a function of the weight-input product as follows

$$output = w_0 + w_1x_1 + w_2x_2 + w_3x_3 + ... + w_nx_n \tag{2.58}$$

or in a simplified form as

$$output = \sum_{i=0}^{n} w_i x_i \tag{2.59}$$

where i =0, 1, 2, 3...n and n is the total number of inputs.

ANN learns to meet a target output by using all possible combinations of w_i. For example, $w_1 = 0.6$, $w_2 = -2.7$, and $w_3 = 7.8$. The best combination indicates the correct learning method used. There are two ways to determine how good a specific combination is. Firstly, by comparing the output of the combination with the target output; the combination that results in the agreement between these two values is a good combination, and will be selected. If there is no agreement achieved, a combination that yields the closet calculated output to the target output will be selected. Secondly, by looking at the error in calculating the output of the combination; the combination with the least error is considered a good one.

2.4.3 Genetic algorithm and genetic programming

Genetic algorithms (GA) are a machine learning method inspired by biological evolution [82]. They based on the ideas of natural selection, mating and mutation in evolutionary theory, in order to produce a better offspring. In GA, hypotheses are normally described by bit strings whose interpretation depends on the application. A variant of GA, known as Genetic Programming, uses computer programs instead of bit strings for describing the hypothesis.

In GA, the best hypothesis is searched for from a space of candidate hypotheses known as a population, and there is an optimised numerical measure for the problem at hand, called the hypothesis fitness. This hypothesis fitness is determined differently depending on the task. For example, if the learning task is finding the best classification algorithm for classifying ultrasound B-scan images, the fitness could be the accuracy of the algorithms in classifying training data. If the task is to learn a strategy for playing chess, fitness could be defined as the number of games won by the individual when playing against other individuals in the current population.

A typical genetic algorithm process normally consists of a selection process, crossover, and mutation. Initially, a number of hypotheses are generated at random to create a population, which can be labelled as population P. A fraction from population P are identified at the beginning to go through each of the processes. For example, 90% of the population with high fitness values remain in the population, 9% of the population will go through crossover and 1% of the population will go through mutation. In the new population, the hypotheses fitness are evaluated. This process is repeated in a loop until a desired fitness is achieved.

In the crossover process, two parent strings “mate” to produce two new offsprings by copying bits strings from each other. The bit at position i in each offspring is copied from the bit at position i in one of the two parents. The choice of which parent contributes to the bit at position i for the offspring is determined by an operator called a crossover mask. This is constructed from n 1s, followed by 0s to complete the string. This results in the first n bits being contributed by one parent, and the remaining bits by the second parent. Figure 2.9 illustrates an example using two parent strings; 10110 and 00111, and a crossover mask of 11000. The first offspring string on the top right is therefore constructed from the first 2 bits of parent 10110 and the last 3 bits of parent 00111. The bits from the parent strings contributing to offspring are underlined to highlight the crossover. A second offspring (bottom right) is constructed from the

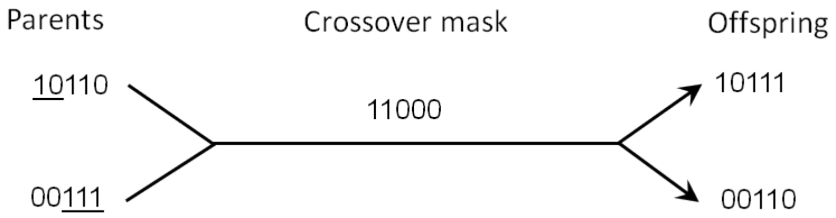

Figure 2.9: Crossover of two parent strings using the crossover mask producing two new offsprings. The underlined bit in the parent strings indicates the bit used to form the offspring on the top right.

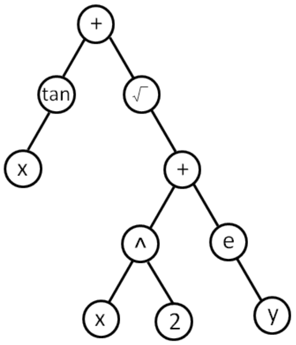

Figure 2.10: Tree representation of $\tan(x)+\sqrt{x^2+e^y}$ typically used in Genetic Programming.

non-underlined bits of the parents.

The example shown demonstrates what is known as a single-point crossover. For parents with much longer bit strings, it is also possible to conduct a two-point crossover, or a uniform crossover. Further details of these are outside the scope of this study, however more information on various crossover operators can be found in [82].

The final step in GA is the mutation, where a small change is made randomly on a parent string to produce a new better offspring. For example, say a parent string has a bit string of 10111. The mutation can swap the value of the fourth bit to produce an offspring of 10101.

In this study, GP was used, where the hypotheses are computer programs rather than bit strings. The fitness of the individual program in the population is typically determined through the accuracy of executing the programs on a set of training data. The computer programs manipulated by GP are typically respresented by trees corresponding to the parse tree of the program. A node in the tree represents a function call and the arguments to the function are given by its descendant. Figure 2.10 shows the

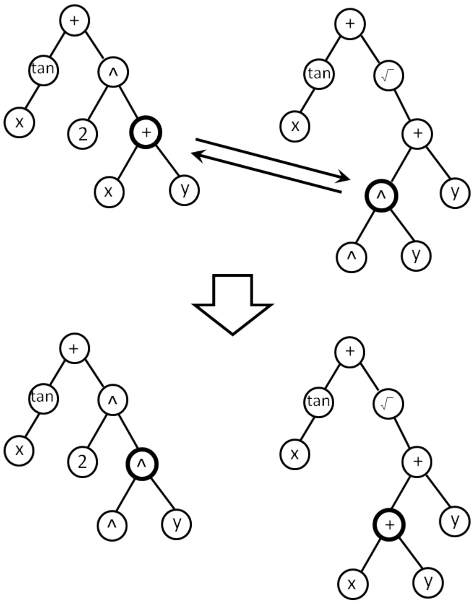

Figure 2.11: Cross over operation between two nodes (shown in bold) producing two new offspring.

tree representation for the function tan(x)+$\sqrt{x^2 + e^y}$. To apply the GP to a particular domain, the primitive functions (e.g. sin, cos, tan, $\sqrt{}$, *exponential*,+ , -) need to be defined together with the terminals (e.g. x, y, constants such as 2). The crossover operation between two parent progams is performed by replacing a subtree of a program to another program, as illustrated in Figure 2.11. A node is choosen at random from each parent to be exchanged with one another. They are shown by the bold nodes and the reverse arrow indicates the operation. The bigger arrows shows the outcome of the crossover, where two child program trees are created.

Chapter 3

Experimental details and finite element analysis

In this chapter, the details of the experiments are discussed, including the specification of the EMATs used, the geometry of the surface cracks considered, and the new experimental set up for scanning EMATs and the laser receiver along the sample surface. Finally, the details of a two-dimensional model produced using a commercial FEA package is presented.

3.1 EMAT designs

The EMATs used in the experiments were made using coils made of copper wire, and cylindrical permanent magnets [42]. Enameled copper wire of diameter 0.315 mm was used for the coil in the transmitter EMATs, while a thinner copper wire of diameter 0.08 mm was used for the receiver EMAT; the transmitter requires a thicker wire because of the high pulsed current flowing through it from the pulse generator. In contrast, the receiver requires a thinner wire to reduce noise when detecting the electromagnetic wave induced by the ultrasound as it propagates under the bias static magnetic field provided by the permanent magnet. The copper wires are wound around the outside of the the permanent magnet as shown in Figure 3.1 to form a linear coil. A cylindrical brass holder of 36 mm diameter and 45 mm height is used to house the permanent magnet as shown in Figure 3.1. A layer of 100 μm thick plastic is attached to the open base of the brass holder for protection of the coil. The brass holder is designed to shield the coil and the magnet from physical damage that could break the coil or affect their

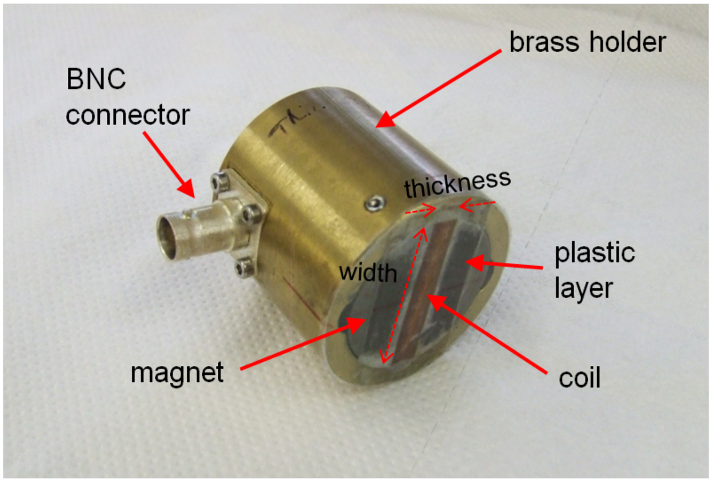

Figure 3.1: An EMAT made from a copper wire coil, wound around a cylindrical permanent magnet, is placed in a brass holder for protection from physical damage.

consistency of performance. The ends of the coil are connected to a BNC connecter for easy connection to the pulsed generator (generation) or an analog-to-digital converter (ADC)(detector).

The optimal width of the coil or the number of turns comprising of the EMAT coil depends on the role of the EMAT. In general, a wider coil has more area to generate and detect ultrasound compared to a thin coil. A wide coil will give a high amplitude signal and high signal-to-noise ratio (SNR) when used as a receiver EMAT. When deciding on the optimal number of turns, the self-inductance of the coil needs to be taken into account [41]. This must be sufficiently small so that it will not affect the rise time of the pulse current in the generation EMAT. A typical rise time for an optimised EMAT is of the order of microseconds. .

A thick coil would detect the signals over a larger area than a thin coil. Thus, the detected velocities over this area will be averaged. If a measurement is to detect the position of a crack for instance, the accuracy of the measurement will be limited by the size of the coil,giving a spatial averaging effect. A wide coil will therefore give a higher SNR at the expense of the measurement accuracy. Conversely, a thin coil will give a higher accuracy but with lower SNR. Thus, there must be a trade-off between these two in deciding the suitable coil width. In this experiment, the coils for the receivers are made using 10 turns of wire, with a width of approximately 1.5 mm. This is comparable to the size of the crack width, which is 1 mm. The coil for the transmitter is made using eight turns of coils, with a width of 1 mm.

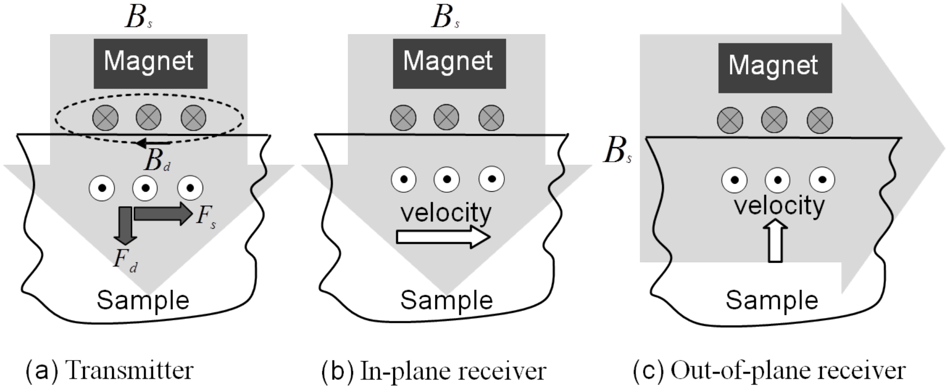

Figure 3.2: Magnetic fields and coil arrangement for transmitter and receiver EMATs. (a) The static, B_s and dynamic, B_d fields produce Lorentz forces F_s and F_d respectively. The predominantly in-plane (b) and out-of-plane (c) sensitivity of the receivers are shown by the open arrows.

Cylindrical permanent magnets made from NdFeB, grade N50, with 35 mm diameter and 20 mm height were used to apply the bias static magnetic field to the transmitter and receiver coils. The orientation of the magnetic fields is illustrated in Figure 3.2. For the transmitter shown in (a), the direction of the magnetic field is approximately normal to the sample surface [98]. This results in a large in-plane component of the force F_s due to the static field alone (Section 2.2.1.2). For the receiver, the intended sensitivity of detection, which will be either in the in-plane or out-of-plane direction relative to the sample surface, dictates the direction of the static field which needs to be applied, as shown in Figure 3.2(b) and (c). A predominantly in-plane receiver has the bias field acting normal to the sample surface, while a predominantly out-of-plane receiver has the bias field acting parallel to the surface. For brevity, the predominantly in-plane receiver is called the in-plane receiver, and the predominantly out-of-plane receiver is called the out-of-plane receiver, throughout this thesis.

The directionality of the transmitter EMAT is determined by placing the transmitter (T) and the in-plane receiver (R) on a square 60 mm thick aluminium sample, as shown Figure 3.3(a). The transmitter is fixed approximately at the centre of the plate and generate ultrasound wave which will propagate outwards. The Rayleigh wave generated by the transmitter is detected by the receiver, at a fixed distance for different angles θ. The distance between the centre of the coils of the transmitter and receiver EMATs is fixed at 150 mm, and the receiver coil is kept perpendicular to the imaginary line drawn from the centre of the transmitter coil, as shown in Figure 3.3(a). In Fig-

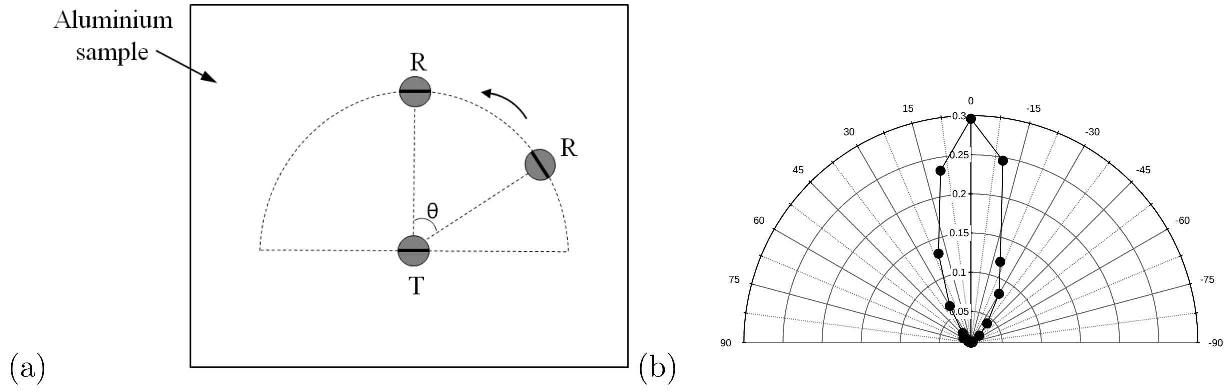

Figure 3.3: (a) Experimental set up to measure the directionality of the transmitter EMAT on a square aluminium sample. The transmitter (T) is fixed approximately at the centre of the sample, and the receiver (R) detects the signal at different angles θ at a fixed distance away. The result is plotted in (b). The angle axes represents θ and the radius is the amplitude of the signal (arbitrary units).

ure 3.3(b), the amplitude of the Rayleigh wave is plotted on a polar plot.In this plot, θ is assigned as negative in the first quadrant and positive in the second quadrant. The transmitter is found to generate Rayleigh waves with a spread of $\pm 30°$ from the origin. Most of the high amplitude wave is concentrated within $\pm 10°$ from $\theta = 0°$ and for 10° to $\pm 30°$ the amplitude is relatively low. The small spread is acceptable because the separation between the transmitter and receiver used in the experiment is small, which is 150 mm. At this separation, the wavefront of the incoming Rayleigh waves can still be approximated as a plane wave, when they reach the receiver.

3.2 Surface crack samples

Surface cracks can come in various shapes and sizes, as explained in Section 1.5. In this study, three categories of surface cracks are considered; full-width crack, narrow crack and rough crack. The full-width crack has the same width as the aluminium bar, as shown in Figure 3.4, hence it can be viewed as infinitely long and oriented perpendicular relative to the incoming Rayleigh wave. The narrow crack has a finite width, as shown in Figure 3.5, and is positioned at the centre of the sample surface, such that waves can be diffracted around the crack edges. These two types of cracks are artificial and were introduced to aluminium bar samples through two different machining method. Saw was used to make the full-width crack, and electrical discharge machining (EDM) was used to make the narrow crack. EDM is a process of machining electrically conductive materials using precisely controlled sparks that occurs between an electrode and a workpiece in the presence of dielectric fluid. The electrode act like a cutting tool to cut the workpiece. The saw cannot make a cut not to be full face if a constant depth slot is required. For this reason, the EDM was used for the narrow crack. The narrow crack has fine opening of (300 μm) and it also requires the EDM to be done in the middle of the sample surface. Such machining creates a “pocket” on the surface without cutting the sample edges. The EDM method was found to meet these requirements. The rough crack sample used is a real defect on an aluminium billet provided by industry, which contains surface breaking cracks, as shown in Figure 3.6.

Aluminium is chosen above other materials, for example steel, to produce these samples for a number of reasons. Firstly, the ultrasound propagation in aluminium is isotropic for non single crystal material, which makes it easier to focus on the interaction of the ultrasound wave with a crack. It has been reported that aluminium bars supplied by manufacturers can have different surface characteristic due to manufacturing process [95]. For this reason, the aluminium bars used in this study were initially prepared by removing 3 mm from the surface, where the cracks were going to be introduced. Secondly, it is non-magnetic, therefore only the Lorentz mechanism needs to be considered for EMAT transduction [42]. In addition, being non-magnetic allows easy scanning of the sample to be done with a small scan step (0.1 mm) using an x-y stage, as there is no strong attraction force between the EMATs and the sample.

In order to generate a Rayleigh wave in the aluminium bar samples, the product of the frequency of the wave and the thickness of the bar has to be large enough to give an approximation to a half-space, as explained in Section 2.1.3 [53]. The EMAT transmitter generates a broadband frequency (50-450 KHz) wave, with a central frequency of ‘235 KHz, as shown in Figure 3.17. For this bandwidth, the thickness of the aluminium bar was chosen to be approximately 60 mm, based on the longest wavelength. The width of the sample has to larger than the diameter of the EMAT holder (46 mm) ; Therefore, the width was chosen to be approximately 60 mm. The length of the sample needs to be about a metre long so that it can fit on the x-y stage (Figure 3.7), but be long enough for the EMATs to be scanned on the sample surface without reflections interfering with the signals. To maximise the number of cracks on each aluminium bar, the cracks are located on more than one surface of the bar. For a surface which has more than one crack, the cracks were separated by approximately 300 mm with the same minimum distan from the end of the bar to minimise wave reflections.. Table 3.1(a) lists the cracks used in the experiment, with their dimensions.

Figure 3.4 illustrates an example of full-width crack on the surface of an aluminium bar. The crack is produced by machining a 1 mm thick slot on the sample surface at an angle θ to the surface and with a vertical depth d. The 1 mm slot thickness ensures that the crack faces are not in contact.The list of all full-width cracks used in the experiment is given in Table 3.1(a). In general, there are three groups of samples; The first group contains 90° cracks with depth ranging from 1 mm to 20 mm. The second group contains 3 mm and 5 mm deep cracks of various angles to the surface. The third group contains 45^o cracks with depth ranging from 1.5 mm to 15 mm. For the inclined cracks, there will be two values of angle relative to the wave propagation direction available for measurement; an acute angle and an obtuse angle for scanning from the other direction.

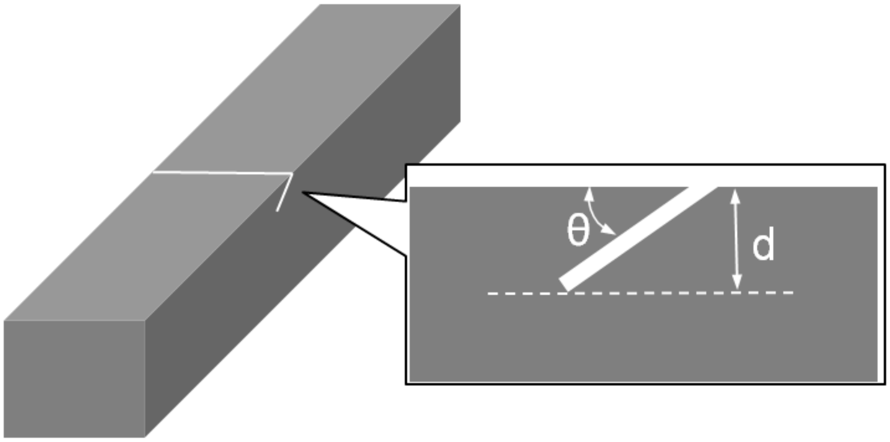

Figure 3.4: Full-width crack on the surface on an aluminium bar. The inset shows the geometry of the crack, where θ is the inclination angle from surface, and d is the vertical depth. The list of all cracks with different θ and d values are given in Table 3.1(a).

The geometry of the narrow cracks on the surface of an aluminium bar is illustrated in Figure 3.5. The crack is located at the centre of the bar width to keep it away from from the edge reflections. From the top of the aluminium bar only the crack opening is physically visible, and the dimension of the crack width w can be measured using a ruler like real defects. The cracks have a 300 μm wide opening, and smooth interior faces and a flat bottom. A cross-section view of the crack from the side of the aluminium bar is shown in the bottom right of Figure 3.5. The figure indicates the inclination angle of the crack from the surface (θ) and the vertical depth d, and is similar to the geometry of the full-width cracks described earlier. All the narrow cracks have d =5 mm. Two values of θ, 90° and 25°, are considered, as listed in Table 3.1(b). For each angle there are two different crack widths, 10 mm and 20 mm.

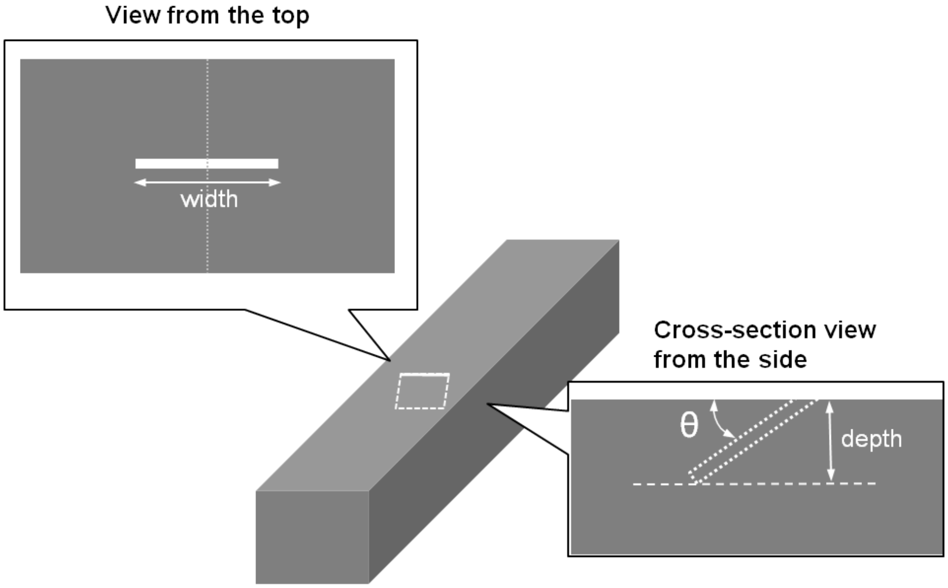

Figure 3.5: Narrow crack geometry

Real surface-breaking defects have also been investigated. A photograph of a section of an aluminium billet supplied by industry containing two rough cracks was captured using an optical microscope and is shown in Figure 3.6. The cracks were found on the billet during manufacture. Two cracks across the bar width can be seen; Crack 1, on the left hand side, has a length of approximately 26 mm. The close up view of this crack shows that the crack opening is small, of the order of microns. Crack 2, on the right hand side, has a wide opening and originates from the right hand edge of the sample. These two cracks grow almost parallel to each other with approximately 5 mm separation between them.

3.3 Pitch-catch EMAT system

A pitch-catch system is used for all EMAT measurements made in this study. The system consists of an EMAT transmitter "pitching" ultrasonic waves to an EMAT receiver ("catch") set a certain distance away. In contrast to the pulse-echo approach which detect the reflection from a defect (Section 1.4), this system can operate significantly faster as there is no requirement to wait for the reflections of the ultrasonic waves.

(a) List of full-width cracks

Crack depth/mm	θ/degree
1.5	45
2	90
3	15, 22.5, 35, 45, 55, 67.5, 75
5	15, 22.5, 35, 45, 55, 67.5, 75, 90
10	45, 90
15	45, 90
20	90

(b) List of 5 mm deep narrow cracks

θ/degree	Crack width/mm
90	20 and 10
25	20 and 10

Table 3.1: List of full-width cracks and narrow cracks.

In the pitch-catch measurement, ultrasonic waves travel down the sample and interact with defects before detection. The measurement therefore relies on the wave transmission, rather than the wave reflection, in order to detect and size cracks [23]. In this way, the risk of deeper cracks masking small cracks, as shown in Figure 1.5, can be minimised when the cracks are closely spaced.

Figure 3.7 shows a schematic diagram of the main experiment set up for an EMAT transmit-receive system. LabVIEW is used to control the experiment, and the EMATs are positioned above the surface of the aluminium bar sample which is placed on the x-y stage and fixed in place. The table has an arm which the EMATs are mounted to, and this is then scanned along the sample surface. The arm is moved by a motor that is capable of moving a smallest step equivalent to 1/100 of a milimetre. During the experiment, the choice of the scanning step is dictated by the type of measurement; typically, 0.5 mm scanning step is used for far-field measurements and 0.1 mm scanning step is used for near-field measurements. The full details of these measurements will be explained in Chapter 4. The speed of the motor was set to 4 mm/s for all measurements. When LabVIEW was set to run a scan, the detected signals were recorded after each scan step before moving the EMAT another step.

The pulsed current for the EMAT transmitter comes from a pulse generator (shown on the left in Figure 3.7) which is designed and built in-house. The pulse generator is capable of generating a pulsed current with a repetition rate variable from 1 Hz to a maximum of 100 Hz. In most measurements, the pulse rate is set to 8.5 Hz, to make

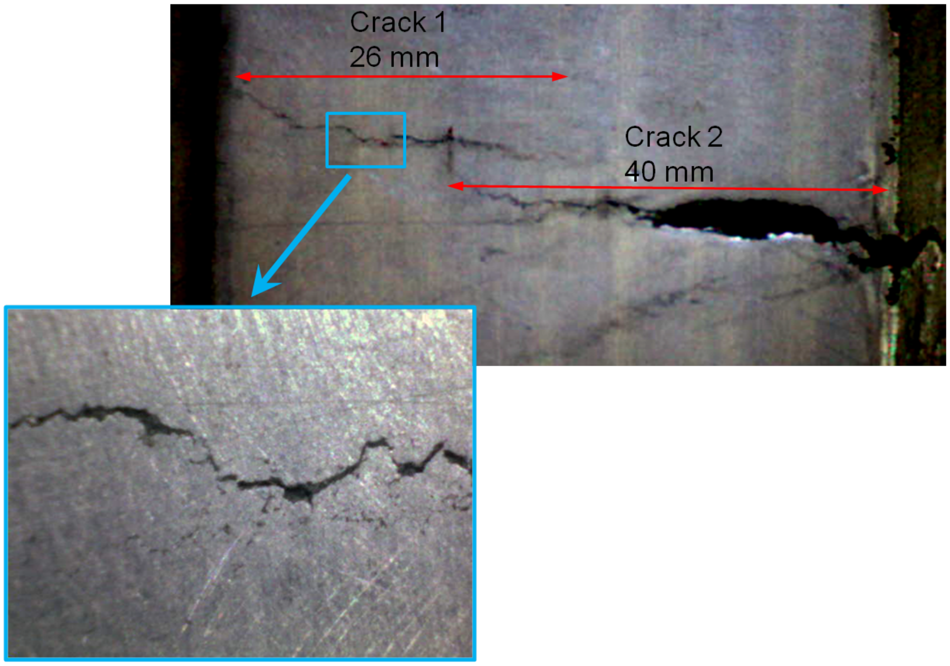

Figure 3.6: A photo of a machined surface of an aluminium billet containing two rough cracks. The inset shows a close up view of Crack 1.

sure that the pulse generator properly triggers the analog-to-digital converter (ADC), and also not to heat the EMAT too much. The ADC used is a PicoScope which has 250 MHz bandwidth, 1 GS/s maximum sampling rate, and 8-bit resolution. Figure 3.8 shows the current pulse sent to the transmitter which has a duration of about 6 μs, with a shape close to a sine wave and a peak-to-peak amplitude of 10 units (arbitrary) .

A pre-amplifier which is designed in-house is used to amplify the current from the receiver before sending it to the ADC. The signals are displayed in real-time on the computer monitor and also saved to the computer's memory. Signal averaging is applied before saving, to remove some of the noise from the x-y stage itself. 16-20 signal averages was found to give a good signal for analysis.

Several configurations can be used for scanning EMAT in order to detect defects. Two methods are implemented here and are illustrated in Figure 3.9. In Figure 3.9(a), the transmitter EMAT is held at a fixed postion relative to a crack or the bar end, while the receiver EMAT is moved away from the transmitter towards and over to the other side of the crack. At each scan position the signal is recorded. The objective of this method is to vary the separation between the transmitter and receiver, which can aid to

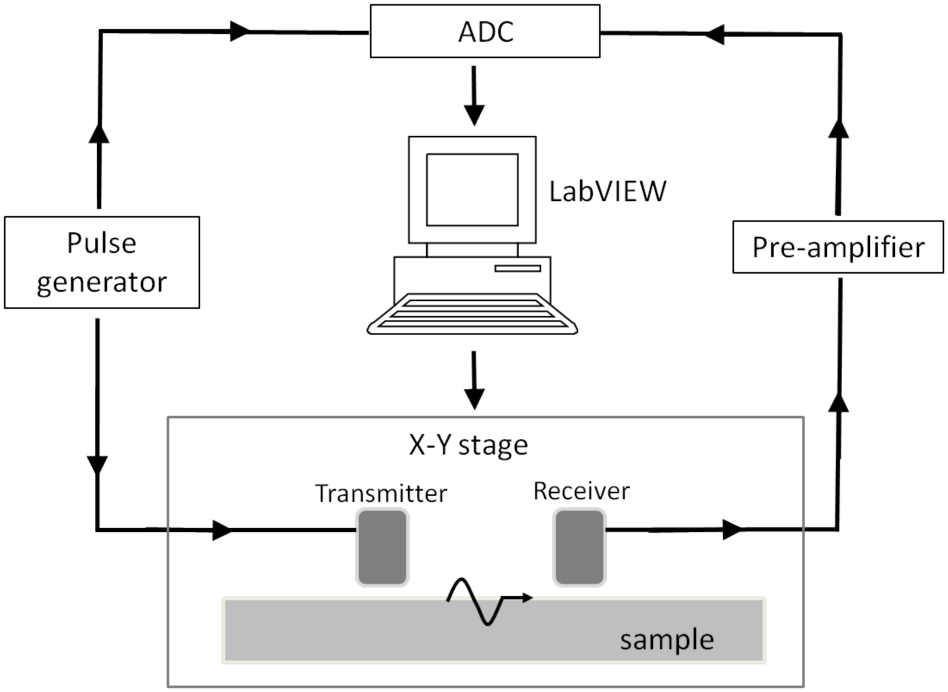

Figure 3.7: Schematic diagram of the experimental set up

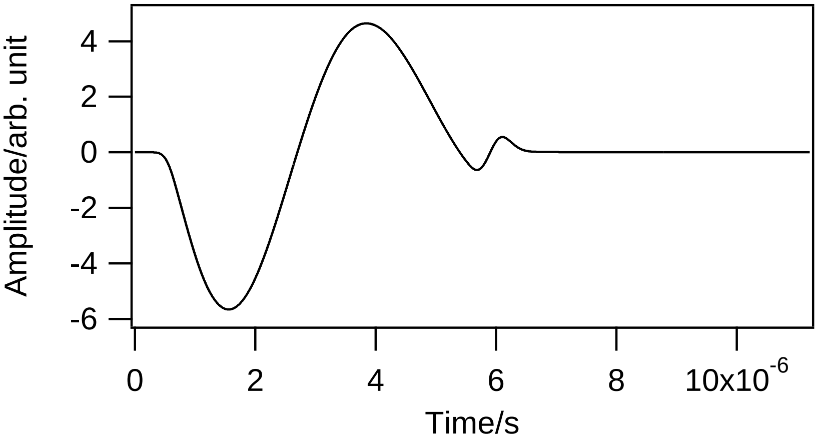

Figure 3.8: Pulsed current sent to the transmitter EMAT.

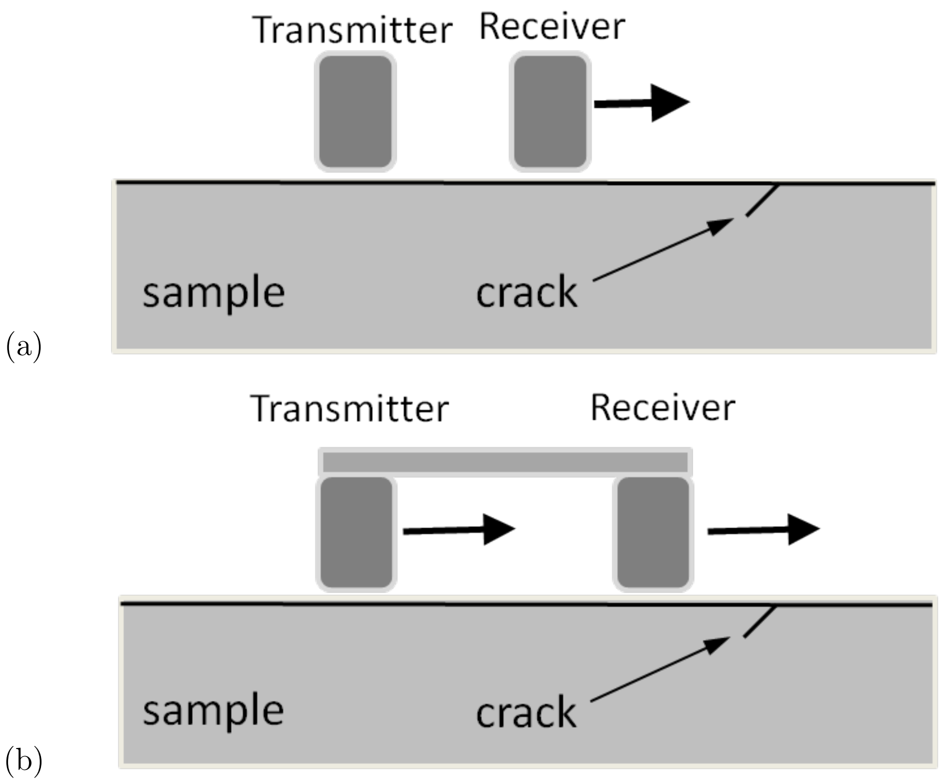

Figure 3.9: Methods of scanning EMATs on aluminium bar sample. (a) Scan receiver only, while keeping transmitter at a fixed position, (b) Both EMATs are scanned together with fixed separation.

identify the wave modes present in the sample. Further details of this will be covered in Section 4.1. In Figure 3.9(b), the transmitter and receiver EMATs are mounted to an aluminium holder (Figure 3.10) to keep the separation between them fixed at 150 mm apart. This separation is found to be the best in minimising the interaction of bulk wave (reflected from the underside of the sample) with the Rayleigh wave arrival time for certain sample thickness. The whole unit is then scanned together towards a crack, with the receiver at the front so that wave propagation is in the same direction as scanning. By keeping the separation fixed, the incident Rayleigh wave will always arrive at the same time for the same material, making it easier for B-scan monitoring. For an optimal separation, the reflections of bulk waves from the underside of the sample can also be minimesed

The receiver was made with small width (1.5 mm) to increase the spatial resolution of crack detection. In all measurements, the lift-off of the EMATs is kept at 100 μm from the sample surface.

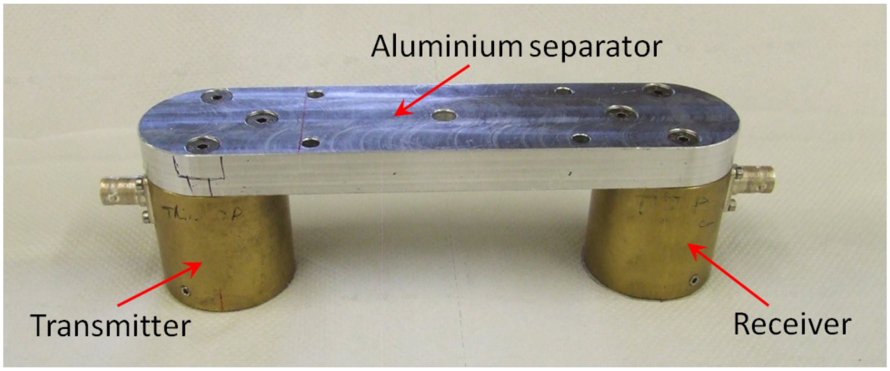

Figure 3.10: The transmitter and receiver EMATs used in pitch-catch mode with fixed separation, for scanning as illustrated in Figure 3.9(b).

3.4 EMAT generation and laser detection

A laser-based ultrasonic receiver, AIR-1550-TWM, designed and manufactured by Intelligent Optical Systems, Inc. (IOS) [115] has also been used with the EMAT transmitter to study the scattering of Rayleigh waves around narrow width cracks. The use of a laser detection system allows near-point-like detection to be made in the close vicinity of the cracks, which can give detailed information about the wave diffraction at the crack edges (Section 2.3). With the receiver EMAT, the diffraction effect is averaged over the area covered by the finite size coil. Measurements made using the laser receiver and the receiver EMAT can be compared to see how the wave diffraction will affect the EMAT measurement. Once this relation is known, adjustments can be made to the EMAT measurements when narrow cracks are found during inspection.

The laser receiver, which detects small surface displacements, is based on a homodyne interferometer, using a photorefractive polymer as an adaptive beam combiner [107]. The working principle of this type of interferometer is explained in Section 2.3. Here, the experimental set up for detecting narrow cracks is explained.

In Figure 3.11, the schematic diagram of the experimental set up is shown. The main parts of this set up can be grouped into three components; 1. ultrasonic generation using the EMAT transmitter, 2. ultrasonic detection using the laser receiver unit, and 3. the data acquisition using the oscilloscope and the computer. The first component employs the same EMAT transmitter and pulse generator as used for the scans described in Section 3.3, in order to keep the same frequency bandwidth of the generated ultrasound. The second component consists of the laser receiver head connected to the demodulator and the splitter drawer. The splitter drawer contains a variable fiber splitter used to

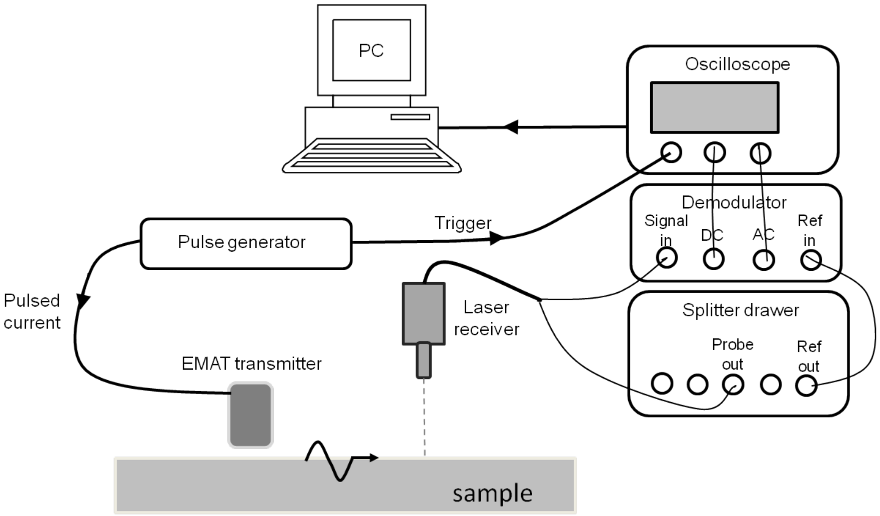

Figure 3.11: Schematic diagram of the set up for EMAT-IOS experiment

divide the fiber laser input into reference and probe beams. In addition, it also sends a red beam through the probe fiber towards the head to act as a guide for alignment. The reference beam is sent to the demodulator for the two-wave mixing process, while the probe beam is sent to the laser receiver head through a fibre-optic cable. The head focuses the probe beam to a spot, and uses the same aperture to collect the backscattered return light from the target. The return light is then collimated and focused back to into the fibre bundle for delivery to the demodulator. The two-wave mixing process (explained in Section 2.3) is conducted in the demodulator by combining the reference signal and the signal reflected from the sample [107]. The resulting signal is recorded as AC voltage and the probe beam reflectivity on the sample is recorded as a DC voltage, using the oscilloscope. Both signals can be shown on the oscilloscope, and are used to calibrate the actual displacement amplitude. In order to minimise the noise, an average of 16 signals were calculated.

A linear stage was mounted on the laboratory optical bench next to the aluminium sample. The laser receiver was held by a retort stand which is positioned on the linear stage with the laser beam directed towards the sample surface. Before the laser receiver is set to scan the sample, the laser beam has to be focussed. To do that, the separation between the laser head and the surface of the sample is initially set to about 45 mm, based on the manufacturer instructions. Finer adjustment of the separation is done by changing the separation and measuring the DC signal to detemine the exact focal point. The system requires that the DC reading is kept between 0.5-3.0 V, because outside this range the calibration is non-linear.

A test scan is carried out by moving the laser receiver to various points along the scan lines in order to check the focusing of the laser. This is an important step to do prior to run the full scan. The procedure for scanning the laser receiver close to the narrow crack is depicted in Figure 3.12. The EMAT transmitter is positioned at 130 mm from the crack and fixed approximately at the centre of the bar width. As the crack and the EMAT transmitter are symmetrical on the sample surface, only one half of the surface is scanned. This area around the narrow crack is evenly divided into 28 scan lines with a separation of 1 mm. The lines are numbered from 0 to 27, with 0 being the line at the centre and 27 at the edge of the sample. The laser receiver is scanned along each scan line from a separation of 110 mm to 180 mm from the EMAT transmitter, as shown in Figure 3.12. The scan step used varies during the measurement; in the far-field a 0.5 mm scan step is used, and as the receiver moves closer to the crack, approaching the near-field, a smaller step of 0.1 mm is used.

The third component, which is the data acquisition, is done automatically using a LabVIEW program that controls the scanning of the laser receiver. When the program is running, at each scan point, the oscilloscope will average the signals before saving the data on a memory stick. Once this is done, the laser receiver is moved to the next scan point. The procedure is repeated until the full scan of a line is completed. This is similar to the scanning method for receiver EMAT only, as illustrated in Figure 3.9(a).

3.5 EMAT lift-off effects

The measurements made using EMATs are sensitive to the distance from the sample surface to the coil in the EMAT [42, 116, 117]. As this lift-off increase, the EMAT efficiency drops resulting in a smaller amplitude signal.

A simple experiment was performed to study the effects of the changes in the lift-off on the EMAT measurements on a section of an aluminium sample. The experimental set up is illustrated in Figure 3.13. Transmitter and in-plane receiver EMATs were held in fixed separation, as in Figure 3.10. Plastic sheets, each of 100 μm thick, were stacked to raise both EMATs the same distance from the sample surface. The EMATs are raised from zero lift-off (no plastic sheet) to a maximum height of 2 mm, with 0.2 mm increments. One increment is equivalent of adding two layers of the plastic sheet underneath each EMAT. Signals were recorded at each increment. The height of

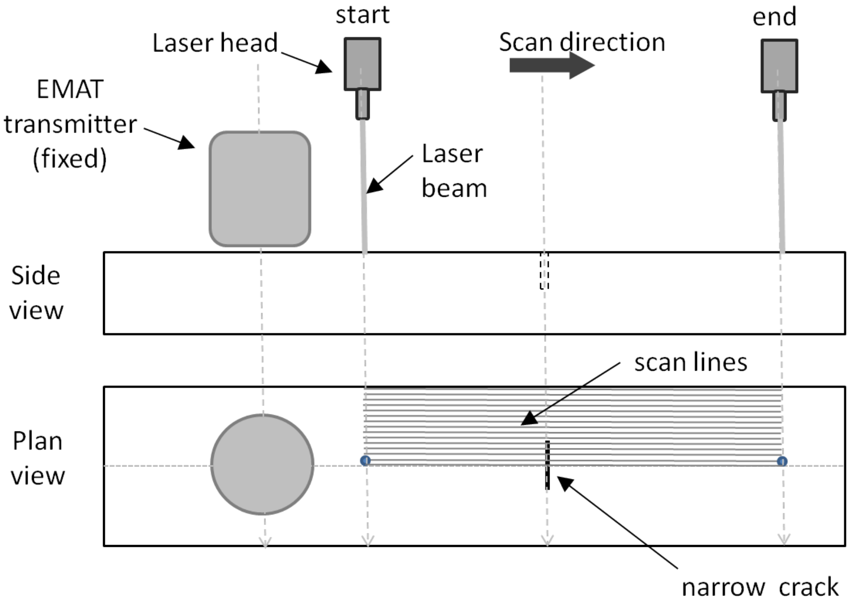

Figure 3.12: Method for scanning the laser receiver on the surface of an aluminium sample containing a narrow crack.

the lift-off was assumed to be the total thickness of the plastic sheets. There will be some errors due to very small variations in thickness or deformation of the sheet, but the lift-off obtained using this method has been found to be reliable, leading to (within errors) reproducible results.

The experiment was initially conducted on a section of sample with no defect, and then repeated on a section containing a 90° 3 mm deep slot. The objective of this is to quantify the effect of lift-off changes on the transmission coefficient. Typically, a measurement on a defective section is compared with the measurement made on a section that has no slot, in order to estimate the crack depth. Thus, the lift-off effects for both cases need to be understood.

Figure 3.14(a) shows the peak-to-peak amplitude of the recorded Rayleigh wave plotted as a function of lift-off. The two sets of data are shown; open circle represent no slot, while solid circles represenet the 90° 3 mm deep slot. In general, the measured peak-peak amplitude of both data sets decreases as the lift-off increases, with the "no slot" data maintaining higher amplitude than its counterpart, as expected. The trend follows an exponential decay as shown by the solid and dashed lines. With the values of the amplitudes of the Rayleigh waves from both data sets, the transmission coefficient,

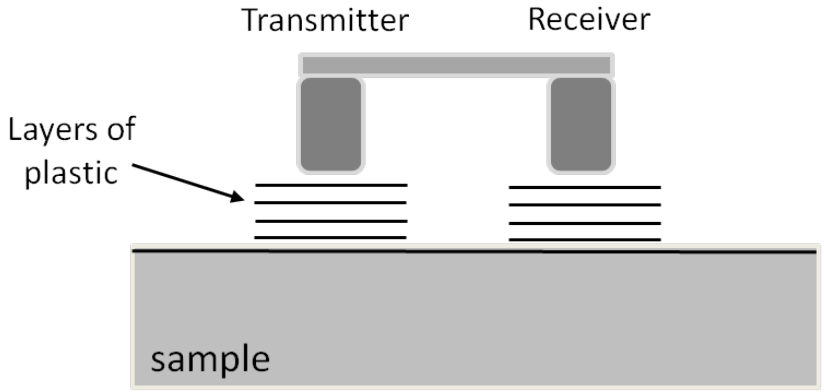

Figure 3.13: Experimental set up to study the effects of lift-off. To increase the lift-off, layers of 100 μm thick plastic sheet are stacked beneath the transmitter and receiver, held in fixed separation. The spacing between the plastic layers is exaggerated in the figure.

C_T for the Rayleigh wave can be calculated by dividing the amplitude from the slot data by the amplitude from the no slot data(see also Equation 4.6 in Chapter 4). The calculated C_T is plotted as a function of lift-off, as shown in Figure 3.14(b). The error bars in the plot are calculated based on the SNR of the signal. For the same slot, 90° 3 mm deep, the measured C_T varies between 0.63 and 0.92 as the lift-off increases from zero to 2 mm.

It is clear that the lift-off is not only affecting the Rayleigh wave signal amplitude, but it may also affect the calculation of C_T. In Chapters 4 and Chapter 5, the calculated value of C_T is used for sizing the crack depth, using a calibration made on a known sample. Therefore, in all experiments involving EMATs, the lift-off should be kept fixed at minimum value possible to give a large SNR.

The change in the signal amplitude with lift-off can be understood by comparing the fast Fourier transforms (FFT) of the signal at various lift-offs as shown in Figure 3.15. It is known that the frequency content will affect the transmission . The figure shows the normalised FFTs of signals recorded on a section with no slot in (a) and on a section with the 90° 3 mm deep slot in (b). As the lift-off increases from zero to 2 mm, the relative magnitudes of the FFTs decrease. For the "no slot data" in (a), the upper frequency boundary maintains approximately at 450 kHz, except when the lift-off exceeds 1.2 mm. Meanwhile, in (b), the upper boundary shifted slightly to a

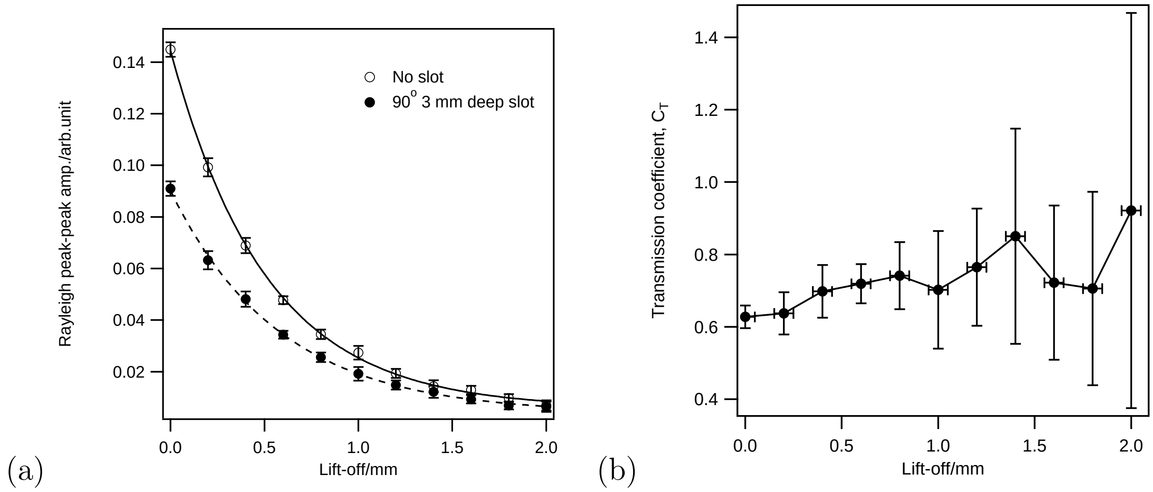

Figure 3.14: Rayleigh wave peak-peak amplitude for increasing lift-off from sample surface (a). Comparison measurements are shown for a section with no slot (open circles) and for a section containing a 90° 3 mm deep slot (closed points). The error in calculating the transmission coefficient of Rayleigh passing underneath the slot increases with the lift-off (b).

lower value as the lift-off increased. The centre frequency in (a) is shifted to lower frequency as the lift-off increase up to 1.2 mm, while in (b), the centre frequency is approximately fixed at 185 kHz. Figure 3.16 shows the plot of the centre frequency against the lift-off for both data, and the difference between them is clear. The "no slot" data varies accordingly with the lift-off up to a lift-off value of 1.2 mm, while for the 90° 3 mm deep slot data, the centre frequency is fixed around 185 kHz. This shows that the slot acts like a bad low-pass filter, where signal of frequency less than 185 kHz is allowed to pass underneath the slot while higher frequencies are effectively blocked by the slot.

The frequency content of the Rayleigh wave varies with lift-off when there is no slot present, with the variation of the magnitude and a shift in the centre frequency. In the presence of a slot, the upper boundary of the frequency bandwidth drops as the lift-off increases. These changes with lift-off affect the Rayleigh wave signal amplitude in each measurement. As a result, the transmission of the Rayleigh wave for a given slot may not be the same when the measurement is made at different lift-off, but it may agree with a certain error.

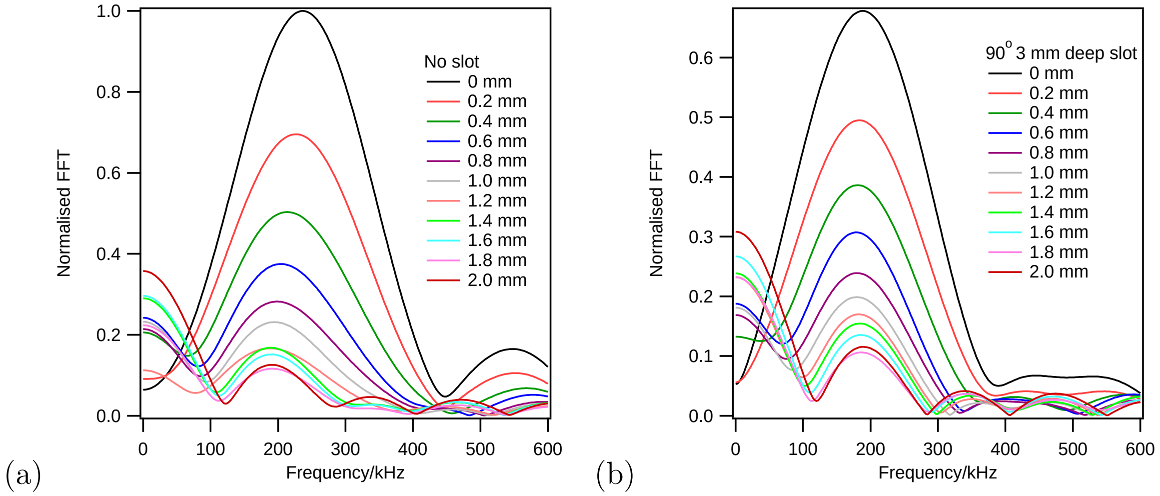

Figure 3.15: Normalised fast Fourier transform of a Rayleigh wave for various lift-offs from the sample surface,for a a section that contains no slot (a) and in a section that contains a 90° 3 mm deep slot (b).

3.6 Finite element analysis model

Finite element analyis (FEA) modelling is a numerical technique used for understanding the propagation and the interaction of ultrasound waves with defects . With FEA, a prediction of the wave interaction can be made prior to performing experiments, which can help in designing the actual experiments, plus samples and defects with different geometries can be created in the model with a specific dimension varied [118]. For example, the defect depth or the defect orientation, can be easily changed to a wide range of values. The model can also simulate defects that are not possible experimentally, such as inlined cracks with very small angle (using vary small element size). FEA is also used here to verify the experiment results and visualise wave propagation within the sample.

A commerial FEA package, PZFlex, has been used. PZFlex uses square elements to build a full model. The elements need to be at most $\lambda/20$ in size in order to avoid numerical dispersion in the model, where λ is taken as the central frequency.

For EMAT generation, there are contributions to the generation from the dynamic and static generation forces [116]. The relative contribution from each of these two forces depends on the form of the pulsed current as this carries the time information for the pulse, and the design of EMAT. Therefore, the measured current pulse from the generation pulser and EMAT used here is used to model the generation source.

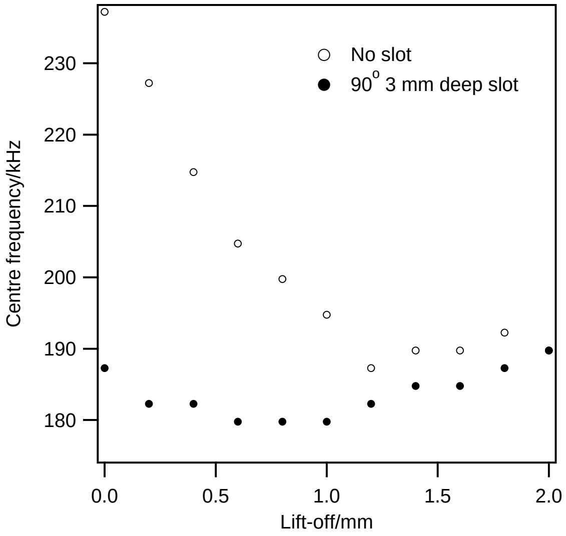

Figure 3.16: Plot of centre frequency of FFT as a function of lift-off.

Figure 3.17 shows the FFTs of the Rayleigh wave when using the experimental and the model results, using the experimental current pulse to model the EMAT generation. The generated Rayleigh wave is broadband, centered at about 238 kHz, and experiment and model show very good agreement. This is a requirement when comparing the results from experiments and models. The frequency bandwidth corresponds to the depth for which the Rayleigh wave is concentrated. A significant difference in the frequency bandwidth, between experiment and model will result in the Rayleigh wave interaction being different for the experiment and model, and a different C_T will be found.

The dimensional requirement for each model depends on the geometric complexity of the crack. Full width cracks such as shown in Figure 3.4, have their width extend across the bar width, and so can be approximated as as infinitely long defects which are normal to the incoming Rayleigh wave. Therefore, the FEA model can be reduced to a two-dimensional model, as illustrated in Figure 3.18, which shows how the model is set up.

In Figure 3.18, the positions of the generation and detection of the ultrasound wave are shown by the red and black arrows respectively. The generation position is fixed at an element, while the detection is made at several elements to simulate a scan made using an EMAT receiver.Wave velocities (differential of displacements) are recorded in the model. The model has a total length of 504 mm. The generation source (Figure 3.8) is applied to the location shown by the red arrow, at a position corresponding to 20%

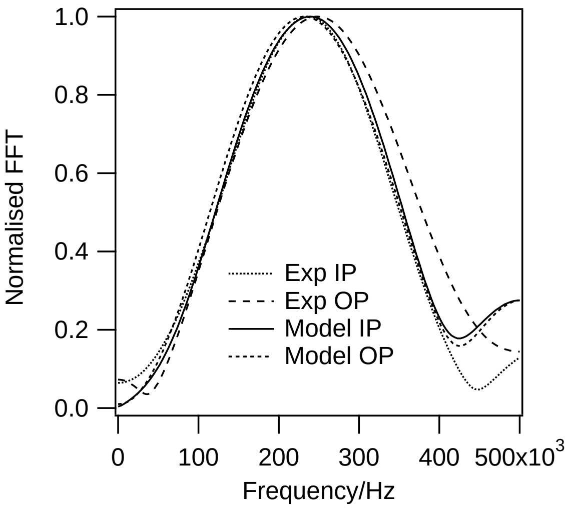

Figure 3.17: Fast Fourier transform of Rayleigh waves, showing the in-plane (IP) and out-of-plane (OP) components for the experiment and model.

of the total length, measured from the left-hand side of the model. The wave velocity is recorded at every element (size of 1.29 μm) within a region of 50 mm around the crack, as indicated by the black arrows. The distance between the crack and the generation source is set to be 200 mm. Absorbing boundaries are applied to the bottom and the left and right hand sides of the model, and effectively, the model is an infinite half-space, where the reflections from the left- and right-hand sides and the bottom can be ignored. The crack, as shown in the figure, is set to be at an angle θ from the surface and extend to a vertical depth d. With FEA model, the interaction inside the sample can be visualised as shown by the colours in Figure 3.18. In this way, the interaction of ultrasonic waves with the defect can be understood better through observation on the propagation of specific modes of interest and their subsequent mode conversion.

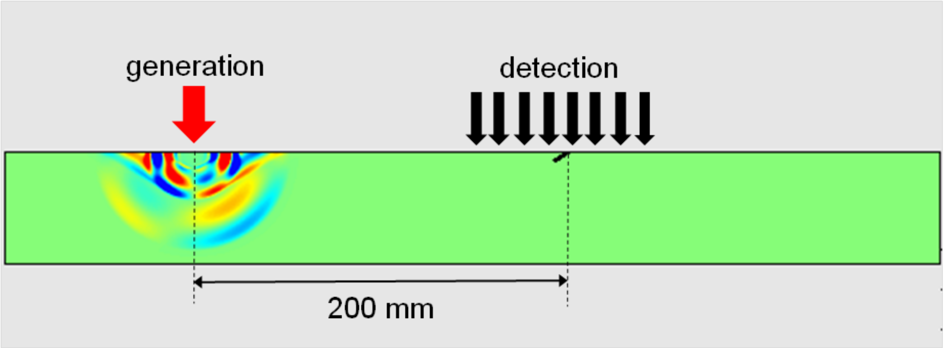

Figure 3.18: The full-width cracks are modelled as a two-dimensional finite element analysis model using PZFlex. Ultrasound generation is set at 200 mm from the crack. Wave velocity is recorded at at each element within 50 mm of the crack as indicated by the black arrows. The top surface boundary is set as free and the other boundaries are set as absorbing.

Chapter 4

In-plane and out-of-plane EMAT measurements of Rayleigh wave interactions with full-width surface cracks

Part of this chapter has been published as reference [119].

Surface cracks can have a complex geometry, as explained in Chapter 1. Each crack geometry can pose a different threat to the material structure, and hence they may require different action. For example, the difference between a crack propagating normal to the surface, and a crack propagating inclined at an angle to the surface, on a rail track can lead to different remedial action. Normal cracks are usually associated with weld breaks and only require the section to be re-weld, while the presence of inclined cracks with angles about $20° - 30°$ from the surface can indicate rolling contact fatigue, which will require a different remedial action depending on the crack depth [4,46]. For shallow inclined cracks up to 1 mm deep, the defective section can be treated by removing a milimetre of the surface to prevent the crack from continuing growing into the rail, while for deeper cracks the best action would be to remove the defective section from service as it could cause the rail to break. Therefore, it is crucial to distinguish normal and inclined cracks, and also to accurately determine the depth of inclined cracks before taking taking any measures.

An ultrasound method measuring the vertical depth of surface cracks has been developed recently, exploiting the transmission of a Rayleigh wave, passing underneath a crack [23]. The method uses calibrated transmission measurements on cracks grow normal to the surface, of known depth in aluminium samples to gauge the vertical depth of other cracks on the same material. Although the method works for the normal cracks, it is not necessarily directly applicable for inclined cracks. There is a danger in assuming that all surface cracks can be viewed as normal to the surface, because it can lead to incorrect characterisation of crack depth.

In this chapter, the angle dependence of the Rayleigh transmission for various inclined cracks has been investigated, and is discussed in Section 4.2. The length of the cracks on the surface cover the whole width of the aluminium bar samples used in the experiment, as explained in Section 3.2, hence they are classed as full-width cracks. A characterisation method to discriminate between normal and inclined cracks, based on a signal enhancement pattern in the B-scan images, is presented in Section 4.3, followed by the explanation of the enhancement in Section 4.4. Crack inclination angles are estimated using the enhancement measurements both in the in-plane and out-of-plane components of the Rayleigh wave velocity, and this is described in Section 4.5, and the dominance of each specific velocity component is discussed in the following section. In the majority of the measurements and simulations, both the in-plane and out-of-plane velocity components of the wave modes present in the signal, resulting from the Rayleigh wave interaction with the cracks, were recorded and analysed. This is to enable full understanding of the interaction of both velocity components in the crack, which much of the previous work has not considered.

The samples used for these measurements are made from aluminium, with a machined slot on the surface to simulate the crack, as explained in Section 3.2. With a full-width crack, the diffraction of the Rayleigh wave on the surface is negligible as the crack width can be approximated as infinitely long compared to the incident wave, and perpendicular to the direction of wave propagation. The interaction considered here is predominantly due to the crack geometry in two-dimensions only.

4.1 Wave modes identification

A pair of EMATs acting respectively as a transmitter and an in-plane receiver are used in a pitch-catch configuration, as explained in Section 3.3. In a preliminary experiment to identify the wave modes present, the transmitter EMAT was fixed at 200 mm from a crack and an in-plane EMAT receiver was scanned with 0.5 mm steps, starting at

50 mm from the crack on the same side of the crack as the transmitter, and scanned to an equal distance on the other side of the crack. At each scan point, the time domain signal detected by the receiver (A-scan) was recorded automatically in a LabVIEW routine. The A-scans were appended into a matrix to form an image representation of the scanned data, known as a B-scan. In a B-scan, the x and y axes show the time and scan distance respectively, while the grayscale represents the signal amplitude: black shows the maximum negative signal value (trough) while white shows the maximum positive signal value (peak).

Figure 4.1 (a) shows a typical B-scan of a surface crack propagating normal to the sample surface of depth 5 mm. The main wave modes indicated in the figure can be identified through their arrival time. The origin of the various reflected, transmitted, and mode-converted wave modes come from the interaction of the Rayleigh wave with the crack. When the Rayleigh wave reaches the crack, some of the low frequency components are transmitted underneath the crack, propagating to the other side of the crack. Some of the low frequency components are also reflected back. The high frequency components, however, can travels down to the crack tip, reflect back to the top of the crack and propagate in opposite direction to the incoming wave. At the crack tip, a number of wave modes are generated; the Rayleigh wave is mode-converted to longitudinal and shear bulk waves. It has been reported that the crack tip acts as a secondary source of ultrasound waves [72].

The arrival time of these various mode can be calculated based on the geometry illustrated in Figure 4.2 as follows:

Incident Rayleigh wave, R (Figure 4.2(b))

$$t_{IR} = (x_1 - x_2)/c_R \tag{4.1}$$

Reflected Rayleigh wave, R-R (Figure 4.2(c))

$$t_{RR} = (x_1 + x_2 + 2kl)/c_R \tag{4.2}$$

Mode converted longitudinal wave, R-L (Figure 4.2(d))

$$t_{R-L} = (x_1 + l)/c_R + \sqrt{x_2^2 + l^2}/c_L \tag{4.3}$$

Mode converted shear wave, R-S (Figure 4.2(d))

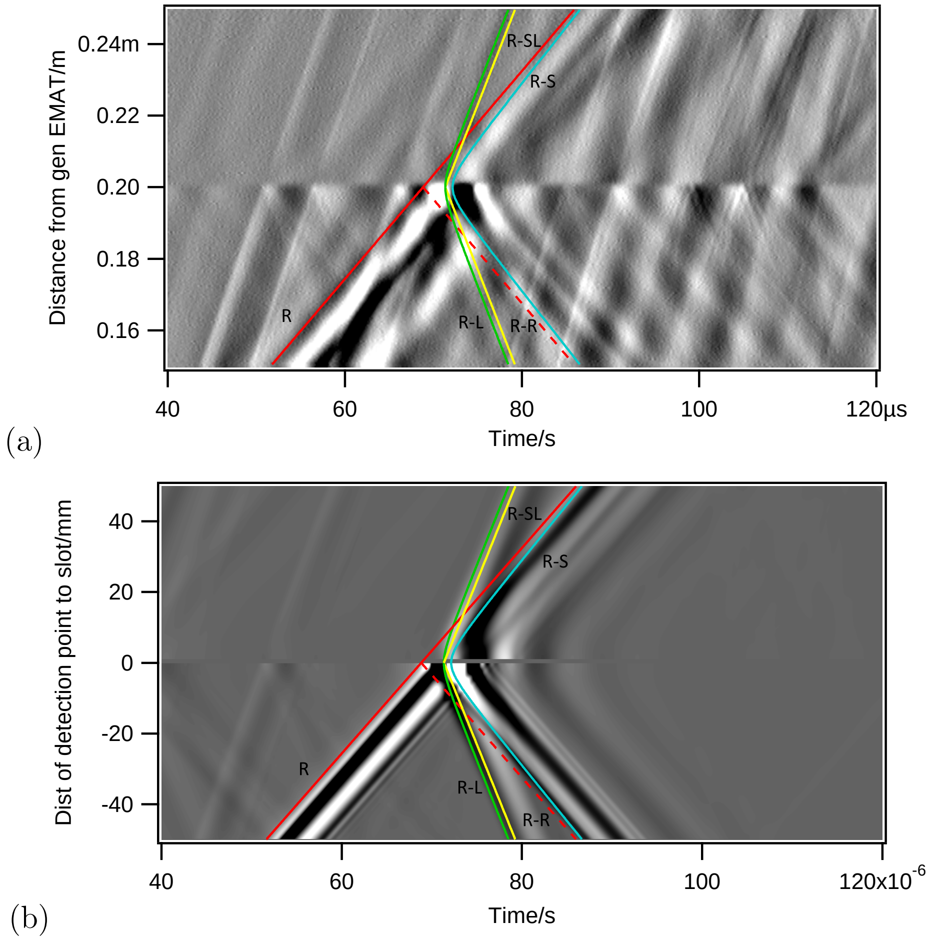

Figure 4.1: (a) In-plane B-scan of a normal (90^o) crack, depth = 5 mm from experiment and (b) 2D FEM model . The main wave modes are the incident Rayleigh (R), reflected Rayleigh (R-R), and mode-converted surface skimming longitudinal wave (R-L).

$$t_{R-S} = (x_1 + l)/c_R + \sqrt{x_2^2 + l^2}/c_S \tag{4.4}$$

Mode converted surface skimming longitudinal wave, R-SL (Figure 4.2(e))

$$t_{R-SL} = (x_1 + l)/c_R + (x_2 + l)/c_L \tag{4.5}$$

where x_1 is the distance from generation point to the crack, x_2 is the distance from the detection point to the crack, $k \geqslant 0$ is the number of reverberations at the crack, and l is the length of the crack [72]. The Rayleigh wave speed is c_R = 2885 ms^{-1}, the longitudinal wave speed is c_L= 6374 ms^{-1} and the shear wave speed is c_S =3114 ms^{-1}.

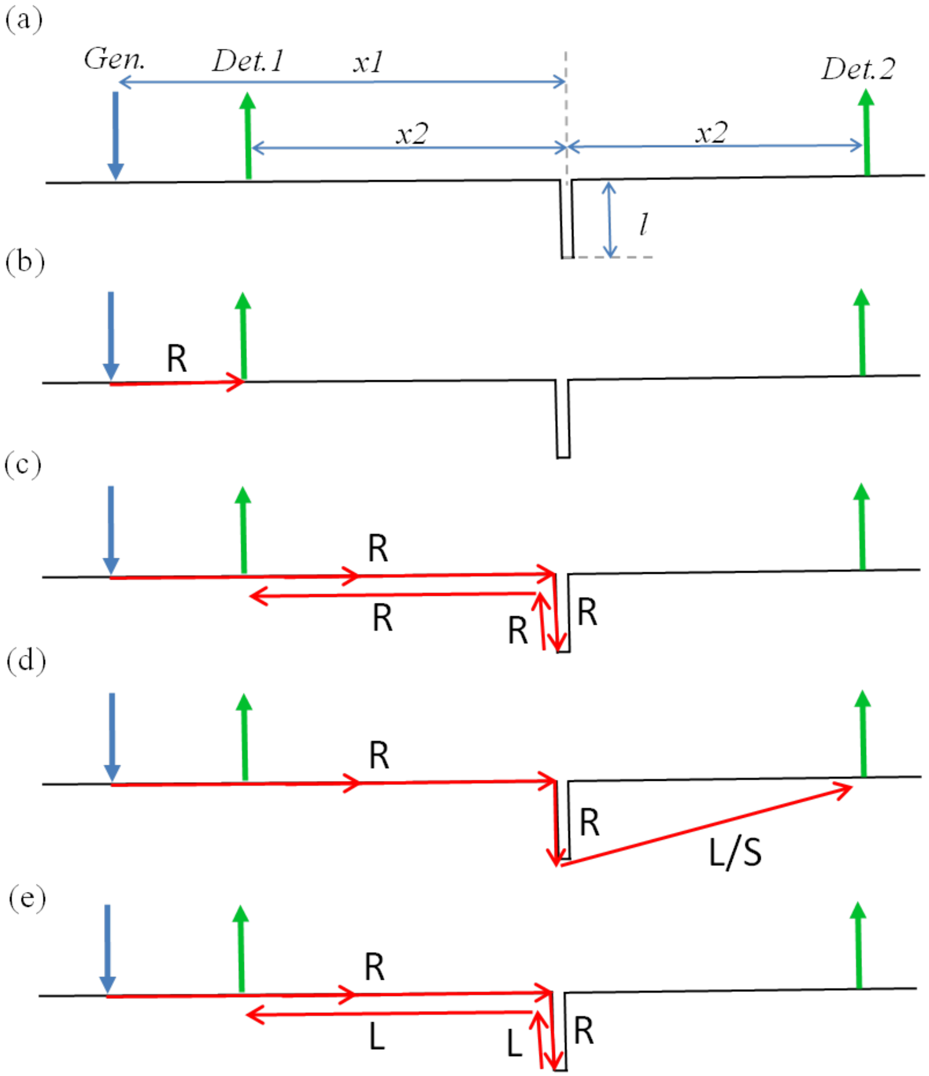

Figure 4.2: (a) Geometry of a normal (90°) crack with generation (Gen.) and detection points (Det.1 and Det. 2). (b)-(e) Travel paths of waves reflected, transmitted and mode converted at the crack. R denotes Rayleigh wave, L denotes longitudinal wave, and S denotes shear wave. L/S indicates that the mode can either be L or S.

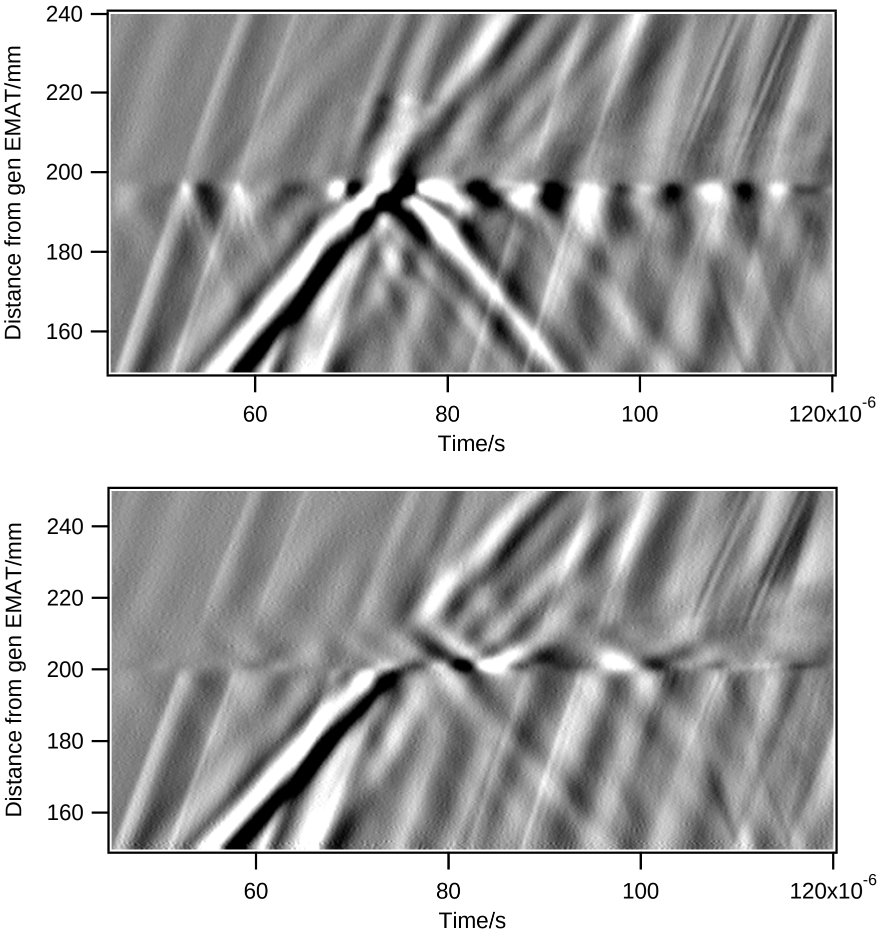

(a)

(b)

Figure 4.3: Experimental B-scans of an inclined crack, 22.5°, depth=5 mm, from two directions. (a) The acute angle, 22.5° and (b) The obtuse angle, 157.5° relative to the incident wave direction.

Some of the wave modes indicated by the arrival time lines are not clearly visible in the B-scan from the experiment (Figure 4.3) as there are multiple relfections of surface skimming longitudinal waves and bulk waves (longitudinal and shear) that interfere with the main wave modes. These bulk waves which are generated by the transmitter EMAT, are reflected at the underside of the sample. To see the main surface wave modes more clearly, Figure 4.1 (b) shows the B-scan generated from a two dimensional FEA model for the same size crack. In the model, all the boundaries except the top surface are set to be absorbing. Thus, the bulk wave reflections are removed.

In Figure 4.3, B-scans are shown for scans made on an inclined crack, of angle 22.5° (vertical depth=5 mm) with scanning done in opposite directions. In (a), the EMAT receiver is scanned towards the acute angle (22.5°) of the crack, while in (b) towards the scanning direction of EMATs are reversed , and hence the angle relative to the incident wave is now 157.5°. The B-scan in (a) contains extra features when compared with the B-scan for normal cracks (Figure 4.1). There is a prominent alternating black and white enhancement pattern which cannot be explained using the wave modes identified earlier, nor by their reflections. Meanwhile, for the obtuse angle (Figure 4.3(b)) the alternating pattern is still observed but is less prominent and occurs when the detector is positioned after the crack. This behaviour is also observed in the 2D model, as shown in Figure 4.4. The difference in the enhancement features between normal and inclined cracks can be used to distinguish the type of crack and classify defects into categories, and this is presented in Section 4.3. The origin of this enhancement pattern will be explained in Section 4.4. A procedure for characterising cracks based on the enhancement features will be explained in details in Chapter 5.

4.2 Angle dependence of transmission measurements in the far-field

Surface crack characterisation can be done by observing the transmission of Rayleigh wave propagating underneath a crack [22,23,53,120]. The experimental technique used for the experiments reported in the rest of this chapter used the pitch-catch EMAT system explained in Section 3.3, where a transmitter and a receiver EMATs are fixed at 150 mm apart using an aluminium holder. In the experiment, the EMATs are placed above the surface of the aluminium samples (keeping 0.1 mm lift-off) containing machined slots (refer to Table 3.1 for list of slots) to simulate surface cracks of various depth and inclination. For transmission measurement, the transmitter and receiver EMATs are positioned such that the crack is at position between them, where each EMAT is at an equal distance (75 mm) to the crack. This is to make sure that both EMATs are in the far-field of the crack . The near-field of the crack is defined as the region around the crack where constructive and destructive interference of the waves occurs. The far-field is the region beyond the near field where the wave front has become uniform. At this distance, the transmitted Rayleigh wave has recovered following the interaction with the crack. Thus, the transmission coefficient can be reliably measured. In-plane and out-of-plane wave velocity measurements were done separately using the same EMAT transmitter with corresponding in-plane or out-of-plane EMAT receiver.

A surface crack acts like a low-pass filter to the incoming broadband Rayleigh wave,

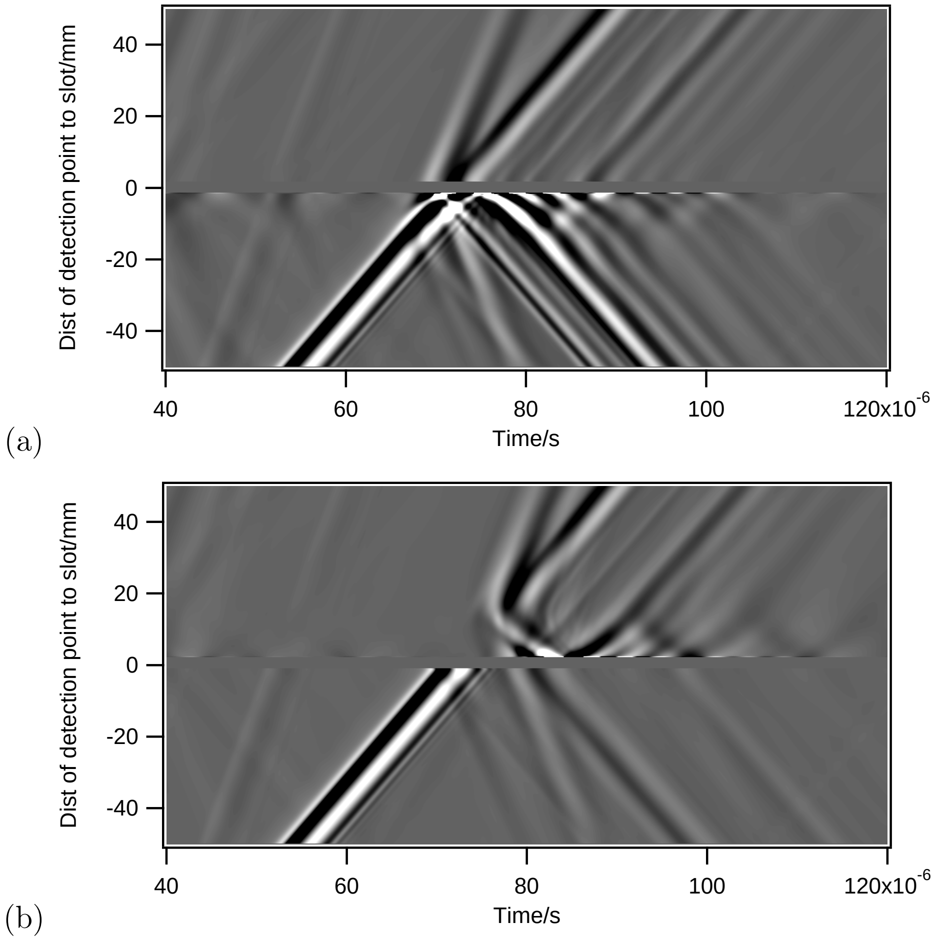

Figure 4.4: Model B-scans from 2D models of an inclined crack, of angle 22.5° and vertical depth=5 mm, scanned from two directions; (a) the acute angle, (22.5°) and (b) the obtuse angle, (157.5°).

where the cut-off frequency is related to the crack's normalised depth, d/λ (see Figure 3.4 for definition of d) [23]. For a broadband Rayleigh wave, the depth of a slot can be gauged from the changes in the amplitude and frequency content by comparing a reference signal, measured on a section of a sample clear of defects, to the signal transmitted in a defective region (Figure 4.5). For this analysis, the changes in the time-domain signals are analysed through a measurement of the peak-to-peak amplitude of the Rayleigh wave at the clear section and at the defective region . The calculation of the transmission coefficient, C_T is done using

$$C_T = \frac{A_t}{A_i}, \tag{4.6}$$

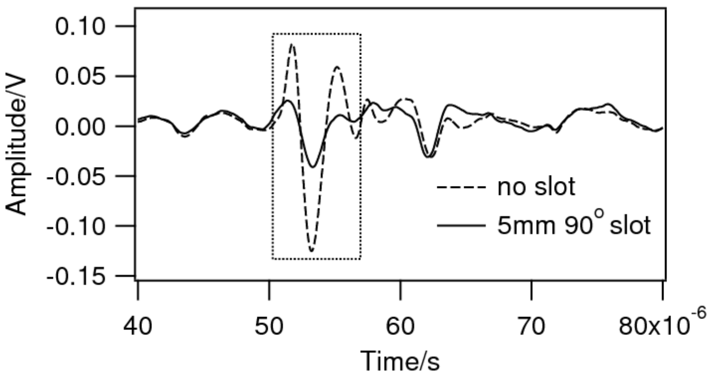

Figure 4.5: A-scans of the out-of-plane measurements of a sample with a 5 mm deep 90° slot, and over a section with no slot. The dotted box indicates the Rayleigh wave.

where A_t and A_i are the measured peak-to-peak amplitudes of the transmitted (defective region) and incident (measured in the clear section) Rayleigh wave respectively. C_T contains contributions from all the frequencies present, and is calculated for both the in-plane and out-of-plane measurements. Figures 4.6 and 4.7 show C_T plotted as a function of crack depth, d, for the experimental and model data respectively. C_T are plotted separately for in-plane and out-of-plane components, for different crack inclinations. For experimental data (Figure 4.6), 90°, 45°, and 135° cracks are considered, while for model data (Figure 4.7), an extra set of data for 22.5° cracks is added. The data for 135° cracks are measured from scanning the EMATs in the opposite direction on the 45° crack samples. As shown in Figure 4.6 , the transmission data for 45° and 135° inclined cracks are almost identical.

A fit for each data set is shown by the solid or dashed line, assuming an exponential decay of peak-peak amplitude with depth, which is suggested by Equations 2.27 and 2.28 for in-plane and out-of-plane Rayleigh waves velocities. Once this transmission-depth relationship is achieved through calibrations on cracks of known depths for a particular material, it can be used to gauge the depths of other cracks in the same material through a measurement of C_T [23]. Small differences between the experimental and model calibration curves can be attributed to crack roughness, small variations in frequency content of the Rayleigh wave signal, differences in crack opening size, and most importantly, the finite size of the receiver EMAT used in the experiment.

It is clear that, for the model and experiment, there is a significant difference between the calibration curve for 90^o and 45^o cracks, for depths between 1 mm and 15 mm. The difference in the calibration could lead to significant errors in depth characterisation if a

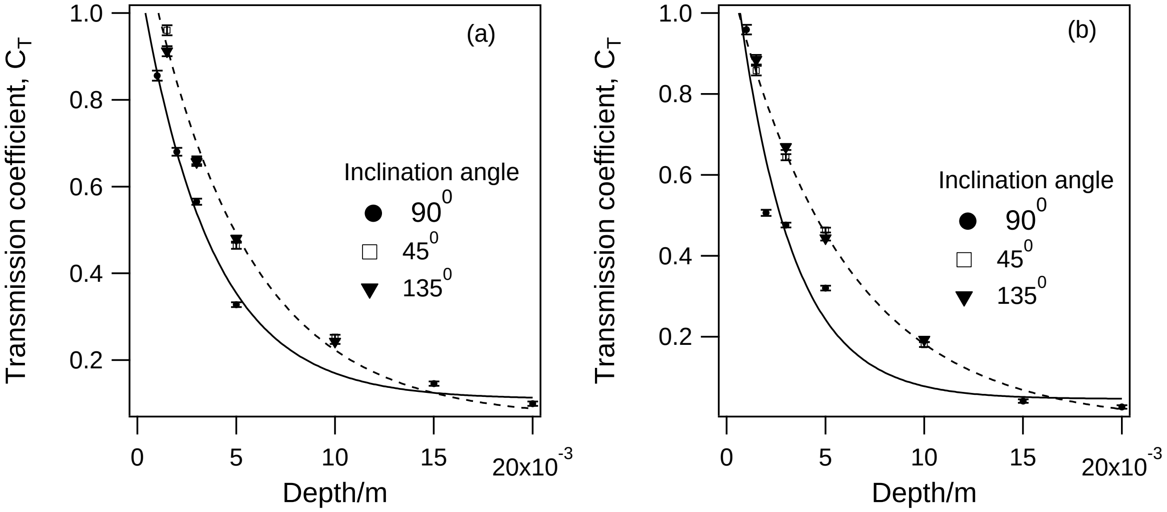

Figure 4.6: Experimental transmission calibration curve. In-plane(a) and out-of-plane(b) components.

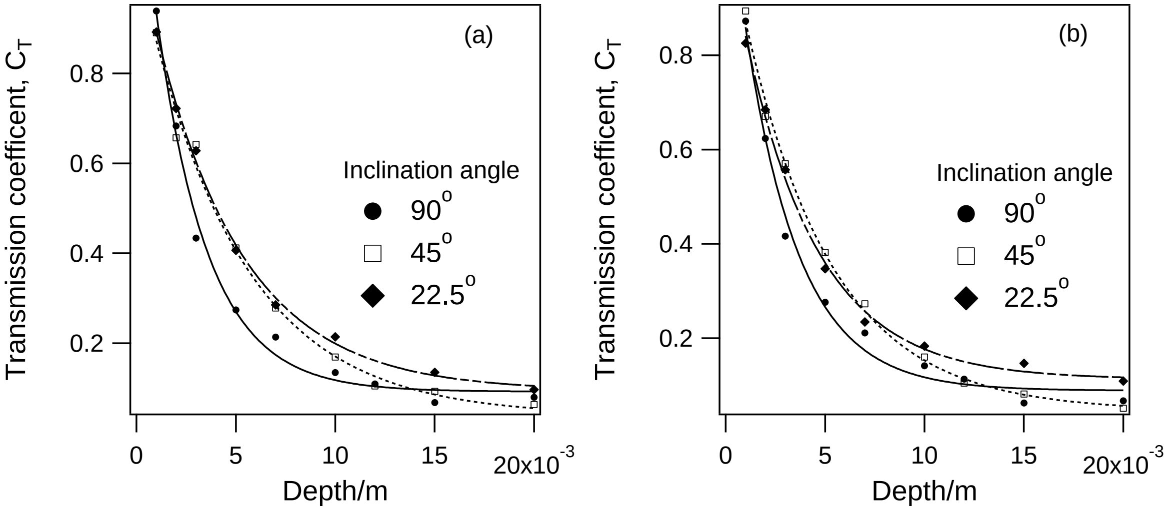

Figure 4.7: 2D FEA model transmission calibration curve. In-plane (a) and out-of-plane (b) components.

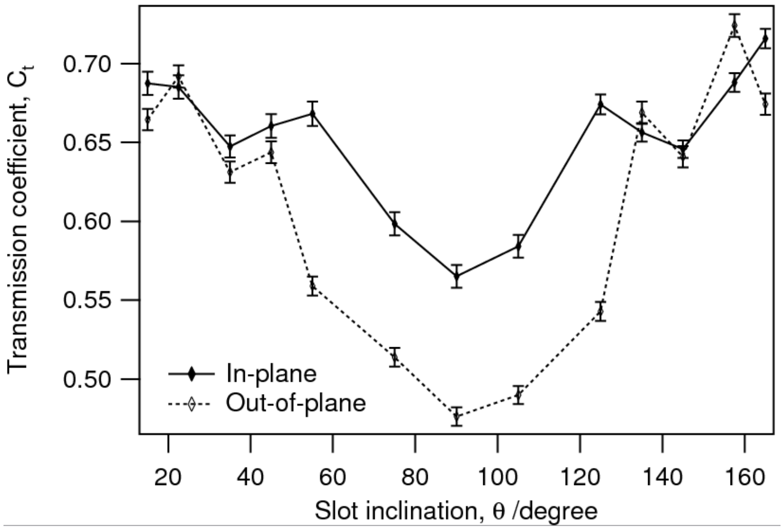

Figure 4.8: Variation of transmission coefficient, C_t with slot inclination, θ for 3 mm deep slots.

wrong calibration curve was applied to an unknown defect. For example, if a 45° crack of depth was characterised using the 90° calibration curve, and the measured C_T of 0.4 would lead to underestimation of the depth by approximately 2.3 mm. However, the 22.5° calibration curve (Figure 4.7) shows only a small difference from the 45° calibration for crack depths up to approximately 7 mm. Hence, a 22.5° crack can be characterised to a reasonable accuracy using the 45° calibration curve, and vice versa.

The variation of C_T with crack inclination is shown in Figure 4.8 for 3 mm deep (vertical depth) cracks. This shows that C_T is approximately symmetric about 90° for both in-plane and out-of-plane measurements. It can be seen that there is only a small variation in C_T for cracks of angles less than 45°, compared to the difference between cracks of 90° and 45° for this depth. This confirms that calibration curves cannot be blindly used for characterising any surface defects without at least some extra information about the crack orientation. Ideally, there should be a calibration curve for each angle; that however, is not practical as it is very time consuming and costly, and would require full knowledge of a crack angle. However, a smaller subset of calibration curves, covering inclined defects (10°-45°) and 90° cracks would give a reasonable characterisation for most defects, and classification of defects into "inclined" or "normal" classes can be done using the procedure described in the next section.

4.3 Crack characterisation using B-scan images

B-scans provide useful information about the section of the sample where the scan was made. For example, a defective section can be identified through the reduction of the magnitude in the grayscale, indicating a drop in the signal amplitudes, when a defect is present there will be less transmission. The presence of a defect can then be confirmed by the reflection of Rayleigh waves at the defect, as shown in Figure 4.1 and Figure 4.3, or by the enhancement pattern.

Figure 4.9 shows the out-of-plane B-scans from 3 mm vertical depth cracks of different inclination θ, where (a) $\theta = 90°$, (b) $\theta = 22.5°$, and (c) θ is the obtuse angle of (b), 157.5°, for the fixed EMATs separation. The wave modes described in Section 4.1 (Equations 4.1-4.5) are again present in the B-scans, but with slight different arrival times due to the fixed distance between transmitter and receiver EMATs; the incident Rayleigh wave, IR arrives at the same time (about $52\,\mu s$) for each scan position. The differences between the B-scans are very clear; the first feature is the change in the arrival time of the Rayleigh wave once it has been transmitted underneath the crack which has been calculated in [72] and [79] for normal and angled defect respectively. For the obtuse angle in (Figure 4.9(c)), the transmitted Rayleigh wave only recovers back to its original arrival time when the receiver is in the far-field. This time delay is governed by the defect length and the inclination angle, and can be used for identification of defects [73].

Furthermore, the enhancement pattern for each crack inclination shown here is also strikingly different. The enhancement observed for a 90° crack shown in Figure 4.9(a) is fully understood, and is due to constructive interference of the incident Rayleigh wave with its reflection from the crack, and the mode-converted surface skimming longitudinal wave.However, the enhancement patterns shown in Figure 4.9(b) and (c) are stronger and have a longer time dependence, forming an alternating black and white pattern with different starting times. The enhanced signal observed for the normal crack extends to about 58 μs, while the 22.5° crack produces an enhancement pattern that spans to the end of the time scale shown here. In addition, the enhancement magnitude has a dependence on crack inclination, being stronger for the shallow angle. The mechanism and angle dependance of this signal enhancement are explained in Section 4.4.

In Figure 4.10, the in-plane B-scans of the same cracks are shown. Again, an extended enhancement pattern is observed for the angled cracks, 22.5° and 157.5° in

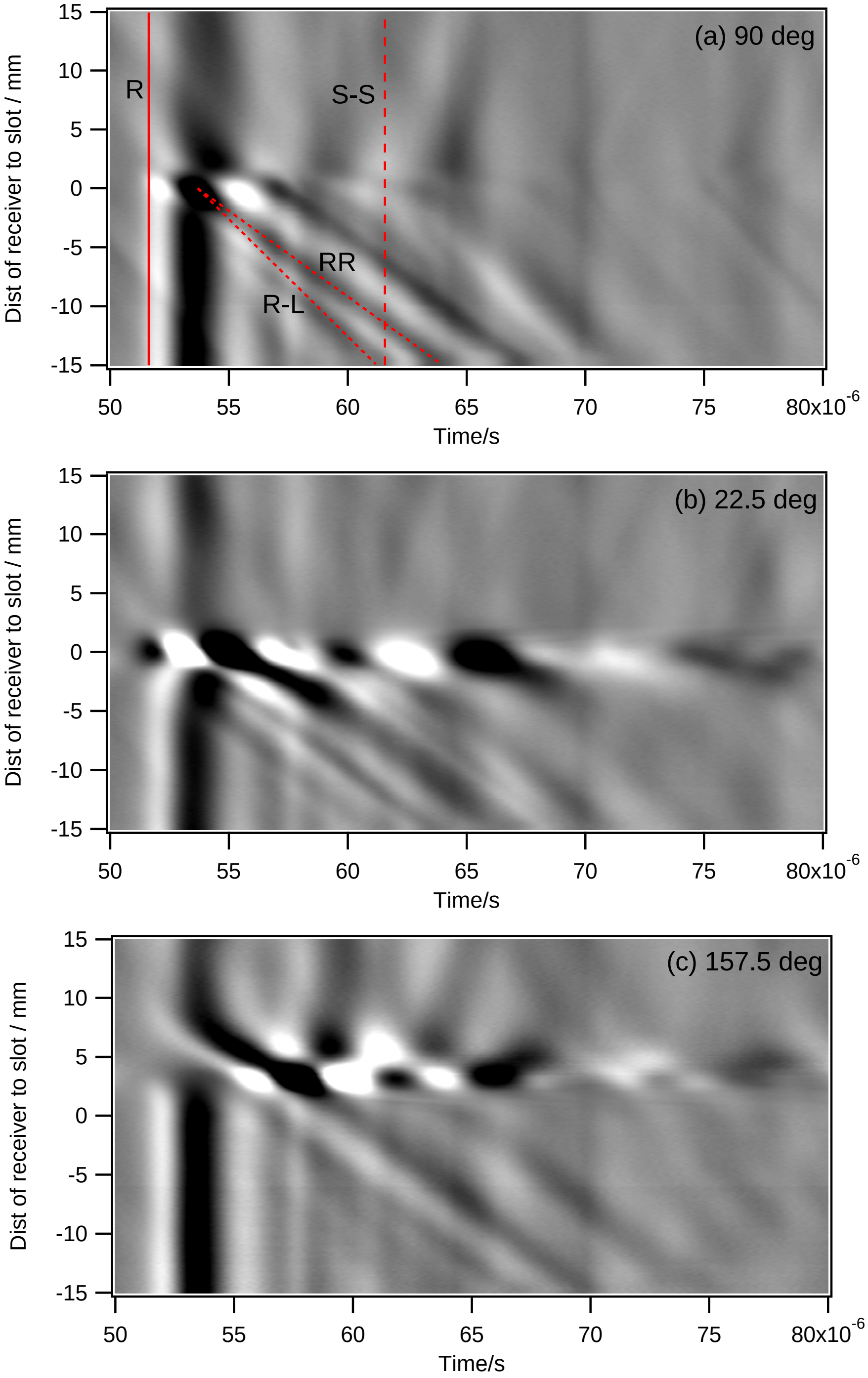

Figure 4.9: Experimental B-scans of the data from out-of-plane measurements showing the enhancement pattern from 3 mm cracks of different inclinations, θ; (a) 90^o, (b) 22.5^o , and (c) 157.5^o, and expected arrival times for selected mode.

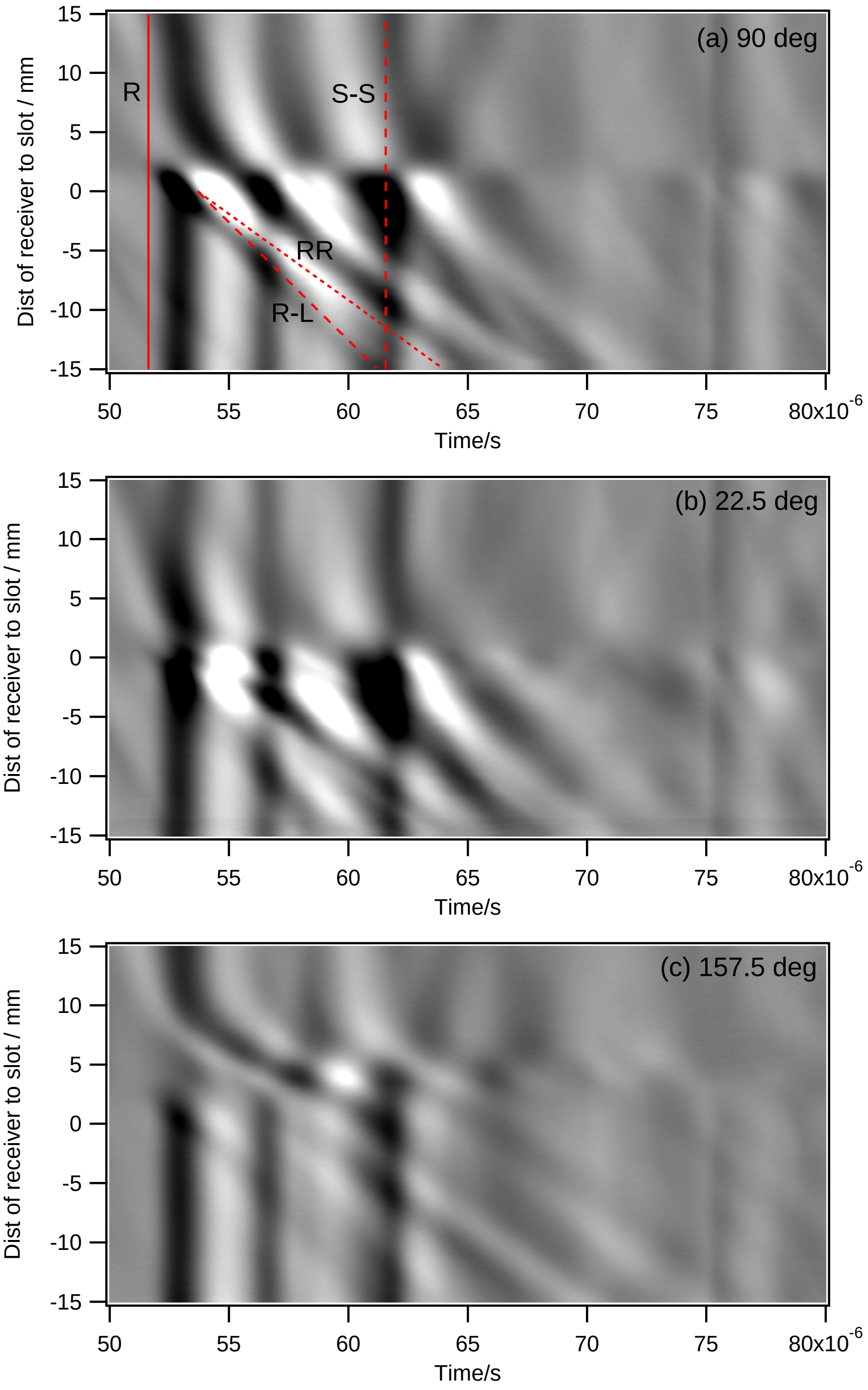

Figure 4.10: Experimental B-scans of the data from in-plane measurements showing the enhancement pattern from 3 mm cracks of different inclinations, θ; (a) 90°, (b) 22.5° , and (c) 157.5°, and expected arrival times for selected mode.

(b) and (c). However, a slightly extended pattern is present in (a) for the 90° crack. In this case, the enhancement pattern is due to the geometry of the aluminium sample. To understand this, refer to Figure 4.11 which illustrates the EMAT transmitter and receiver arrangement on the top surface of the aluminium sample. Here, s denotes the separation between the two transducers and h is the sample thickness. In addition to the surface waves, the EMAT transmitter used in the experiment also generates bulk waves and these are reflected on the underside of the sample. The diagram in Figure 4.11 (a) shows the path when there is no mode conversion is taking place. For example, shear to shear (S-S) or longitudinal to longitudinal (L-L). The arrival time of these wave modes can be calculated based on the geometry of the sample as follows:

Longitudinal to longitudinal (L-L)

$$t_{L-L} = \frac{2n}{C_L}\sqrt{(\frac{s}{2n})^2 + h^2} \tag{4.7}$$

Shear to shear (S-S)

$$t_{S-S} = \frac{2n}{C_S}\sqrt{(\frac{s}{2n})^2 + h^2} \tag{4.8}$$

where n is the number of reflections on the underside. When there is a longitudinal to shear (L-S) mode conversion, as shown in Figure 4.11 (b), the arrival time can be calculated using

$$t_{L-S} = \frac{1}{C_L}\left[\left[s\left(\frac{C_L}{C_L + C_S}\right)\right]^2 + h^2\right]^{1/2} + \frac{1}{C_S}\left[\left[s\left(\frac{C_S}{C_L + C_S}\right)\right]^2 + h^2\right]^{1/2}. \tag{4.9}$$

Based on the calculation of t_{L-L}, t_{S-S} and t_{L-S} using the dimension from the aluminium sample used in the experiment and for n=1, the S-S mode is found to arrive close to the Rayleigh wave at 61.6 μs as indicated by the dashed red line in Figure 4.10 (a). The other two modes, L-L and L-S arrive much earlier at $t_{L-L} = 30.4\mu s$ and $t_{L-S} = 43.4\mu s$, and they are not shown in the B-scan. As the S-S mode arrive shortly after the Rayleigh wave, they form a pattern which looks similar to the extended enhancement pattern observed for angled cracks. The S-S mode is present in all in-plane B-scans, as shown in (b) and (c) for the angled cracks. However, it is not observed in the out-of-plane B-scans in Figure 4.9. This is because reason is, the S-S mode is dominated by in-plane motion, which is detected by the in-plane EMAT.

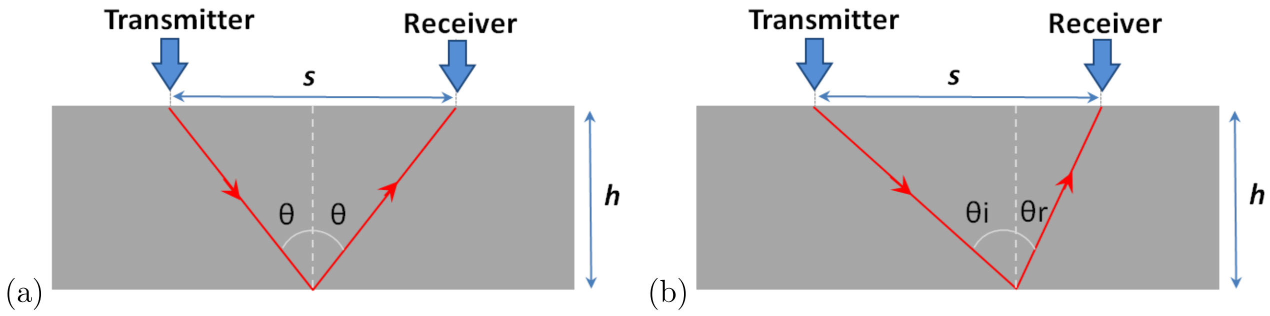

Figure 4.11: Bulk-wave reflection on the underside on aluminium sample. (a) No mode conversion. (b) Mode conversion.

So far, only the B-scans for 3 mm vertical depth cracks have been presented. In order for the extended enhancement features to be applicable for crack classification, it is important to confirm that the same features are also observed for a crack of different depth. Figure 4.12 shows the out-of-plane B-scan for a 5 mm deep, 22.5° crack. When compared to the B-scan of the 3 mm deep crack of the same crack inclination (Figure 4.9(b)), this B-scan confirms the similarity in the enhancement features. Firstly, it has the prominent alternating black and white pattern that extends to much longer than the period of the Rayleigh wave pulse. Secondly, the mode converted surface skimming longitudinal wave is generated and the reflection of the Rayleigh wave is observed. The first feature is the most important in terms of crack classification as it indicates whether the crack grows normal to surface or grows at an angled to the surface. The magnitude of the enhancements for 3 mm and 5 mm deep cracks may differ slightly, however for classification this is not a main concern as the objective of distinguishing normal and angled crack has been achieved. In Section 4.5, the analysis looks more closely at the actual magnitude of the enhancement.

The image analysis of B-scans reveals information regarding the section of the sample where the scan is made. Firstly, the presence of a defect and its position can be determined through the change in the colourscale and the enhancement. Secondly, classification of a crack into normal (or near-normal) and inclined can be done using the enhancement feature, which is required for choosing the correct calibration curve for crack depth measurement. Finally, the orientation of the crack tip, i.e whether it is facing (acute angle) or opposing (obtuse angle) the direction of the incident Rayleigh wave can be determined.

In reality, it is almost impossible to rely on human input to analyse the B-scan images while the scan is running continuously at high speed. For that reason, an

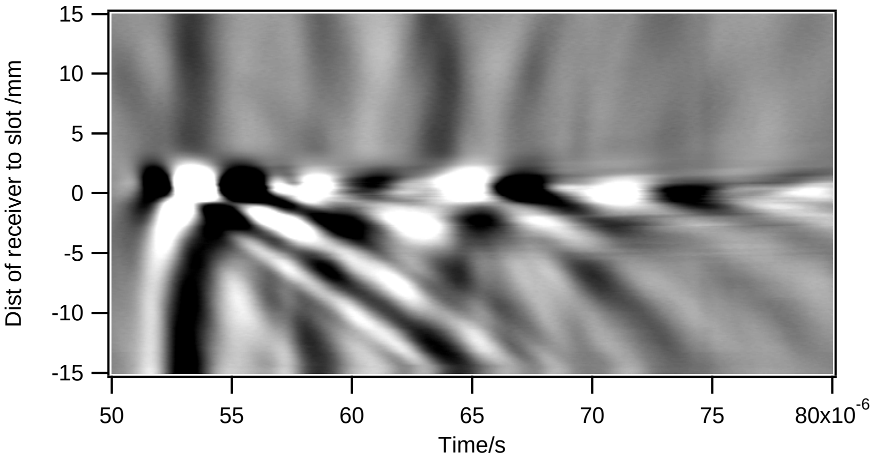

Figure 4.12: B-scan of out-of-plane measurement of a 22.5°, 5 mm (vertical depth) crack.

automated image classification program based on a machine learning method known as genetic programming has been developed to extract this information from a B-scan [121]. The details of the program, which gives high accuracy (>95%) for a small data set, are presented in Section 5.1. The program essentially learns the differences described here between B-scans for normal and angled cracks, from a set of available data, and automatically creates a program to classify other B-scan images.

4.4 Mode conversion and signal enhancements

The striking patterns observed in the B-scans (Section 4.3) and the high magnitude enhancement behaviour caused by the inclined cracks can be understood better with the help of the 2D FEA model. Figures 4.13 and 4.14 shows the snapshots of Rayleigh wave interactions with a 22.5°, 5 mm deep crack. The velocity is plotted in the colour scale. Figure 4.13 shows the in-plane velocity components while the Figure 4.14 shows the out-of-plane velocity components. The region of the sample containing the crack is enlarged to focus on the interaction close to the crack, and hence the boundaries shown here, except for the top surface, are not the actual sample dimension.

Figures 4.13(a) and 4.14(a) show the in-plane and out-of-plane velocity components of a Rayleigh wave approaching the crack. The profile of each component is clearly distinguishable from their variation with the distance from the top surface. At about a quarter of the centre wavelength, λ, below the surface, the in-plane component

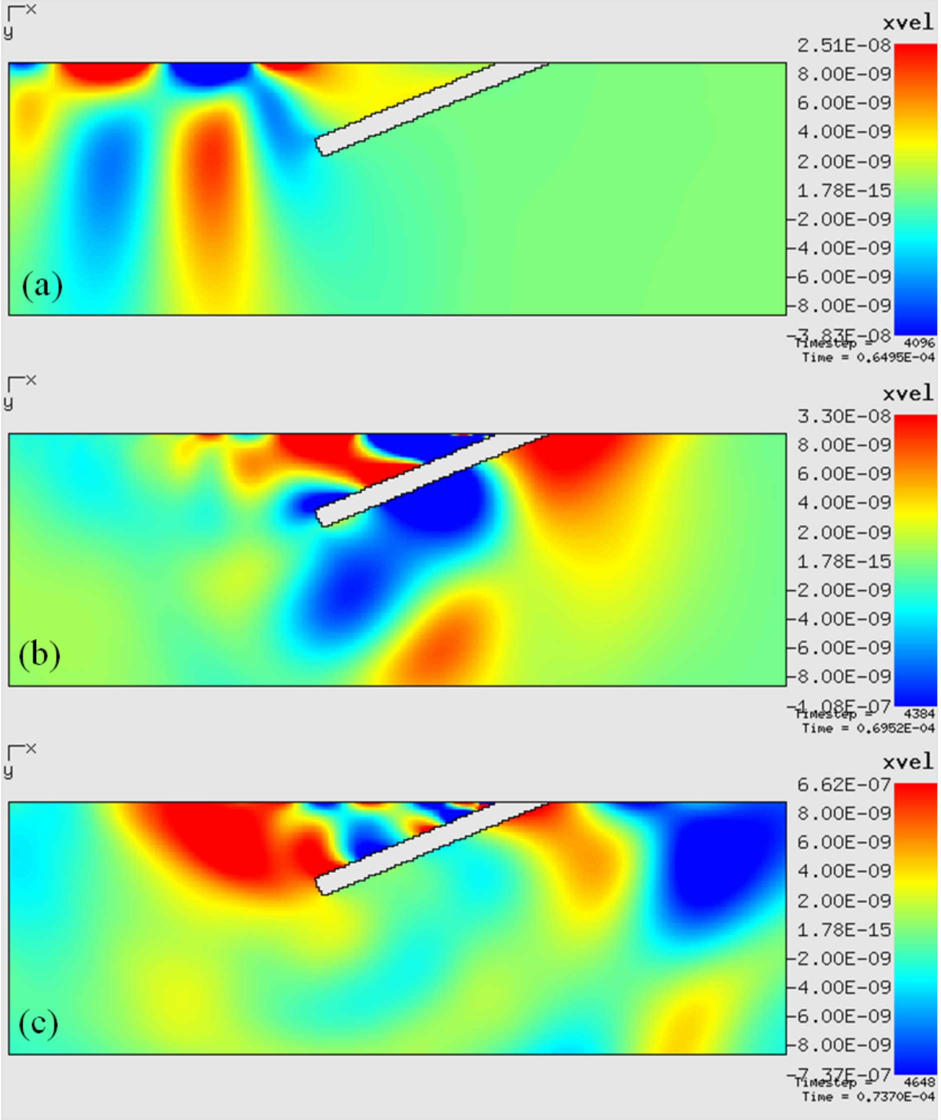

Figure 4.13: Snapshots of 2D FEA model showing the interaction of in-plane Rayleigh wave velocity component with a 22.5°, 5 mm deep crack. (a) Incoming wave approaching the crack, (b) interaction caused mode conversion to Lamb-like wave, and (c) aftermath of the interaction.

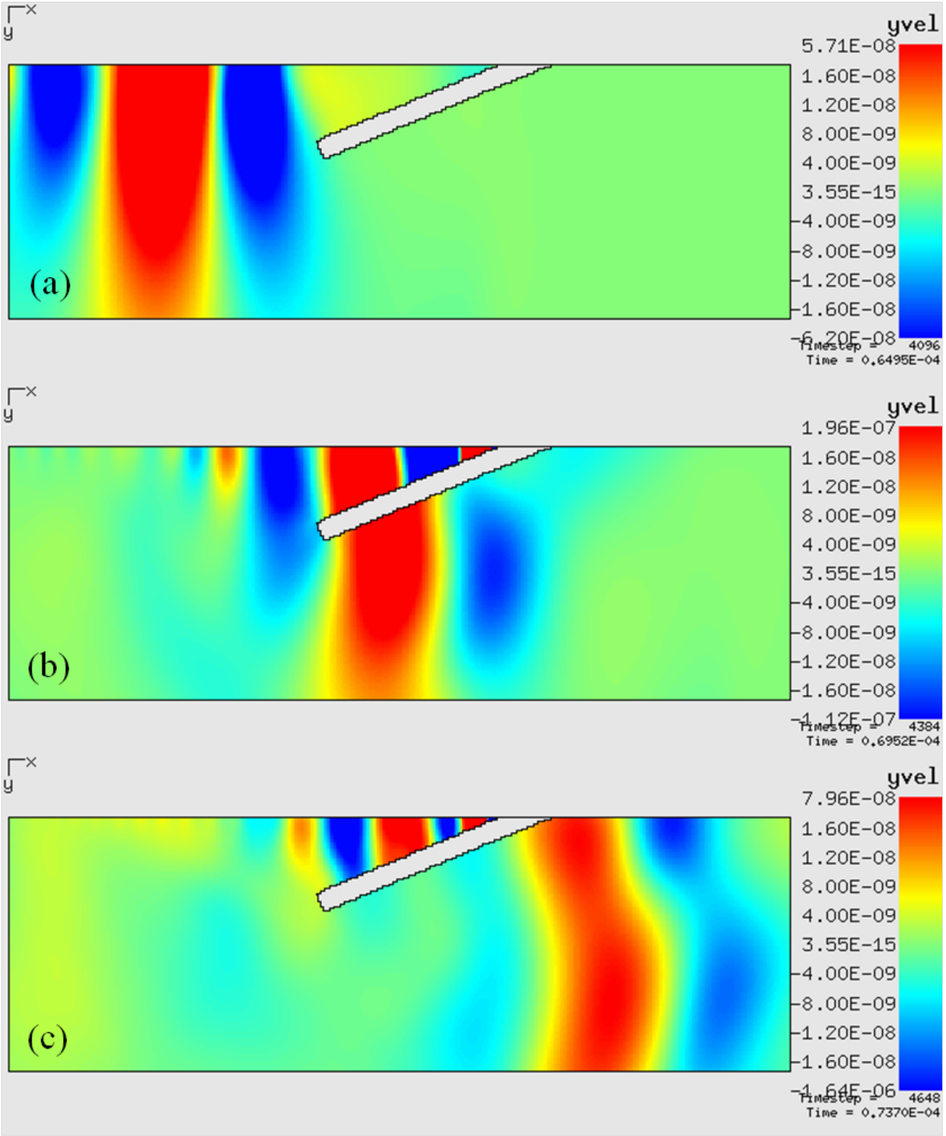

Figure 4.14: Snapshots of 2D FEA model showing the interaction of out-of-plane Rayleigh wave velocity component with a 22.5°, 5 mm deep crack. (a) Incoming wave approaching the crack, (b) interaction caused mode conversion to Lamb-like wave, and (c) aftermath of the interaction.

(Figure 4.13(a)) exchanges its direction before gradually diminishing with depth. The out-of-plane component in Figure 4.14(a), on the other hand, maintains the direction profile while the amplitude gradually decreases with depth. This behaviour agrees with the theoretical calculation in Section 2.1.3 (Figure 2.1).

The interaction of the broadband Rayleigh wave with the crack in the near-field, shown in Figures 4.13(b) and 4.14(b), can be explained in two parts. Firstly, the crack as a whole acts like a low-pass filter, where some of the low-frequency components are transmitted underneath the crack and continue propagating. This is the same behaviour as for normal cracks, as reported in [23], although it has been shown earlier that the transmission coefficient, C_T will be different for inclined cracks. Secondly, the high-frequency components and some of the low-frequency components are confined inside the tapered section formed by the crack. There are also mode-conversions of Rayleigh wave to bulk wave and surface skimming longitudinal wave at the crack tip; these have been reported in detail in [69, 70, 79].

The tapered section forming the defect can be viewed as a wedge [71]. As the Rayleigh wave enters this wedge, it propagates from a section of sample which has the full sample thickness, to the one which has a smaller, varying thickness within the wedge. The local thickness decreases to a very small value as the wave moves towards the wedge tip. Within the wedge, the confined wave changes behaviour as the wavelengths for all frequency components are now larger than, or at least comparable with, the local thickness. In this region, the wave becomes more like a guided wave, and, will be dispersive [22, 122]. The snapshots in Figures 4.13(c) and 4.14(c) show the aftermath of the interaction. The transmitted wave travels along the underside face of the crack and moves towards the surface. There, predominantly low-frequency waves will continue propagating on the surface, affected minimally by the crack. The wave trapped by the wedge section is reflected back as a guided wave within the wedge and progressively mode converted back to a Rayleigh wave as it propagates into the section which has the full sample thickness.

To account for the change in the local thickness and the resulting change in the velocity of the surface wave, the wedge is divided into N small elements of constant width, $\triangle x$, and each element has a local thickness, d_i, as illustrated in Figure 4.15. The number of elements, N, is calculated by dividing the horizontal projection of the crack length on the surface, l, by Δx. For a wedge of angle θ the local thickness, d_i of an element a distance x away from the tip can be calculated using:

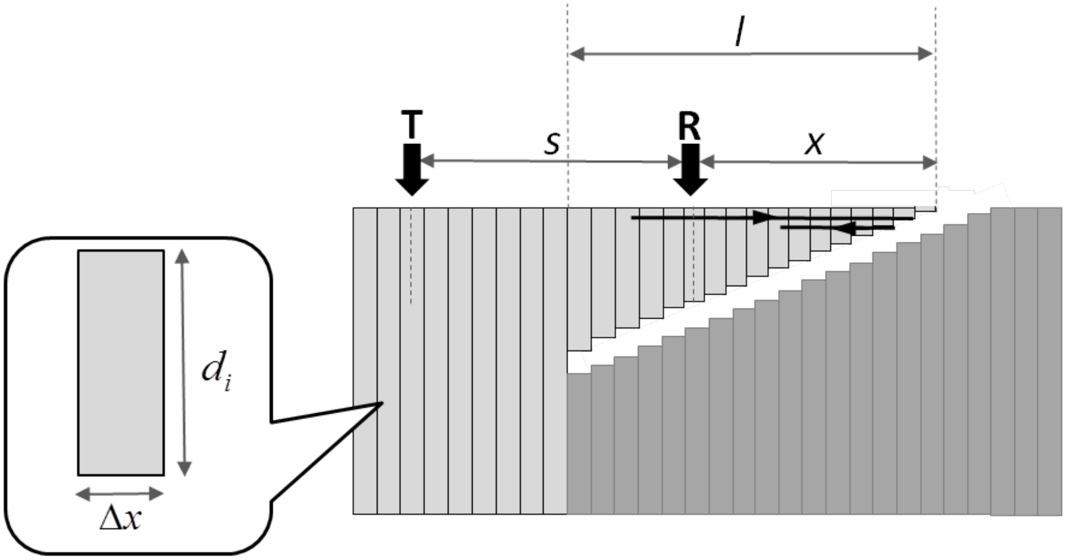

Figure 4.15: The tapered section formed by the crack can be viewed as a wedge. It is divided into N elements of constant width, $\triangle x$ and local thickness, d_i. l is the horizontal projection of the crack length on the surface. T and R show the position of the EMAT transmitter and receiver.

$$d_i = xtan\theta \tag{4.10}$$

Based on the Rayleigh-Lamb frequency equations (Equations2.30 and 2.31), the rapid change in d_i will cause a mode-conversion to a Lamb-like wave. The product of frequency f and d_i is known as the frequency-thickness, and fd_i is used to identify the Lamb wave mode present by referring to the dispersion curve (Figure 2.2). With the broadband frequency content generated by the EMAT transmitter (Figure 3.17), one would expect to deal with only the fundamental modes (zero order symmetric S0 and anti-symmetric A0) for the range of d_i in the wedge, where the maximum fd_i value is 2 MHzmm. For a particular mode with phase velocity c_p, the group velocity c_g in each element in the wedge can be calculated using [22]:

$$c_g = c_p^2 \left[c_p - (fd_i) \frac{dc_p}{d(fd_i)} \right]^{-1} \tag{4.11}$$

The calculated c_g for the fundamental first and second order symmetric and anti-symmetric Lamb wave modes are plotted as a function of fd_i in the dispersion curve given in Figure 2.2. The time it takes for each mode to propagate over each small element of width Δx depends on this velocity and can hence be calculated using:

$$t_e = \frac{\Delta x}{c_g(f, d_i)}. \tag{4.12}$$

In order to calculate the total propagation time in the wedge, c_g is evaluated for each element by referring the d_i value to the dispersion curve (Figure 2.2) for each frequency present in the broadband incident signal. The total wave propagation time in the wedge, $t_w(f)$, can be approximated by adding t_e from all elements, i.e

$$t_w(f) = \int_0^l \frac{1}{c_g(f, d_i)} dx \approx \sum_{i=0}^{N} \frac{\triangle x}{c_g(f, d_i)}. \tag{4.13}$$

The EMAT transmitter, T, and receiver, R, used in the experiment were fixed at a separation of s while scanning towards the crack. For the full thickness section prior to the defect, the wave propagates at the Rayleigh wave speed, C_R. When the receiver is at a distance x from the wedge tip, which corresponds to the Mth element from the start of the wedge, where $M = N - {}^{x}/_{\Delta x}$, the arrival time of the incident wave $t_i(f)$ can be approximated as:

$$t_i(f) = \frac{s - (l - x)}{C_R} + \sum_{0}^{M} \frac{\triangle x}{c_g(f, d_i)} \tag{4.14}$$

The arrival time of the wave reflection at the receiver R, $t_r(f)$ can be approximated as

$$t_r(f) = \frac{s - (l - x)}{C_R} + \sum_{0}^{M} \frac{\triangle x}{c_g(f, d_i)} + 2 \times \sum_{M}^{N-M} \frac{\triangle x}{c_g(f, d_i)} \tag{4.15}$$

Using Equations 4.14 and 4.15, the arrival times of the incident and reflected waves can be calculated when the receiver is close to the crack and within the wedge area. However, the broadband nature of the signal needs to be considered; t_i and t_r must be evaluated at each receiver position, for all the frequency components generated by the transmitter. This calculation was done using a routine programmed in IgorPro. Initially a starting frequency of 0.05 MHz was chosen to evaluate t_i and t_r at each element towards the crack, and this was extended by repeating the calculation for other frequencies with a small frequency increment (1 kHz).

The top figure in Figure 4.16 shows the experimental out-of-plane B-scan of the 22.5^o, 5 mm deep crack. The striking alternating black and white enhancement pattern can be seen clearly at a position close to the slot (scan distance = 0 mm). Within the red box drawn in the B-scan, the incident Rayleigh wave starts to arrive at later times

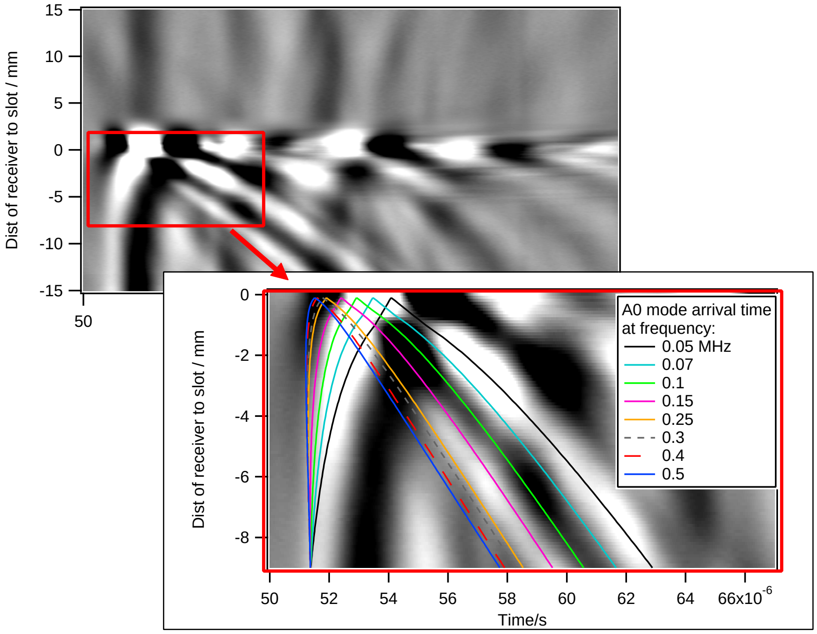

Figure 4.16: Arrival time of A0 Lamb wave mode appended on the experimental out-of-plane B-scan of 22.5^o, 5 mm deep crack. The lines show the arrival time calculated for different frequencies.

as it approaches the crack. The change in the arrival time forms a curved set of black and white lines. Based on the group velocity dispersion curve (Figure 2.2), the Lamb wave A0 mode travels at much lower speed than the S0 mode, and the speed drops drastically as the the freqency-thickness decreases, as observed here.

The bottom figure in Figure 4.16 shows the arrival times of the A0 mode calculated at different frequencies, appended on the enlarged B-scan representing the red box in the top figure. The calculation covers the scan distance that corresponds to the horizontal projection of the wedge on the surface, which is 9 mm in length, with the calculation using an element width of $\triangle x = 0.1$ mm. Approaching the crack, the lines that represent the calculated arrival time for different frequencies start to diverge. Lower frequency components travel more slowly as they approach the crack tip, and hence arrive later than the original Rayleigh wave arrival time. As the frequency increases, the lines become less spread out but the curved nature of the arrival time is still observed very close to 0 mm. These calculated arrival times of the incident Lamb wave A0 mode agree very well with the curved feature of the enhancement pattern. This supports the Rayleigh to Lamb-like wave mode-conversion hypothesis.

In addition, the arrival times of the reflected A0 mode, t_r, which is described by

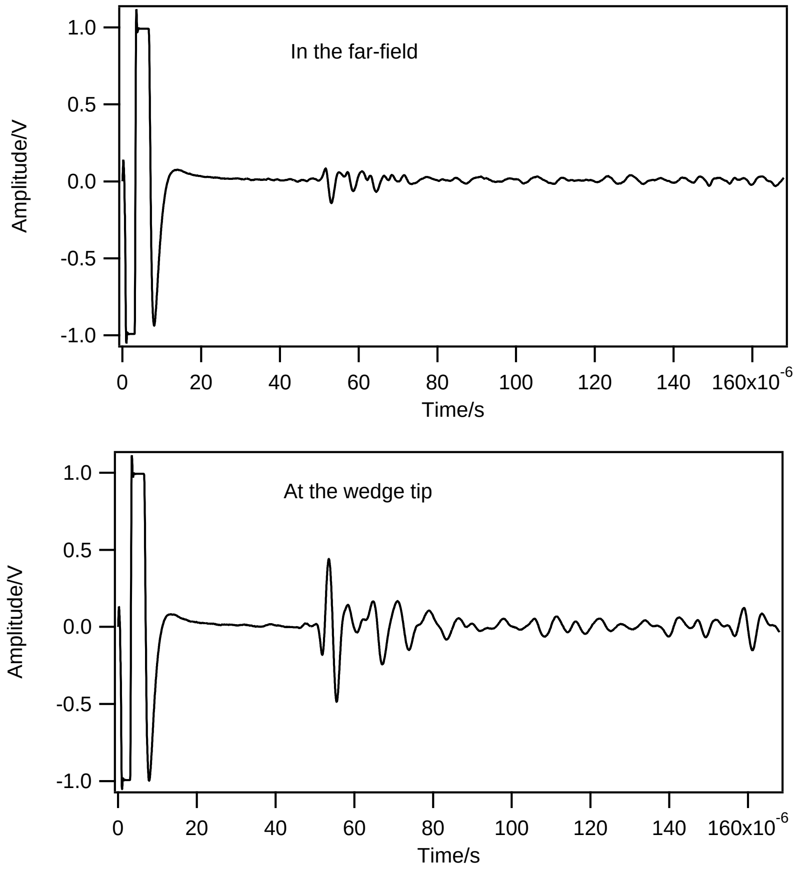

(a)

(b)

Figure 4.17: A-scans from out-of-plane measurements of 22.5, 5 mm deep crack recorded in the far-field (a) and at the crack's wedge tip (b).

Equation 4.15, also show a good agreement with the reflected wave pattern in the B-scan. The high magnitude alternating black and white pattern close to the wedge tip can be understood by considering the interference of the broadband incident Lamb wave A0 mode with the corresponding reflected waves. The highest enhancement magnitude should be observed at the crack tip, where the differences in the arrival times on incident and reflected waves are very small. For the finite size EMAT receiver used in the experiment, the signal enhancement detected is the contribution from all points within the effective coil area of width approximately 1 mm. Practically, the signal enhancement observed would be smaller than due to the averaging of all signals within this area. This will be discussed further in Section 6.3.

Figure 4.17 compares the A-scans from the out-of-plane measurements of the 22.5°, 5 mm deep crack recorded in the far-field at scan distance = -15 mm (a), and at the crack's tip (b). Apart from the obvious high amplitude signal in (b), the wave pulse has a slightly different shape at the wedge tip and is broader in time. To further confirm the mode conversion, the frequency content of the signal as a function of time needs to be calculated for the wedge tip measurement and compared with the expected arrival times of the A0 mode at the wedge tip calculated using Equation 4.14 for all frequencies in the EMAT range (0.05-0.50 MHz). To do that, a spectrogram [96] of the A-scan in Figure 4.17 (b) was computed. The signal was divided into segments, with each segment having 1074 time points, giving a frequency resolution of 155 kHz. Each segment is windowed with a Gabor window before a fast Fourier transform (FFT) is applied. The process is repeated every 11 time points so that the FFT from each segment will overlap with the previous one.

The calculated arrival times of the A0 and S0 modes are plotted on the computed spectrogram shown in Figure 4.18. At low frequencies, the signal is dominated by a mode arriving close to the expected arrival time of an A0 mode, and some dispersion is clear. Meanwhile, the evidence of any mode arriving close to the arrival time of S0 is not clear. This indicates that the out-of-plane measurement is predominantly sensitive to the A0 mode but not to the S0 mode [22]. The spectrogram, although only showing the predominant A0 mode, provides additional evidence of the Rayleigh wave mode-conversion to a Lamb-like wave at the wedge tip.The dominance of the Lamb wave anti-symmetric mode, A0, over a symmetric mode, S0, or vice versa, and the sensitivity of the EMAT measurements will be discussed in Section 4.6, following the quantitative analysis of the signal enhancement presented in the next section.

4.5 Signal enhancement measurements in the near-field

The measurements of the Rayleigh wave transmission coefficient C_T presented in Section 4.2 have shown the C_T dependency on the crack inclination, θ. Thus, further analysis is required which will approximate θ, in order to apply the correct depth calibration for a particular crack. The presence of inclined cracks can be detected by the prominent enhancement pattern in the B-scans presented in Sections 4.3 and 4.4, which is caused by the mode-conversion of the indicent wave at the wedge tip and observed when an EMAT receiver is very close to the crack.In this section, the magnitude of the signal enhancement in the in-plane and out-of-plane components for cracks of various vertical depths and inclinations are presented, and their relationship with the crack

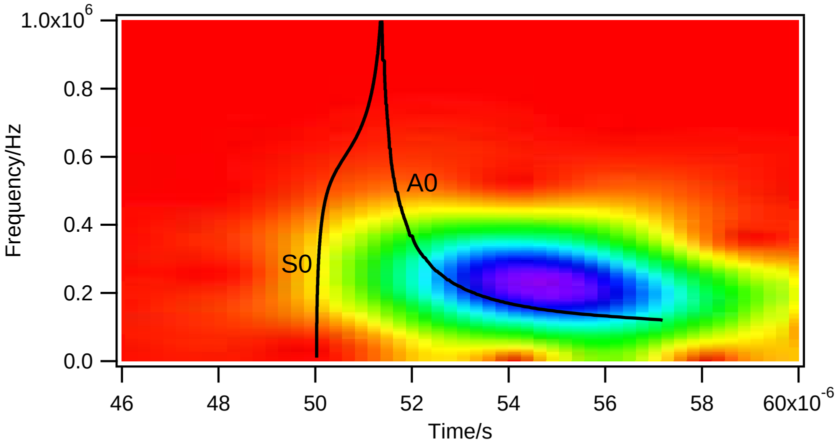

Figure 4.18: Spectrogram of the out-of-plane signal recorded experimentally at the wedge tip of 22.5, 5 mm deep crack (Figure 4.17 (b)). The solid lines show the calculated arrival times of the $S0$ and $A0$ modes for the different frequencies present in the ultrasound pulse.

depth and crack inclination are investigated. The ratio between the two components has been calculated for cracks of different angles but with the same depth for 3 mm and 5 mm vertical depths, and this can be used to measure approximate crack angle.

The Rayleigh wave peak-peak amplitude is measured every 0.1 mm during the scan, with the amplitude plotted as a function of scan distance. This is shown in Figure 4.19 for 3 mm deep cracks of three different inclinations; 22.5°, 45°, and 90°, for the in-plane and out-of-plane components . At positions close to the cracks peaks are observed, giving a quantitative measure of the expected signal enhancement. The size of these peaks show a significant dependence on the crack inclination, with different values for the in-plane and out-of-plane enhancement component. A new parameter, the enhancement factor, F_E, is introduced as the measure of the enhancement, by normalising the maximum enhanced amplitude, A_E, at the peak by the reference amplitude, A_i:

$$F_E = \frac{A_E}{A_i} \tag{4.16}$$

F_E is calculated for both the in-plane and out-of-plane measurements. In Figure 4.20, F_E is plotted as a function of the crack depth for 90° and 45° cracks for in-plane and out-of-plane experimental measurements. The lines are given as a guide-to-the-eye to show the general trend in the data and are not intended to show the full behaviour . For a crack of less than 2 mm vertical depth, F_E increases for both angles. For greater crack depths, the 45° cracks show a large increase in the enhancement, up

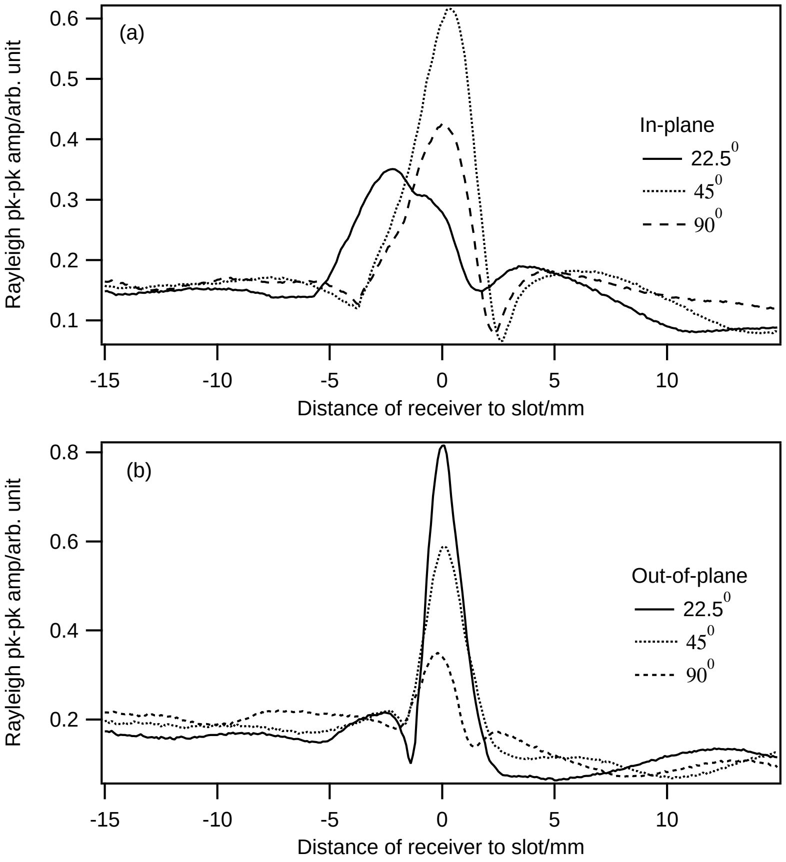

Figure 4.19: Variation of the Rayleigh wave amplitude with the scan distance for samples containing 3 mm vertical depth slots of different inclinations. (a) In-plane, and (b) out-of-plane.

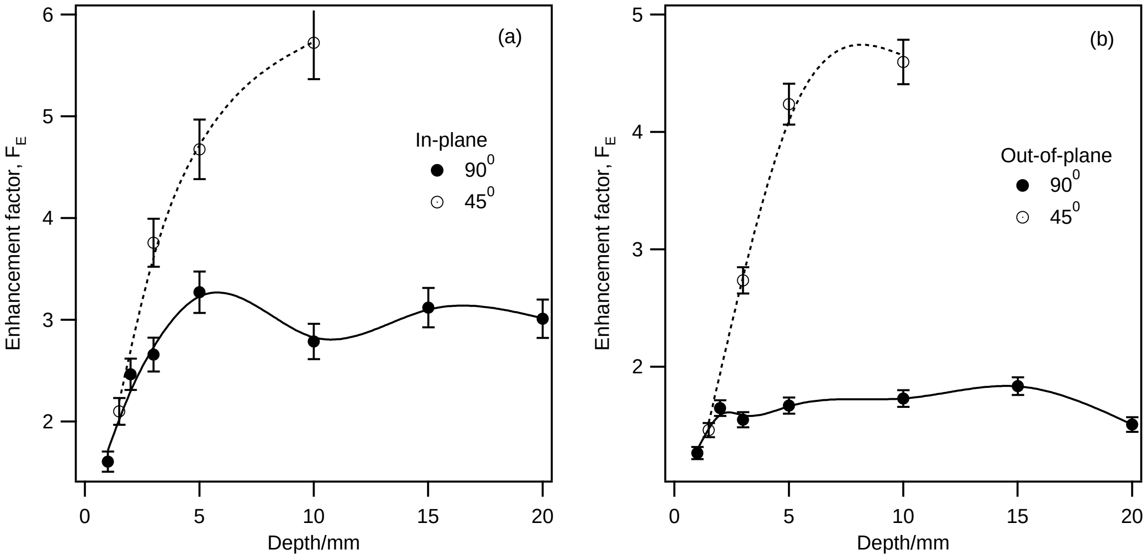

Figure 4.20: Enhancement factor F_E as a function of depth for 90° and 45° cracks, for (a) in-plane and (b) out-of-plane experimental measurements. The lines are a guide to the eye to show the trend of the data.

to a value of 5.7 times the incident Rayleigh wave amplitude in the in-plane and 4.6 in the out-of-plane measurements for 10 mm deep cracks. The 90° cracks, however, show F_E increasing with depth from zero up to 5 mm, before becoming near to a constant value of about 3 in the in-plane and 1.7 in the out-of-plane.

The trend shown by the 90^o crack enhancements with increasing crack depth agrees with the behaviour shown by the theoretical calculation of in-plane Rayleigh wave velocities with depth, shown in Figure 2.1, where the Rayleigh wave velocity increases gradually with increasing depth before becoming to near constant value for depth greater than $d/\lambda = 0.4$. For a central wavelength of 12.6 mm, 5 mm deep crack correspond to a normalised depth of $d/\lambda = 0.40$. This implies that, for the 90^o cracks, the interaction shows that the characteristic of the incident wave agree with the characteristics of the Rayleigh wave, with the interaction occurring primarily within a fraction of a wavelength from the surface.

For the 45^o cracks, the large F_E values clearly exceed the enhancement limit which can be attributed to an interaction of the incident and reflected Rayleigh waves with the mode-converted surface skimming longitudinal wave. This supports the earlier explanation given in Section 4.4 for the enhancement observed on inclined cracks, where a Rayleigh wave is mode-converted to a Lamb-like wave. In Figure 4.21, F_E is plotted against the crack inclination, θ, for 3 mm deep cracks, for both the in-plane and out-of-

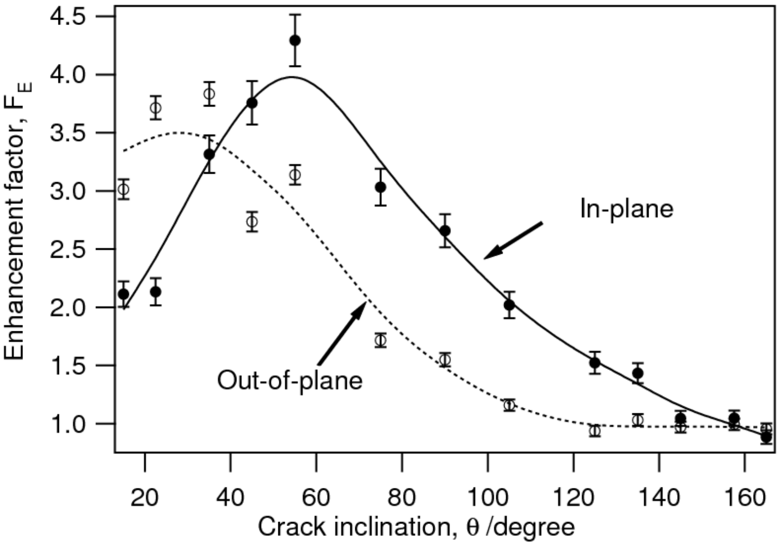

Figure 4.21: Variation of enhancement factor, F_E with crack inclination, θ.

plane components. The crack depth of 3 mm was chosen such that F_E is still increasing with increasing depth for all crack inclinations . Figure 4.21 shows the expected results for a 90° crack, where the in-plane enhancement is larger than the out-of-plane due to the contribution from the mode-converted surface skimming longitudinal wave [70]. In the small angle region (15°-35°), the out-of-plane component shows a possible maximum F_E, however, experimental difficulties in producing reliable samples and models with high enough node density precludes an extension of the discussion to angles of less than 15°. . In the in-plane components, F_E increases to a maximum at 55° before decreasing to a value of 1 at large θ values, where the Rayleigh wave propagation is relatively undisturbed by the presence of the crack.

The absolute magnitude of each enhancement component measured here is applicable for the smooth-sided full-width machined slots used in this experiment, but cannot necessarily can be directly applied to real defects. There are factors which must be considered, such as the scattering reflection pattern from rough surface defects, and the finite size of the crack-width on the surface, that contribute to the actual enhancement measured. In this experiment, the coil of the EMAT has a small width and a large number of averages has been done to improve the small signal to noise ratio (SNR). In practice, the EMAT coil has to be wider in order to get high SNR with less or without signal averaging for faster inspection. Hence, the there will be more spatial averaging. However, these effects shoud affect the in-plane and out-of-plane enhancements equally. It is therefore beneficial to study the ratio of the in-plane ($F_{E(IP)}$) and out-of-plane

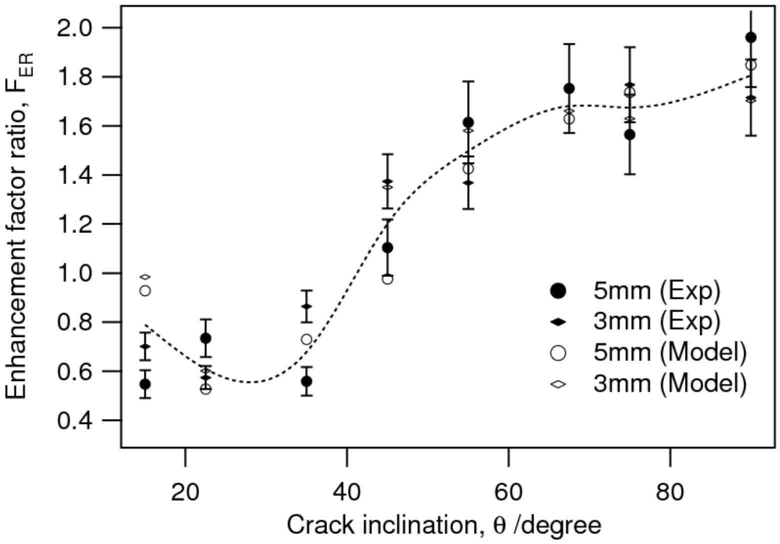

Figure 4.22: Variation of enhancement factor ratio, F_{ER} with crack inclination, θ.

($F_{E(OP)}$) enhancements F_{ER}

$$F_{ER} = \frac{F_{E(IP)}}{F_{E(OP)}}. \tag{4.17}$$

F_{ER} was calculated for 3 mm and 5 mm cracks of various inclinations, using model and experimental results, and these are plotted as a function of the crack inclination in Figure 4.22. Error bars shown are calculated by considering the signal-to-noise ratio in each measurement. A guide to the eye is given by the dashed line to show the general trend of the data, but is not intended to be an accurate fit. Nonetheless, there are only small differences between the 3 mm and 5 mm data in both the experiment and model, implying that the curve can be used for approximating the crack inclination regardless of the depth, provided that they are within a certain depth range. The estimation is accurate to within $10^o - 15^o$ according to the error bars, which is sufficient to give an idea of the correct calibration curve to be used for gauging the crack depth. The plot in Figure 4.22 shows F_{ER} is less than 1 for the small angle region ($15^o - 35^o$) and increases gradually above 1 for angles greater than 45^o. This shows that the out-of-plane component is found to be more dominant than the in-plane in the small angle region, and the opposite is the case outside this region, as expected from the previous discussion.

4.6 In-plane and out-of-plane dominance and sensitivity to EMAT measurements

The enhancement factor ratio F_{ER} plotted against the crack inclination in Figure 4.22 can be explained through the depth profile of Lamb wave. In the small angle region (15°-35°), where F_{ER} is less than one, the broadband Rayleigh wave splits into the A0 and S0-like mode as it is incident on the crack. These modes have arrival times that depend on the frequency, as discussed in Section 4.4. For the broadband wave use here (0.05-0.5 MHz), the S0 mode travels significantly faster than the A0 mode. The A0 mode travels slower with a speed close to the Rayleigh wave. The window set to measure the Rayleigh wave peak-to-peak amplitude for the enhancement measurement will cover the A0 mode but not the S0 mode, hence the enhancement measurements l detect the A0 mode.

The dominance of a particular displacement component over the other (in-plane versus out-of-plane) has been discussed in detail for a number of Lamb wave modes and for a range of frequency-thickness values in Chapter 8 of reference [22] for aluminium plates. Here, the concept is applied to the A0 mode generated within the wedge tip, by approximating the detection region close to the tip as a very thin plate. From reference [22], the displacements (in-plane$u$ and out-of-plane w) for antisymmetric modes at position x can be calculated using

$$u = ikA_1 \sin(px) + qB_2 \sin(qx) \tag{4.18}$$

and

$$w = pA_1 \cos(px) - ikB_2 \cos(qx) \tag{4.19}$$

where $p = \sqrt{\frac{\omega^2}{c_L^2} - k^2}$ and $q = \sqrt{\frac{\omega^2}{c_T^2} - k^2}$. ω denotes the angular frequency and k is the wavenumber. A_1 and B_2 are constants and can be determined by applying the traction-free boundary conditions, as explained in details in [22]. The equations gives some idea of the displacement depth profile across the sample thickness. The in-plane component u is antisymmetric about the centre of the plate while the out-of-plane component, w is symmetric. This can be observed in the plots shown in Figure 4.23.

For the 22.5°, 5 mm deep crack discussed earlier, the local thickness d_i at a distance

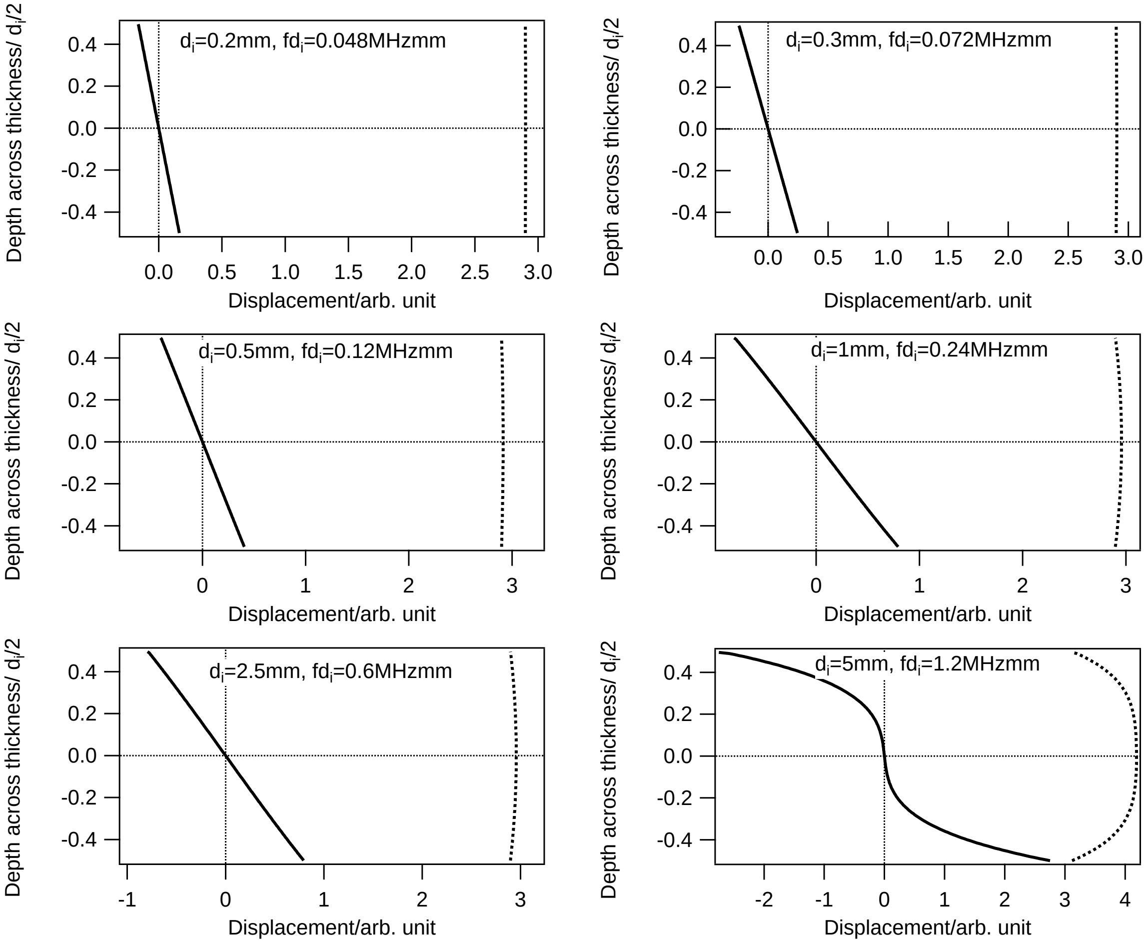

Figure 4.23: Depth profile of in-plane (solid line) and out-of-plane (dotted line) displacement of Lamb wave A0 mode on an aluminium plate with various frequency-thickness, fd .

of 0.5 mm to the wedge tip is calculated as 200 μm, and a frequency$f$ value of 240kHz was chosen to make the frequency-thickness fd_i to be 0.048 MHzmm. The depth profile of an A0 mode with this fd_i value is shown in the top left plot in Figure 4.23. The y-axis in the plot represents the position through the plate thickness, where the origin is the centre of the plate. Arbitrary units are used on x-axes to show the relative magnitude of the displacement between the in-plane (solid line) and out-of-plane components (dotted line) at a given thickness. For this thin plate, the variation of the displacement throughout the plate thickness is very small in the in-plane component, with no variation in the out-of-plane components.

The other plots in Figure 4.23 shows the depth profile for various fd_i (0.12 MHzmm, 0.24 MHzmm, 0.6 MHzmm, and 1.2 MHzmm). Each plot shows the behaviour at the crack tip for higher fd_i. In general, as fd_i decrease from 0.6 MHzmm to 0.048 MHzmm the out-of-plane component maintains its dominance over the in-plane component. An important feature to note is the relative magnitude of each component on the sample surface, where the detection is made. The out-of-plane displacements have values of approximately three while the in-plane displacements have values between one and zero. Consequently, with such out-of-plane dominance it is more likely that experiments will detect the A0 mode in the out-of-plane direction for small angles cracks. On the other hand, for $fd_i = 1.2$ MHzmm, the in-plane and out-of-plane displacement values are fairly close. This behaviour is similar to the Rayleigh wave.

For the angles in the range of 45°-90°, F_{ER} is larger than one, due to the small spreading of the A0 arrival time, as the angles become close to 90^o. In this region, there is a limited mode conversion to Lamb-like wave as the angle is large (large fd_ivalue). The contribution from the mode-converted surface skimming longitudinal wave becomes more significant and gradually gives rise to the in-plane enhancement. As a result, the in-plane component has a larger enhancement than the out-of-plane component. This is closer to the signal enhancement observed for a 90^o crack.

4.7 Summary

The EMAT measurements on full-width surface cracks have provided more understanding of the 2D interaction of Rayleigh waves with normal and inclined surface cracks, and this could be very beneficial for characterising defects. With a set of scans along the defective area on the sample surface using the in-plane and the out-of-plane EMAT receivers, the presence of a crack and its position can be determined. Initial classification into normal/inclined can be made using the out-of-plane B-scans. Further analysis in the near-field can reveal an estimate of the crack inclination, in order to choose the correct depth calibration curve for accurate depth sizing using the far-field transmission.

The prominent enhancement patterns observed for inclined cracks have been explained through the change in the frequency-thickness within the wedge formed by the crack, causing a mode conversion of Rayleigh wave to Lamb-like wave. This finding is supported by the calculation of the Lamb wave A0 mode arrival time and also the spectrogram of the enhanced signal, showing some dispersion. The enhancement pattern is dictated by the wave structure of the Lamb wave mode present close to the wedge tip. A dominant displacement in a particular direction will give a higher sensitivity to the measurement made in that direction.

The findings in this chapter are utilised in the following chapter for fully characterising surface cracks, where a procedure is developed to initially discriminate between normal and inclined cracks, before laying down the analysis steps required to estimate the depth of a given crack. The procedure is tested on unknown defects and rough defects, and it shows good results. The work on the crack classification using the B-scan images is taken further in Section 5.1, where an automated program is developed based on machine learning to classify the B-scan images into defect/no defect and normal/inclined.

Chapter 5

Classification and characterisation of full-width surface cracks using EMAT measurements

Part of this chapter has been published in references [119] and [121].

This chapter describes how the EMAT measurements on full-width cracks, presented in Chapter 4, can be used to fully classify and characterise cracks growing normal to the surface, and cracks growing inclined to to the surface. There are two main parts to this chapter; the first part describes an automated image classification program developed to classify the B-scan images from normal and inclined cracks based on relevant features. The program was based on a machine learning method known as genetic programming, and was developed through a collaboration with Dr. Colin G. Johnson and Dr. Phillip T. Cattani, who are researchers in the School of Computing at the University of Kent and experts in machine learning and automated classification. My contribution in the collaboration work was to provide useful B-scan images that contains relevant features to identify cracks, and expert view of what the images mean. I am also involved in giving instructions for the program usage. The automated image classification program works based on evolutionary algorithm, a method inspired by biological evolution, applying processes such as selection, mutation and crossover to improve a population of programs. This allows automatic creation of programs that extract relevant features from the images.

In the second part of this chapter, a full procedure is proposed for characterising surface cracks using a system comprising a pair of EMATs with a fixed separation, scanned along the sample surface. The procedure uses analysis that can determine the presence of cracks, accurately estimate the crack vertical depth for normal and inclined cracks, and give an estimate of the crack inclination from the surface. It can also determine the orientation of inclined cracks; i.e whether the crack tip for an angled crack is facing the incoming wave or facing the opposite direction. The procedure has been validated on two machined slots and the results show excellent agreement with the measured values. Finally, the procedure has been tested on rough cracks present on the surface of an aluminium billet. The procedure gives a good estimation of the crack depths, and factors that could affect the measurements of the rough cracks are discussed.

5.1 Automated B-scan image classification using machine learning

In Chapter 4, it has been shown that initial crack classification can be done through recognising features in the B-scan images that are associated with a certain crack type. The features can indicate the presence of a crack, determine whether it is normal to the surface 90° or inclined at different angle, and determine the orientation with respect to the wave propagation direction for an inclined crack. The prominent alternating black and white enhancement pattern observed for angled cracks (Figures 4.9 and 4.12) acts as a fingerprint to show the presence of inclined cracks. Identification using this feature, however, requires an operator to have experience or expert knowledge in order to be able to spot the correct features in the B-scans and classify the defects.

The same issue, of requiring an expert to view images in order to make a decision, has been seen in other research and application areas. For example, in medicine, a doctor or a medical technician are trained to spot abnormalities in images such as x-rays, MRI scans, foetal ultrasound scans, and CT scans in order to diagnose patient's illness. In biology, scientists need to distinguish hundreds of biological cells based on images captured under microscopes. In NDT, observing features in the ultrasound B-scan images can be a laborious task if the scanning process covers a large area, generating a continuous feed of images. Furthermore, the decision whether a particular section is defective or not, need to be made on the test site, demanding a very quick and robust system. These requirements justify the need for an automated image classification to recognise the features in the B-scan images and reduce human dependency.

Machine learning provides suitable tools for automated image classification [123, 124]. The main objective of the automated image classification proposed here is to classify an unknown B-scan image on a defect/no defect, and an inclined/not inclined basis, based on the knowledge from a set of training data. A machine learning algorithm known as genetic programming has been used for this task [82]. This technique has the advantage over another commonly used algorithm for automated image classification, known as Artificial Neural Networks (ANN) [125], because the process steps used for analysis in the genetic programming are recorded, allowing an expert to check the analysis procedures. ANN suffers from poor interpretability in the sense that the symbolic meaning behind the learned neural networks are random, and they are effectively black boxes.

The automated image classification employed consists of two main parts. In the first part, relevant features from the B-scan images are extracted using a genetic programming (GP) program. The program applies the evolutionary steps discussed in Chapter 2 to a population of programs. Here, the “features” are the generated numbers produced by the maths functions in the program, which will be explained further in Section 5.1.1. This does not necessarily mean the enhancement features as discussed in Chapter 4. In the second part, an open source data mining sotfware called Weka [114] is used to perform the classification of the data B-scan images data based on the generated features.

5.1.1 Feature extraction using Genetic Programming

The extraction of useful features in the B-scan images is done in a number of steps. An overview of the steps are as follows. It starts with a selection process, where the main program chooses individual smaller programs called genomes, based on some criteria. The selected genomes are then put through the evolution process, where each of them is iterated many times until the desirable conditions are met. Genomes that have a high fitness value will be choosen for the classification process.

Each genome consists of feature-extracting image processing functions and mathematical functions. The former set includes functions that carry out analysis on the image, such as adjusting the contrast, increasing the pixel value, focusing on a particular area, or stretching the image. The mathematical functions are mainly basic statistical functions such as mean, median, and variance, and operate by measuring a chosen pixel or area on the images. Simple mathematical operations such as addi-

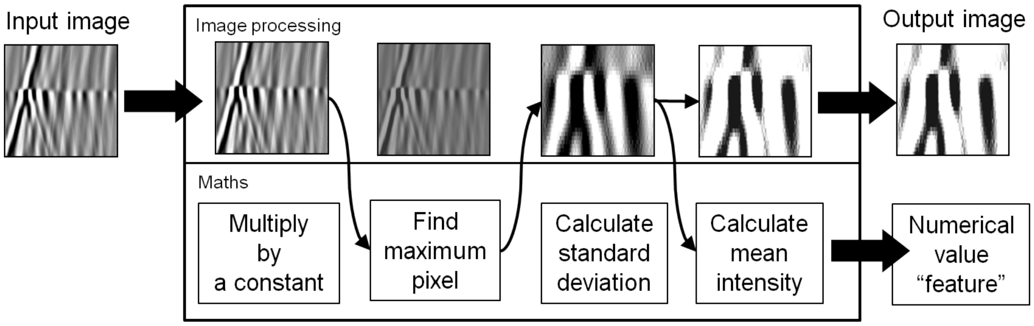

Figure 5.1: The "station" shows an example of how the Genetic Programming program performs image and mathematical functions to an input B-scan image.

tion and subtraction are also performed. For classification purposes, a numerical value is required as an attribute for an image; thus, at least one mathematical function is executed in a genome, and is preferably the final step.

In the selection process, the main program seeks a set of genomes from all available genome programs to form a population. A mathematical function called the fitness function evaluates the quality of each individual genome in the program (see Section 5.1.2). These are then ranked based on their fitness values. The selection method is a combination of two well-known techniques known as *elitism* and *random selection*. The *elitism* technique always selects the fittest individuals in the population for reproduction. Initially, all genomes are ranked based on their fitness value. The highest scoring genome is selected first, then followed by a *random selection* of genomes from the fittest half of the population. The reason a *random selection* method is used in combination with the *elitism* is to maintain diversity in the population.

An example of a genome operating on a B-scan image is illustrated in Figure 5.1. The program platform, known as the station, is divided into two rows of two different types of function; the image processing functions and the maths functions. Within the station, any function, apart from the first one (the starter function), can take the output from any of the preceding functions, and this can be either an image or a numerical value. To enable the program to work, the B-scan images are set in the grayscale format(size 256×256 pixels) and fed into the image function. The arrows in Figure 5.1 show an example of one possible analysis path using the set of functions that make up a genome. Once the input image is in the station, a maths function finds the maximum pixel in the input image. This identifies the area where the signal enhancement is likely to be occuring, and the program takes a close-up of that area. Following this, an output image is generated through a small modification in the contrast,and the mean intensity of the close-up area is calculated. The output of the genome comes in two forms: an output image and numerical value, which is called the feature.

All genomes that pass through the selection process are set to mutate and iterated many times until any of the following conditions are met; the genome has passed the chosen number of generations, or it has exceeded the minimum fitness value. The features are recorded in a text file whenever the fitness value exceeds borh the minimum value and the current best fitness value. A cross over operation as discussed in Section 2.4.3 was not performed in the main program as it was found to hinder the performance, compared to the execution of mutation alone.

For the classification between two image classes such as defect/no defect, the main program requires an equal number of images from each class for training. Thus, for defect vs no defect classification, 15 images from each class were used, and for the normal cracks vs angled cracks classification, 27 images from each class are used. For each classification, all images were input into the main program simultaneously. Thus, the number of features generated in this process will be the same as the number of input images.

5.1.2 Fitness functions

The fitness function evaluates how good a genome program is in extracting useful features that distinguish between two different classes of images. Two fitness functions, Fisher's Ratio and Entropy, are used simultaneously in the program.

Fisher's Ratio

Fisher's Ratio is defined as the ratio of the square of the difference in mean values between two classes ($m1$ and $m2$), divided by the sum of the variances of the two classes ($v1$ and $v2$):

$$Fisher's\,Ratio = \frac{(m1 - m2)^2}{v1 + v2}. \tag{5.1}$$

A good genome program or feature would maximise the scatter between the classes ($m1$-$m2$), but at the same time minimise the scatter within the classes ($v1$ and $v2$); this is what the Fisher's Ratio measures, i.e. the statistical separateness of the two classes. Poor separation is indicated by a low value, and a good separation between the classes is given a high value.

Entropy

The measure of disorder or uncertainty in a system is called entropy. In a system where there are supposedly two classes of items, the entropy is zero when there is 100% certainty that an item belongs to one of the two classes. Similarly, entropy would be maximum of 1 when there is a maximum uncertainty that an item belongs to a certain class.

The value of entropy is calculated by initially sorting the feature values associated with each image and the known image class in an array. The highest half of the feature value is retained to form a new array, and the other half of the array with the lowest feature values are discarded. The reason the lowest half is discarded, is to create a system where low values indicates one class, while the higher values indicates the other. This method checks whether his has happened.

The entropy is calculated in the new array using

$$Entropy = (-(p1)log_2(p1)) - ((p2)log(p2)) \tag{5.2}$$

where $p1$ and $p2$ are the probabilities of the first and second class of images respectively appearing in that array. The probability $p1$ is the ratio of imageswhich belong to class 1, to the total number of images in the new array, while the probability $p2$ is simply $1 - p1$. It is worth mentioning that the entropy defined in Equation 5.2 is a simplified version of the implementation of entropy, and it will only work when the number of the images from each class in the initial array is equal.

However, the number of images from each class are not always equal. In the case where the number of images are different, a normalised version of the entropy function is used. In the normalised version, the class that has larger number of images, say N_{large} is used to calculate entropy. The value from each image are sorted in an array, and the highest N_{large} images is used to calculate the entropy using Equation 5.2. For example, consider two classes of images; A and B. Class A has 80 images and Class B has 20 images. The total number of images in the initial array would be 100. The images are then sorted according to their value and the highest 80 images are selected for entropy calculation, while the lowest 20 images are discarded. In the new array, the number of images from each class are counted, to calculate the ratio of each class to the new array size of 80. This yields the probabilities value of $p1$and $p2$, and thus the entropy can be calculated using the equation.

5.1.3 Classification using Weka

The features generated by the program described in Section 5.1.1 are used for classification using an open source data-mining software called Weka [114]. Weka used the fitness function values; Fisher's ratio and entropy, described in Section 5.1.2 to classify the images based on the features. A number of classfication algorithms are run in Weka, in order to make a comparison between the predicted class, according to the values of the various features, and the actual class, using the designated value for the class provided by an expert. In this way, the genome program can be checked to see whether it is creating useful features which can be used to accurately predict the class of the image of this type.

The quality of each successful genome is tested by measuring their predictive ability using Weka. A cross-validation method has been used to train the machine learning algorithms in Weka using the generated attributes. This means that, for each test, a certain portion of the data is set aside for testing, while the remainder is used for training. A 10-fold cross-validation was chosen based on the small size of the dataset (30 images in total for defect/no defect and 54 images for normal/angled cracks). Therefore, approximately 90% of the images were used for the training, while approximately 10% were used to blindly test whether the prediction based on the learned classification method was accurate.

5.1.4 Results

For the defect vs no defect classification, Weka achieved highest accuracy (>95%) using the Multi Layer Perceptron algorithm, while for the normal vs angled classification, the best accuracy of 92.59% was achieved using Weka implementation of the decision tree algorithm known as J48. The first classification task achieved the highest accuracy because the task was not difficult; there is a clear difference in the features for B-scans with a defect and with no defect. For the second task, the accuracy is slightly lower due to four misclassifications from the total of 54 images; two misclassification in each class.

Although good accuracy was achieved for both classification tasks, more input B-scan images data are required to verify the automated classification program it it is to be used in an industrial setting. With a small dataset, there is a danger of overfitting, where a good accuracy is obtained from the known examples, but the program performs poorly when it is used on a set of generalised examples of the same phenomenon. This is possible even with the use of 10-fold cross validation, where the cross validation can only help to exploit diversity that is already present in the dataset. For dataset containing images of similar features, this not very effective and it is likely that the quality deteriorates as the size of the date set decreases.

5.1.5 Discussion of automated B-scan image classification using machine learning.

The genetic programming approach used here for extracting useful features from the B-scan images of defective and non defective samples has shown excellent results when tested with a small set of training data (30 images for defect/no defect and 54 images for inclined/normals cracks). Accuracy higher than 90% was achieved when the useful extracted features were tested with several classification algorithms in Weka. The method shows promise for application as a real defect detection system that relies on B-scan image analysis, in order to determine the presence of defects and also the defect type.

However, for a more realistic representation of the accuracy of this program, a larger dataset is needed to both train and test the program. Real surface cracks normally have rough faces that can be contacting with each other or in partial contact [126]. The enhancement pattern will be slightly different for these cracks when compared to the enhancement for machined slot, albeit with a similar alternating black and white pattern for an inclined defect, and the program needs to learn other variations of the enhancement features. In addition, real cracks normally have a smaller width, i.e not usually extending to the full-width of the sample, as discussed in Chapter 4 and 6. The signal enhancement will still be observed for this type of crack as shown in Chapter 6, but again the exact enhancement features in the B-scans may be slightly different from the image used here for training. The experiment on full-width cracks acts as a feasibility study, before moving on more complicated features that can be found in narrow cracks.

For extracting useful features from the B-scan images, the genetic programming method used here has advantages over other machine learning methods which are more commonly used in NDT, which are based on neural networks. With genetic programming, all the analysis steps in each routine are recorded, allowing one to work backwards to check the analysis which has been done on the data. Any error or misdirection in the analysis steps can be identified and rectified before the program is set to run again. Alternatively, one can pick a suitable smaller set of operations to be included in the final optimised program. Once a set of useful features has been extracted using the genetic programming method, the features must be imported into one of a number of different classification algorithms. For this part of the program, the genetic programming method is not in force anymore, and the classifier with the highest accuracy should be selected to be included in the optimised full analysis program. This means that a classifier based on ANN can be used if it has the best accuracy, but the feature classification is based on will be known due to the use of genetic programming.

Ideally, the genetic program will be incorporated into the EMAT scanning system for detecting surface defects. In this way, the program will operate automatically with minimal human dependency. The use of this method is not necessarily limited to the EMAT system presented here, but it can also be extended to cover other ultrasound testing systems that generate B-scan images.

5.2 Crack characterisation procedure

The surface crack characterisation procedure shown later in Figure 5.2 was developed based on the findings from the EMAT measurements of the in-and out-of-plane components of Rayleigh wave presented in Chapter 4, and using the B-scan classification analysis described above. The objectives of this procedure are to determine the crack vertical depth, d, the crack orientation (whether it is facing or opposing the incoming Rayleigh wave), and to give estimate of the crack inclination, θ, to the sample surface. The dimension for d and θ are shown in Figure 3.4. Measurements in the far-field and near-field are taken in a single scan made across a defective area on the sample surface. Scans can either be done separately for each component (in-plane or out-of-plane) using a pair of transmit and receive EMATs, or simultaneously by using a transmit EMAT paired with two receivers, one for each component. Initial validation of this procedure, presented in Section 5.2.1, is conducted using a trolley to move the EMATs together at fixed separation (Figure 3.9(b)) and keeping a constant lift-off from sample surface.

The signals recorded from the scans made over defective areas are analysed in two parallel routines. One routine performs B-scan image analysis, and the other one mea-

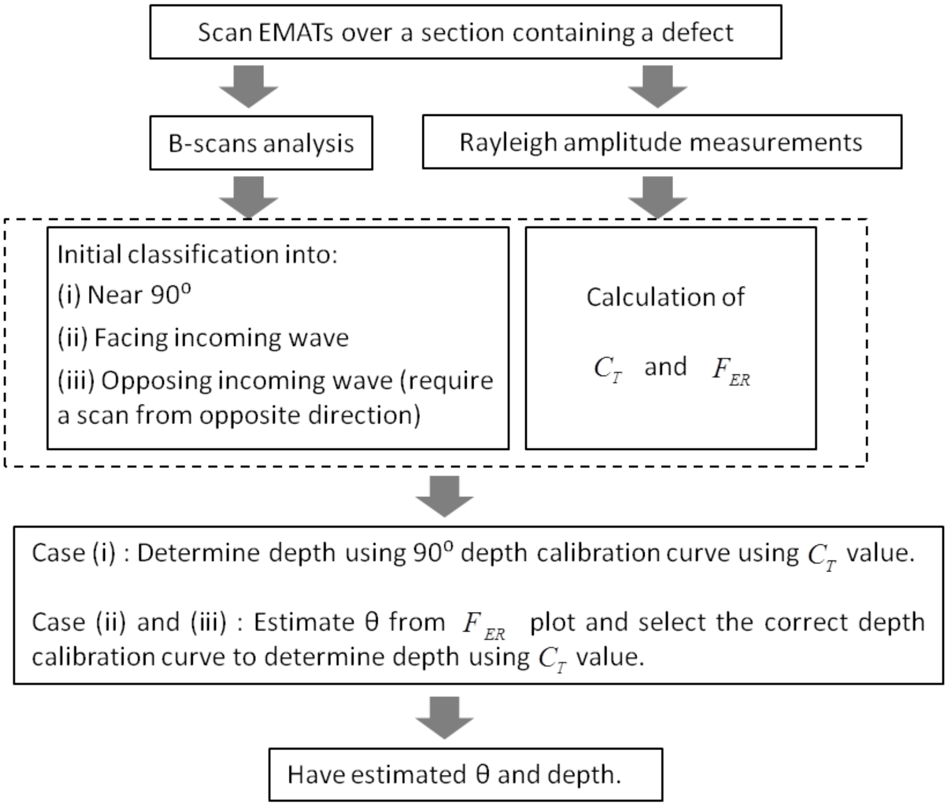

Figure 5.2: Procedure for characterising surface crack

sures the Rayleigh wave peak-peak amplitude as a function of scan distance, and calculates the transmission coefficient, C_T, and the enhancement factor ratio, F_E, defined in Equations 4.6 and 4.17. In the B-scan image analysis, initial crack classification is conducted based on findings described in Section 4.3, where the crack can be classified as near 90° (case (i)) or inclined. For an inclined crack, the orientation of the crack tip can be classified further into *facing the incoming wave* (case (ii)) or *opposing it* (case (iii)). The latter requires a scan to be made in the opposite direction to the first scan so that the incoming wave is facing the crack tip, as in case (ii). Classification can be done using a trained operator, or the system describe in Section 5.1.

If the crack is judged to be near 90° characterisation requires only the calculation of the Rayleigh wave transmission coefficient, C_T, in order to determine the crack depth using a known calibration curve for 90° cracks. Inclined cracks also require calculation of the enhancement factor ratio, F_{ER}, to estimate the crack inclination θ before choosing the correct depth calibration curve to determine the crack depth. This has been discussed in Section 4.5.

In Section 5.2.1, the result of testing of this procedure on aluminium samples containing machined and real surface cracks is presented. Firstly, a procedure validation was performed on two machined cracks on the surface of an aluminium bar where the inclination and depth of the cracks are not known prior to analysis. Secondly, the procedure was tested on a rough crack on the surface of an aluminium billet. The results from the initial validation made on the machined cracks show good agreement with later measurements made using a ruler , and shows a promising prospect for real world applications for the characterisation system. The test on the rough cracks experienced some issues that are not encountered when dealing with machined cracks, such as the crack face roughness, the contact between the crack faces (closed or partially closed), and the variation in the crack depth. However, the procedure still characterised the rough cracks reasonably well.

5.2.1 Validation on two unknown machined slots

The procedure depicted in Figure 5.2 was tested on two machined slots with depth and angle unknown prior to analysis of the ultrasonic measurements. However, the slots are visible on the aluminium sample surfaces, and their dimensions can be measured visually using a ruler (for the vertical depth) and protractor (for the angle from surface). The slots, which are labelled as Crack 1 and Crack 2, were measured as 4±0.2 mm (at 30°±3°) and 7±0.2 mm (at 45°±3°) respectively. The slots are full-width, i.e their width extends to the edges of the sample.

The experimental set up for this validation is shown in Figure 5.3. It follows the method explained in Figure 3.9(b), where the transmitter and receiver EMATs were held together by an aluminium separator bar at 150 mm apart. The lift-off from the sample surface to the EMAT coil was fixed at 0.1 mm. The pair of EMATs were scanned with 0.5 mm steps across each crack, initially in the direction shown by the solid arrow, with the scan distance measurement reset prior to scanning Crack 2. Following initial analysis steps, the scan needs to be repeated in the opposite direction shown by the open arrow, if the defect is found to be opposing the incoming wave (case(iii) in Figure 5.2).

B-scans images were constructed after the receiver EMAT had travelled a distance of 100 mm across each crack; this is to keep the crack features at the centre of the B-scan. Figure 5.4 shows the out-of-plane B-scans for (a) Crack 1 and (b) Crack 2 , for the scan made in the direction shown by the solid arrow in Figure 5.3. The enhancement pattern indicates the position and the type of the crack (Chapter 4). Based on the observed

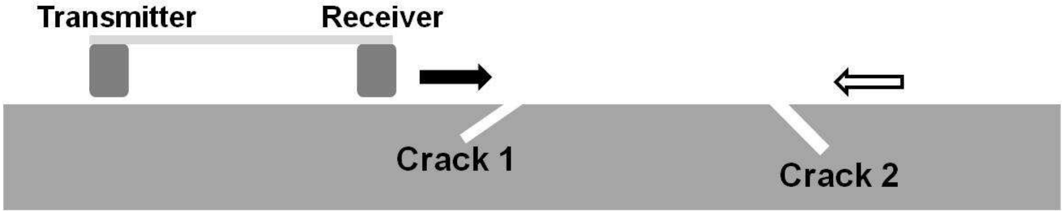

Figure 5.3: Experimental set up for validating the procedure shown in Figure 5.2. The details are explained in the text.

enhancement pattern, where an alternating black and white pattern is very prominent, Crack 1 is classified as an inclined crack with the acute angle of the crack facing the incoming Rayleigh wave. Meanwhile, the B-scan in Figure 5.4(b) shows a significant delay of the Rayleigh wave arrival time and very faint but clear alternating black and white pattern following this delay. These features are attributed to an inclined crack with the tip facing away from the incoming wave (obtuse angle). A second scan is made for Crack 2 in the opposite direction (open arrow in Figure 5.3), with the B-scan for this scan shown in Figure 5.5.

Figure 5.6 shows the normalised Rayleigh wave peak-to-peak amplitude as a function of scan distance for Crack 1 and Crack 2, when the incoming wave was set to face the acute angle of the cracks. This correspond to solid arrow for Crack 1 and open arrow for Crack 2. The amplitudes are shown for in-plane (solid line) and out-of-plane (dotted line) components. For Crack 1, the out-of-plane component shows a higher enhancement than its in-plane counterpart, with $F_{E(IP)} = 3.20$ and $F_{E(OP)} = 4.89$. For Crack 2, the enhancements factors are $F_{E(IP)} = 5.10$ and $F_{E(OP)} = 4.30$. Thus, the enhancement factor ratio of the in-plane component to the out-of-plane component, F_{ER}, for Crack 1 is 0.65 and for Crack 2 is 1.18. The inclination θ of each crack is estimated using the interpolation plot in Figure 4.22. For Crack 2, θ is estimated as 45°, while for Crack 1 the estimation yields two possible values, 20° and 34°. Based on the individual enhancement in each component, there is a higher likelihood that the angle is 34°. The depth of both cracks are hence estimated using the 45° calibration curve (based on the variation seen in Figure 4.6). The results are summarised in Table 5.1, showing a comparison with the measurement made visually using a ruler and a protractor on the side of the sample. Crack 1 is estimated as 4.5 ± 0.6 mm, while Crack 2 it is estimated as 7.4 ± 0.6 mm. The estimated values from the procedure show an excellent agreement with the visual measurements (Crack 1: 4 ± 0.2 mm (at $30° \pm 3°$); Crack 2: 7 ± 0.2 mm

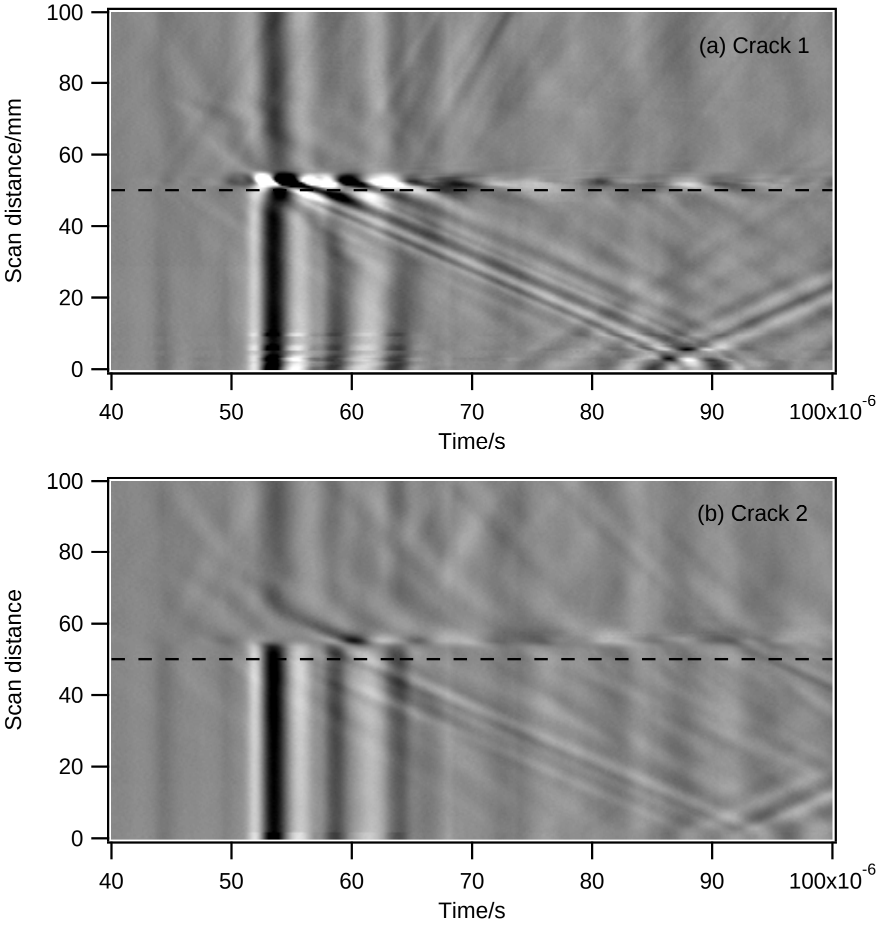

Figure 5.4: B-scans using the out-of-plane receiver in the direction shown by the solid arrow in Figure 5.3. The dotted lines indicate the position of the first crack edge encountered in the scan.

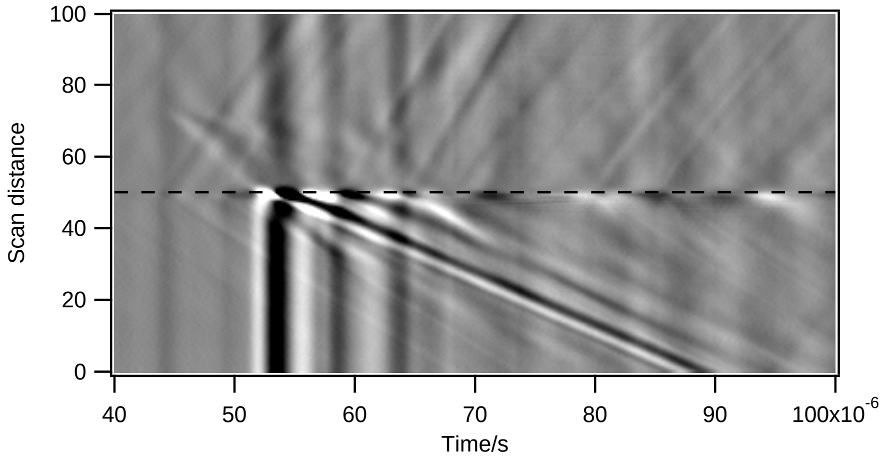

Figure 5.5: B-scan of Crack 2 for a scan in the direction shown by the open arrow in Figure 5.3, made using the out-of-plane receiver.

Crack	Visual measurement		Ultrasound measurement	
	Depth/mm	Angle	Depth/mm	Angle
Crack 1	4±0.2	30°±3°	4.5±0.6	34°±10°
Crack 2	7±0.2	45°±3°	7.4±0.6	45°±10°

Table 5.1: Comparison of results of the unknown cracks from the visual measurement and the ultrasound measurement following the procedure in Figure 5.2.

(at 45° ± 3°)).

5.2.2 Discussion on the validation of the procedure

The characterisation procedure presented here has been proved to distinguish between normal and inclined cracks, and to estimate the vertical depth using the appropriate depth calibration curve. It has been tested on artificial cracks made from machining slots on aluminium samples with a finite width opening and smooth parallel faces. This, however, is a simplified version of real surface cracks that are encountered in industrial environments. Real surface cracks usually have rough faces, and they are not always parallel. It is also possible to have cracks that have contacting or partially contacting faces [126, 127].

With regards to these features, the individual enhancement of each component of Rayleigh wave close to the crack is expected to be lower due to the scatter of the

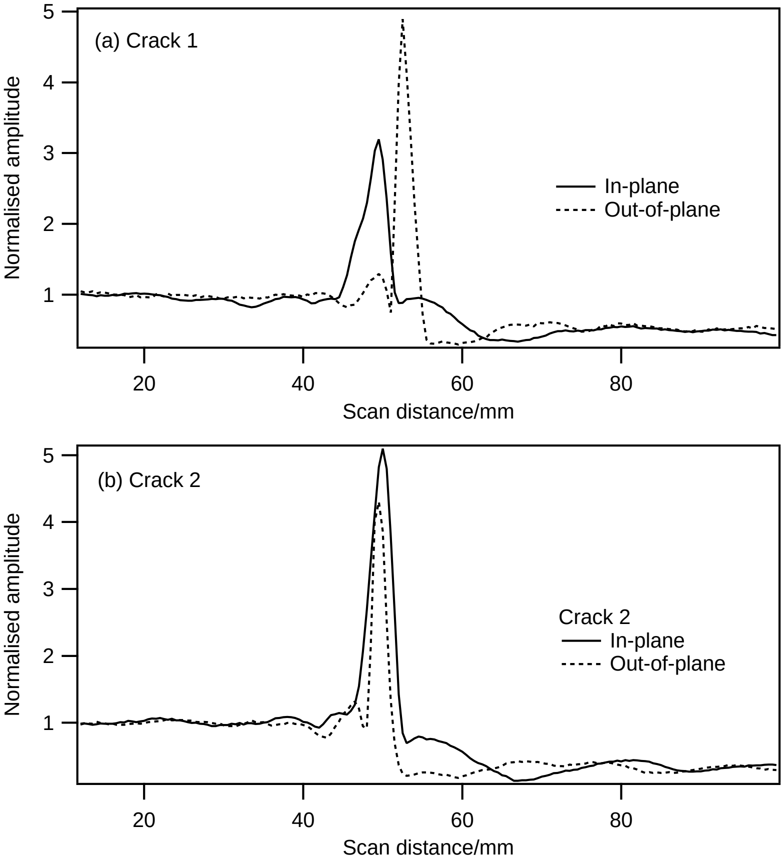

Figure 5.6: Normalised Rayleigh wave peak-to-peak amplitude in the in-plane and out-of-plane components as a function of scan distance for Crack 1(a) and Crack 2 (b).

reflected waves. However, the ratio between them should not be too far from the values measured on smooth cracks, because the roughness will affect both components similarly. It has also been proven that the depth of inclined cracks in the angle range between 15° and 35° can be safely estimated using a 45° depth calibration, as can the cracks with angles around 45°. Therefore, a small error in determining F_{ER} should not result in a significant difference in the depth estimation for inclined cracks.

5.2.3 Test of procedure on rough cracks on the surface of an aluminium billet

Figure 5.7 shows a photograph of the surface of an aluminium billet containing two rough cracks, with more details of the cracks given in Section 3.6. The sample shown in the figure is the same sample reported in [13], where a laser ultrasound measurement was used to study non-linear enhancement effects, with crack depth measurements done using ACPD. Here, the sample has been used for testing the EMAT measurement procedure shown in Figure 5.2; the ACPD measurement from the reference (also shown in Figure 5.10) is used as a comparison for the depth measurement made when following the procedure.

In Figure 5.7, the red square indicates the area covered by the scan made using the EMATs. The area covers almost three-quarters of Crack 1, and the shallower part of Crack 2. The procedure explained in Section 5.2 is applied to the cracks using scans made with in-plane and out-of-plane EMAT receivers separately. The EMATs are scanned in the direction indicated by the blue arrow.

The B-scans of the out-of-plane and the in-plane measurements made on the cracks are shown in Figure 5.8. Both B-scans indicate that the position of the cracks is around 30 mm on the scan. The in-plane B-scan shows a clearer picture of the individual enhancements, where there are two enhancements, each one correspond to one of the cracks. The separation between the two enhancement indicates the gap between the two cracks is clearly visible.The enhancement pattern n indicates that both cracks are more likely to be 90° or near 90° cracks, as there is no prominent alternating black and white pattern to show that mode-conversion to a Lamb-like wave is taking place, as explained in Section 4.4. For cracks close to 90°, the incident Rayleigh wave that strikes the corner of the crack is mode converted to both bulk and surface skimming longitudinal waves [72]. Some of the surface skimming longitudinal wave is reflected back along the sample surface, while some propagates down the crack tip and is reflected

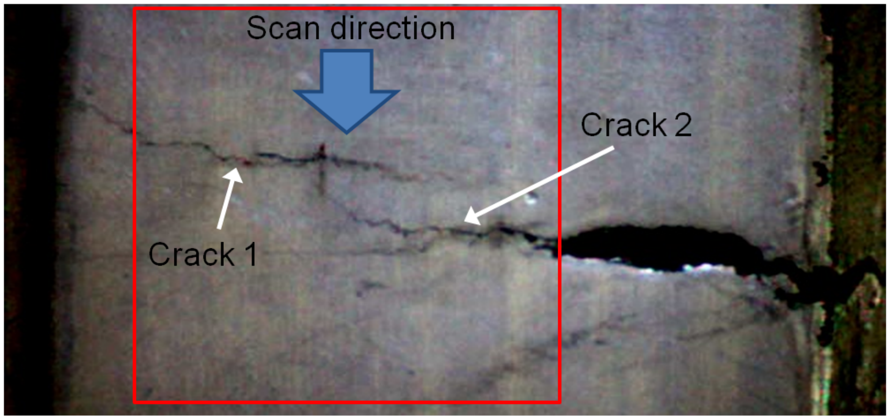

Figure 5.7: A photograph of the rough cracks with the blue arrow showing the direction of scan. The red square indicates the area covered by the EMAT coil when scanning over the cracks on the aluminium billet.

back to the crack opening. The latter will lose more energy due to the scattering on the rough faces of the crack. The former, which has mainly in-plane motion on the surface, in the near-field of the crack, will be detected by the in-plane EMAT receiver. Thus, it gives a clearer picture of the enhancement in the in-plane B-scan compared to the out-of-plane B-scan.

Rayleigh wave peak-to-peak amplitudes are measured for both the in-plane and out-of-plane measurements and are plotted as a function of scan distance in Figure 5.9. The presence of the two cracks are confirmed by the two peaks centred on a scan position of approximately 30 cm. Following the crack characteristion procedure for "near 90°" cracks explained in Section 5.2, the transmission coefficient of the Rayleigh wave, C_T is calculated for both components. For the in-plane, $C_T = 0.34$, and for the out-of-plane $C_T = 0.33$. Using the 90° depth calibration curve in Figure 4.6, the transmission coefficient values yield depth values of 5.2 mm and 4.0 mm respectively for the in-plane and out-of-plane components. This corresponds to the overall Rayleigh wave transmission underneath both cracks. The estimated values are compared with ACPD measurements reported in [13], as shown in Figure 5.10. There is a good agreement between the in-plane and out-of-plane EMAT measurements with the ACPD measurement for Crack 1. Meanwhile, for Crack 2, both EMAT measurements have shown a disagreement with the ACPD measurement.

.

As shown in Figure 5.10, the EMAT used has a finite width and the measurements cover parts of Crack 1 and Crack 2. Majority of Crack 1 is covered by the EMAT,

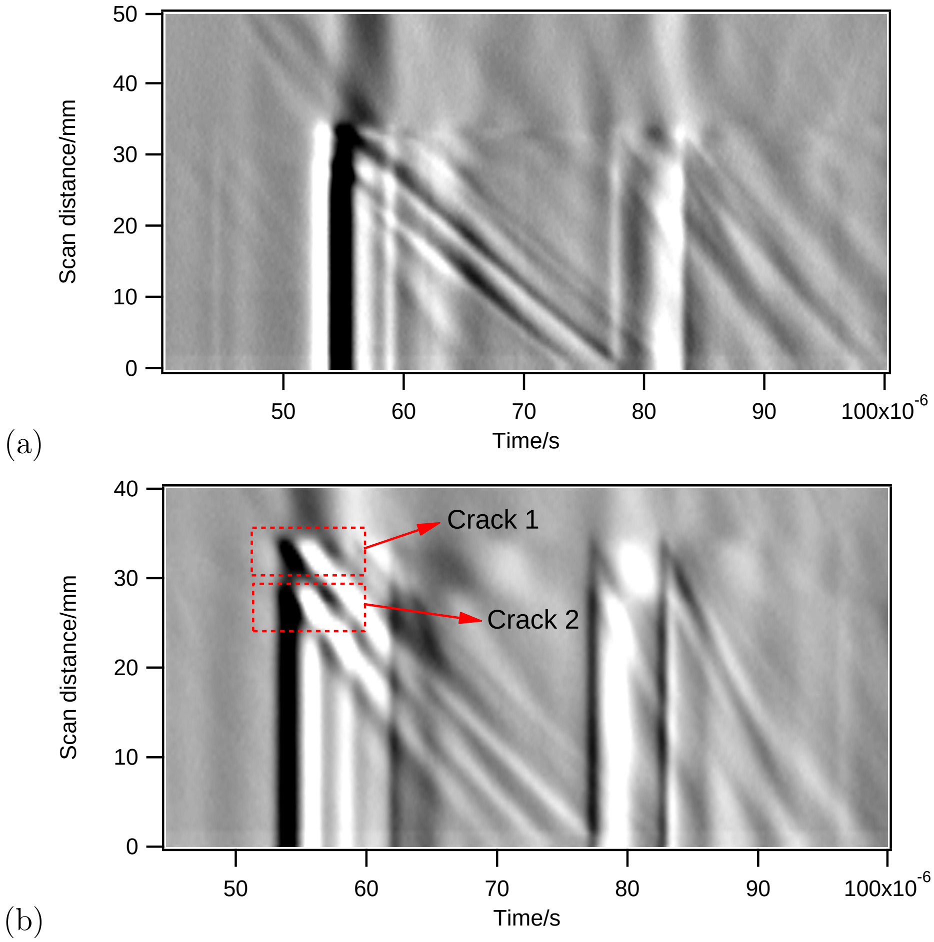

Figure 5.8: Out-of-plane (a) and in-plane (b) B-scans of the rough cracks. Two sets of enhancement and reflections are observed in the B-scans, with the in-plane B-scan showing clearer features.

while only a fraction of Crack 2 is under this coverage. Crack 1 has an average depth of 4.1 mm with a small variation in the depth across its width, with a standard deviation of 1.2 mm. Crack 2 has a large variation in depth, starting from approximately 4 mm and increasing to deeper than 40 mm at the edge of the aluminium billet, with an average depth of 22.1 mm with a standard deviation of 14.4 mm. The shallower portion of Crack 2 is covered by the edge of the EMAT. However, because the sensitivity of detection decreases at the EMAT edge, due to the spreading of the bias magnetic field of the permanent magnet (Figure 2.3), the measured transmission is higher than would be expected if the whole crack affected it. The overall measured transmission is mainly due to Crack 1, which is the first one encountered in the scan, and the one that has more effecs on the EMAT measurement, thus the measured depth reflects more the

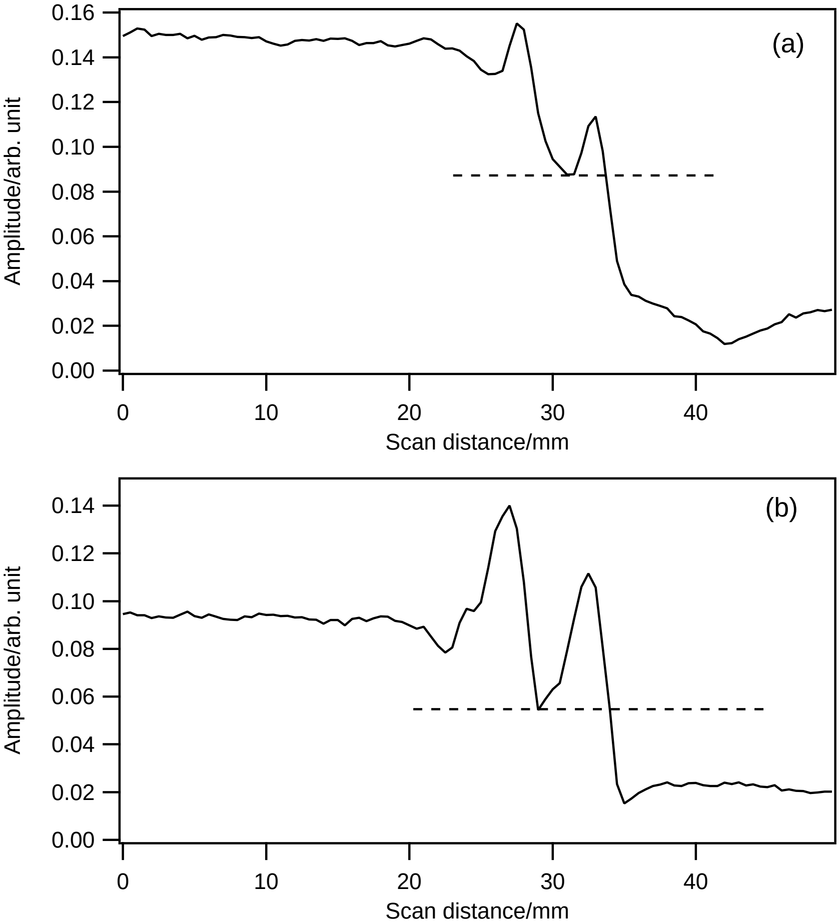

Figure 5.9: Rayleigh wave peak-to-peak amplitude plotted as a function of the scan distance. (a) shows the out-of-plane component and (b) shows the in-plane component. The dotted lines indicate the reference line for the peak on the right that correspond to Crack 1.

depth of Crack 1.

The enhancement factor F_E is also calculated for both components. Figure 5.9 shows that there are two peaks in each component corresponding to each crack. The first peak in the signal amplitude encountered in the scan corresponds to Crack 2 while the second peak corresponds to Crack 1. F_E calculated for Crack 2 are $F_{E(IP)} = 1.50$ and $F_{E(OP)}$=1.05, giving a ratio F_{ER}=1.43. For Crack 1, the first dip after the first peak in the plot, as indicated by the dashed line is used as the reference for calculating F_E. It gives $F_{E(IP)} = 2.07$ and $F_{E(OP)}$=1.30, thus the ratio F_{ER}=1.59. Using the angle estimation plot in Figure 4.22, and assuming that the cracks are acute angled, the inclinations for Crack 1 and Crack 2 are estimated as 60° and 52° respectively.

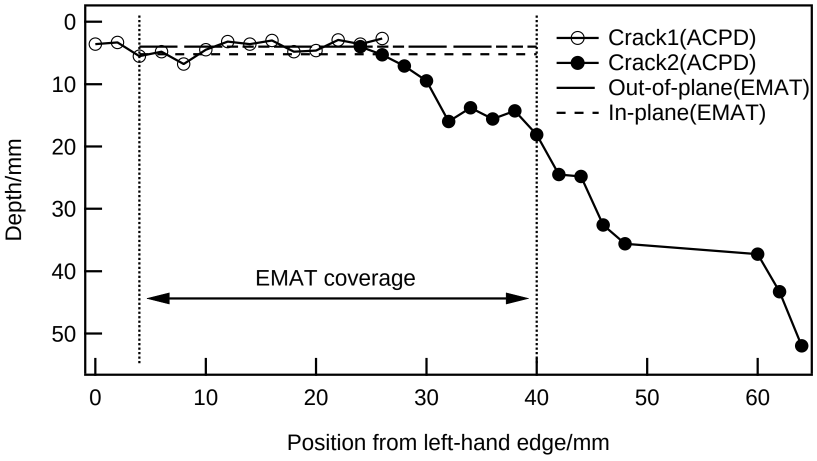

Figure 5.10: The depths of Crack and Crack 1 from APCD measurements in reference [13] is compared with the estimated depths using in-plane and out-of-plane EMAT measurements following procedure in Figure 5.2.

5.2.4 Discussion on the test of procedure on the rough cracks

The test conducted on the rough cracks has shown both the advantages and limitations of the procedure presented in Figure 5.2 . Firstly, it has shown that rough cracks can be detected through the enhancement features on the B-scan images. The machine learning program explained Section 5.1 can be used to recognise the features and classify them into normal/angled defect. Secondly, two cracks positioned closely together can be distinguished in the B-scan and through the Rayleigh wave amplitude measurements, as shown in Figure 5.8 and Figure 5.9. If the cracks are within the near-field of each other, the inclination of the first crack encountered in the scan can be characterised using the F_{ER} value, with the reference value calculated in the near-field of the crack. For the second crack, the reference can be estimated from the dip after the enhancement of the first crack.

The procedure shows a good estimation of the crack depth if the crack is approximately uniform, as shown by Crack 1, but if the crack depth has a varying depth, such as is the case for Crack 2, the estimation will give an average depth over the area covered by the EMAT. For a very deep crack, a threshold depth may need to be introduced, so that the procedure gives a “deeper than” output for cracks outside its detection range. This range can be evaluated from the frequency bandwidth of the signal used and from the calibration shown in Figure 4.6.

Chapter 6

Effects of crack width on Rayleigh wave transmission

The study of Rayleigh wave interaction with surface defects has been an active area of research [23,53,54,56,57,59,62,65,69,72]. While the previous research investigated these interactions, the majority of the research were based on the assumption that the crack width is infinitely long compared to the incoming Rayleigh wave. This certainly is not true for many more realistic defects, especially when the crack has a finite width and is comparable with the size of the Rayleigh wave beam. For example, rolling contact fatigue (RCF) cracks founds in rails have typical crack width of 5 mm to 20 mm [3]. The term narrow-width crack is used in this thesis to refer to this type of crack. This issue is investigated in this chapter.

This chapter proceeds as follows. Experiments were initially performed using an EMAT transmitter with a laser interferometer as receiver, to map the diffraction around 90° and 25° cracks of different widths, which were chosen to represent normal and inclined cracks. A second set of experiments were then performed using an EMAT transmitter and an out-of-plane EMAT receiver with the measurements compared with those using the laser receiver. The spatial averaging effect of the EMATs receiver is discussed here. The viability of a pair of EMATs to be used for real crack detection, where the width may be less than the EMAT width, is explored. Results from EMAT measurements of cracks of different widths are discussed in the light of characterising realistic surface cracks and suggestions are made on how to deal with situations where the EMATs are expected not to be able to size the crack depth accurately using Rayleigh wave transmission. Based on the viability study, EMAT techniques show promising possibilities for use real applications, in particular for detecting RCF cracks in rails.

6.1 Rayleigh wave diffraction around narrow-width cracks

When a propagating plane wave encounters a small obstacle, some of the wave bend around the obstacle to get past it. The is what a diffraction is. Real surface cracks typically have a surface length or width of finite size. Thus, when a Rayleigh wave is used to characterise them, it will suffer from diffraction effect around the crack edges. The wave transmission will be affected, due to the delay of Rayleigh wave component that has been diffracted at the crack edges. As the wave transmission is crucial to crack depth estimation using the method explained in Chapter 4, the diffraction at the crack edges will most likely to affect the depth estimation and may cause some errors. It is important therefore to know how much the diffraction affects the transmission. Another important point is whether, with the additional diffraction factor, the strong alternating black and white enhancement pattern can still be observed and used for inclined cracks.

The diffraction was studied experimentally using an EMAT as transmitter and a laser interferometer [107] as receiver on aluminium bars, as shown in Figure 3.12. The full experimental details are explained in Section 3.4. The laser interferometer was chosen as the method for detection because it detects surface displacements over the small area illuminated by the laser. This allows for detailed mapping of the ultrasonic wave around the crack during a scan, which cannot be done easily using the EMAT receiver due to the finite size of the coil. The EMAT transmitter was fixed at 130 mm from the crack, while the laser receiver was scanned from 20 mm away from one side of the crack to 30 mm on the other side of the crack. The width of the aluminium bar, as shown in Figure 3.12 is divided into two,with only one half scanned to record the diffraction, and the results are mirrored to give a full mapping across the width of the bar. This one-half section was divided into 27 sections, each 1 mm apart, and a scan was made along each section. Surface displacements measured along each scan line were used to reconstruct the interaction and thus give surface displacement snapshots at a given time.

Two sets of cracks, each at an angle of either 90° or 25° to the sample surface, have been used as, explained in Chapter 3. For each type of crack, two crack widths have been considered; 20 mm and 10 mm. The first one was chosen to investigate the case when the size of the EMAT is comparable with the crack width, and the second one is for the case when the crack width is significantly smaller than the size of the EMAT.

6.1.1 Diffraction around 90° cracks

Figure 6.1 shows maps of the out-of-plane displacement in a chosen area of two samples, at different times t during propagation of the wave. Each sample contains a 90° crack located at the centre of the sample transverse to the incident wave, at 130 mm on the scan distance as indicated in the figure. The cracks have different widths; 10 mm and 20 mm. The maps of the displacements at different times for each crack are shown in two columns. The left column shows the maps for the 10 mm wide crack and the right column shows the maps for the 20 mm wide crack. Descending down the column, the time increases from t_1 shortly after generation of the wave to t_5, after the wave has interacted with the crack. At $t_1$and t_2, the Rayleigh wave approaches the crack from the left end of the maps. At t_3, the Rayleigh wave has reached the crack. At t_4, the Rayleigh wave is about to pass the crack, and diffraction can be observed. Finally, the Rayleigh wave has fully passed the crack at t_5.

The laser receiver measurements give an images of resolution 1 mm by 1 mm. The distance across the width of the aluminium bar is shown by the y-axes, where the origins (0 mm) indicate the position of the centre of the bar, and the distance is given as the offset from the centre. The x-axes show the scan distance of the laser receiver relative to the centre of the coil in the EMAT transmitter. Thus, the position of the crack is at 130 mm on the scan distance axes (x-axes), and this is inidcated in Figure 6.1 at time $t = t_1$ as a black line.

The Rayleigh wave approaches the cracks with a wavefront that is approximately a line near the centre, but curved at the edges, shown in Figure 6.1 at times t_1 and t_2. The shape of the wavefront is determined by two factors here; firstly, the size of the coil in the EMAT transmitter, and secondly the directionality of the ultrasound wave generated. The EMAT transmitter consists of a 35 mm wide coil, covering the area from -17.5 mm to 17.5 mm on the maps. Within this region, the wavefront can be seen in the figure as approximately a line. Meanwhile, outside this region, the wavefront starts to curve slightly due to the small spread in the ultrasound wave generated. The spreading of the generated wave has been discussed in Section 3.1, and limited when using this EMAT designs.

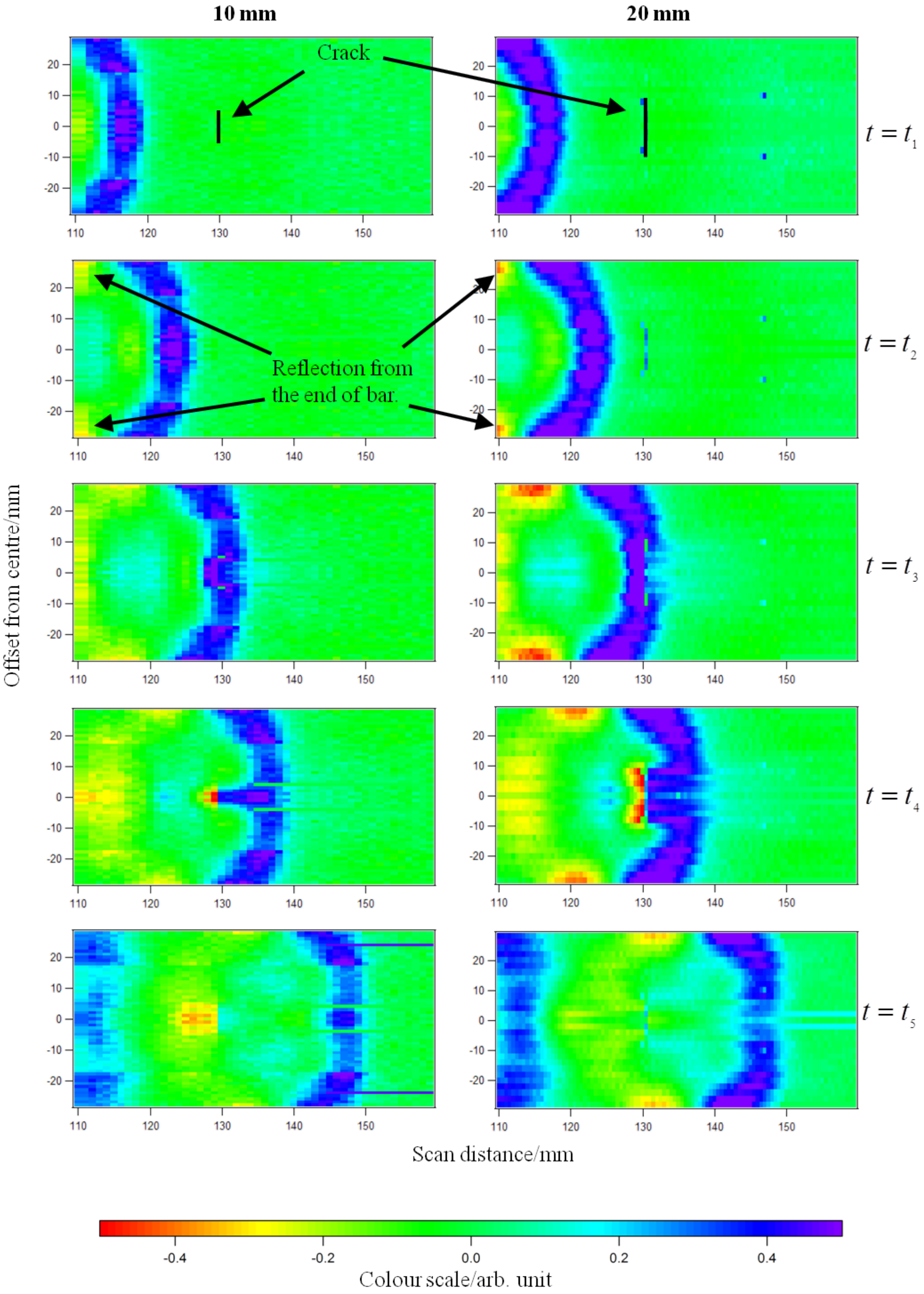

Figure 6.1: Diffraction on 5 mm deep, 90° cracks of 10 mm width (left) and 20 mm width (right).

The reflection of the Rayleigh wave from the left end of the bar (shown in Figure 3.12) starts to appear in this window at time t_2, as indicated in Figure 6.1, and it becomes more prominent at time t_3. At t_4, the reflection from the crack can be observed clearly to appear in front of the crack. This is in addition to the earlier reflection from the left end of the bar.

The interaction of the Rayleigh wave with the crack, leading to signal enhancement, starts to take place at time t_3. It can be seen that, for both cracks, the magnitude of the Rayleigh wave as indicated by the colour scale increases in front of the crack (before scan distance =130 mm). The wider crack 20 mm, shows a greater area with the increased magnitude shown by the colour scale, compared to the 10 mm wide crack.

The diffraction of the Rayleigh wave at both cracks of different widths is shown at time $t = t_4$. It is very clear that the diffraction is different for 10 mm and 20 mm wide cracks. The diffraction caused by the 10 mm wide crack shows that the crack is still detectable although its size is smaller than the width of the EMAT coil. At time $t = t_4$, the incoming Rayleigh wave reached the cracks, and diffracted at both ends of the cracks edges. The smaller crack, 10 mm wide, diffracts the incoming wave causing it to bend around the edges. In the meantime, some of the Rayleigh wave is transmitted underneath the crack. Since the path length for the this transmission is longer than for the wave diffracted around the crack edges on the surface, the arrival time of the transmitted wave will be slightly later. Similar diffraction and transmission occurs to the Rayleigh interacting with the 20 mm wide crack, except in this case the shadow behind the crack is larger, according to the crack width.

At time $t = t_5$, Rayleigh wave has propagated far enough from the cracks to be considered in the far-field. The transmitted portion of the Rayleigh wave that propagated underneath the crack has fully recovered from the interaction. The wavefront of the Rayleigh wave can be seen to regain an approximate to their original shape, but with a smaller displacement magnitude at the centre, where the crack has blocked some of the Rayleigh wave from passing through.

6.1.2 Diffraction around 25° cracks

The diffraction of the Rayleigh wave at 25° cracks of two different widths is shown in Figure 6.2. The images in the figure are arranged in a similar manner to the images for the 90° crack (Figure 6.1). Here, the positions of the cracks are at scan distance =130 mm, which is the position of the crack opening at the surface. Since the cracks are inclined at 25° from the sample surface, their horizontal tip projection would be approximately 10.7 mm in front of the crack opening relative to the scan. Therefore, interaction can take place for the detector at this distance in front of the crack opening. In Figure 6.2, at time t_1, a surface skimming longitudinal wave has reached the crack ahead of the Rayleigh wave, with this interaction shown by the non-zero magnitude at the crack position. As this wave entered the wedge formed by the crack, it will get mode converted to a guided wave. This is similar to the Rayleigh wave.

Rayleigh wave interaction with the 25° narrow-width cracks shows some interesting features. As the Rayleigh waves approaches the cracks at time t_2, there is an oscillating pattern present preceeding the wavefront, just before the wavefront reaches the crack location. The pattern length on the y-axes corresponds to the width of each crack. The wider crack (20 mm) therefore shows a clearer and more prominent picture of the oscillation. It is expected that mode-conversion to a Lamb-like wave is taking place as the Rayleigh wave enters the wedge formed by the inclined crack (Section 4.4). The oscillating pattern shown at time $t = t_2$ therefore reinforces this expectation. Once the mode conversion has taken place, the Lamb-like wave travels at significantly different speed from the speed of Rayleigh wave, depending on the frequency-thickness product. What is shown in the figure is the symmetric mode S0 which travels faster than the Rayleigh wave speed within the wedge.

At time $t = t_3$, the Rayleigh wave interaction with the crack is taking place. As the wavefronts gradually passed along the wedge formed by the crack some of the waves are reflected back, while some of the waves are again transmitted. It is clear that the reflection is stronger than the transmission, based on the colour scale. While comparing the reflections from both cracks, the 20 mm crack shows stronger reflection compared to the 10 mm wide crack. This agrees with the expectation that cracks with larger area should reflect more. At time $t = t_4$, the Rayleigh wave gradually recovers from the interaction. At time $t = t_5$, the transmitted wave has recovered from the interaction., with low transmission at the centre of the wavefront.

6.2 Signal enhancement in the near-field of the crack

Enhancement of the Rayleigh wave is expected to occur in close proximity to a crack [57, 69, 70, 72]. As described in Chapter 4, the enhancement for inclined cracks has a much higher magnitude compared to a similar depth normal crack, due to the mode-conversion

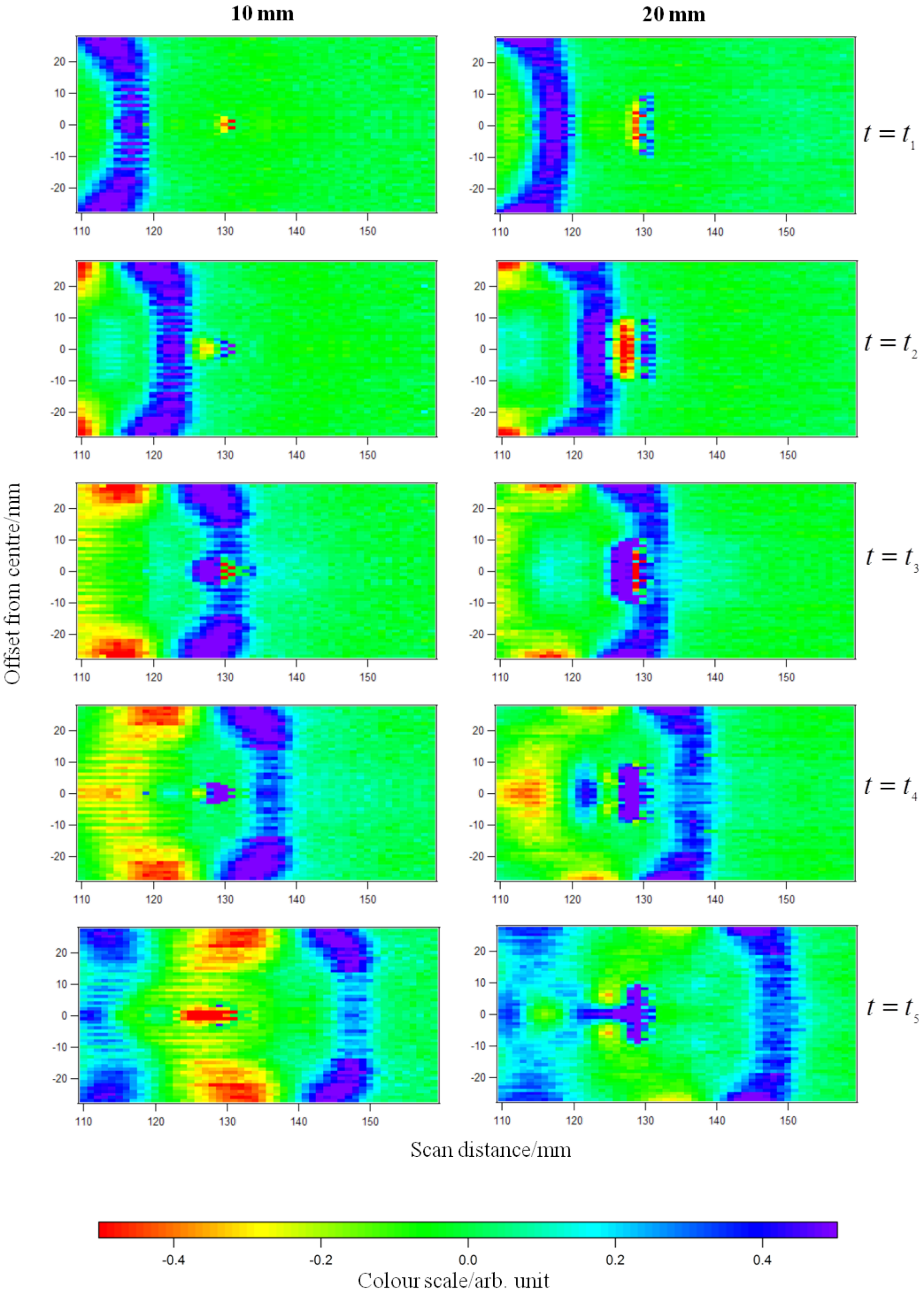

Figure 6.2: Diffraction on 5 mm deep, 25° cracks of 10 mm width (left) and 20 mm width (right)

in the wedge formed by the inclined crack. For the case of narrow width cracks, the enhancement is still expected to occur; however, the magnitude may also depend on the crack width.

Figure 6.3 shows B-scans from the laser interferometer measurements made across the centre of 5 mm deep, 20 mm wide cracks of angle (a) 90° and (b) 25° to the surface. These correspond to the measurement made along a scan line that at the centre of the bar (0 mm om Figure 6.1 and Figure 6.2). In each B-scan, the enhancement of the Rayleigh wave is observed close to the position of the crack opening, at scan distance=130 mm as expected. The forms of the enhancement patterns for both cracks agree with the earlier results on full-width cracks described in Section 4.3, where the inclined crack (25°) shows a prominent oscillating black and white pattern that spans to cover the whole time axis shown here. In contrast, the enhancement at the normal crack (90°) does not have the oscillating pattern, and only occurs at the arrival time of the incident and reflected Rayleigh waves. What is important here, is that the prominent enhancement pattern for the inclined crack can still be observed for cracks of small finite width. As the size of the laser spot is significantly smaller than the crack width, this is expected.The Rayleigh wave peak-peak amplitude is measured along each scan made across the crack to determine the magnitude of the resultant enhancement.

Figure 6.4 shows the measured peak-peak amplitude of the Rayleigh wave plotted as a function of scan distance, at various scan line positions relative to the centre of the aluminium bar (centre of the crack). The crack for this data is 5 mm deep, 20 mm wide, and inclined 25° to the surface. For comparison purposes, the traces are offset from the origin.Sharp peaks that correspond to Rayleigh wave enhancement are present up to 9 mm away from the centre of the crack along the bar width. No peak is observed for the measurement made at the edge of the crack, which is at 10 mm from the centre of the crack. Despite that, there is a small dip in the amplitude at the position of the crack (scan distance=130 mm), indicating the opening on the surface where the laser inteferometer does not detect any displacement. Furthermore, the enhancement peaks at the centre of the bar width and 5 mm from the centre have slightly different magnitudes. For the enhancement at 9 mm from the centre, which is 1 mm from the crack edge, the enhancement peak is lower in magnitude, as expected due to the diffraction of the ultrasonic wave round the crack edges.

The peak-peak amplitudes of the Rayleigh wave along the scan lines on this crack are plotted using a colour scale in Figure 6.5. The Y-axis is mirrored about the origin to give a picture of the enhancement across the crack width, and the figure only shows the

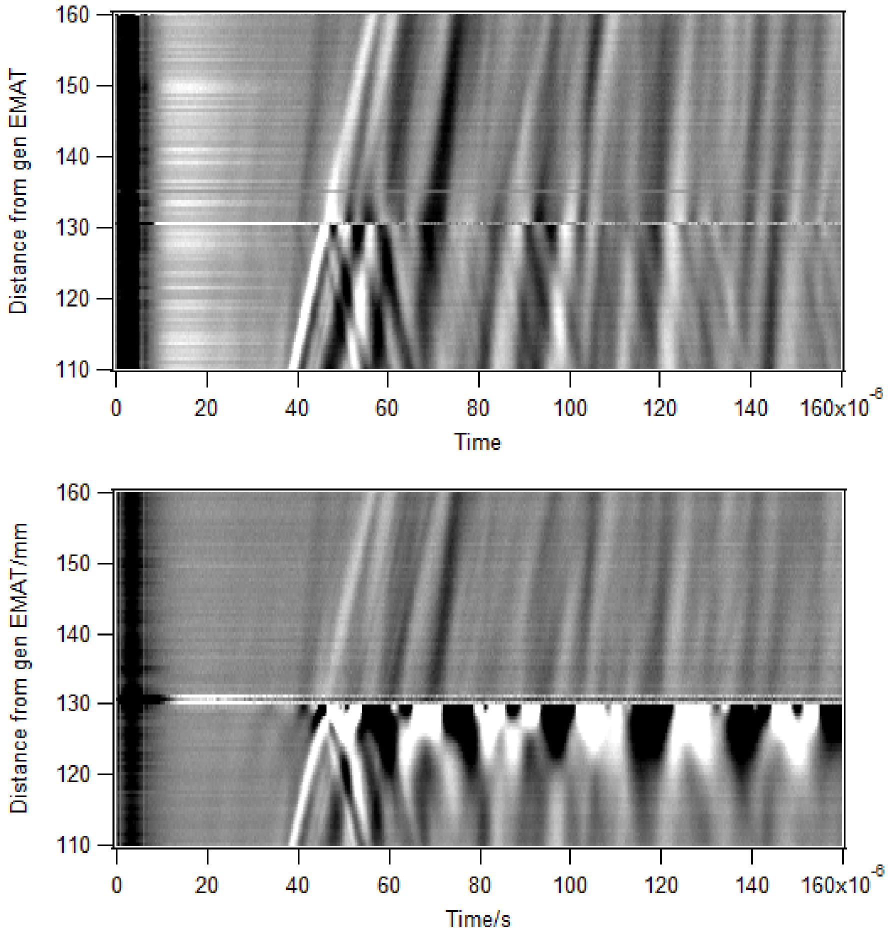

(a)

(b)

Figure 6.3: Enhancement observed from IOS measurement made across the centre of 5 mm deep, 20 mm wide cracks; (a) 90° and (a) 25°.

amplitude up to ±12 mm from the centre of the aluminium bar so that the enhancement is clear. Across the crack width, there is a small variation in the enhancement profile. High magnitudes, indicated by the blue/green colour, are observed in front of and very close to the crack. They are however, not perfectly uniform across the crack width. Theoretically, this should not be the case because the wavefront of the Rayleigh wave is approximately flat, when approaching the crack, and hence the enhancement profile should be uniform along the crack width, except when the detection is close to the edge of the crack. At this position, the enhancement is expected to be different as more of the wave can go round the edges, and therefore the reflection will be different. An explanation of the non-uniform profile shown by the enhancement can be done by considering experimental issues. Firstly, the EDM method used to machine the cracks can introduce roughness to the crack opening and the crack face. If this is the case it is also possible that the orientation of the crack may not be perfectly perpendicular to the main axis of the sample at all places, resulting in a slight tilting of the crack face to the incoming ultrasonic wave at certain positions. Secondly, another source of error could come from the motor used to scan the laser interferometer. A small change in the scan step could shift the detection point away from the position of the maximum enhancement along the scan line. Consequently, this would affect the enhancement profile.

Based on the enhancement plot shown in Figure 6.5, it is clear that the maximum amplitudes corresponding to the enhancement are not fixed at one position on the scan for the narrow-width cracks; this variation is again due to crack roughness, and errors from the motor. Therefore, to calculate the enhancement factor, F_E, it is important to find the maximum amplitude in the region close to the crack for each scan. This has been taken into account when calculating the enhancement factor for each crack using Equation 4.16. The enhancement factors calculated for each narrow-width crack are plotted as a function of the offset from the centre of the aluminium bar in Figure 6.7. The plots in the figure are grouped based on the crack width; (a) 10 mm and (b) 20 mm for 90° and 25° cracks. An obvious contrast between (a) and (b) is the widths of the enhancements, which reflect the widths of the actual cracks.

In order to compare the enhancement factors for 10 mm and 20 mm wide cracks, a single value from each crack width is required as a comparison value. Therefore, the average of the F_E values is chosen. There are two types of averaging calculation used here. The first one is a simple average of the F_E over the crack width to give a mesure of what is expected when using a small detection point. The second one takes the

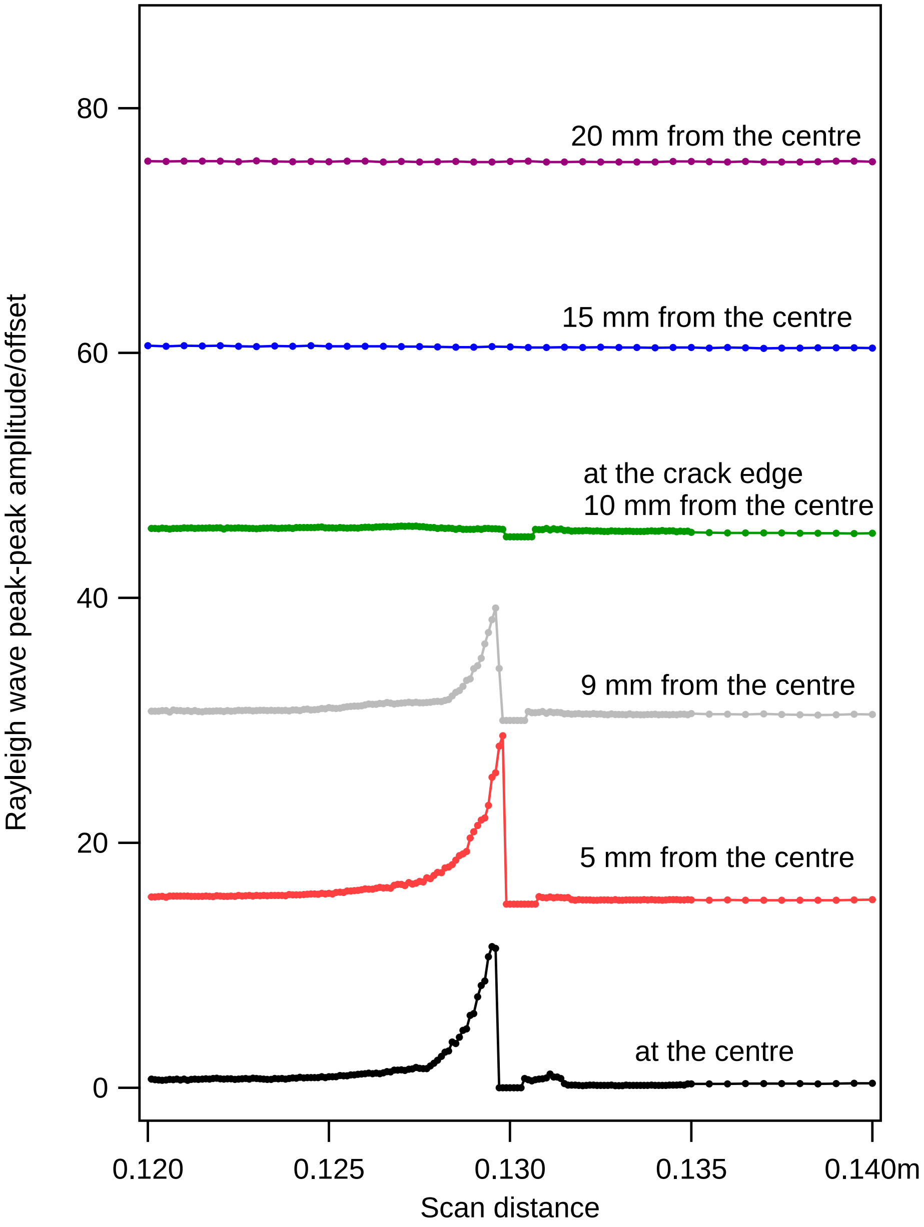

Figure 6.4: Rayleigh wave peak-peak amplitude as a function of scan distance at various position relative to the centre of the aluminium bar containing a 5 mm deep, 20 mm wide, 25° crack.

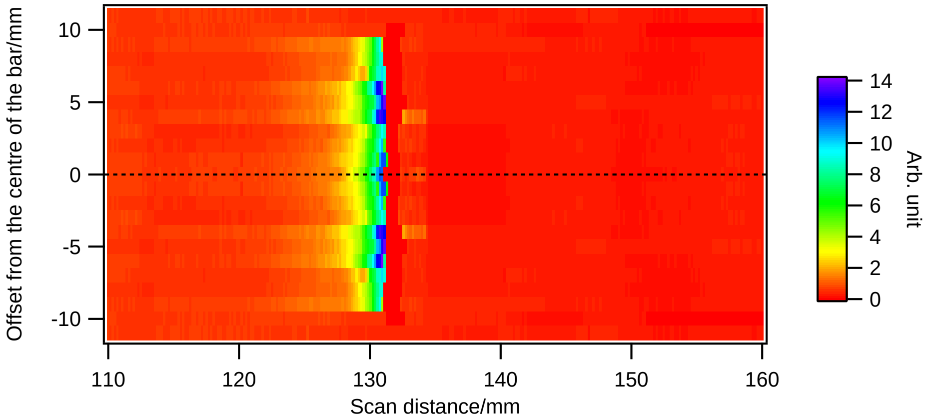

Figure 6.5: Rayleigh wave peak-peak amplitudes are plotted in colour scale to show the enhancement effects around a 5 mm deep, 20 mm wide 25° crack. The crack position is at scan distance=130 mm.

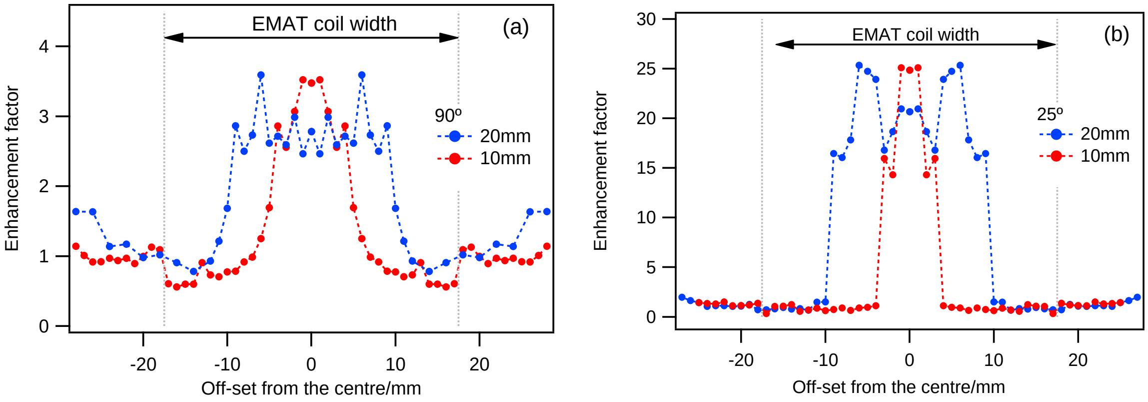

Figure 6.6: Enhancement factor across the 90° (a) and 25° (b) cracks with different widths.

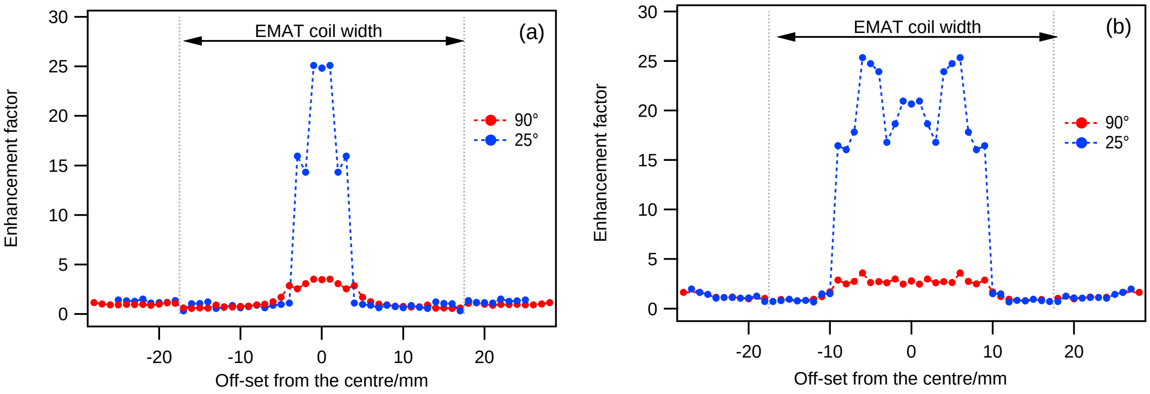

Figure 6.7: Enhancement factor for 90° and 25° cracks with crack width of (a)10 mm and (b) 20 mm. The x-axes show the offset from the centre of the aluminium bar.

	90°		25°	
Crack width	Crack width F_E	Coil width F_E	Crack widthF_E	Coil width F_E
10 mm	3.10 ± 0.40	1.48 ± 0.31	20.04 ± 5.80	5.10 ± 0.28
20 mm	2.80 ± 0.30	2.10 ± 0.36	20.14 ± 3.50	11.61 ± 0.34

Table 6.1: Average enhancement factors F_E calculated over crack width and EMAT coil width for 90° and 25° cracks of 10 mm and 20 mm crack widths.

average of all values over the width of the receiver EMAT coil, to give representation of the expected enhancement which would be measured using an EMAT. These average values are shown in Table 6.1. The EMAT coil has a finite area of generation and detection. For the case of detection discussed here, the EMAT receiver coil will see the enhancement as an overall effect within the detection area. As a results the detected signal is, in effect, an average of the total signal detected within the coil area when using the laser inteferometer. This is called the spatial averaging effect of the EMAT, which will be explained in Section 6.3. The average of F_E over the coil width is also shown in Table 6.1.

For 90° cracks, the crack width averages of F_E for 10 mm and 20 mm wide cracks are 3.10 ± 0.40 and 2.80 ±0.30 respectively. Meanwhile, for 25° cracks, the crack width average of F_E are 20.04 ±5.80 and 20.14 ±3.50, for 10 mm and 20 mm wide cracks.The values for the 90° cracks are in agreement within errors, and similar case is observed for the 25° cracks. For the coil width averages of F_E, the value for 10 mm and 20 mm wide 90° cracks are 1.48 ± 0.31 and 2.10 ±0.36 respectively. For the 25° cracks, the values are 5.10 ± 0.28 and 11.61 ±0.34.

Based on these values, cracks with the same depth and inclination from the surface, but with different width, will have approximately the same enhancement factor when measured with a small detection point compared to the crack width. Therefore, the distinction between normal and inclined cracks can be made based on the enhancement factor, in addition to the prominent enhancement pattern shown in the B-scan (Figure 6.3). However, the distinction does not hold when the detector has a large finite size compared to the width, in this case the coil of the EMAT receiver. As shown in Table 6.1, the average F_E over the coil width for 90° cracks shows a small difference of 0.74 between cracks of width 10 mm and 20 mm. This difference however escalates to 6.51 for 25° cracks. The average F_E over the EMAT coil width is therefore expected to increase with the size of the crack width.

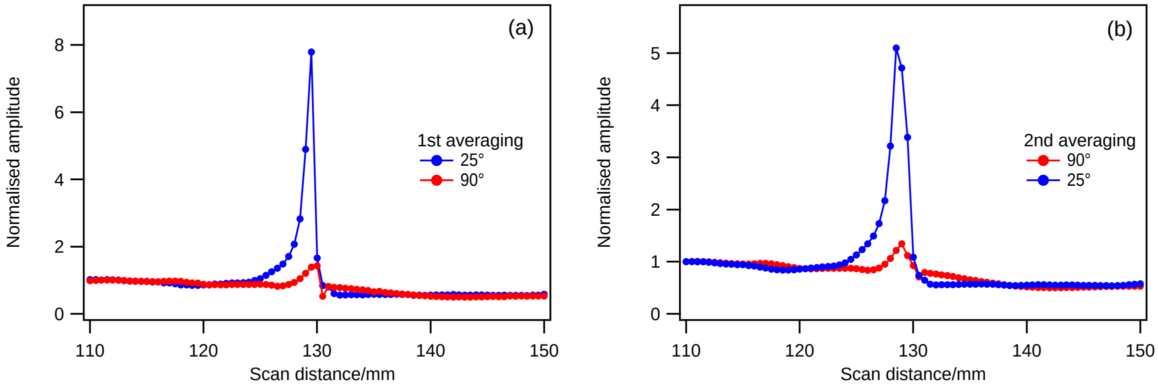

Figure 6.8: First (a) and second (b) steps of spatial averaging analysis on 5 mm deep, 20 mm wide cracks of two inclinations to the surface: 90° and 25°.

6.3 Spatial averaging effect

An ultrasonic receiver with a finite area of detection will have a spatial resolution similar to the size of the detection area. This is known as the spatial averaging effect. A measurement made using EMATs for detection can suffer from this effect, due to the finite size of the coil used in the EMAT. In this section, the spatial averaging effect for the EMAT measurements of narrow-width cracks is investigated by considering the area covered by the EMAT during a scan on an aluminium bar. Surface displacement measurements made using the laser interferometer are used to compare with the EMAT measurements.

A scan made using a linear EMAT coil can be viewed as a rectangular detection area moved along the sample surface containing a crack. At each position during the scan, the rectangle detects the majority of the signals within the area and effectively calculates the average. Also, as it moves along during the scan, for small scan steps it continually overlaps partially the previous area. In order to use the Rayleigh wave peak-peak amplitude data from laser measurements and compare to the EMAT measurement, two averaging steps need to be done. The first step is to average the Rayleigh wave peak-peak amplitude data from the laser measurements along the width of the sample, over a distance equivalent to the horizontal length of the EMAT coil, which is 35 mm (parallel to the crack). In the second step, an average of the peak-peak amplitude (Figure 6.8 and 6.9) within the width of the EMAT (1.5 mm) is calculated at each scan step (0.1 mm). The resultant average at each scan point consists of the data from previous scan steps, and thus they overlap.

Crack width	90° crack	25° crack
10 mm	1.23	2.27
20 mm	1.34	5.10

Figure 6.10: Enhancement factors F_E calculated for 90° and 25° cracks with 10 mm and 20 mm crack widths after second step of spatial averaging analysis.

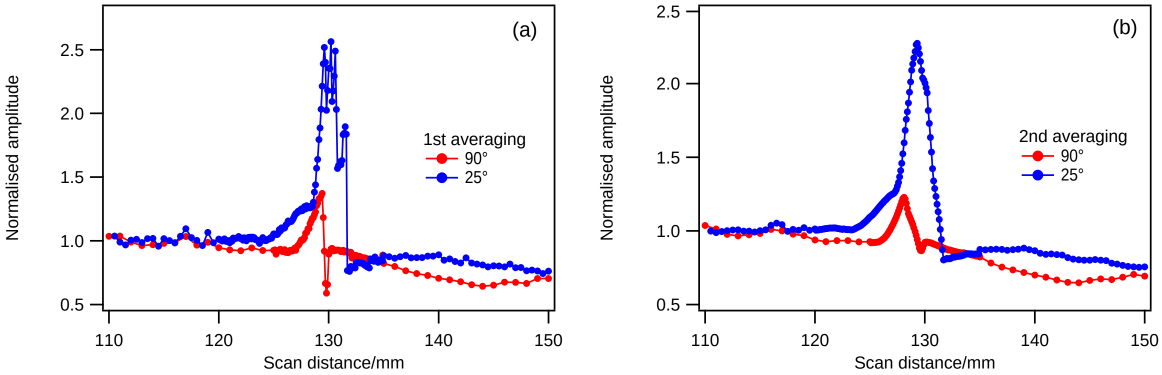

Figure 6.9: First (a) and second (b) steps of spatial averaging analysis on 5 mm deep, 10 mm wide cracks of two inclinations to the surface: 90° and 25°.

The results of the two-step averaging are shown in Figure 6.8 for 20 mm wide cracks and in Figure 6.9 for 10 mm wide cracks. Plot (a) in each figure shows the results after the first step of averaging, and plot (b) in each figure shows the results after the second step of averaging. In Figure 6.8(a), after the first step of averaging was applied, the 90° and 25° cracks have an F_E value of 1.43 and 7.80 respectively. These values drop to 1.34 and 5.10 respectively, when the second step of averaging is applied. For the case of 10 mm wide cracks (Figure 6.9), in the first step the F_E values for the 90° and 25° crack are 1.37 and 2.56 respectively. The values drop slightly, as shown in (b), when the second step of averaging is applied. For wide crack (20 mm), the change in F_E after the second step of averaging is large, compared to narrower crack (10 mm), particularly for the inclined crack (25°). The value of F_E for each crack after the second spatial averaging analysis is summarised in Table 6.10

The F_E values shown in the Table 6.1 agree with what is expected for 90° and 25° cracks. Inclined cracks (25°) should have higher enhancement compared to normal cracks (90°). In terms of crack widths, cracks with bigger width is expected to give higher enhancement compared to smaller width cracks.

6.4 Comparison of EMAT measurements on cracks with different widths

In order to test the viability of EMAT measurements to detect and characterise realistic cracks, a set of scans have been made on the narrow-width cracks using an EMAT transmitter and an out-of-plane receiver EMAT, using the configuration described in Figure 3.9(b) in Section 3.3. The centre line of the EMATs is kept at the centre of the aluminium bar when scanning along the bar, perpendicular to the cracks. Figures 6.11 and 6.12 show the B-scans generated for 90° and 25° cracks of widths 10 mm and 20 mm. The prominent alternating black and white enhancement pattern for inclined cracks is observed for the 25° cracks in (b) in each figure. This confirms that the EMATs which were used for full-width cracks (Chapter 4) are still able to detect crack with smaller width (smaller than the width of EMAT coil), and indicate the orientation (normal/inclined) of the crack. The enhancement pattern expected for 90° crack is also observed for the 10 mm and 20 mm wide 90° cracks, as shown in Figures 6.11(a) and 6.12(a).

The Rayleigh wave peak-peak amplitude was measured at each scan point, and plotted as a function of scan distance relative to the crack position. Figures 6.13 and 6.14 show the comparison of the amplitude measured for the narrow-width cracks and the full-width cracks (Chapter 4). The amplitudes here have been normalised to their respective reference amplitudes, to make them convenient for comparison. Figure 6.13 shows the comparison for 90° cracks (cracks normal to the surface) with crack widths of 10 mm, 20 mm and full-width across the bar width. There is a clear difference in the transmitted amplitude in the positive distance, for the three different crack widths. As the crack widths get larger, the transmission becomes lower; wider cracks block more of the Rayleigh wave from propagating around the crack, compared to smaller width crack, therefore the transmission is higher for small-width cracks. This has been shown earlier in the diffraction of waves around the 90° crack in Figure 6.1, where the Rayleigh waves can be transmitted around the edges of the cracks. This is also the case for the transmission on inclined cracks shown in Figure 6.14. The inclined cracks shown here are at slightly different inclinations to the surface, where the full-width data was taken for 22.5°, and narrow-width for 25°. However, they are acceptable for comparison as the difference in expected Rayleigh transmission for 22.5° and 25° cracks is small, as shown in Figure 4.8. The stronger enhancement for the inclined cracks somehwhat hides the

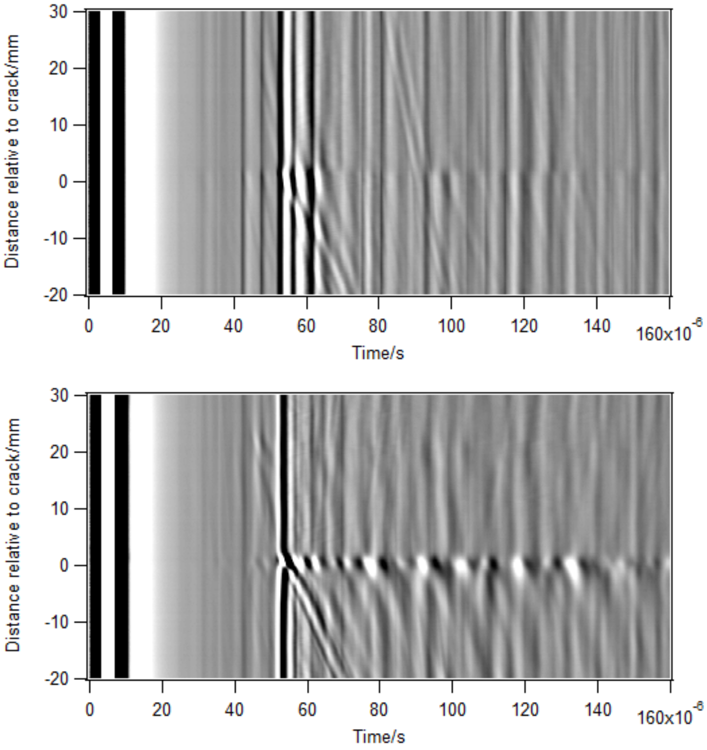

(a)

(b)

Figure 6.11: Enhancement observed from outof-plane EMATs measurement made across the 5 mm deep, 10 mm wide cracks; (a) 90° and (a) 25°.

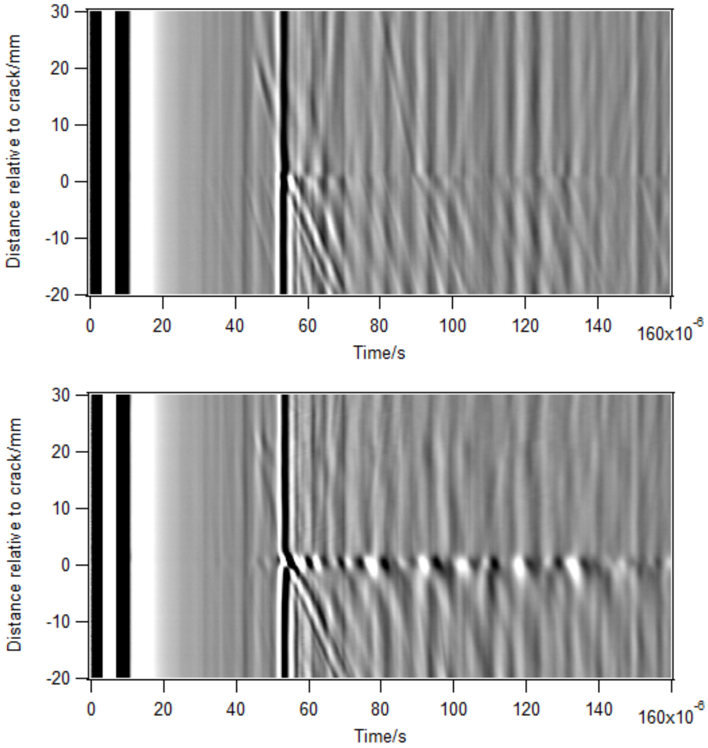

Figure 6.12: Enhancement observed from outof-plane EMATs measurement made across the 5 mm deep, 20 mm wide cracks; (a) 90° and (a) 25°

transmission part of the plot, showing the expected small differences in transmission for the different widths.

The enhancement observed for 90° cracks in Figure 6.13 shows that the enhancement factor F_E (maximum normalised amplitude) is approximately the same for full-width and 10 mm wide cracks, but smaller for 20 mm wide crack. However, as the crack width increases from 10 mm to full-width one would expect the value of F_E to increase. This means that the F_E value for 10 mm crack width should be lower than the value for 20 mm crack width as opposed to what has been observed. It is worth noting however that the transmission behaves as expected. To explain this disagreement, the incident Rayleigh wave in the B-scans (Figures 6.11 and 6.12) must be referred to. In these B-scans, the Rayleigh wave profile is the same, except for 90° crack with 10 mm width (Figure 6.11), where the wave appears broader; there is a wave mode arriving immediately after the Rayleigh wave. The wave could possibly be a reflection from one end of the sample as the crack is located close to one end. It is also possible that the wave could be a mode converted bulk wave, generated at the bottom of the sample. This wave may be affecting the measured Rayleigh wave peak-peak amplitude. Therefore, the normalised peak-peak amplitude for the 90° crack with 10 mm width may be higher in general compared to the other cracks in used, resulting in a higher F_E value.

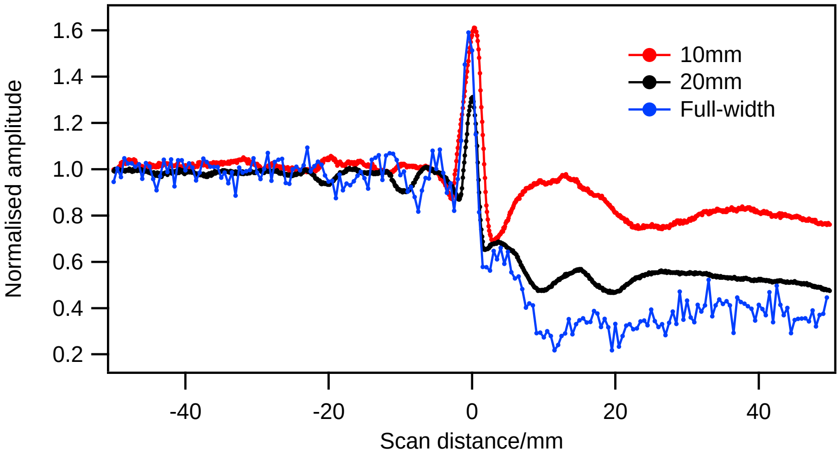

Figure 6.13: Plot of normalised Rayleigh wave peak-peak amplitude as a function of scan distance using out-of-plane EMAT measurements on 5 mm deep 90° cracks of different widths; 10 mm, 20 mm and full-width. The origin indicates the position of the cracks.

Figure 6.14 shows the enhancement observed for the 22.5° (full-width) and 25° (10 mm and 20 mm widths) cracks. Only 22.5° crack is experimentally available for full-width crack, therefore it is used for 25° crack comparison. In Figure 6.14, the relation between the crack width and the F_E value is clear; the F_E value increases with the crack width. The values are 1.75 (10 mm), 3.67 (20 mm), and 5.05 (full-width). These F_E values are higher than the value for full-width 90° crack (Figure 6.13) as expected. In terms of practical application for normal/inclined crack classification, the F_E value can be used. A simple rule could dictate that, a crack that produces a high F_E would be an inclined crack, and a crack that produces a lower value would be a normal (90°) crack.

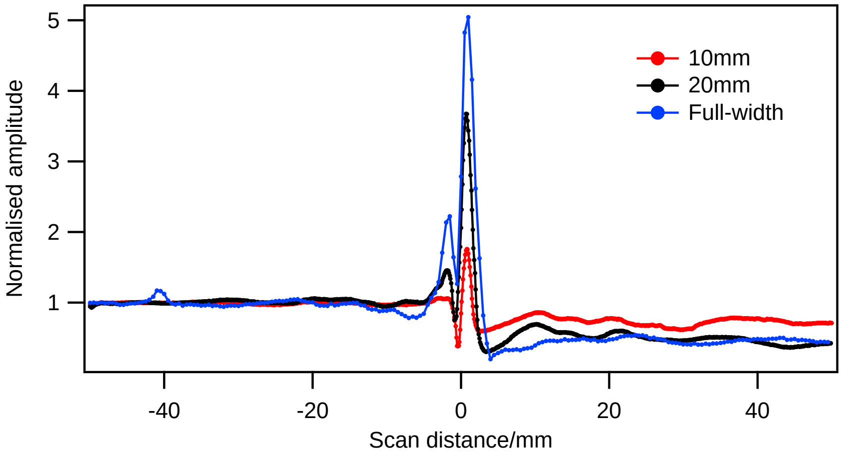

Figure 6.14: Plot of normalised Rayleigh wave peak-peak amplitude as a function of scan distance using out-of-plane EMAT measurements on 5 mm deep 25° cracks of 10 mm and 20 mm widths, and on a 5 mm deep 22.5° crack with full-width. The origin indicates the position of the cracks.

6.5 Conclusions

For narrow-width cracks, the Rayleigh wave can transmit not only underneath the crack, as is the case for full-width cracks, but also around the edges of the crack, as shown in Figures 6.1 and 6.2. The transmission was used to estimate the crack vertical depth, as explained in Chapter 4, however, with the presence of the transmission around the edges, a depth estimate which is based on the calibration on full-width cracks will not necessarily be accurate. However, measurements made using EMATs can still be used to detect the presence of defects based on the drop in Rayleigh wave transmisison, and determine whether the crack is normal or inclined based on the enhancement pattern near the crack as shown in Figures 6.11 and 6.12, with an approximate depth given by the transmission.

The issue of the variation in the Rayleigh wave transmission for different crack widths can be overcomed if the typical crack width, sometimes refered to as surface length, is known, and the EMAT is made based on this information. The variation in the Rayleigh wave transmission was greatest where the crack width was smaller than the horizontal length of the EMAT coil. Therefore, for practical use, a smaller EMAT can be made to avoid this variation and reduce error in the depth estimation. The size of the EMAT has to be smaller than the typical crack width, to replicate the results from full-width cracks (Chapter 4). However, the EMAT should not be too small such that the signal-to-noise ratio is large. A trade off between the typical crack width and signal-to-noise ratio has to be considered when building EMATs for particular applications in characterising surface cracks. The EMAT used here was made based on the size of standard commercially available magnets. For real applications, a custom made magnet can be chosen, thus the size of the EMAT can be tailored. This study has explored the possibility of using EMATs for crack detection following the underlying scientific understanding, and has proven that it is viable.

Chapter 7

Rayleigh wave interaction with branched surface cracks: an FEA model approach

Branching is one of the main features of surface breaking cracks, as discussed in Section 1.5 [3]. This can be associated with high risk to the structure, which requires immediate action to be taken, if the cracking can be detected. Branched cracking can be more severe than simple defects as the cracking can grow in more than one direction. This chapter discusses different types of branch geometry in surface cracks and their corresponding interaction with surface ultrasonic waves, with the most relevant geometry for rolling contact fatigue (RCF) considered. This is due to the requirement of the rail industry for detecting these type of cracks, and also a continuation from the earlier study presented in Chapter 4. Rayleigh wave interaction with this crack geometry is modelled using finite element analysis (FEA), results from the model are presented and discussed. Results from the analyses performed on the model data show useful features that can be used to determine the presence and the size of the branch when using B-scans. The presence of the branch can affect transmission of the Rayleigh wave, and this is discussed with a view for accurate depth estimation. A number of suggestions are made for practical applications and possible future work.

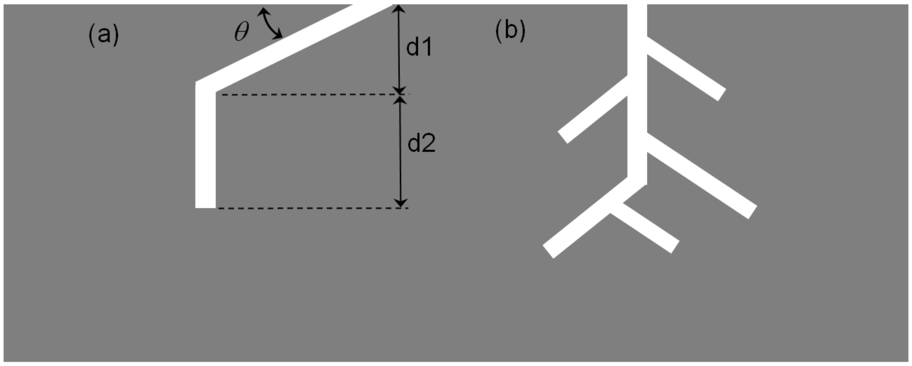

Figure 7.1: Simplified geometry of surface breaking cracks. (a) Rolling contact fatigue and (b) Stress corrosion cracking.

7.1 Consideration of the geometry of branched crack

Real surface cracks can have a complicated geometry, as described in Section 1.5. They can initially grow normal to the surface, or at an angle from the surface. In both situations, the cracks may then grow branches. Figure 7.1 shows a simplified geometry for two types of branched cracks that pose a real challenge in NDE. The geometry shown in Figure 7.1(a) depicts a rolling contact fatigue (RCF) crack, and the geometry shown in Figure 7.1(b) is to simulate the stress corrosion cracking (SCC). The RCF crack in (a) typically grows at an initial angle θ of 20°-30°, with branching starting at depths between 5 mm - 10 mm from the surface [3, 4, 47]. At these depths, the branch can either grow back to the surface, causing a section to spall, or grow vertically down to the bottom as depicted in Figure 7.1(a) [3]. Between the two possibilities, the latter is more dangerous because it is likely to break the rail. For SCC, branching can occur at any point along the main vertical crack, as shown in Figure 7.1(b), and each branch can grow more branches. The geometry of SCC is therefore more complicated to consider compared to the geometry of RCF cracks. An experimental and computer simulation work on the influence of SCC on ultrasonic examination has been reported in [128].

The simplified geometry of the RCF crack shown in 7.1(a) is considered in this chapter using a FEA model. The spalling of a section can cause damage to the rail surface, however, it is generally not considered as a serious defect as the section spalled is relatively small. If however, the RCF starts to grow into the rail, it is likely to break the rail. The results of this can cause trains to derail while moving at high speed [46]. If the crack can be detected and characterised as a serious defect, the section of rail

θ	d_1	d_2
15°	5	5,10,15
22.5°	3	1,3,5,7,10,15
	5	1,3,5,7,10,15
30°	3	1,3,5,7,10,15
	5	1,3,5,7,10,15

Table 7.1: List of branched cracks modelled in FEA with geometry specified by θ, d_1, and d_2 (see Figure 7.1).

that contains the crack can be removed and replaced. Thus, the capability to identify branches in RCF cracks is one of the main priorities in the crack characterisation process on rail. The earlier work presented on inclined full-width cracks in Chapter 4 has laid good foundations for this study. Once the interaction of Rayleigh waves with inclined cracks has been understood, the complexity of the problem can be increased by adding the branch feature. This is a step towards characterising real cracks.

The FEA model used for modelling inclined cracks has been extended by adding a vertical slot at the bottom tip of the inclined crack to follow the geometry of RCF crack shown in Figure 7.1(a). The length of the branch from the tip is labelled as d_2. The thickness of the branch is set to match the thickness of the main crack, so that the whole crack has constant thickness. In the FEA model, the values of θ, d_1 and d_2 are varied within the limit of typical RCF cracks. The model was computed in two-dimension, similar to the full-width crack in Chapter 4. The list of all branched cracks modelled is shown in Table 7.1. The effects of varying these values on Rayleigh wave propagation are analysed.

7.2 FEA model results

The results for the crack with θ=22.5°, d_1=5 mm, and d_2=5 mm are shown in Figure 7.2 and Figure 7.3 for out-of-plane and in-plane velocities respectively. The subfigures (a), (b), (c), (d) and (e) in each figure show the interactions at the same instances in time. The images in Figure 7.2 and Figure 7.3 do not show the actual size of the whole model, but have been enlarged to focus on displaying the wave velocities around the branched crack. Hence, the generation source and its position are not shown in the figures. The magnitude of the wave velocity is indicated by the colour scheme, which is set to autoscale at each time instance.

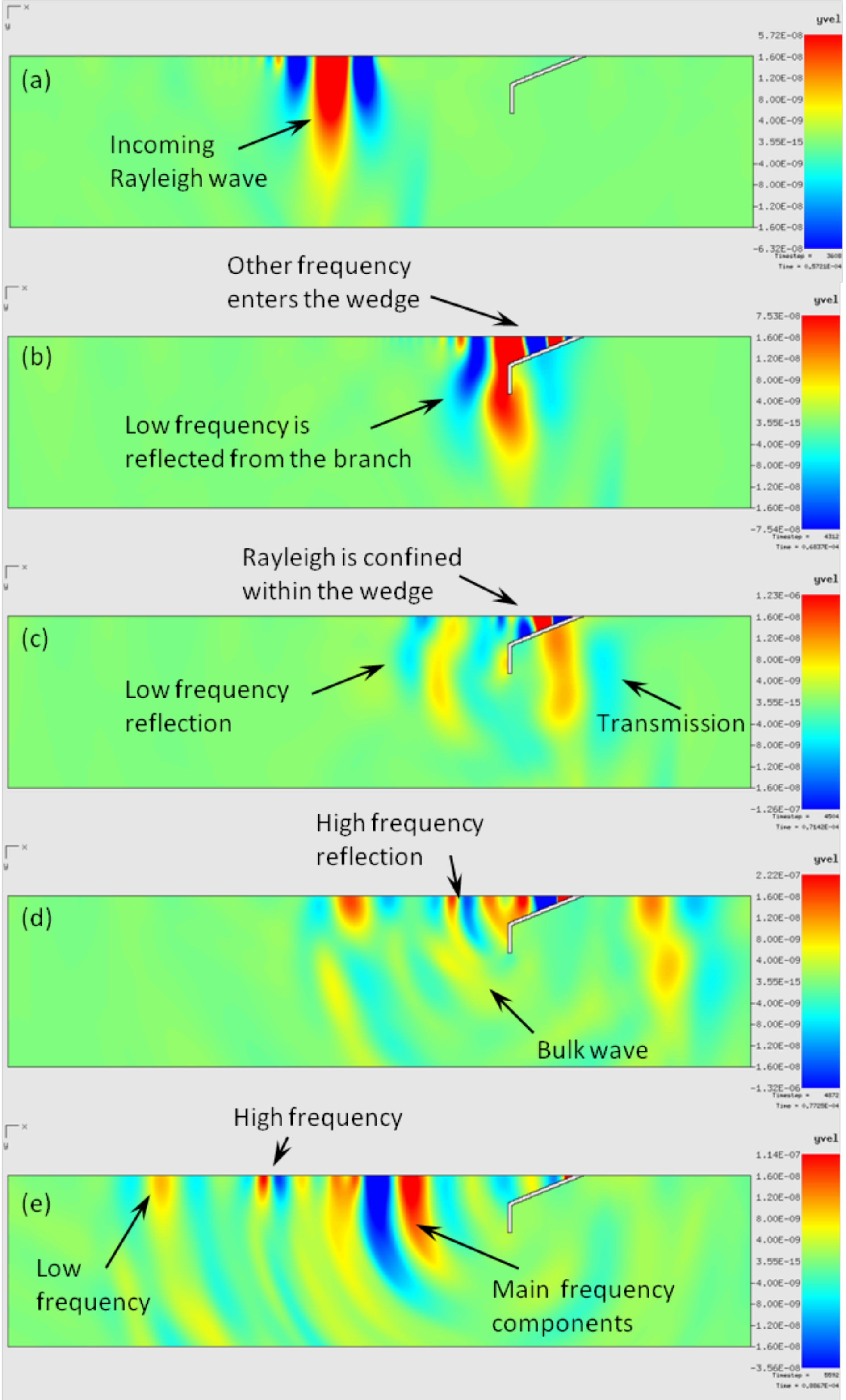

Figure 7.2: FEA showing the interaction of out-of-plane Rayleigh wave velocity with 5 mm deep 22.5° crack with a branch of 5 mm in length.

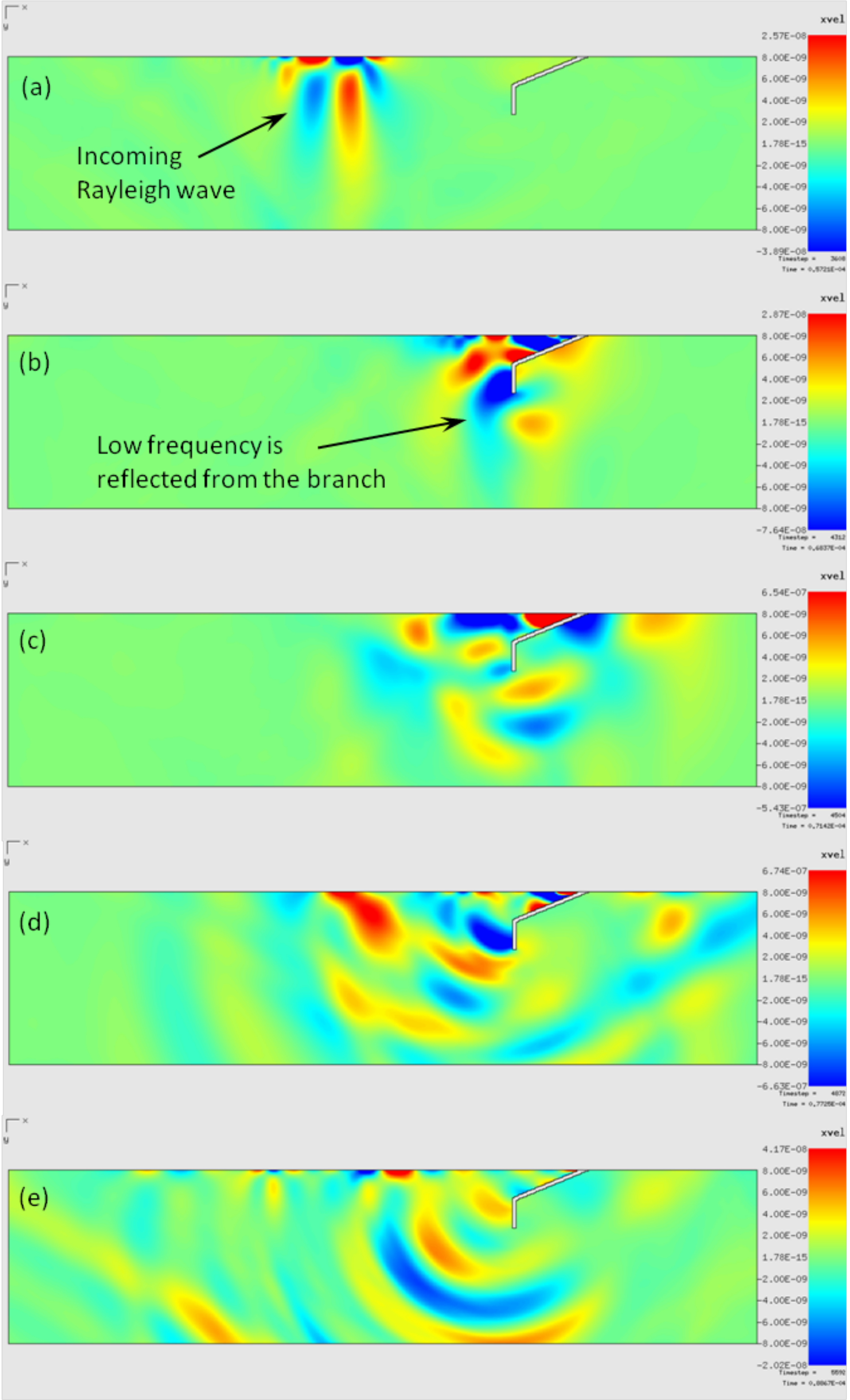

Figure 7.3: FEA showing the interaction of in-plane Rayleigh wave velocity with 5 mm deep 22.5° crack with a branch of 5 mm in length

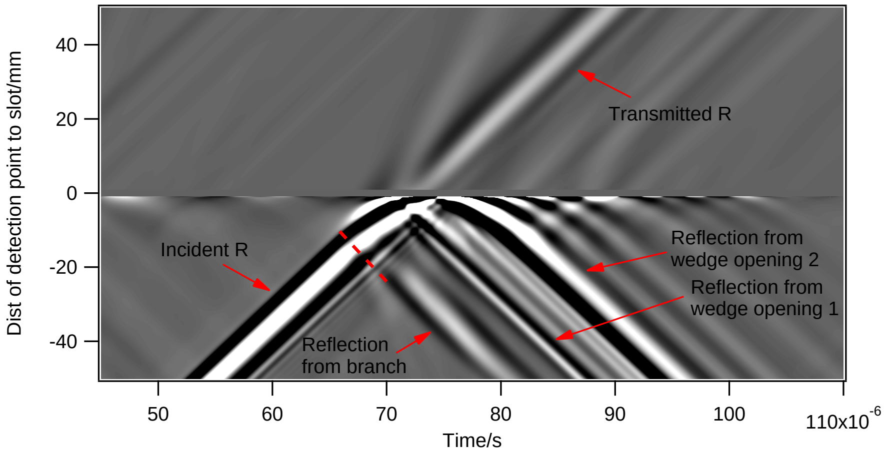

Figure 7.4: B-scan of a modelled branched crack with θ= 22.5°, d_1= 5 mm, and d_2= 5 mm. The greyscale shows the magnitude of the out-of-plane velocity component. R denotes the Rayleigh wave.

Figure 7.2(a) shows an incident Rayleigh wave approaching the crack. The generated Rayleigh wave is broadband in nature and was based on experimental EMAT generation described in Section 3.6. As expected, most of the energy is confined within one wavelength below the surface [53].

In Figure 7.2(b), the interaction of the Rayleigh wave with the crack starts to take place, as some of the low frequency components of the Rayleigh wave, which penetrate deeper into the sample are reflected from the branch, and some are transmitted. Meanwhile, the remaining wave energy enters the wedge section formed by the inclined part of the crack. A B-scan of the model data presented here is shown in Figure 7.4. The B-scan is labelled with the incident, transmitted and reflected Rayleigh waves only for the convenience of describing the Rayleigh wave interaction. Detailed analysis of wave mode arrival times and mode conversion will be presented in Section 7.3. The incident Rayleigh wave shown in Figure 7.2(a), and the reflection from the branch (Figure 7.2(b)) are identified in the B-scan. These two wave modes interfere at a distance in front of the crack opening, as indicated by the red dashed line in the B-scan. Therefore, the position of the branch along the scan path can be determined from the B-scan.

As the interaction progresses, as shown in Figure 7.2(c), the low frequency reflections propagate away from the defect, with the reflection travelling at the same speed as the incident Rayleigh wave. This is confirmed by the B-scan (Figure 7.4), where the reflection has a negative slope given by velocity of the incident Rayleigh wave. Some of the low frequency components are also transmitted to the other side of the branch, propagating underneath the inclined part of the crack, with the transmission of the Rayleigh wave dependant on the total crack depth. The B-scan shows the transmitted Rayleigh wave is much fainter than the incident wave, indicating a drop in amplitude. The components of the Rayleigh wave that enter the wedge section now become dispersive, due to the change in the local thickness within the wedge, with mode-conversion to Lamb-like waves, as explained in Section 4.4. In the B-scan, the alternating black and white enhancement pattern at the position of the crack opening indicates this dispersion.

Figure 7.2(d) shows reflections of the wave energy which entered the wedge section. A high frequency component is reflected at the tip of the wedge, and continues propagating with close to the Rayleigh wave speed for the majority of the wedge. The rest of the wave energy, which has undergone mode conversion throughout the wedge, are now also reflected from the wedge tip. When these waves hit the corner between the inclined section and the branch, some of the waves are mode converted to bulk waves, as indicated in Figure 7.2(d). A surface skimming longitudinal wave is also generated at the corner and travels down to the bottom tip of the crack. At this stage, the low frequency transmitted wave has fully recovered from the interaction, and continues propagating along the surface.

Figure 7.2(e) shows a snapshot after the interaction has taken place. As the reflected Lamb-like waves exit the wedge and enter the full thickness of the modelled aluminium bar, they are mode converted back into Rayleigh waves. This Rayleigh wave contains most of the main frequency component of the incident Rayleigh wave shown in Figure 7.2(a), but now with a more spread-out pattern. The interaction results in three groups of Rayleigh wave reflections from the crack, which are separated from each other in terms of their arrival time. This is also shown clearly in the B-scan (Figure 7.4). Each group is associated with different frequency components of the Rayleigh wave and reflections from different parts of the branched crack.

In order to validate the frequency content of the Rayleigh wave reflections, a spectrogram was computed for the data recorded at distance = -50 mm in the B-scan (Figure 7.4). At this distance from the crack, the reflected Rayleigh wave has recovered from any mode conversion to Lamb-like waves it may have experienced in the wedge section, and thus it is convenient to separate the different groups of reflections. The spectrogram was computed following the same procedure for a non-branch 5 mm deep, 22.5° crack described in Section 4.4. Figure 7.5 shows the computed spectrogram, with the A-scan shown underneath. The incident Rayleigh wave arrives at 52 μs and shows

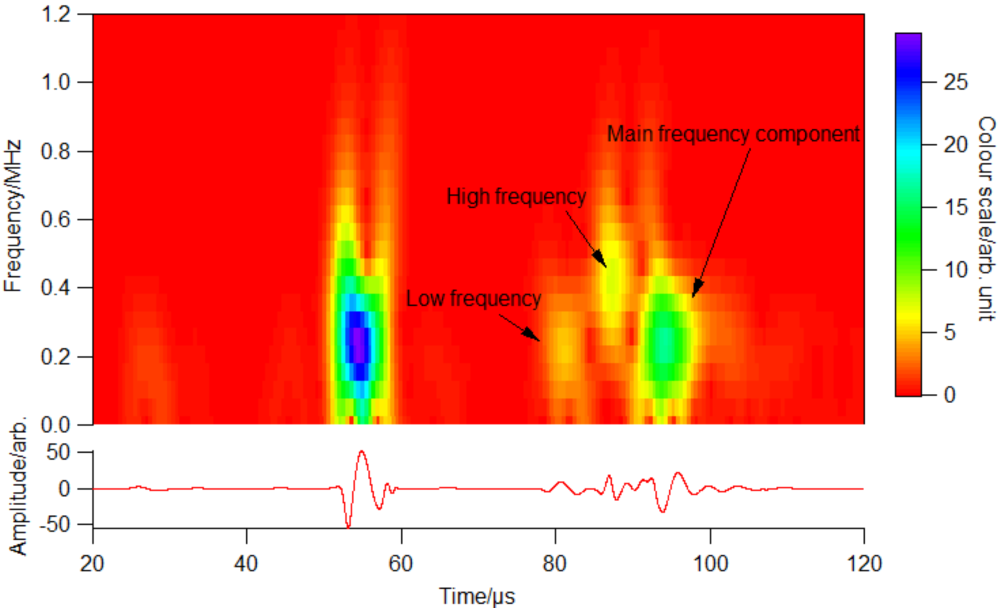

Figure 7.5: Spectrogram (top) of the out-of-plane velocity signal (bottom) at -50 mm from a 5 mm deep 22.5° crack with 5 mm branch.

all generated frequency content. The first reflection, assigned to be a low frequency reflection from the branch, arrives at approximately 78 μs and, as expected, consists of mostly low frequency components. This appears as faint yellow, indicating low magnitude, in good agreement with the model snapshots shown in Figure 7.2(e).

Following the reflection from the branch, the first reflection from the wedge section arrives approximately at 86 μs. This has mostly high frequency content, with higher magnitude compared to the earlier reflection. This reflection also shows a good agreement with the observation made on Figure 7.2(e). Finally, the second reflection from the wedge section, which starts to arrive at approximately 93 μs and shows a slight broadening compared to the indicent wave, shows the rest of the frequency content of the reflected Rayleigh wave. This reflection exits the wedge as Lamb-like wave, but is mode converted back to a Rayleigh wave when entering the full thickness of the modelled aluminium bar. The mode conversion is due to the change in the product of the frequency-thickness of the wave.

This observation is rather interesting as it gives a potential technique for the detection and characterisation of the branch on RCF cracks considered here. One may argue that, two different groups of reflections with different arrival times, can also arise in the case of two closely spaced cracks of different depths, such as the example given

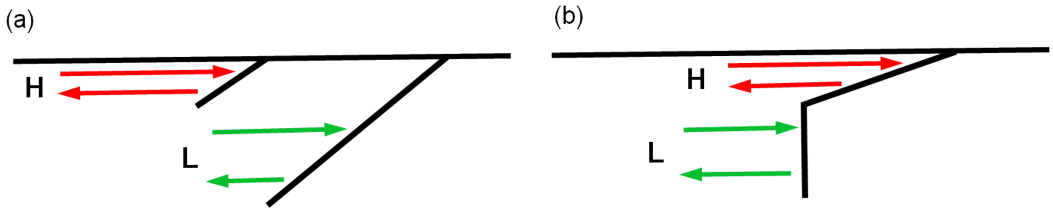

Figure 7.6: Difference between the Rayleigh wave reflected from (a) two closely spaced cracks with different depth, and from (b) a branched crack. The red arrow labelled with H represents the high frequency component and the green arrow labelled with L represents the low frequency components.

in Figure 7.6(a). Indeed, there certainly will be two groups of reflections, each associated with each crack. However, the reflection from each crack will have a frequency content dependent on the depth of each crack, and this will aso affect the arrival time. The shallow crack will reflect mostly high frequency components, with the remaining wave energy transmitted, and then reflected from the deep crack. The high frequency component reflection will therefore arrive earlier than the second, predominantly low frequency component. This is the opposite to the case of the branched crack shown in Figure 7.6(b), where the low frequency reflection from the branch arrives earlier than the high frequency reflection from the wedge section. To conclude, the distinction between two closely spaced cracks and a branched crack can be made by analysing the arrival time of each reflection in the frequency domain. For this purpose, the time-frequency representation method used, the spectrogram, is proven to be useful.

7.3 Analysis of Rayleigh wave reflections and mode-conversions

Based on the FEA model results, the wave modes present and generated during the interaction can be identified. The arrival time for each wave mode can be calculated by considering the travel path, either moving towards or moving away from the branched crack, and the instantaneous velocities (Section 4.1). Figure 7.7(a) shows the geometry of the crack and the position of the generation and detection points, with all distances identified. The generation point (Gen.) is fixed at a distance s from the crack opening, while the detection points are set at a distance x on either side of the crack. Det. 1 indicates the positions in front of the crack, which are assigned as negative distance, and the opposite is the case for Det. 2. $x1$, $x2$, and $x3$ are given by

$$x1 = \sqrt{(x - d_1/\tan\theta)^2 + (d_1 + d_2)^2} \tag{7.1}$$

$$x2 = \sqrt{(x + d_1/\tan\theta)^2 + (d_1 + d_2)^2} \tag{7.2}$$

$$x3 = \sqrt{(x - d_1/\tan\theta)^2 + d_1^2} \tag{7.3}$$

Travel paths for typical reflected, mode converted and transmitted waves are shown in Figure 7.7(b)-(g). In these figures, R denotes the Rayleigh wave, C denotes the longitudinal wave, and S denotes the shear wave. R/C indicates that the travel path is the same for Rayleigh and surface skimming longitudinal waves. The same applies to C/S. The Rayleigh waves mode conversion to Lamb-like waves in the wedge section of the crack is not shown in the figure, and is not covered in the calculation made in this section. The calculation of the arrival time of mode converted Lamb-like waves has been described in detail in Section 4.4. Here, only the high frequency and the low frequency components of Rayleigh waves are considered in the arrival time calculation, and each component is indicated H and L prefix respectively. The wave speed used for Rayleigh wave, c_R, is 2885 ms^{-1}, for longitudinal wave speed, c_l, is 6300ms^{-1}, and for shear wave, c_S, is 3110ms^{-1}. The arrival time of the incident Rayleigh wave is given by

$$t_{Ri} = (s - x)/c_R \tag{7.4}$$

Figure 7.7(b) shows the reflection of the high frequency component (labelledHRr) from the wedge section. The Rayleigh wave is reflected back in addition to the surface skimming longitudinal wave ($HRCr$). Their arrival time can be calculated using Equation 7.5 and 7.6.

$$t_{HRr} = (s + x)/c_R \tag{7.5}$$

$$t_{HRCr} = s/c_R + x/c_l \tag{7.6}$$

The arrival time of the low frequency component reflected (LRr) from the branch as shown in Figure 7.7(c) is given by

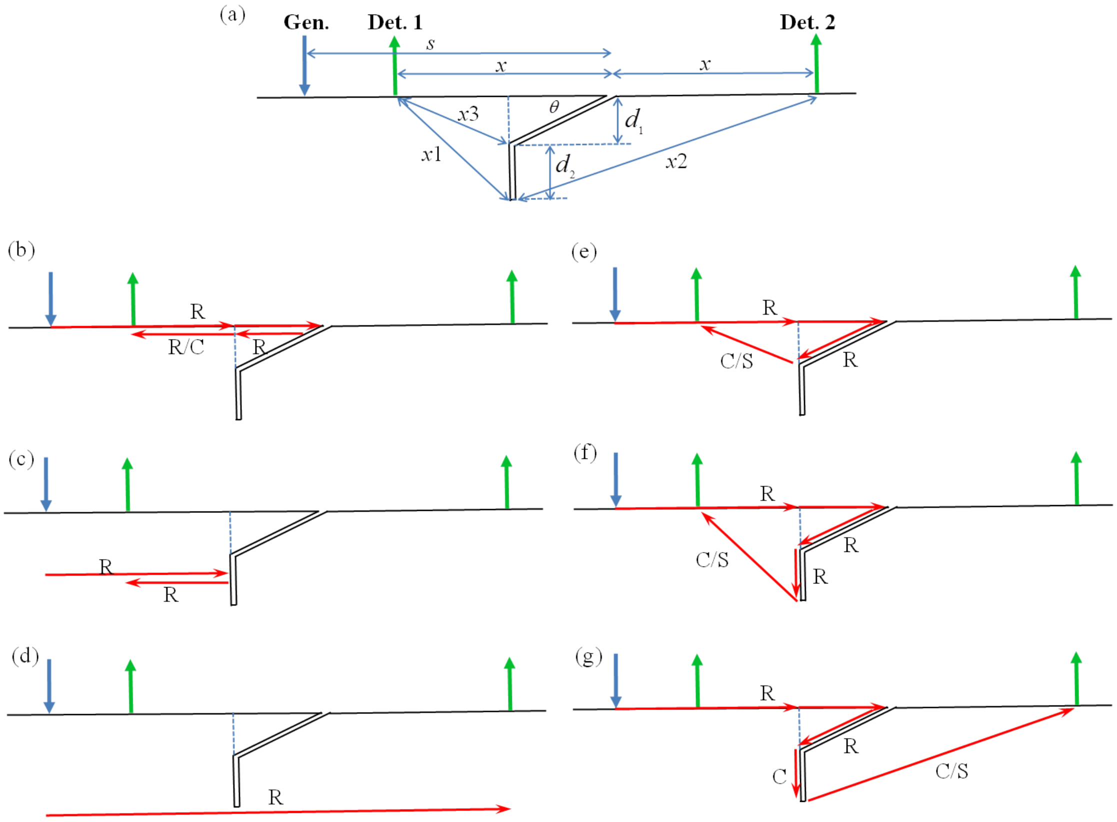

Figure 7.7: (a) Geometry of the modelled branched crack with generation (Gen.) and detection points (Det.1 and Det. 2). (b)-(g) Travel paths of waves reflected, transmitted and mode converted at the crack. R denotes Rayleigh wave, C denotes longitudinal wave, and S denotes shear wave.

$$t_{LRr} = (s + x - 2 \times (d1/\tan\theta))/c_R. \tag{7.7}$$

Some of the low frequency component (LRt) can transmit underneath the crack as shown in Figure 7.7(d), the arrival time of this wave mode is therefore

$$t_{LRt} = (s + x)/c_R. \tag{7.8}$$

For the mode conversion, longitudinal ($Cr0$) and and shear ($Sr0$) shown in Figure 7.7(e), the arrival time are

$$t_{Cr0} = s/c_R + (d_1/\sin\theta)/c_R + x3/c_l \tag{7.9}$$

and

$$t_{Sr0} = s/c_R + (d_1/\sin\theta)/c_R + x3/c_s \tag{7.10}$$

For the mode conversion shown in Figure 7.7(f) and (g), the arrival times of the longitudinal ($Cr1$ and $Ct1$) waves and the shear ($Sr1$ and $St1$) waves are as follows

$$t_{Cr1} = s/c_R + (d_1/\sin\theta)/c_R + d_2/c_R + x1/c_l \tag{7.11}$$

$$t_{Sr1} = s/c_R + (d_1/\sin\theta)/c_R + d_2/c_R + x1/c_s \tag{7.12}$$

$$t_{Ct1} = s/c_R + (d_1/\sin\theta)/c_R + d_2/c_R + x2/c_l \tag{7.13}$$

$$t_{St1} = s/c_R + (d_1/\sin\theta)/c_R + d_2/c_R + x2/c_s \tag{7.14}$$

Figure 7.8 shows the in-plane (a) and out-of-plane (b) B-scans for the crack with θ=22.5°, d_1=5 mm, and d_2=5 mm. The arrival times of the main wave modes described above were calculated using Equations 7.5-7.14, and appended as coloured lines on the B-scans. Longitudinal waves C, and shear waves S are labelled with subscripts "r" and "t" to indicate reflections and transmissions. The incident Rayleigh wave Ri interferes with its high frequency reflection (HRr) and mode-converted surface skimming longitudinal wave ($HRCr$) at the origin, which is the position of the crack. The low frequency reflection (LRr) on the other hand, interferes with the incident wave Ri at appoximately 12 mm in front of the crack (-12 mm on y-axis), when detection is at the position of the branch. Based on the grey scale on the B-scans, the amplitude of LRr is also lower than the other Rayleigh wave reflections. This can be seen clearly in the out-of-plane B-scan in Figure 7.8(b).

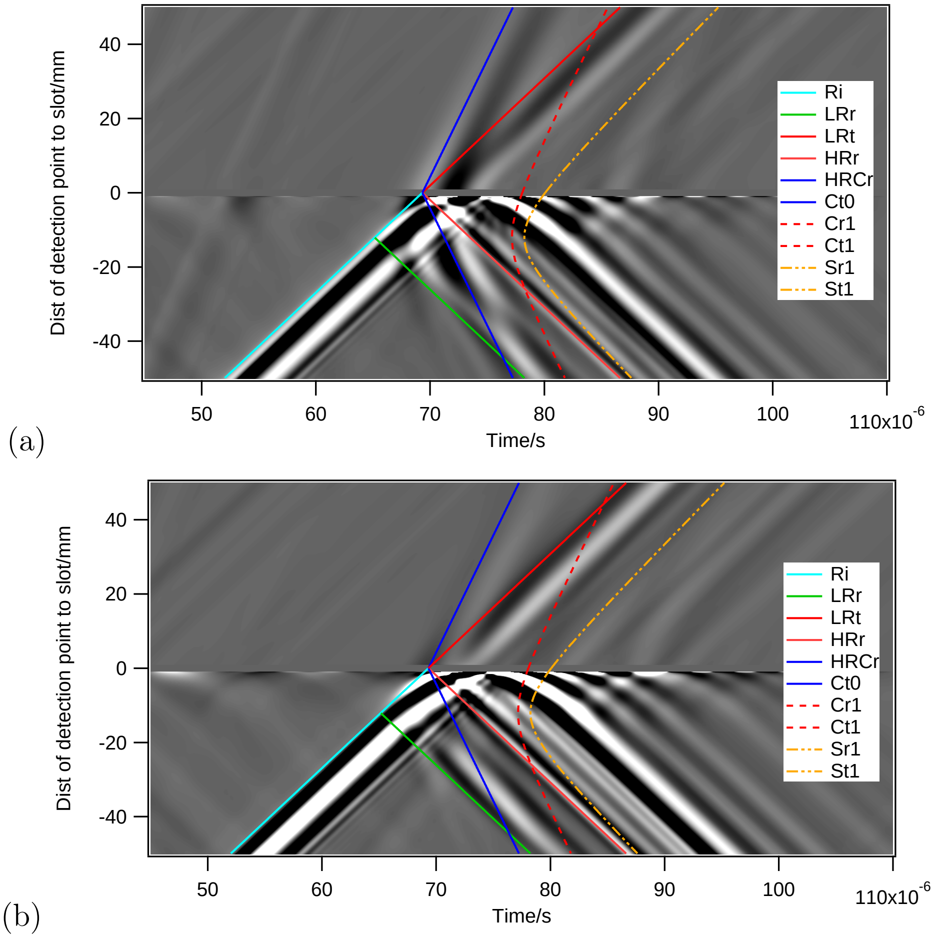

(a)

(b)

Figure 7.8: In-plane (a) and out-of-plane (b) velocity B-scans for Rayleigh interaction with 5 mm deep 22.5° crack with 5 mm branch.

In order to see the effects of the branch length on the low frequency Rayleigh wave reflection (LRr) (Figure 7.8), A-scans from 5 mm deep 22.5° cracks with different branch lengths (1 mm, 3 mm, 5 mm, 7 mm, and 10 mm) are plotted together in Figure 7.9 for in-plane (a) and out-of-plane (b) components. The A-scans are the data recorded at -40 mm distance to slot, in Figures 7.8. The low frequency Rayleigh wave reflections are indicated by the dashed box in each figure. In principal, a longer branch should reflect more of the incoming wave than a shorter branch [53]. This can be observed clearly for the out-of-plane A-scans in Figure 7.9(b). To accurately relate the relation between the reflection of this wave and the branch length, the peak-peak amplitudes were measured, and the reflection coefficients C_r were calculated using

$$C_r = \frac{A_r}{A_i} \tag{7.15}$$

where A_r is the reflected peak-peak amplitude and A_i is the reference peak-peak amplitude. C_r is plotted as a function of branch length in Figure 7.10 for in-plane and out-of-plane data. The general trend in both components shows that C_r increases as the branch length increases, which is in agreement with the expectation. There is a slight difference between the values of C_r between the two components. The in-plane component in general has higher C_r value compared to the out-of-plane component. As shown in the B-scan in Figure 7.8, the mode converted surface skimming longitudinal wave ($HRCr$) arrive fairly close to the low frequency Rayleigh wave reflection at positons further than -20 mm away from the slot. The reflected amplitude A_r was measured in this region, and therefore would be affected slightly. The effect would be greater in the in-plane component as the mode converted surface skimming longitudinal wave ($HRCr$) has mainly in-plane motion.

7.4 Effects of the branch length on Rayleigh wave transmission

When a branch starts growing from the tip of an inclined crack, it will increase the total depth of the crack from the sample surface. Consequently, the transmission of the Rayleigh wave propagating underneath the crack will change. As described in Section 4.2, the crack depth can be estimated from measurements of the transmission by comparing the value of the calculated transmission coefficient, C_t, to the correct depth calibration curve. For cracks close to 90°, the correct calibration is using the normal depth calibration, while for inclined cracks, the 45° calibration can give a reasonably good depth estimation (Section 5.2.1). However, for the case of branched cracks, the cracks consist of both normal and inclined parts, and the decision to choose one calibration over the other is not clear.

To study the effect of the branch length on the transmission, a 22.5° crack with d_1=5 mm was modelled with different branch lengths d_2. The values of d_2 used are

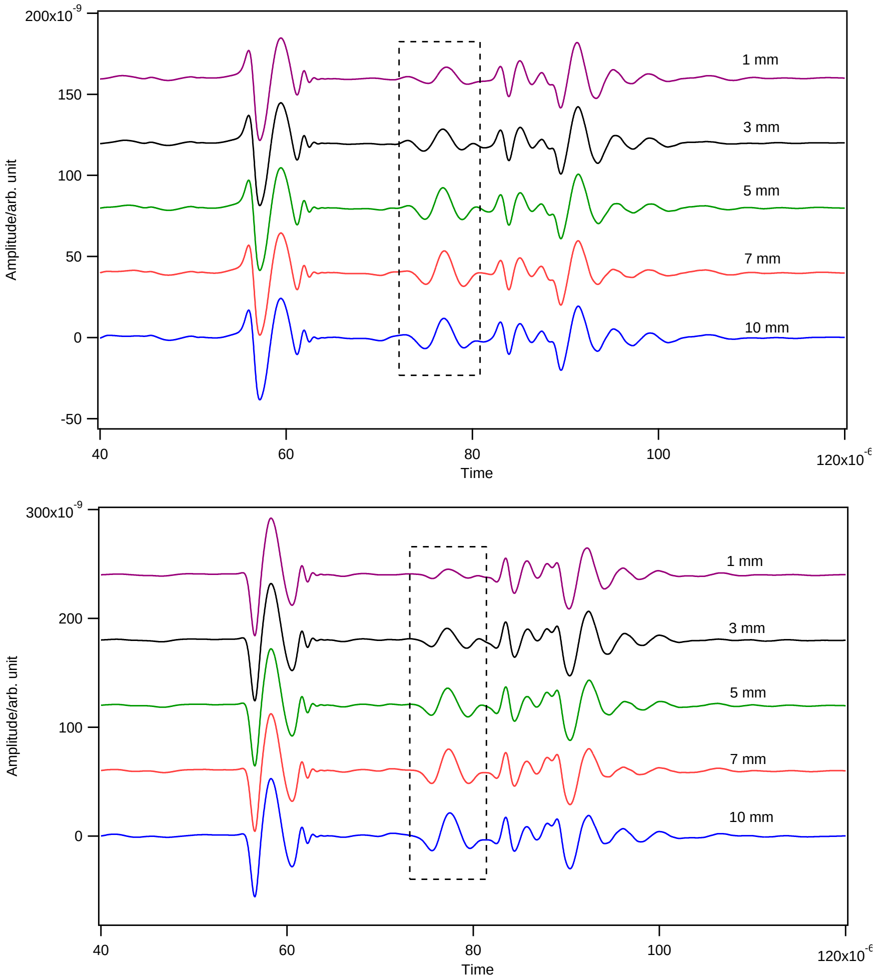

(a)

(b)

Figure 7.9: A-scans of 5 mm deep 22.5° crack for different branch length at -40 mm distance to slot. In-plane (a) and out-of-plane (b) data.

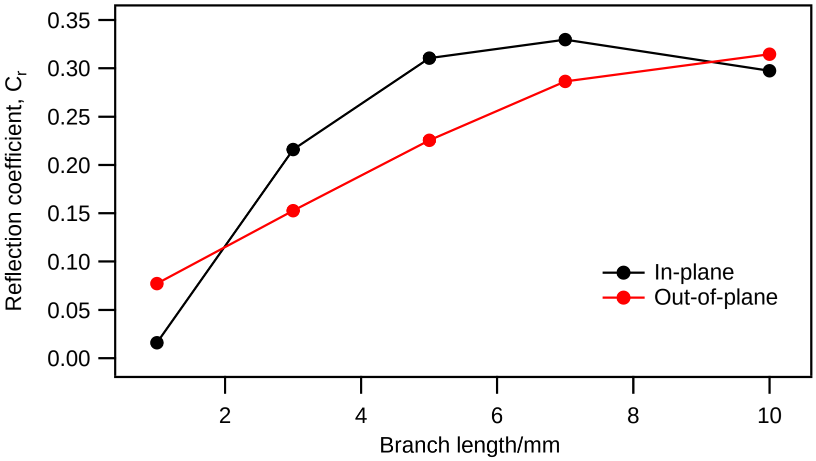

Figure 7.10: Reflection coefficient as a function of branch length for 22.5° 5 mm deep crack.

1, 3, 5, 7 and 10 mm, which makes the total depth of the crack 6, 8, 10, 12 and 15 mm respectively. The value of C_t was calculated for each crack using Equation 4.6 from Section 4.2. Figure 7.11 shows the calculated C_t appended onto the 90° and 45° calibration curves, with each calculated C_t from the branched crack labelled with the value of d_2. When d_2 is 1 mm, the calculated C_t is close to the 45° calibration. As the value of d_2 increases, C_t remains close to the 45° calibration, and eventually lies on the fit curve. When d_2=10, the total depth is 15 mm. At this stage, there is no practical difference between the two calibrations as the crack depth is larger than the central wavelength of the Rayleigh wave pulse (12.6 mm).

The C_t trend shown by the 22.5° crack with various branch lengths is rather interesting. As the length increases, one may expect that the transmission would be closer to the transmission from the 90° crack, since the branch grows vertically. However, the results show that, as the branch length gets longer, the transmission remains similar to the transmission from an inclined crack. The reason for this because the top part of the crack, which interacts with all frequencies, dominates the transmission. The bottom part of the crack (where the branch is) that is deeper than the central wavelength (12.6 mm) woud be less affected.

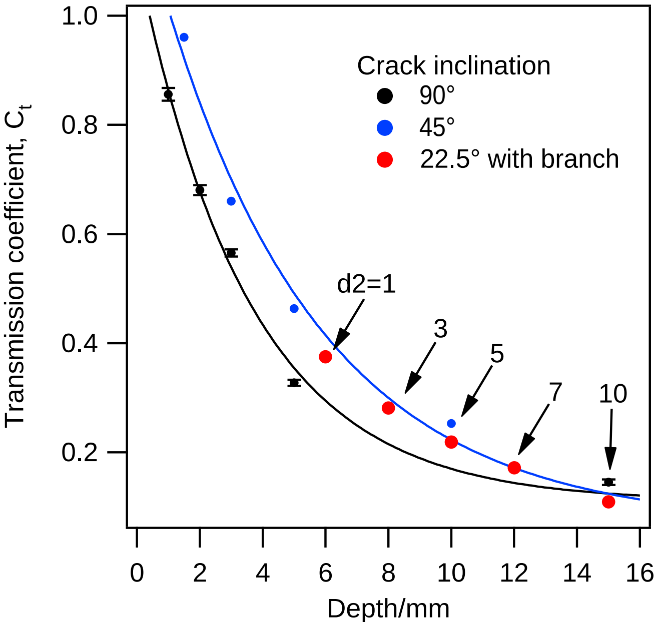

Figure 7.11: Calculated transmission coefficient of branch cracks with θ=22.5°, d_1 =5 mm appended on the experimental in-plane depth calibration curve for 90° and 45° cracks. The lengths of the branch d_2 are 1 mm, 3 mm, 5 mm, 7 mm and 10 mm.

7.5 Characterisation of branched cracks

Surface cracks with branches are more difficult to characterise than simple defects due to the complexity in the geometry. However, by scanning the area around the crack, a B-scan can be generated. In the B-scans a number of Rayleigh wave reflections can be observed to arrive at different times, and they are well separated from each other. The key to detecting the presence of a branch on the crack is to look for earlier arriving low frequency reflections from the branch, as a portion of the low frequency component of the incoming Rayleigh wave will be reflected directly from the branch before the wave enters the crack wedge section. This causes this part of the low frequency component to be reflected much earlier than the other frequency components. In terms of implementation in RCF crack detection, B-scans are sufficient to show the low frequency reflection, as described in Section 7.3. In addition, the spectrogram can also display the low frequency reflection clearly in the time-frequency domain. Detection of the presence of the branch is essential for analysing the integrity of that section of rail. Thus, as soon as the branch is detected and rail breakage may occur, the section of the rail needs to be replaced [3, 4].

The total depth of branched cracks, $d_1 + d_2$, can be estimated by calculating C_t and referring to the inclined crack depth calibration. This has been shown in Section 7.4, where the actual depth of branched cracks are close to the calibration made from he tinclined crack. Once the total depth is calculated, the length of the branch on the crack can be calculated as following; From the B-scan, the low frequency reflection interferes with the incoming Rayleigh wave at the position of the branch along the scan line. The position of the crack opening can be identified through the prominent enhancement pattern. The distance between these two positions is the length of the inclined part of the crack on the surface (horizontal projection on the surface). Let us say that this distance is l_{crack}. Using the knowledge that the RCF crack has θ of approximately 20°-30°, the value of d_1 can be calculated by considering the geometry between l_{crack} , d_1, and θ. Thus, d_1 can be calculated following the relationship in Equation 7.16. The length of the branch d_2 can then be calculated by subtracting d_1 from the total depth gained from the transmission measurement.

$$d_1 = l_{crack} tan\theta \tag{7.16}$$

Equation 7.16 gives a good estimation of d_1 and d_2 provided that the typical value of θ can be assumed, such as in the case of RCF cracks. For a more general case where the value of θ is not known, for example in SCC, θ can be estimated by calculating the enhancement factor ratio F_{ER} of the in-plane to the out-of-plane component (Equation 4.17). Details of the enhancement factor F_E measurement for each component are described in Section 4.5, and θ can be estimated using the plot of F_{ER} against θ in Figure 4.22.

The characterisation steps for branched cracks explained here can be incorperated into the crack characterisation procedure described in Section 5.2 for more detailed characterisation of surface cracks. A new category for the branched cracks can be added to the initial classification using B-scans, based on the low frequency reflection feature. Following this classification, the Rayleigh wave amplitude measurements lead to the calculation of C_t and F_{ER}. For branched cracks, the calculation of the total depth and the length of the branch are as explained above.

7.6 Conclusions

The interaction of Rayleigh waves with inclined cracks with vertical branches as illustrated in Figure 7.1, has been studied through the use of a two-dimensional FEA model. The presence of a branch at the tip of the inclined crack caused a portion of the low frequency incident Rayleigh wave to be reflected earlier than the other frequencies. A spectrogram was generated from the signal recorded at 40 mm distance relative to the crack opening. The frequency content in the time domain shown in the spectrogram confirmed that there is a separation between the low frequency reflection of Rayleigh waves from the branch, and the later reflections from the inclined section. In terms of practical applications, a B-scan generated from scanning a branched crack can be used as an initial indication to detect the crack. The arrival time calculations for different mode conversions during the interaction have been made, and show a good agreement with the B-scan. A characterisation method has been proposed for estimating the crack length, and can be incorporated with the procedure described in Section 5.2 for characterising full-width cracks.

Chapter 8

Conclusions

This chapter draws together the conclusions of the main findings described in this thesis, and discusses how they are relevant to the characterisation of surface cracks, particularly RCF-like cracks. Suggestions are made for potential future work.

8.1 Main findings

The comparison of the Rayleigh wave transmission coefficient measurements made between cracks growing normal to sample surface, and cracks growing inclined to the surface, proved that the transmission coefficient is different for these types of crack. This has consequences for the crack depth sizing method previously reported, which assumed that surface cracks grow normal to the surface [23]. Depth calibrations made using the calibration for normal crack should not be used for sizing inclined cracks, as it will cause underestimation of the depth. For accurate sizing of crack depth, a separate calibration is needed for inclined cracks. 45° calibration works well for most inclined cracks, and 90° calibration is best for near 90° cracks. This was explained in Chapter 4.

The B-scan images generated from scan data give an indication of whether the crack is normal to or inclined to the surface, through the enhancement pattern. Inclined cracks have a stronger enhancement compared to normal cracks, with an alternating black and white pattern that exists for a significant amount of time. The stronger and prominent enhancement pattern for inclined cracks is caused by Rayleigh wave mode conversion to Lamb-like waves at positions close to and within the near-field of the crack. Inclined cracks form a wedge section that has varying local thickness. As the Rayleigh wave propagates from the section that has the full thickness of the aluminum sample, to the section within the wedge, the frequency-thickness product changes rapidly causing mode conversion to Lamb-like waves. This was confirmed through the arrival time calculations of the Lamb wave fundamental anti-symmetric mode (A0). The signal enhancement caused by this mode conversion can be used as a fingerprint to identify inclined cracks in the B-scans (Chapter 4 and 5).

The enhancement factor in the in-plane and out-of-plane components can be used to estimate the crack inclination, with a reasonable accuracy, giving an idea of which calibration to use. Using the information from B-scans and Rayleigh wave amplitude analysis, the distinction can be made between normal and inclined cracks. Crack orientation can then be determined from the enhancement factor and estimation of the crack angle and better sizing of crack vertical depth can be made. An analysis procedure has been created for characterisaton of surface crack (Chapter 5).

A machine learning program has been developed through a collaboration with experts in Genetic Programming for pattern recognition. The program learns the specific pattern in the B-scan asscociated with a certain crack type, and use the information to classify a given B-scan image as defective/non-defective or normal/inclined. Input from an ultrasonic expert was required, in particular on what kind of pattern features can be used for the association with each crack. The main attention was given to the difference between the enhancement pattern for normal and inclined cracks. Other differences include the changes in the greyscale, wave arrival time, and the position of reflected waves. After training was conducted using a small set of data from experiments and FEA models, the program reached more than 90% accuracy in classifying image (Chapter 5). The level of accuracy and the running speed of the program show potential for use in automated recognition of B-scan images. In theory, this can be integrated with the amplitude based analysis, and can provide real-time analysis results. More work would be required to put this into realisation in practical terms.

EMAT measurements can be affected by the size of the crack width. This has been confirmed experimentally with measurements made on two cracks of widths smaller or comparable with the width of EMAT coil. For these cracks, Rayleigh waves incident on the crack are diffracted at each crack edge. Transmission of the Rayleigh wave is different compared to the transmission for full-width cracks, therefore the calibration made using either normal and inclined full-width cracks might not be accurate. Suggestion has been made to use a smaller width EMAT to detect small cracks, such that the crack width is comparable or larger than the width of EMAT (Chapter 6).

One realistic feature of real surface cracks is branching. For RCF-like cracks, the most dangerous case is when the branch grows vertically into the bulk of the rail, and can cause the rail to break. It is therefore important to detect the branch at the earliest opportunity before the condition get worse. A set of FEA models were computed to see the interaction of Rayleigh wave with a branched crack (Chapter 7). The results confirm that the presence of the branch can be detected from the low-frequency reflection from the branch. This is best viewed in B-scans, where a low-frequency reflection arrives earlier than the rest other reflections. Confirmation of the frequency content can be made using a spectrogram. The findings on the branched cracks model can be included in the procedure for characterising surface cracks presented in Chapter 5.

8.2 Development for future work

The study reported here has laid the theoretical framework in understanding the interaction of Rayleigh waves with inclined surface cracks, with a view for detecting and characterising RCF-like cracks. From here, the study can be taken further into various areas, as discussed below.

For better understanding of the Lamb-like wave mode conversion in the wedge, it would be interesting to study the interaction with incident Rayleigh waves of higher frequencies, greater than 1 MHz. In this way, higher order Lamb wave modes waves are expected to be present, depending on their frequency-thickness value. The calculation of the arrival time can be made for the higher frequency waves as well as the fundamental waves. High frequency broadband Rayleigh waves can be generated using laser ultrasound, and this would be useful for the experiments. It is also recommended to compare the behaviour of various modes of the Lamb-like wave progating in the wedge with Lamb wave in plates, which can help to better understand the sensitivity of detection.

The machine learning approach, genetic programming, has shown a viable use in B-scan classification, and the results from the small data set show a very high identification accuracy. It is worth exploring this method in more detail, using a larger data set with more diversity in the B-scan features. For example, B-scans with a high noise level, more backwall reflections, or smaller enhancement features could be used. A random B-scan image (greyscale plot generated randomly) can also be used to test the accuracy of the program. Statistical consideration should also be taken into account, for example, how many input images are required to acheive a significant result.

The work on the 2D FEA modelling of branched cracks can be taken further in two ways initially. Firstly, this can be done through experimental validation. Aluminium samples can be machined using EDM, for example, to have full-width branched cracks as described in Chapter 7. The experimental method would be the same as that described for full-width cracks in Chapter 3. Secondly, the model can be computed with branched cracks of more complex geometry, for example, the geometry of SCC illustrated in Figure 7.1, to allow consideration consideration of more realistic defects.

To overcome the issue of Rayleigh wave diffraction around narrow-width cracks, smaller EMATs can be used. The size of the EMATs must be smaller than the crack width so that the incident wave sees it as closer to an infinitely large crack. A study based on a report into RCF on rails, such as in [3], can be used as a guide to determine the optimal size. Small EMATs would require smaller permanent magnets and reduced coil dimensions. Therefore, the performance of the EMATs may be different and this should be a given specific attention. A different coil configuration may be needed for transmitter EMAT in order to generate the same bandwidth as the EMATs used in this study. Alternatively, if a different bandwidth is generated, a calibration can again be made on known artificial cracks, such as machined slots of known depths and inclinations. For application on rail tracks, small EMATs with high directionality could be used in an array to cover the full width of the track. Analysis would be required for each pair of transmitter and receiver EMATs, and the results could give more detailed information about any defect in the scanned area.

The analysis procedure described in Section 5.2 has been tested off-line in a laboratory environment, and has shown promising potential for real-time processing. More work is needed for integrating the different analysis steps into one main system for an on-line inspection application. The main challenge would be to include the image processing step for classifying the B-scans. Such a system should be tested and validated on a range of more realistic cracks that have RCF features. Following this, the study can then be extended to steel samples with other cracking geometry.

References

[1] R. Halmshaw, *Non-destructive Testing; Second Edition*, E. Arnold, Ed. Hodder & Stoughton, 1991.

[2] R. A. Cottis, "Guides to Good Practice in Corrosion Control: Stress Corrosion Cracking," Online: www.npl.co.uk/upload/pdf/stress/pdf, prepared at Corrosion and Protection Centre UMIST under contract from NPL for the Department of Trade and Industry.

[3] R. PLC, "Rolling contact fatigue in rails; a guide to current understanding and practice," Railtrack guideline: RT/PWG/001, 2001.

[4] D. F. Cannon, K. O. Edel, S. L. Grassie, and K. Sawley, "Rail defects: an overview," *Fatigue & Fracture of Engineering Materials & Structures*, vol. 26, pp. 865–886, 2003.

[5] D. E. Bray and R. K. Stanley, *Nondestructive evaluation: A Tool in Design, Manufacturing, and Service Revised Edition*, N. Stanton and A. Demby, Eds. CRC Press, 1997.

[6] W. R. Irving, *Continuous casting of steel.* Institute of Materials(Great Britain), 1993.

[7] D. E. Bray and D. McBride, *Nondestructive Testing Techniques*, R. D. Stewart, Ed. John Wiley & Sons, Inc., 1992.

[8] K. Milne, P. Cawley, P. B. Nagy, D. C. Wright, and A. Dunhill, "Ultrasonic Non-destructive Evaluation of Titanium Diffusion Bonds," *Journal of Nondestructive Evaluation*, vol. 30, no. 4, pp. 225–236, Dec 2011.

[9] D. J. Griffiths, *Introduction to Electrodynamics, 3rd Ed.* Prentice-Hall, Inc., 1999.

[10] T. V. Venkatasubramanian and B. A. Unvala, "An AC Potential Drop System For Monitoring Crack Length," *Journal Of Physics E-Scientific Instruments*, vol. 17, no. 9, pp. 765–771, 1984.

[11] H. Saguy and D. Rittel, "Flaw detection in metals by the ACPD technique: Theory and experiments," *NDT & E International*, vol. 40, no. 7, pp. 505 – 509, 2007.

[12] G. Sposito, P. Cawley, and P. B. Nagy, "An approximate model for three-dimensional alternating current potential drop analyses using a commercial finite element code," *NDT & E International*, vol. 43, no. 2, pp. 134–140, Mar 2010.

[13] S. Dixon, B. Cann, D. L. Carroll, Y. Fan, and R. S. Edwards, "Non-linear enhancement of laser generated ultrasonic Rayleigh waves by cracks," *Nondestructive Testing and Evaluation*, vol. 23, pp. 25–34, 2008.

[14] I. S. Grant and W. R. Phillips, *Electromagnetism*, F. M. D. J. Sandiford and A. C. Phillips, Eds. John Wiley & Sons, 1990.

[15] A. Sophian, G. Tian, D. Taylor, and J. Rudlin, "A feature extraction technique based on principal component analysis for pulsed Eddy current NDT," *NDT & E International*, vol. 36, no. 1, pp. 37–41, JAN 2003.

[16] F. Lingvall and T. Stepinski, "Automatic detecting and classifying defects during eddy current inspection of riveted lap-joints," *NDT & E International*, vol. 33, no. 1, pp. 47 – 55, 2000.

[17] W. Yin and A. J. Peyton, "Thickness measurement of non-magnetic plates using multi-frequency eddy current sensors," *NDT & E International*, vol. 40, pp. 43–48, 2007.

[18] J. Bowler, "Pulsed eddy current inversion for the determination of crack shape," in *Electromagnetic Nondestructive Evaluation*, 1997, pp. 263–269.

[19] R. S. Edwards, A. Sophian, S. Dixon, G. Tian, and X. Jian, "Dual EMAT and PEC non-contact probe: applications to defect testing," *NDT & E International*, vol. 39, no. 1, pp. 45–52, Jan 2006.

[20] J. Blitz and G. Simpson, *Ultrasonic Method of Non-destructive Testing; Non-destructive Evaluation Series*, S. Palmer and W. Lord, Eds. Chapman and hall, 1996.

[21] J. P. Charlesworth and J. A. G. Temple, *Engineering Application of Ultrasonic Time-of-Flight Diffraction*, M. J. White, Ed. Research Studies Press Ltd., 2001.

[22] J. L. Rose, *Ultrasonic Waves in Solid Media.* Cambridge University Press, 1999.

[23] R. S. Edwards, S. Dixon, and X. Jian, "Depth gauging of defects using low frequency wideband Rayleigh waves," *Ultrasonics*, vol. 44, no. 1, pp. 93–98, 2006.

[24] Y. Fan, S. Dixon, R. S. Edwards, and X. Jian, "Ultrasonic surface wave propagation and interaction with surface defects on rail track head," *NDT & E International*, vol. 40, no. 6, pp. 471–477, Sep 2007.

[25] P. A. Petcher and S. Dixon, "Parabola detection using matched filtering for ultrasound B-scans," *Ultrasonics*, vol. 52, no. 1, pp. 138–144, JAN 2012.

[26] P. A. Petcher and S. Dixon, "A modified Hough transform for removal of direct and reflected surface waves from B-scans," *NDT & E International*, vol. 44, no. 2, pp. 139–144, MAR 2011.

[27] S. E. Burrows, K. L. McAughey, R. S. Edwards, and S. Dixon, "Sol-gel prepared bismuth titanate for high temperature ultrasound transducers," *RSC Advances*, vol. 2, no. 9, pp. 3678–3683, 2012.

[28] R. Kazys, A. Voleisis, and B. Voleisiene, "High temperature ultrasonic trasnducers: review," *Ultragarsas(Ultrasound)*, vol. 63, pp. 7–17, 2008.

[29] S. Palmer and S. Dixon, "Industrially viable non-contact ultrasound," *Insight*, vol. 45, no. 3, pp. 211–217, 2003.

[30] R. E. Green, "Non-contact ultrasonic techniques," *Ultrasonics*, vol. 42, no. 1-9, pp. 9–16, APR 2004.

[31] I. Baillie, P. Griffith, X. Jian, and S. Dixon, "Implementing ultrasonic inspection system to find surface and internal defects in hot, moving steel using EMATs," in *Review of Progress in Quantitative Nondestructive Evaluation*, vol. 28, 2009, Proceedings Paper, pp. 1711–1718.

[32] W. Wright, D. Hutchins, G. Hayward, and A. Gachagan, "Ultrasonic imaging using laser generation and piezoelectric air-coupled detection," *Ultrasonics*, vol. 34, pp. 405 – 409, 1996.

[33] C. B. Scruby and L. E. Drain, *Laser Ultrasonics: Techniques and Applications.*, A. E. de Barr, Ed. Adam Hilger, Bristol, 1990.

[34] I. Arias and J. D. Achenbach, "Thermoelastic generation of ultrasound by line-focused laser irradiation," *International Journal Of Solids And Structures*, vol. 40, no. 25, pp. 6917–6935, DEC 2003.

[35] S. Dixon, C. Edwards, and S. B. Palmer, "Generation of ultrasound by an expanding plasma," *Journal Of Physics D-Applied Physics*, vol. 29, no. 12, pp. 3039–3044, DEC 14 1996.

[36] R. J. Dewhurst and Q. Shan, "Optical remote measurement of ultrasound," *Measurement Science & Technology*, vol. 10, no. 11, pp. R139–R168, NOV 1999.

[37] J. P. Monchalin, "Optical detection of ultrasound," *IEEE Transactions on Ultrasonics Ferroelectrics and Frequency Control*, vol. 33, no. 5, pp. 485–499, SEP 1986.

[38] W. Grandia and C. Fortunko, "NDE applications of air-coupled ultrasonic transducers," in *1995 IEEE Ultrasonics Symposium Proceedings*, 1995, pp. 697–709.

[39] T. J. Robertson, D. A. Hutchins, and D. R. Billson, "Capacitive air-coupled cylindrical transducers for ultrasonic imaging applications," *Measurement Science & Technology*, vol. 13, no. 5, pp. 758–769, MAY 2002.

[40] W. M. D. Wright and D. A. Hutchins, "Air-coupled ultrasonic testing of metals using broadband pulses in through-transmission," *Ultrasonics*, vol. 37, no. 1, pp. 19–22, JAN 1999.

[41] X. Jian, S. Dixon, R. S. Edwards, and J. Reed, "Coupling mechanism of electromagnetic acoustical transducers for ultrasonic generation," *Journal of The Acoustical Society of America*, vol. 119, pp. 2693–2701, 2006.

[42] M. Hirao and H. Ogi, *EMATs for Science and Industry.* Kluwer Academic Publishers, 2003.

[43] R. Ribichini, F. Cegla, P. B. Nagy, and P. Cawley, "Experimental and numerical evaluation of electromagnetic acoustic transducer performance on steel materials," *NDT & E International*, vol. 45, pp. 32–38, 2012.

[44] F. Hernandez-Valle and S. Dixon, "Initial tests for designing a high temperature EMAT with pulsed electromagnet," *NDT & E International*, vol. 43, no. 2, pp. 171–175, MAR 2010.

[45] S. Ghosh and V. Kain, "Effect of surface machining and cold working on the ambient temperature chloride stress corrosion cracking susceptibility of AISI 304L stainless steel," *Materials Science and Engineering: A*, vol. 527, pp. 679 – 683, 2010.

[46] Office of Rail Regulation, "Train Derailment at Hatfield: A Final Report by the Independant Investigation Board," Tech. Rep., July 2006.

[47] S. L. Grassie, "Squats and squat-type defects in rails: the understanding to date," *Proceedings of the Institution of Mechanical Engineers, Part F: Journal of Rail and Rapid Transit*, vol. 226, pp. 235–242, 2012.

[48] A. Turnbull, "Stress Corrosion Cracking: Mechanisms," in *Encyclopedia of Materials: Science and Technology (Second Edition)*, second edition ed., E. in Chief:Â Â K. H. JÃŒrgen Buschow, R. W. Cahn, M. C. Flemings, B. I. (print), E. J. Kramer, S. Mahajan, , and P. V. (updates), Eds. Oxford: Elsevier, 2001, pp. 8886 – 8891.

[49] R. Newman, "2.09 - Stress Corrosion Cracking," in *Shreir's Corrosion*, E. in Chief:Â Â Tony J.A. Richardson, Ed. Oxford: Elsevier, 2010, pp. 864 – 901.

[50] Y. Huang and J. Titchmarsh, "TEM investigation of intergranular stress corrosion cracking for 316 stainless steel in PWR environment," *Acta Materialia*, vol. 54, pp. 635 – 641, 2006.

[51] K. R. Trethewey, "Some observations on the current status in the understanding of stress-corrosion cracking of stainless steels," *Materials & Design*, vol. 29, no. 2, pp. 501 – 507, 2008.

[52] X. Jian, Y. Fan, R. S. Edwards, and S. Dixon, “Surface-breaking crack gauging with the use of laser-generated Rayleigh waves,” *Journal of Applied Physics*, vol. 100, no. 6, SEP 15 2006.

[53] I. A. Viktorov, *Rayleigh Waves and Lamb Waves-Physical Theory and Application*. Plenum, New York, 1967.

[54] B. Q. Vu and V. K. Kinra, “Diffraction of Rayleigh-waves in a half-space .1. Normal edge crack,” *Journal Of The Acoustical Society Of America*, vol. 77, pp. 1425–1430, 1985.

[55] M. Hirao, H. Fukuoka, and Y. Miura, “Scattering of Rayleigh surface waves by edge cracks: Numerical simulation and experiment,” *Journal Of The Acoustical Society Of America*, vol. 72, pp. 602–606, 1982.

[56] D. A. Mendelsohn, J. D. Achenbach, and l. M. Keer, “Scattering of elastic-waves by a surface-breaking crack,” *Wave Motion*, vol. 2, pp. 277–292, 1980.

[57] J. L. Blackshire and S. Sathish, “Near-field ultrasonic scattering from surface-breaking cracks,” *Applied Physics Letters*, vol. 80, no. 18, pp. 3442–3444, MAY 6 2002.

[58] J. K. Na and J. L. Blackshire, “Interaction of rayleigh surface waves with a tightly closed fatigue crack,” *NDT & E International*, vol. 43, no. 5, pp. 432 – 439, 2010.

[59] R. Blake and L. Bond, “Rayleigh wave scattering from surface features: wedges and down-steps,” *Ultrasonics*, vol. 28, no. 4, pp. 214 – 228, 1990.

[60] J. A. Cooper, R. A. Crosbie, R. J. Dewhurst, A. D. W. Mckie, and S. B. Palmer, “Surface acoustic-wave interactions with cracks and slots - a noncontacting study using lasers,” *IEEE Transactions On Ultrasonics Ferroelectrics And Frequency Control*, vol. 33, pp. 462–470, 1986.

[61] J. D. Achenbach, A. K. Gautesen, and D. A. Mendelsohn, “Ray analysis of surface-wave interaction with an edge crack,” *IEEE Transactions on Sonics and Ultrasonics*, vol. 27, pp. 124–129, 1980.

[62] L. Bond, “A computer model of the interaction of acoustic surface waves with discontinuities,” *Ultrasonics*, vol. 17, pp. 71 – 77, 1979.

[63] R. Blake and L. Bond, "Rayleigh wave scattering from surface features: up-steps and troughs," *Ultrasonics*, vol. 30, no. 4, pp. 255 – 265, 1992.

[64] V. Babich, V. Borovikov, L. Fradkin, V. Kamotski, and B. Samokish, "Scatter of the Rayleigh waves by tilted surface-breaking cracks," *NDT & E International*, vol. 37, no. 2, pp. 105–109, MAR 2004.

[65] B. V. Budaev and D. B. Bogy, "Rayleigh-wave scattering by a wedge," *Wave Motion*, vol. 22, pp. 239–257, 1995.

[66] B. V. Budaev and D. B. Bogy, "Rayleigh wave scattering by a wedge .2." *Wave Motion*, vol. 24, pp. 307–314, 1996.

[67] B. V. Budaev and D. B. Bogy, "Rayleigh wave scattering by a wedge. II (vol 24, pg 307, 1996)," *Wave Motion*, vol. 35, p. 275, 2002.

[68] L. Knopoff and A. F. Gangi, "Transmission and reflection of Rayleigh waves by wedges," *Geophysics*, vol. XXV, pp. 1203–1214, 1960.

[69] R. S. Edwards, S. Dixon, and X. Jian, "Enhancement of the Rayleigh wave signal at surface defects," *Journal Of Physics D-applied Physics*, vol. 37, no. 16, pp. 2291–2297, 2004.

[70] R. S. Edwards, X. Jian, Y. Fan, and S. Dixon, "Signal enhancement of the in-plane and out-of-plane Rayleigh wave components," *Applied Physics Letters*, vol. 87, no. 19, 2005.

[71] R. S. Edwards, B. Dutton, A. R. Clough, and M. H. Rosli, "Enhancement of ultrasonic surface waves at wedge tips and angled defects," *Applied Physics Letters*, vol. 99, no. 9, p. 094104, 2011.

[72] X. Jian, S. Dixon, N. Guo, and R. Edwards, "Rayleigh wave interaction with surface-breaking cracks," *Journal Of Applied Physics*, vol. 101, no. 6, 2007.

[73] A. R. Clough, B. Dutton, and R. S. Edwards, "Ultrasonic Rayleigh wave enhancement from angled defects in aluminium," in *Review of Progress in Quantitative Nondestructive Evaluation*, vol. 30, 2011, pp. 137–144.

[74] B. Dutton, A. R. Clough, and R. S. Edwards, "Near Field Enhancements from Angled Surface Defects; A Comparison of Scanning Laser Source and Scanning

Laser Detection Techniques," *Journal of Nondestructive Evaluation*, vol. 30, no. 2, pp. 64–70, JUN 2011.

[75] X. Jian, S. Dixon, N. Guo, R. S. Edwards, and M. Potter, "Pulsed Rayleigh wave scattered at a surface crack," *Ultrasonics*, vol. 44, pp. e1131–e1134, 2006.

[76] S. Boonsang and R. Dewhurst, "Enhancement of laser-ultrasound/electromagnetic-acoustic transducer signals from Rayleigh wave interaction at surface features," *Applied Physics Letters*, vol. 82, pp. 3348–3350, 2003.

[77] S. Boonsang and R. Dewhurst, "Signal enhancement in Rayleigh wave interactions using a laser-ultrasound/EMAT imaging system," *Ultrasonics*, vol. 43, pp. 512–523, 2005.

[78] B. Dutton, M. H. Rosli, and R. S. Edwards, "Defect feature extraction using surface wave interactions and time-frequency behaviour," in *Review of Progress in Quantitative Nondestructive Evaluation*, vol. 29, 2010, pp. 647–654.

[79] B. Dutton, A. Clough, M. Rosli, and R. Edwards, "Non-contact ultrasonic detection of angled surface defects," *NDT & E International*, vol. 44, no. 4, pp. 353 – 360, 2011.

[80] C. Ni, Y. Shi, Z. Shen, J. Lu, and X. Ni, "An analysis of angled surface-breaking crack detection by dual-laser source generated ultrasound," *NDT & E International*, vol. 43, no. 6, pp. 470–475, SEP 2010.

[81] W. Meeker, V. Chan, R. Thompson, and C. Chiou, "A methodology for predicting probability of detection for ultrasonic testing," in *Review of Progress in Quantitative Nondestructive Evaluation*, vol. 20, 2001, pp. 1972–1978.

[82] T. M. Mitchell, *Machine Learning*, C. L. Liu, Ed. McGraw-Hill Companies, Inc., 1997.

[83] E. P. Moura, R. R. Silva, M. H. S. Siqueira, and J. M. A. Rebello, "Pattern recognition of weld defects in preprocessed TOFD signals using linear classifiers," *Journal of Nondestructive Evaluation*, vol. 23, pp. 163–172, 2004.

[84] F. Bettayeb, T. Rachedi, and H. Benbartaoui, “An improved automated ultrasonic NDE system by wavelet and neuron networks,” *Ultrasonics*, vol. 42, pp. 853–858, 2004.

[85] S. Sambath, P. Nagaraj, and N. Selvakumar, “Automatic Defect Classification in Ultrasonic NDT Using Artificial Intelligence,” *Journal of Nondestructive Evaluation*, vol. 30, pp. 20–28, 2011.

[86] S. G. Pierce, K. Worden, and G. Manson, “A novel information-gap technique to assess reliability of neural network-based damage detection,” *Journal of Sound And Vibration*, vol. 293, no. 1-2, pp. 96–111, MAY 30 2006.

[87] G. P. Zhang, “Neural networks for classification: a survey,” *IEEE Transactions on Systems, Man and Cybernetics - Part C: Applications and Reviews*, vol. 30, pp. 451–462, 2000.

[88] H. D. Cheng, J. Shan, W. Ju, Y. Guo, and L. Zhang, “Automated breast cancer detection and classification using ultrasound images: A survey,” *Pattern Recognition*, vol. 43, no. 1, pp. 299–317, JAN 2010.

[89] A. Fathi and A. Aghakouchak, “Prediction of fatigue crack growth rate in welded tubular joints using neural network,” *International Journal of Fatigue*, vol. 29, no. 2, pp. 261 – 275, 2007.

[90] K. Worden, G. Manson, G. Hilson, and S. Pierce, “Genetic optimisation of a neural damage locator,” *Journal of Sound and Vibration*, vol. 309, pp. 529 – 544, 2008.

[91] G. Manson, K. Worden, and D. Allman, “Experimental validation of a structural health monitoring methodology. Part III. Damage location on an aircraft wing,” *Journal of Sound And Vibration*, vol. 259, no. 2, pp. 365–385, JAN 9 2003.

[92] J. D. N. Cheeke, *Fundamentals and Application of Ultrasonic Waves*, D. Basu, Ed. CRC Press, 2002.

[93] B. A. Auld, *Acoustic fields and waves in solids, Vol I.* Krieger Publishing Company, 1990.

[94] L. Rayleigh, “On Waves Propagated along the Plane Surface of an Elastic Solid,” *Proceedings of the London Mathematical Society*, vol. s1-17, no. 1, pp. 4–11, 1885.

[95] S. Dixon, C. Edwards, and S. B. Palmer, "Rayleigh wave dispersion on extruded aluminium," *Insight*, vol. 40, pp. 632–634, 1998.

[96] M. Niethammer, L. Jacobs, J. Qu, and J. Jarzynski, "Time-frequency representation of Lamb waves using the reassigned spectrogram," *Journal of the Acoustical Society of America*, vol. 107, pp. L19–L24, 2000.

[97] M. Niethammer, L. Jacobs, J. Qu, and J. Jarzynski, "Time-frequency representations of Lamb waves," *Journal of the Acoustical Society of America*, vol. 109, no. 5, Part 1, pp. 1841–1847, MAY 2001.

[98] S. Dixon and S. Palmer, "Wideband low frequency generation and detection of Lamb and Rayleigh waves using electromagnetic acoustic transducers (EMATs)," *Ultrasonics*, vol. 42, no. 10, pp. 1129–1136, AUG 2004.

[99] G. Alers, "A history of EMATS," in *Review of Progress in Quantitative Nondestructive Evaluation*, vol. 27, 2008, Proceedings Paper, pp. 801–808.

[100] X. Jian, S. Dixon, K. Quirk, and K. T. V. Grattan, "Electromagnetic acoustic transducers for in- and out-of plane ultrasonic wave detection," *Sensors and Actuators A-physical*, vol. 148, no. 1, pp. 51–56, NOV 4 2008.

[101] X. Jian, S. Dixon, R. S. Edwards, K. Quirk, and I. Baillie, "Effect on ultrasonic generation of a backplate in electromagnetic acoustic transducers," *Journal of Applied Physics*, vol. 102, no. 2, JUL 15 2007.

[102] X. Jian and S. Dixon, "Enhancement of EMAT and eddy current using a ferrite back-plate," *Sensors and Actuators A-physical*, vol. 136, no. 1, pp. 132–136, MAY 1 2007.

[103] R. H. Randall, F. C. Rose, and C. Zener, "Intercrystalline thermal currents as a cource of internal friction," *Phys. Rev.*, vol. 56, pp. 343–348, 1939.

[104] D. O. Thompson and D. K. Holmes, "Dislocation contribution to the temperature dependence of the internal friction and young's modulus of copper," *Journal of Applied Physics*, vol. 30, no. 4, pp. 525–541, 1959.

[105] E. R. Dobbs, *Electromagnetic generation of ultrasonic waves, in Physical Acoustics X*. Academic Press, New York, 1973, vol. 10.

[106] R. Ribichini, P. Nagy, and H. Ogi, "The impact of magnetostriction on the transduction of normal bias field emats," *NDT & E International*, vol. 51, pp. 8 – 15, 2012.

[107] M. Klein, G. Bacher, A. Grunnet-Jepsen, D. Wright, and W. Moerner, "Homodyne detection of ultrasonic surface displacements using two-wave mixing in photorefractive polymers," *Optics Communications*, vol. 162, pp. 79–84, 1999.

[108] D. R. Carvalho and A. A. Freitas, "A hybrid decision tree/genetic algorithm method for data mining," *Information Sciences*, vol. 163, no. 1-3, pp. 13–35, Jun14 2004.

[109] M. Friedl and C. Brodley, "Decision tree classification of land cover from remotely sensed data," *Remote Sensing of Environment*, vol. 61, no. 3, pp. 399 – 409, 1997.

[110] M. Amarnath, V. Sugumaran, and H. Kumar, "Exploiting sound signals for fault diagnosis of bearings using decision tree," *Measurement*, vol. 46, no. 3, pp. 1250–1256, APR 2013.

[111] M. Markey, G. Tourassi, and C. Floyd Jr., "Decision tree classification of proteins identified by mass spectrometry of blood serum samples from people with and without lung cancer," *Proteomics*, vol. 3, no. 9, pp. 1678–1679, 2003.

[112] S. Thomassey and A. Fiordaliso, "A hybrid sales forecasting system based on clustering and decision trees ," *Decision Support Systems*, vol. 42, no. 1, pp. 408 – 421, 2006.

[113] J. R. Quinlan, *C4.5: programs for machine learning.* Morgan Kaufmann, San Francisco, 1993.

[114] M. Hall, E. Frank, G. Holmes, B. Pfahringer, P. Reuteman, and I. H. Witten, "The weka data mining software; an update," *SIGKDD Explorations*, vol. 11, 2009.

[115] *AIR-155-TWM Laser Ultrasonic Receiver; FHY and FHPS measurement heads; Splitter drawer with guide module; Fiber probe laser: Instuction manual for University of Warwick*, 3rd ed., Intelligent Optical System, Inc., 2520 W.237th Street, Torrance, CA 90505, September 2009. [Online]. Available: http://www.intopsys.com

[116] X. Jian, S. Dixon, R. S. Edwards, and J. Morrison, "Coupling mechanism of an EMAT," *Ultrasonics*, vol. 44, pp. E653–E656, 2006.

[117] J. P. Morrison, S. Dixon, M. D. G. Potter, and X. Jian, "Lift-off compensation for improved accuracy in ultrasonic lamb wave velocity measurements using electromagnetic acoustic transducers (EMATs)," *Ultrasonics*, vol. 44, pp. E1401–E1404, 2006.

[118] W. Hassan and W. Veronesi, "Finite element analysis of rayleigh wave interaction with finite-size, surface-breaking cracks," *Ultrasonics*, vol. 41, pp. 41 – 52, 2003.

[119] M. H. Rosli, R. S. Edwards, and Y. Fan, "In-plane and out-of-plane measurements of Rayleigh waves using EMATs for characterising surface cracks," *NDT & E International*, vol. 49, pp. 1–9, 2012.

[120] R. S. Edwards, S. Dixon, and X. Jian, "Characterisation of defects in the railhead using ultrasonic surface waves," *NDT & E International*, vol. 39, no. 6, pp. 468–475, 2006.

[121] M. H. Rosli, R. S. Edwards, B. Dutton, C. G. Johnson, and P. T. Cattani, "Identifying surface angled cracks on aluminium bar using EMATs and automated computer system," in *Review of Progress in Quantitative Nondestructive Evaluation*, vol. 29, 2010, Proceedings Paper, pp. 1593–1600.

[122] M. El-Kettani, F. Luppe, and A. Guillet, "Guided waves in a plate with linearly varying thickness: experimental and numerical results," *Ultrasonics*, vol. 42, no. 1-9, pp. 807–812, 2004.

[123] C. M. Bishop, *Pattern Recognition and Machine Learning.* Springer, 2006.

[124] I. T. Nabney, *NETLAB: algorithms for pattern recognitions.* Springer, 2002.

[125] C. M. Bishop, *Neural Networks for Pattern Recognition.* Oxford University Press, 1995.

[126] R. Thomas, B. W. Drinkwater, and D. Liaptsis, "The reflection of ultrasound from partially contacting rough surfaces," *Journal Of The Acoustical Society Of America*, vol. 117, no. 2, pp. 638–645, 2005.

[127] D. Liaptsis, B. W. Drinkwater, and R. Thomas, “The interaction of oblique incidence ultrasound with rough, partially contacting interfaces,” *Nondestructive Testing and Evaluation*, vol. 21, no. 3-4, pp. 109–121, Sep-Dec 2006.

[128] O. Dupond, V. Duwig, and T. Fouquet, “Influence of stress corrosion crack morphology on ultrasonic examination performances,” in *Review of Progress in Quantitative Nondestructive Evaluation*, vol. 28, 2009, pp. 89–96.